PACIFIC EARTHQUAKE ENGINEERING
RESEARCH CENTER

Envelopes for Seismic Response Vectors

Charles Menun

Armen Der Kiureghian

PEER 1999/08
JULY 1999

Technical Report Documentation Page

1. Report No.	2. Government Accession No.	3. Recipient's Catalog No.
UCB/PEER 1999/08		

4. Title and Subtitle	5. Report Date
ENVELOPES FOR SEISMIC RESPONSE VECTORS	July 1999
	6. Performing Organization Code: UCB/ENG 9374
7. Author's	8. Performing Organization Report No.: UCB/PEER 1999/08
Charles Menun and Armen Der Kiureghian	
9. Performing Organization Name and Address: Pacific Earthquake Engineering Research Center (PEER), University of California, Richmond Field Station, 1301 South 46th Street, Richmond, CA 94804	10. Work Unit No. (TRAIS)
	11. Contract or Grant No.: RTA-59A131
12. Sponsoring Agency Name and Address: California Department of Transportation (Caltrans), Engineering Service Center - MS#9, 1801 30th Street, Sacramento, CA 95816	13. Type of Report and Period Covered: Final report 6/94-6/30/99
	14. Sponsoring Agency Code

15. Supplementary Notes

This study was sponsored by the California Department of Transportation (Caltrans).

16. Abstract

In the design or analysis of structures for seismic loads, the effects of forces acting simultaneously in a member must be considered. The most common example is the interaction of bending moments and axial load in a column. The usual response spectrum method provides the maximum values of individual responses, but the critical combination of these responses may not involve any of these maxima.

In this report, a response-spectrum-based procedure for predicting the envelope that bounds two or more responses in a linear structure is developed. It is shown that for an assumed orientation of the principal axes along which the ground motion components are uncorrelated, this envelope is an ellipsoid. For the case when the orientation of the principal axes is unknown, a "supreme" envelope is derived that corresponds to the most critical orientation of the axes. The coordinates of these envelopes are computed by using values available in conventional response spectrum analyses, i.e., response spectral shapes in one, two or three directions, and the modal properties of the structure. The response envelope can be superimposed on a capacity surface to determine the adequacy of a given design. The accuracy of the elliptical envelope for linear structures is examined by means of comparison with time-history analyses using artificial and recorded ground motions. It is found that the elliptical envelope has a level of accuracy that is commensurate with its response spectrum bases. The significance of the proposed envelopes is demonstrated by designing the columns of an example reinforced concrete bridge by the proposed and conventional methods. Savings as high as 45% in the required reinforcement ratio are gained by use of the proposed method.

Linear analyses are appropriate for serviceability limit states associated with moderate-intensity ground motions. However, when a structure is subjected to high-intensity ground motions, its behavior is expected to be nonlinear and, hence, the response spectrum method cannot be used. Furthermore, the envelope bounding a vector of responses is usually not elliptical. In this study, a comprehensive investigation is carried out using time-history analyses with artificial and recorded ground motions to simulate and examine the envelopes that bound vectors of seismic responses in a nonlinear structure. New and practical insight into the behavior of nonlinear structures and the effectiveness of current seismic design methodologies is gained by examining these response envelopes in the multidimensional response space. Particularly noteworthy are (1) the adverse effects of near-fault ground motions on the nonlinear response of the structure, (2) the effectiveness of plastic hinges as fuses to limit the forces transmitted to critical elements of the structure and (3) the use of simulated response envelopes to identify the spatial distribution of plastic hinges in the structure and the expected sway mechanism under severe seismic loading.

17. Key Words	18. Distribution Statement
correlation, envelope, interaction, out-crossing, peak response, response vector, response spectrum method, seismic design, seismic analysis	No restrictions. This document is available to the public through the National Technical Information Service, Springfield, Virginia 22161

19. Security Classif. (of this report)	20. Security Classif. (of this page)	21. No. of Pages	22. Price
Unclassified	Unclassified	210	

Envelopes for Seismic Response Vectors

Charles Menun and Armen Der Kiureghian

A report on research sponsored by the California Department of Transportation
Contract RTA-59A131

PEER Report 1999/08
Pacific Earthquake Engineering Research Center
College of Engineering
University of California, Berkeley

July 1999

ABSTRACT

In the design or analysis of structures for seismic loads, the effects of forces acting simultaneously in a member must be considered. The most common example is the interaction of bending moments and axial load in a column. The usual response spectrum method provides the maximum values of individual responses, but the critical combination of these responses may not involve any of these maxima.

In this report, a response-spectrum-based procedure for predicting the envelope that bounds two or more responses in a linear structure is developed. It is shown that for an assumed orientation of the principal axes along which the ground motion components are uncorrelated, this envelope is an ellipsoid. For the case when the orientation of the principal axes is unknown, a "supreme" envelope is derived that corresponds to the most critical orientation of the axes. The coordinates of these envelopes are computed by using values available in conventional response spectrum analyses, i.e., response spectral shapes in one, two or three directions, and the modal properties of the structure. The response envelope can be superimposed on a capacity surface to determine the adequacy of a given design.

The accuracy of the elliptical envelope for linear structures is examined by means of comparison with time-history analyses using artificial and recorded ground motions. It is found that the elliptical envelope has a level of accuracy that is commensurate with its response spectrum bases. The significance of the proposed envelopes is demonstrated by designing the columns of an example reinforced concrete bridge by the proposed and conventional methods. Savings as high as 45% in the required reinforcement ratio are gained by use of the proposed method.

Linear analyses are appropriate for serviceability limit states associated with moderate-intensity ground motions. However, when a structure is subjected to high-intensity ground motions, its behavior is expected to be nonlinear and, hence, the response spectrum method cannot be used. Furthermore, the envelope bounding a vector of responses is usually not elliptical. In this study, a comprehensive investigation is carried out using time-history analyses with artificial and recorded ground motions to simulate and examine the envelopes that bound vectors of seismic responses in a nonlinear structure. New and practical insight into the behavior of nonlinear structures and the effectiveness of current seismic design methodologies is gained by examining these response envelopes in the multidimensional response space. Particularly noteworthy are (1)

the adverse effects of near-fault ground motions on the nonlinear response of the structure, (2) the effectiveness of plastic hinges as fuses to limit the forces transmitted to critical elements of the structure and (3) the use of simulated response envelopes to identify the spatial distribution of plastic hinges in the structure and the expected sway mechanism under severe seismic loading.

ACKNOWLEDGMENTS

The findings, conclusions and recommendations contained in this report were developed as part of Task 3 of the Coordinated Structural Analysis and Design Program at the University of California at Berkeley entitled "Combination of Multi-Axial Forces in Seismic Design." This project was funded by the California Department of Transportation under Contract No. RTA-59A131, whose support is gratefully acknowledged. The work was conducted under the direction of Mr. Li-Hong Sheng at the Caltrans Engineering Service Center. The authors thank him for his leadership and support of this research.

This work was supported in part by the Pacific Earthquake Engineering Research Center through the Earthquake Engineering Research Centers Program of the National Science Foundation under Award number EEC-9701568.

CONTENTS

LIST OF FIGURES

LIST OF TABLES

1 Introduction

1.1 MOTIVATION

In earthquake engineering, the response spectrum method is commonly used to estimate the maximum values of responses acting in linear structures subjected to seismic ground motions. With this method, individual peak modal responses are obtained using a prescribed set of response spectra that characterize the ground motion expected at the location of the structure. These modal maxima are then combined in an appropriate manner to estimate the maximum values of the responses of interest. Combination rules that properly account for correlations between modal responses and between components of ground motion are well developed (e.g., see Rosenblueth and Elorduy, 1969; Singh and Chu, 1976; Der Kiureghian, 1981; Gupta, 1990; Singh and Maldonado, 1991; Der Kiureghian and Nakamura, 1993; Menun and Der Kiureghian, 1998). The 1996 edition of the "Blue Book" issued by the Structural Engineering Association of California observes that response spectrum analysis "is the preferred method (of dynamic analysis) for most buildings" (SEAOC, 1996, page 139).

The conventional response spectrum method is ideally suited to the design or analysis of structural elements that are controlled by the maximum value of a single response quantity; e.g., a beam governed by the maximum bending moment. For members in which the simultaneous action of multiple seismic responses must be considered, e.g., a column subjected to an axial load and bending moments, the critical combination of responses may not coincide with the maximum value of any of the responses. For such cases, an envelope that bounds the evolution of the vector of seismic responses in time is desirable. This envelope can then be superimposed over the capacity surface of the member (commonly known as the interaction diagram) to determine the critical combination of responses. In the current practice, it is common to use the response-spectrum-based estimates of the individual response maxima to construct a rectangular

envelope for this purpose. As shown later, this envelope provides an upper bound that can be overly conservative for many design situations.

In this report, a response-spectrum-based procedure for predicting the envelope that bounds a vector of seismic responses in a linear structure is developed. When the principal directions along which the ground motion components are uncorrelated are known, the envelope that bounds a vector of seismic responses in a linear structure is an ellipsoid that is inscribed within the rectangular envelope described above. Naturally, the elliptical envelope provides a tighter bound on a vector response process than the rectangular envelope. Consequently, improved economy in the design of elements that resist the simultaneous action of multiple seismic responses may be achieved by using the elliptical envelope, rather than the conventional rectangular envelope, for the design calculations. When the principal directions of ground motion are not known in advance, which is normally the case, the uncertainty in the orientation of these directions must also be addressed. We do this by constructing a "supreme" envelope that bounds the union of the elliptical envelopes for all orientations of the principal directions. The supreme envelope is naturally more conservative than any of the elliptical envelopes that it bounds. However, we will see that the supreme envelope is not necessarily overly conservative. In fact, improved economy in design can be realized by using the supreme envelope rather than the conventional rectangular envelope.

Response-spectrum-based procedures are valuable tools for the seismic analysis and design of structures, particularly in the light of the recent recommendation by SEAOC (1995) to consider the effects of serviceability level ground motions during which the structure is to remain linear. However, it is usually uneconomical to proportion structures to remain linear during large magnitude events. Unfortunately, the use of modal superposition in the response spectrum method precludes the direct consideration of nonlinear behavior. The approach usually taken to circumvent this problem is to scale the response spectrum down by a "structural system factor" $R_w > 1$ that is "a measure of the ability of the system to sustain cyclic inelastic deformations without collapse" (SEAOC, 1996, page 123). The structure is then designed to remain linear under this reduced level of seismic input. In this way, the underlying assumption of linear behavior in the response spectrum method is satisfied. However, because the actual ground motion will be more intense than that assumed, the structural elements are expected to yield and must therefore be detailed to sustain the level of nonlinear deformation anticipated for the value of R_w assumed.

Consequently, there is a need to examine the ways in which the envelope that bounds a vector of seismic responses in a linear structure changes when nonlinear elements are introduced. The additional insight gained from such investigations will help us better understand the nonlinear behavior of structures and the effectiveness of current seismic design methodologies.

1.2 OBJECTIVES AND SCOPE

The primary objective of this report is to improve the procedures currently used by structural engineers to design elements that resist the simultaneous action of multiple seismic responses. This objective is achieved by conducting a detailed study of the envelopes that bound vectors of seismic responses in linear and nonlinear structures and by developing ways of incorporating the information provided by these envelopes in the seismic analysis or design of structures. While the issues addressed in this study are closely related to the vector-outcrossing problem in the field of structural reliability, this approach is numerically intensive and involves concepts that are generally not well known or fully understood by the majority of practicing engineers. It is therefore unlikely that any procedure founded upon this reliability-based approach would be adopted by the engineering community. Thus, the emphasis in this work is to extend and improve existing procedures routinely used by practicing engineers.

For linear structures, we formulate a response-spectrum-based procedure for predicting the envelope that bounds a vector of seismic responses. In accordance with its response spectrum basis, the envelope is statistical in nature, i.e., in any given direction in the response space, there is a finite probability that the response vector will exceed the envelope. As discussed earlier, two envelopes are developed: an elliptical envelope for the case in which the principal directions of ground motion are known, and a supreme envelope for the case in which the orientation of the principal directions is uncertain. Closed-form procedures for computing the coordinates of these envelopes using quantities readily available in conventional response spectrum analyses are derived and their accuracy is evaluated for two example structures by means of comparison with time-history analyses using artificial and recorded ground motions. In addition, generic algorithms are developed to facilitate the use of these envelopes in the analysis or design of structures. Finally, the significance of using the elliptical or supreme envelope, rather than the conventional rectangular envelope, in the design of reinforced concrete columns subjected to axial loads and bi-axial bending moments is demonstrated.

For nonlinear structures, the response spectrum method cannot be used to predict the envelopes that bound response vectors. Instead, time-history analyses must be used to simulate these envelopes. In this study, we consider a steel moment frame building in which yielding can occur only in the beam-column connections and at the bases of the columns. Elastic-perfectly-plastic, non-degrading hysteretic elements are introduced at these locations. Geometric nonlinearity due to column buckling is not considered. The envelopes bounding selected response quantities are simulated and studied in detail by using ensembles of artificial and recorded ground motions in order to gain insight into the nonlinear behavior of the structure and the effectiveness of current seismic design methodologies. The results obtained from this study suggest ways in which the information provided by the envelopes that bound seismic response vectors can be used to improve the design of structures located in seismic environments.

1.3 NEW ADVANCES IN THE REPORT

When the principal directions along which the ground motion components are uncorrelated are known, the response-spectrum-based envelope developed in this report is identical to that derived previously by Gupta and Singh (1977) and Anastassiadis (1993). However, this study advances the topic beyond that presented in these earlier works in the following ways:

(1) We use the theory of random vibrations to establish a response-spectrum-based procedure for predicting the peak values of multiple response quantities and the correlation structure that exists between them. This mathematical basis is missing in the previous works, which start with the conventional response spectrum method as their bases.

(2) We develop the response-spectrum-based envelope in a physically intuitive manner, which provides insight as to why the resulting ellipsoid is an appropriate upper bound on the possible combination of responses when the principal directions of ground motion are known. Similar physically motivated interpretations of the envelope are not provided in the previous developments.

(3) Recognizing that the principal directions of ground motion are normally not known in advance, we derive the supreme envelope that accounts for the uncertainty in the orientation of these directions. This uncertainty in the principal directions of ground motion has not been addressed for vector responses in earlier works.

(4) A comprehensive series of time-history analyses are performed in this study to evaluate the accuracy of the elliptical envelope. Attempts to verify the accuracy of the procedure were not conducted in the previous works.

(5) We develop new algorithms to facilitate the use of the elliptical and supreme envelopes with capacity surfaces in order to determine the adequacy of a design. Clearly, such algorithms are necessary if the information that is provided by a response envelope is to be used effectively.

(6) We investigate whether the use of the elliptical or supreme envelope, rather than the rectangular envelope commonly used in the current practice, has any significant effect on the design of structural elements subjected to seismic loads. Previous studies have recognized that the rectangular envelope is conservative relative to the elliptical envelope. However, no research has been conducted to date to quantify the level of conservatism introduced by the use of the rectangular envelope.

(7) Finally, we simulate and examine the envelopes that bound vectors of seismic responses in a nonlinear structure. Because we currently have no means of predicting the envelopes that bound response vectors in nonlinear structures, investigations of this type provide valuable insight into the nonlinear behavior of structures and the effectiveness of current seismic design methodologies. To the authors' knowledge, all research conducted to date on the nonlinear seismic response of structures has considered only single response quantities. The present investigation of the envelopes bounding vectors of responses in nonlinear structures is unprecedented.

1.4 ORGANIZATION OF THE REPORT

Following this introductory chapter, in Chapter 2 we use the theory of random vibrations to establish a response-spectrum-based procedure for predicting the peak values of multiple response quantities and the correlation structure that exists between them.

Using the results derived in Chapter 2, response-spectrum-based envelopes are developed in Chapter 3 for linear structures. Two types of envelopes are developed: (1) an elliptical envelope for the case in which the principal directions of ground motion are known and (2) a supreme envelope for the case in which the principal directions are not known. The treatment of static response quantities acting concurrently with the seismic responses is also addressed in this chapter.

Chapter 4 describes the example structures and the ensembles of ground motions used in the numerical investigations performed in Chapters 5, 7 and 8.

In Chapter 5, a series of time-history analyses using artificial and recorded ground motions are performed to verify the accuracy of the response-spectrum-based envelopes developed in Chapter 3.

In Chapter 6, we describe the ways in which the elliptical or supreme envelope can be used in conjunction with a capacity surface to determine the adequacy of a design and develop generic algorithms for this purpose.

In Chapter 7, design examples are used to investigate whether the use of the elliptical or supreme envelope, rather than the conventional rectangular envelope, has any significant effect on the design of structural elements subjected to seismic loads.

In Chapter 8, a comprehensive series of time-history analyses using artificial and recorded ground motions are used to simulate the envelopes bounding selected response vectors in a nonlinear structure. Based on the observations made in this chapter, ways in which these simulated response envelopes can be used to improve the design of structures located in seismic environments are suggested.

Finally, a summary of the observations made in this study and their significance on the seismic design of structures is presented in Chapter 9.

2 Response Spectrum Method for Response Vectors

2.1 INTRODUCTION

In this chapter, we develop the response spectrum basis for the procedures formulated in Chapter 3. This development parallels work previously done by Der Kiureghian (1981) and Smeby and Der Kiureghian (1985). However, unlike these previous works, which focus on predicting the peak values of scalar response quantities, the derivation described here is for the more general case of predicting the peak values of multiple response quantities and the correlation structure that exists between them.

2.2 THE RESPONSE VECTOR

Consider an N-degree-of-freedom linear and classically damped structure. Let $\mathbf{x}(t) = [x_1(t), x_2(t), \ldots, x_m(t)]^T$ be a time-varying m-vector of responses, where each response component $x_r(t)$, $r = 1, 2, \ldots, m$, is expressed as a linear function of the nodal displacements $\mathbf{u}(t) = [u_1(t), u_2(t), \ldots, u_N(t)]^T$, i.e.,

$$x_r(t) = \mathbf{q}_r^T \mathbf{u}(t) . \tag{2.1}$$

The N-vector $\mathbf{q}_r$ is a function of the stiffness and undeformed geometry of the structure and the superscript T denotes the vector transpose. Typical response quantities of engineering interest, e.g., interstory drifts, axial and shear forces, bending moments and stress components can all be expressed in this form. To describe the m-vector of responses, we introduce the $N \times m$ matrix $\mathbf{Q} = [\mathbf{q}_1, \mathbf{q}_2, \ldots, \mathbf{q}_m]$ so that

$$\mathbf{x}(t) = \mathbf{Q}^T \mathbf{u}(t) . \tag{2.2}$$

When the structure is subjected to three translational components of ground motion, $\mathbf{u}(t)$ satisfies

$$\mathbf{M}\ddot{\mathbf{u}}(t) + \mathbf{C}\dot{\mathbf{u}}(t) + \mathbf{K}\mathbf{u}(t) = -\mathbf{M}\mathbf{I}\ddot{\mathbf{u}}_g(t), \tag{2.3}$$

where a superposed dot denotes differentiation with respect to time, **M**, **C** and **K** are the mass, damping and stiffness matrices, respectively, $\ddot{\mathbf{u}}_g(t) = [\ddot{u}_{g1}(t), \ddot{u}_{g2}(t), \ddot{u}_{g3}(t)]^T$ is the vector of components of ground acceleration and $\mathrm{I} = [\mathrm{I}_1, \mathrm{I}_2, \mathrm{I}_3]$ is the $N \times 3$ influence matrix in which the kth column, I_k, contains the nodal displacements due to a unit displacement in the kth component of ground motion.

It is advantageous to solve (2.3) by modal decomposition. Let $\Phi = [\phi_1, \phi_2, \ldots, \phi_n]$ denote the $N \times n$ matrix of mode shapes included in the analysis, where $n \le N$, and $\mathbf{y}(t) = [y_1(t), y_2(t), \ldots, y_n(t)]^T$ denote the normal coordinates that represent the time-varying amplitudes of these modes. We can then write

$$\mathbf{u}(t) = \Phi\, \mathbf{y}(t) = \sum_{i=1}^{n} \phi_i y_i(t). \tag{2.4}$$

The equality in (2.4) is strictly true only when $n = N$. However, it is common practice to reduce the size of the problem, with negligible loss in accuracy, by including in the analysis only the $n \le N$ modes that contribute significantly to the total response of the structure. When the mode shapes are chosen to satisfy the eigenvalue problem $\mathbf{K}\phi_i = \omega_i^2 \mathbf{M}\phi_i$, $i = 1, 2, \ldots, n$, substituting (2.4) into (2.3) and pre-multiplying by Φ^T yields n uncoupled modal equations

$$\ddot{y}_i(t) + 2\zeta_i \omega_i \dot{y}_i(t) + \omega_i^2 y_i(t) = -\gamma_i^T \ddot{\mathbf{u}}_g(t), \quad i = 1, 2, \ldots, n \tag{2.5}$$

where $\omega_i = [\phi_i^T \mathbf{K} \phi_i / (\phi_i^T \mathbf{M} \phi_i)]^{1/2}$ and $\zeta_i = \phi_i^T \mathbf{C} \phi_i / (2\omega_i \phi_i^T \mathbf{M} \phi_i)$ are the natural frequency and damping ratio of mode i and $\gamma_i^T = [\gamma_{1i}, \gamma_{2i}, \gamma_{3i}] = \phi_i^T \mathbf{M}\mathbf{I} / (\phi_i^T \mathbf{M} \phi_i)$ is the row vector of participation factors associated with the three components of ground motion for mode i. Let

$$d_{ki}(t) = \int_0^t \ddot{u}_{gk}(\tau)\, h_i(t - \tau) d\tau \tag{2.6}$$

denote the displacement response of an oscillator that has the frequency and damping ratio of mode i and is subjected to the kth component of ground motion, where

$$h_i(t) = \frac{1}{\omega_{d_i}} \exp(-\zeta_i \omega_i t) \sin(\omega_{d_i} t) \tag{2.7}$$

is the unit impulse response function of mode i and $\omega_{d_i} = \omega_i \sqrt{1-\zeta_i^2}$. It then follows from (2.5) that $y_i(t) = \sum_{k=1}^{3} \gamma_{ki} d_{ki}(t)$ and, upon substitution of this result into (2.4),

$$\mathbf{u}(t) = \sum_{i=1}^{n} \sum_{k=1}^{3} \phi_i \gamma_{ki} d_{ki}(t). \tag{2.8}$$

Finally, substituting (2.8) into (2.1) yields

$$x_r(t) = \mathbf{q}_r^T \sum_{i=1}^{n} \sum_{k=1}^{3} \phi_i \gamma_{ki} d_{ki}(t) \tag{2.9}$$

as an expression for $x_r(t)$ in terms of the modal responses due to each component of ground motion.

2.3 STATISTICS OF THE RESPONSE VECTOR FOR THREE-COMPONENT GROUND MOTION

Assume $\ddot{\mathbf{u}}_g(t)$ is a zero-mean, stationary Gaussian vector process with the two-sided power spectral density matrix $\mathbf{G}_{\ddot{u}_g \ddot{u}_g}(\omega)$. The cross-power spectral density between modal responses $d_{ki}(t)$ and $d_{lj}(t)$ is given by

$$G_{d_{ki} d_{lj}}(\omega) = H_i(\omega) H_j^*(\omega) G_{\ddot{u}_{gk} \ddot{u}_{gl}}(\omega), \tag{2.10}$$

where $H_i(\omega) = (\omega_i^2 - \omega^2 + 2\mathrm{i}\zeta_i \omega_i \omega)^{-1}$ is the complex frequency response function for mode i, $G_{\ddot{u}_{gk} \ddot{u}_{gl}}(\omega)$ is the (k, l) element of $\mathbf{G}_{\ddot{u}_g \ddot{u}_g}(\omega)$ and represents the cross-power spectral density of ground acceleration components $\ddot{u}_{gk}(t)$ and $\ddot{u}_{gl}(t)$, $\mathrm{i} = \sqrt{-1}$ and an asterisk denotes the complex

conjugate. Given (2.9) and (2.10), standard procedures of the theory of random vibrations (Wung and Der Kiureghian, 1989) yield

$$G_{x_r x_s}(\omega) = \sum_{i=1}^{n}\sum_{j=1}^{n}\sum_{k=1}^{3}\sum_{l=1}^{3}\left(\mathbf{q}_r^T \phi_i \gamma_{ki}\right)\left(\mathbf{q}_s^T \phi_j \gamma_{lj}\right) H_i(\omega) H_j^*(\omega) G_{\ddot{u}_{gk}\ddot{u}_{gl}}(\omega) \tag{2.11}$$

for the cross-power spectral density of responses $x_r(t)$ and $x_s(t)$.

It is a common practice to resolve the translational ground motions into components directed along the structure axes. We assume that one of the structure axes is vertical and denote the components of ground motion along the two horizontal structure axes and the vertical axis as $\ddot{u}_{g1}(t)$, $\ddot{u}_{g2}(t)$ and $\ddot{u}_{g3}(t)$, respectively. As a result of this convention, $G_{\ddot{u}_{gk}\ddot{u}_{gl}}(\omega)$, γ_{ki} and γ_{lj} in (2.11) are associated with the components of ground acceleration directed along the structure axes. Penzien and Watabe (1975) observed that during the strong motion phase of an earthquake the translational ground motion components are uncorrelated along a well-defined orthogonal system of axes whose orientation remains reasonably stable over time. These axes, which are denoted the principal axes of the ground motion, are usually oriented such that the major and intermediate principal axes lie in the horizontal plane and the minor principal axis is vertical. We denote the components of ground acceleration directed along the major, intermediate and minor principal axes as $\ddot{u}'_{g1}(t)$, $\ddot{u}'_{g2}(t)$ and $\ddot{u}'_{g3}(t)$, respectively, and define their diagonal matrix of power spectral densities by $\mathbf{G}_{\ddot{\mathbf{u}}'_g\ddot{\mathbf{u}}'_g}(\omega) = \mathrm{diag}\left[G_{\ddot{u}'_{g1}\ddot{u}'_{g1}}(\omega), G_{\ddot{u}'_{g2}\ddot{u}'_{g2}}(\omega), G_{\ddot{u}'_{g3}\ddot{u}'_{g3}}(\omega)\right]$. The components along any other system of axes obtained by a rotation of these principal axes are naturally correlated. Consequently, unless the principal axes of ground motion coincide with the structure axes, the cross terms corresponding to $k \neq l$ in (2.11) are not zero and must be included in the analysis. We account for these cross terms by relating the components of ground motion directed along the structure axes to the principal components of the ground motion though the rotational transformation

$$\ddot{\mathbf{u}}_g = \mathbf{A}^T \ddot{\mathbf{u}}'_g, \tag{2.12}$$

where $\ddot{\mathbf{u}}'_g(t) = [\ddot{u}'_{g1}(t), \ddot{u}'_{g2}(t), \ddot{u}'_{g3}(t)]^T$ and

$$\mathbf{A} = \begin{bmatrix} \cos\theta & \sin\theta & 0 \\ -\sin\theta & \cos\theta & 0 \\ 0 & 0 & 1 \end{bmatrix}, \tag{2.13}$$

in which the counterclockwise angle θ specifies the orientation of the horizontal principal axes relative to the horizontal structure axes in the horizontal plane, as in Figure 2.1.

Using (2.12), the power spectral density matrices of the ground accelerations directed along the two sets of axes are related through

$$\mathbf{G}_{\ddot{u}_g\ddot{u}_g}(\omega) = \mathbf{A}^T \mathbf{G}_{\ddot{u}'_g\ddot{u}'_g}(\omega)\mathbf{A}\,. \tag{2.14}$$

Substituting the (k,l) element of (2.14) into (2.11) yields

$$\begin{aligned} G_{x_r x_s}(\omega) = \sum_{i=1}^{n}\sum_{j=1}^{n}\left(\mathbf{q}_r^T\phi_i\right)\left(\mathbf{q}_s^T\phi_j\right)\Bigg[& \sum_{k=1}^{3}\gamma_{ki}\gamma_{kj}H_i(\omega)H_j^*(\omega)\,G_{\ddot{u}'_{gk}\ddot{u}'_{gk}}(\omega) \\ & -\sum_{k=1}^{2}\sum_{l=1}^{2}(-1)^{k+l}\gamma_{li}\gamma_{lj}H_i(\omega)H_j^*(\omega)\,G_{\ddot{u}'_{gk}\ddot{u}'_{gk}}(\omega)\sin^2\theta \\ & -\sum_{k=1}^{2}(-1)^k\left(\gamma_{1i}\gamma_{2j}+\gamma_{2i}\gamma_{1j}\right)H_i(\omega)H_j^*(\omega)\,G_{\ddot{u}'_{gk}\ddot{u}'_{gk}}(\omega)\sin\theta\cos\theta\Bigg]. \end{aligned} \tag{2.15}$$

Using the Wiener-Khintchine relation (Soong and Grigoriu, 1993), the covariance σ_{rs} between zero-mean responses $x_r(t)$ and $x_s(t)$ is

$$\begin{aligned} \sigma_{rs} &= \int_{-\infty}^{\infty} G_{x_r x_s}(\omega)\,\mathrm{d}\omega \\ &= \sum_{i=1}^{n}\sum_{j=1}^{n}\left(\mathbf{q}_r^T\phi_i\right)\left(\mathbf{q}_s^T\phi_j\right)\Bigg[\sum_{k=1}^{3}\gamma_{ki}\gamma_{kj}\sigma_{ij}^{(k)} - \sum_{k=1}^{2}\sum_{l=1}^{2}(-1)^{k+l}\gamma_{li}\gamma_{lj}\sigma_{ij}^{(k)}\sin^2\theta \\ &\qquad -\sum_{k=1}^{2}(-1)^k\left(\gamma_{1i}\gamma_{2j}+\gamma_{2i}\gamma_{1j}\right)\sigma_{ij}^{(k)}\sin\theta\cos\theta\Bigg], \end{aligned} \tag{2.16}$$

where

$$\sigma_{ij}^{(k)} = \int_{-\infty}^{\infty} H_i(\omega)H_j^*(\omega)\,G_{\ddot{u}'_{gk}\ddot{u}'_{gk}}(\omega)\,\mathrm{d}\omega \tag{2.17}$$

is the covariance between modal responses $d_{ki}(t)$ and $d_{kj}(t)$.

2.4 THE RESPONSE SPECTRUM METHOD

For the purposes of structural design, the components of ground motions at a site are commonly described by their response spectra, which are functions that specify the maximum response of a single-degree-of-freedom oscillator due to a given component of ground motion for a range of frequencies and damping ratios of the oscillator. Therefore, it is useful to express (2.16) in terms of the response spectra of the principal components of ground motion. This entails the introduction of approximations for the covariance terms $\sigma_{ij}^{(k)}$ and σ_{rs} in (2.16) under the following set of assumptions.

The formulation developed here is an extension of the Complete Quadratic Combination (CQC) modal combination rule developed by Der Kiureghian (1981) for predicting the peak value of a single response quantity resulting from a single component of ground motion. Consequently, the assumptions involved in the following derivation are the same as those originally made by Der Kiureghian (1981). In particular, we assume that (1) each component of the seismic input is a wide-band, zero-mean Gaussian process having a stationary duration that is several times longer than the fundamental period of the structure, (2) the significant modes of vibration are within the range of dominant frequencies of the excitation, and (3) the structure is not too lightly damped ($\zeta_i \geq 0.02,\ i = 1, 2, \ldots, n$). In general, the assumptions are sufficiently satisfied for typical structures subjected to far-field earthquakes with long, stationary phases of strong shaking. We note that for short, impulsive ground motions, such as those commonly recorded during near-field events, the first assumption may not be valid. Unusually stiff or flexible structures can also violate these assumptions.

Following the derivation of the original CQC rule, an approximation for the covariance term $\sigma_{ij}^{(k)}$ in (2.16) is introduced. We first write

$$\sigma_{ij}^{(k)} = \rho_{ij}^{(k)} \sqrt{\sigma_{ii}^{(k)} \sigma_{jj}^{(k)}} \ , \tag{2.18}$$

where $\sigma_{ii}^{(k)}$ is the variance of $d_{ki}(t)$ and $\rho_{ij}^{(k)}$ is the correlation coefficient between modal responses $d_{ki}(t)$ and $d_{kj}(t)$. We then substitute the following approximations for $\rho_{ij}^{(k)}$ and $\sigma_{ii}^{(k)}$ into (2.18).

For $\rho_{ij}^{(k)}$, it has been shown by Der Kiureghian (1980, 1981) that when the significant modes of vibration are within the range of dominant frequencies of the wide-band seismic excitation, the following expression is a good approximation

$$\rho_{ij}^{(k)} \approx \rho_{ij} = \frac{8\sqrt{\zeta_i \zeta_j \omega_i \omega_j}\left(\zeta_i \omega_i + \zeta_j \omega_j\right)\omega_i \omega_j}{\left(\omega_i^2 - \omega_j^2\right)^2 + 4\zeta_i \zeta_j \omega_i \omega_j \left(\omega_i^2 + \omega_j^2\right) + 4\left(\zeta_i^2 + \zeta_j^2\right)\omega_i^2 \omega_j^2}. \tag{2.19}$$

This expression, which is based on response to white noise, is independent of the ground motion components; thus, the superscript on ρ_{ij} is removed as indicated.

When the response is a stationary zero-mean Gaussian process, $\sigma_{ii}^{(k)}$ can be expressed as

$$\sigma_{ii}^{(k)} = \left(\frac{1}{p_i} D_{ki}\right)^2, \tag{2.20}$$

where $D_{ki} = E[\max\ d_{ki}(t)]$ is the mean displacement response spectrum ordinate for mode i due to the kth principal component of ground motion and p_i is a peak factor that has a mild dependence on the power spectral density and the duration of the excitation. We note that the original CQC rule is based upon the conventional absolute value definition of the response spectrum, $D_{ki} = E[\max\ |d_{ki}(t)|]$. The reason for adopting the one-sided definition of the response spectrum in this study will become apparent in Chapter 3. The difference between the two definitions is normally negligible, i.e., less than 5%, for damping ratios typical of conventional structures. We also note that the expectation operator $E[\cdot]$ in the definition of D_{ki} implies that the ground motion $\ddot{u}'_{gk}(t)$, which gives rise to $d_{ki}(t)$, is a realization from an ensemble of ground motions that can be characterized as a stochastic process. As we will discuss in Chapters 4 and 5, this implicit assumption of the response spectrum method places limitations on what we can infer from the time-history results generated from the ensembles of recorded ground motions introduced in Chapter 4.

Substituting (2.18) and (2.20) into (2.16) yields

$$\sigma_{rs} = \sum_{i=1}^{n}\sum_{j=1}^{n} \frac{1}{p_i p_j}\left(\mathbf{q}_r^T \phi_i\right)\left(\mathbf{q}_s^T \phi_j\right)\left[\sum_{k=1}^{3} \gamma_{ki}\gamma_{kj}\rho_{ij} D_{ki} D_{kj} - \sum_{k=1}^{2}\sum_{l=1}^{2} (-1)^{k+l} \gamma_{li}\gamma_{lj}\rho_{ij} D_{ki} D_{kj} \sin^2\theta \right.$$
$$\left. - \sum_{k=1}^{2} (-1)^k \left(\gamma_{1i}\gamma_{2j} + \gamma_{2i}\gamma_{1j}\right)\rho_{ij} D_{ki} D_{kj} \sin\theta\cos\theta \right]. \tag{2.21}$$

Under the assumption that the response is a stationary, zero-mean Gaussian process, the variance σ_r^2 of $x_r(t)$ can be expressed as

$$\sigma_r^2 = \left(\frac{1}{p_r} X_r \right)^2, \tag{2.22}$$

where $X_r = E[\max x_r(t)]$ is the mean of the maximum value of $x_r(t)$ and p_r is a peak factor. Equation (2.22) is clearly analogous to (2.20). Using the relationship $\sigma_{rs} = \sigma_r \sigma_s \rho_{rs}$, in which ρ_{rs} is the correlation coefficient between responses $x_r(t)$ and $x_s(t)$, we can substitute (2.22) into (2.21) to yield

$$X_{rs} = \sum_{i=1}^{n} \sum_{j=1}^{n} \frac{p_r p_s}{p_i p_j} \left(\mathbf{q}_r^T \phi_i \right) \left(\mathbf{q}_s^T \phi_j \right) \left[\sum_{k=1}^{3} \gamma_{ki} \gamma_{kj} \rho_{ij} D_{ki} D_{kj} - \sum_{k=1}^{2} \sum_{l=1}^{2} (-1)^{k+l} \gamma_{li} \gamma_{lj} \rho_{ij} D_{ki} D_{kj} \sin^2 \theta \right.$$
$$\left. - \sum_{k=1}^{2} (-1)^k \left(\gamma_{1i} \gamma_{2j} + \gamma_{2i} \gamma_{1j} \right) \rho_{ij} D_{ki} D_{kj} \sin \theta \cos \theta \right], \tag{2.23}$$

where $X_{rs} = X_r X_s \rho_{rs}$. As discussed by Der Kiureghian (1981), because the response peak factors p_r, $r = 1, 2, \ldots, m$, are approximately weighted averages of the modal peak factors, $p_i, i = 1, 2, \ldots, n$,

$$\frac{p_r p_s}{p_i p_j} \approx 1 . \tag{2.24}$$

Thus, we can write, without much loss in accuracy,

$$X_{rs} = \sum_{i=1}^{n} \sum_{j=1}^{n} \left(\mathbf{q}_r^T \phi_i \right) \left(\mathbf{q}_s^T \phi_j \right) \left[\sum_{k=1}^{3} \gamma_{ki} \gamma_{kj} \rho_{ij} D_{ki} D_{kj} - \sum_{k=1}^{2} \sum_{l=1}^{2} (-1)^{k+l} \gamma_{li} \gamma_{lj} \rho_{ij} D_{ki} D_{kj} \sin^2 \theta \right.$$
$$\left. - \sum_{k=1}^{2} (-1)^k \left(\gamma_{1i} \gamma_{2j} + \gamma_{2i} \gamma_{1j} \right) \rho_{ij} D_{ki} D_{kj} \sin \theta \cos \theta \right]. \tag{2.25}$$

The above expression defines the elements of the "response matrix" introduced in the next section. However, before proceeding, we make the following observations.

First, it should be apparent from the above derivation that, when $r \neq s$, X_{rs} is related to the covariance between responses $x_r(t)$ and $x_s(t)$. The algebraic sign of X_{rs} indicates whether

the responses $x_r(t)$ and $x_s(t)$ are positively or negatively correlated. If $x_r(t)$ and $x_s(t)$ are uncorrelated, then $X_{rs} = 0$; whereas if $x_r(t)$ is proportional to $x_s(t)$, then the two responses are perfectly correlated, i.e., $\rho_{rs} = \pm 1$, and $|X_{rs}| = X_r X_s$.

Second, when $r = s$, (2.25) becomes

$$X_r^2 = \sum_{i=1}^{n}\sum_{j=1}^{n}\left(\mathbf{q}_r^T\phi_i\right)\left(\mathbf{q}_r^T\phi_j\right)\left[\sum_{k=1}^{3}\gamma_{ki}\gamma_{kj}\rho_{ij}D_{ki}D_{kj} - \sum_{k=1}^{2}\sum_{l=1}^{2}(-1)^{k+l}\gamma_{li}\gamma_{lj}\rho_{ij}D_{ki}D_{kj}\sin^2\theta \right.$$
$$\left. - \sum_{k=1}^{2}(-1)^k\left(\gamma_{1i}\gamma_{2j} + \gamma_{2i}\gamma_{1j}\right)\rho_{ij}D_{ki}D_{kj}\sin\theta\cos\theta\right], \qquad (2.26)$$

by virtue of the fact that $\rho_{rr} = 1$ and, therefore, $X_{rr} = X_r^2$. We note that (2.26) is a response-spectrum-based estimate for the square of the expected maximum value of $x_r(t)$ due to multiple components of ground motion. In fact, (2.26) is fundamentally identical to the multi-component modal combination rules developed by Smeby and Der Kiureghian (1985) and López and Torres (1997). Furthermore, considering the case when the structure is subjected to a single component of ground motion directed along the z_1 structure axis shown in Figure 2.1, i.e., $D_{2i} = D_{3i} = 0$ for all modes and $\theta = 0$, (2.26) reduces to

$$X_r^2 = \sum_{i=1}^{n}\sum_{j=1}^{n}\left(\mathbf{q}_r^T\phi_i\gamma_{1i}\right)\left(\mathbf{q}_r^T\phi_j\gamma_{1j}\right)\rho_{ij}D_{1i}D_{1j}, \qquad (2.27)$$

which is the original CQC rule developed by Der Kiureghian (1981).

Finally, we note that $\pm X_r$ can be interpreted as a bounding envelope on $x_r(t)$ as it evolves in time. Thus, the peak values of the individual response components can be used to define a rectangular domain in the m-dimensional response space that envelops the response vector $\mathbf{x}(t)$. This envelope, however, is obviously conservative, as the individual response maxima normally do not occur at the same time. As we will see shortly, when θ is specified, the envelope derived in this study is an ellipsoid in the m-dimensional response space that is inscribed within this conservative rectangular envelope.

2.5 MATRIX FORMULATION

For the derivation of the elliptical envelope in Chapter 3, it is convenient to rewrite (2.25) in a matrix form. Define the $n \times n$ diagonal matrices $\mathbf{D}_k = \text{diag}[D_{ki}]$ and $\Gamma_k = \text{diag}[\gamma_{ki}]$ for $k = 1,2,3$ and the $n \times n$ correlation matrix $\mathbf{R} = [\rho_{ij}]$. We can then rewrite (2.25) in the form

$$X_{rs} = \mathbf{q}_r^T \Phi \Bigg[\sum_{k=1}^{3} \left(\Gamma_k \mathbf{D}_k \mathbf{R} \mathbf{D}_k^T \Gamma_k^T \right) - \sum_{k=1}^{2} \sum_{l=1}^{2} (-1)^{k+l} \left(\Gamma_k \mathbf{D}_l \mathbf{R} \mathbf{D}_l^T \Gamma_k^T \right) \sin^2 \theta$$

$$- \sum_{k=1}^{2} (-1)^k \left(\Gamma_1 \mathbf{D}_k \mathbf{R} \mathbf{D}_k^T \Gamma_2^T + \Gamma_2 \mathbf{D}_k \mathbf{R} \mathbf{D}_k^T \Gamma_1^T \right) \sin\theta \cos\theta \Bigg] \Phi^T \mathbf{q}_s , \qquad (2.28a)$$

$$= \mathbf{q}_r^T \left(\mathbf{Z}_1 + \mathbf{Z}_2 \sin^2 \theta + \mathbf{Z}_3 \sin\theta \cos\theta \right) \mathbf{q}_s \qquad (2.28b)$$

$$= \mathbf{q}_r^T \mathbf{Z} \, \mathbf{q}_s , \qquad (2.28c)$$

where

$$\mathbf{Z}_1 = \Phi \Bigg[\sum_{k=1}^{3} \left(\Gamma_k \mathbf{D}_k \mathbf{R} \mathbf{D}_k^T \Gamma_k^T \right) \Bigg] \Phi^T \qquad (2.29a)$$

$$\mathbf{Z}_2 = \Phi \Bigg[- \sum_{k=1}^{2} \sum_{l=1}^{2} (-1)^{k+l} \left(\Gamma_k \mathbf{D}_l \mathbf{R} \mathbf{D}_l^T \Gamma_k^T \right) \Bigg] \Phi^T \qquad (2.29b)$$

$$\mathbf{Z}_3 = \Phi \Bigg[- \sum_{k=1}^{2} (-1)^k \left(\Gamma_1 \mathbf{D}_k \mathbf{R} \mathbf{D}_k^T \Gamma_2^T + \Gamma_2 \mathbf{D}_k \mathbf{R} \mathbf{D}_k^T \Gamma_1^T \right) \Bigg] \Phi^T \qquad (2.29c)$$

and

$$\mathbf{Z} = \mathbf{Z}_1 + \mathbf{Z}_2 \sin^2 \theta + \mathbf{Z}_3 \sin\theta \cos\theta . \qquad (2.30)$$

One can easily verify that $\mathbf{Z}$ is an $N \times N$ symmetric matrix. For a given structure and response spectra, and for known principal directions of the ground motion, $\mathbf{Z}$ is known and is identical for all response quantities. Furthermore, since $X_{rr} = X_r^2 = \mathbf{q}_r^T \mathbf{Z} \mathbf{q}_r > 0$ for any non-trivial response, $\mathbf{Z}$ is a positive definite matrix.

Collecting (2.28c) for all response pairs, we define the $m \times m$ "response matrix"

$$\mathbf{X} = \mathbf{Q}^T \mathbf{Z} \mathbf{Q} , \qquad (2.31)$$

in which the (r,s) element is X_{rs}. This matrix, which is closely related to the covariance matrix of $\mathbf{x}(t)$, plays a central role in the development of the response-spectrum-based procedure for predicting the envelope that bounds the vector of seismic responses as described in Chapter 3.

z_1, z_2 = structure axes

z_1', z_2' = major and intermediate principal axes of the ground motion, respec-

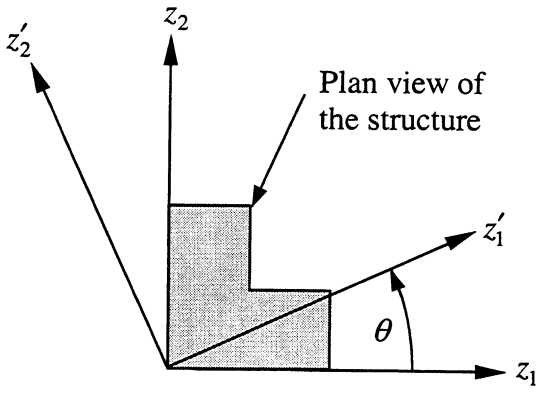

Figure 2.1. Definition of θ.

3 Envelopes for Response Vectors in Linear Structures

3.1 INTRODUCTION

In this chapter, a response-spectrum-based procedure for predicting the envelope that bounds a vector of seismic responses is developed. When the principal directions along which the components of ground motion are uncorrelated are known, the envelope is shown to be elliptical in shape and is identical to that derived previously by Gupta and Singh (1977) and Anastassiadis (1993). In this study, we advance the topic beyond that presented in these earlier works in several distinct ways. First, the procedure developed here is based upon results obtained from the theory of random vibrations that are described in Chapter 2. As a result, the assumptions and approximations involved in the procedure are clearly identified and their ramifications can be understood. The derivations described in the previous works start with the response spectrum method as a basis for the procedure. Consequently, they do not offer as much insight regarding the applicability of the procedure and the conditions under which it might fail to provide accurate results. Second, once the mathematical basis for the method has been established, we demonstrate how the envelope can be constructed in a physically intuitive manner. We will see that this approach is helpful for understanding why the resulting ellipsoid is an appropriate upper bound on the possible combinations of responses. Similar physically motivated interpretations of the envelope are not offered in either of the previous works. Finally, because the principal directions of ground motion are normally not known in advance, an envelope that accounts for the uncertainty in the orientation of these directions is developed. This envelope, which in general is not elliptical, is the union of the elliptical envelopes for all orientations of the principal directions. For this reason, it is called the "supreme" envelope. This uncertainty in the orientation of the principal directions of ground motion is not addressed in the earlier works.

3.2 THE ELLIPTICAL ENVELOPE

In Chapter 2, we defined the $m \times m$ response matrix

$$\mathbf{X} = \mathbf{Q}^T \mathbf{Z} \mathbf{Q}, \tag{3.1}$$

in which the (r,s) element is X_{rs}. Because $\mathbf{Z}$ is symmetric and positive definite, $\mathbf{X}$ is symmetric and positive semi-definite. Furthermore, $\mathbf{X}$ is singular only when there are linearly dependent columns in $\mathbf{Q}$, i.e., when one or more of the responses considered are linear functions of other responses. In the following derivation of the elliptical envelope we first assume that such linear dependence between the response components does not exist so that $\mathbf{X}$ is positive definite and invertible. The case of linearly dependent responses is treated as a special case.

Consider the case where the orientation of the principal directions of ground motion, θ, is known. To derive a response-spectrum-based envelope of the vector response process $\mathbf{x}(t)$ as it evolves in time, consider the projection of $\mathbf{x}(t)$ on a unit vector α in the m-dimensional response space

$$x_\alpha(t) = \alpha^T \mathbf{x}(t). \tag{3.2}$$

When the rth element of α is taken to be unity with all other elements equal to zero, we obtain $x_\alpha(t) = x_r(t)$. For an arbitrary unit vector α, $x_\alpha(t)$ is a linear combination of the elements of the response vector $\mathbf{x}(t)$ and, therefore, of the nodal displacements. Substituting (2.2) into (3.2), one obtains

$$x_\alpha(t) = \alpha^T \mathbf{Q}^T \mathbf{u}(t) = \mathbf{q}_\alpha^T \mathbf{u}(t), \tag{3.3}$$

where $\mathbf{q}_\alpha^T = \alpha^T \mathbf{Q}^T$ is an N-vector of constants that are functions of the stiffness and undeformed geometry of the structure and the specified direction α in the response space. Comparing (2.1) to (3.3), it is evident that (2.26) can be used to estimate $X_\alpha = E[\max\ x_\alpha(t)]$, i.e., the expected peak value of the projection of the response vector along the direction specified by α. Hence, using (2.28c) with $r = s = \alpha$ and (3.1), we can write

$$X_\alpha^2 = \mathbf{q}_\alpha^T \mathbf{Z} \mathbf{q}_\alpha = \alpha^T \mathbf{Q}^T \mathbf{Z} \mathbf{Q} \alpha = \alpha^T \mathbf{X} \alpha. \tag{3.4}$$

Now consider the unit vector along the response axis in direction 1, i.e., $\alpha = [1,0,0,\ldots,0]^T$. Equation (3.4) yields X_1, which establishes the bound $x_1(t) \le X_1$. A similar bound $-X_1 \le x_1(t)$ is obtained by considering the direction vector $\alpha = [-1,0,0,\ldots,0]^T$. These bounds define two hyperplanes that are perpendicular to the x_1 axis and are located at distances $\pm X_1$ from the origin. Note that the distance to the bounding hyperplane in direction α is the maximum value of the projection of $\mathbf{x}(t)$ on α. Hence, this distance should be predicted using the one-sided definition of the response spectrum described in Chapter 2, rather than the conventional absolute value definition of the response spectrum. Next, consider $\alpha = [0, \pm 1,0,\ldots,0]^T$, i.e., unit vectors along the response axis in direction 2. Using (3.4), the bounds $-X_2 \le x_2(t) \le X_2$ on the second response quantity are obtained, which similarly define two hyperplanes perpendicular to the x_2 axis. Continuing this process for the remaining response axes, one obtains m parallel pairs of hyperplanes normal to the response axes. The intersection of the domains between each pair of parallel planes defines an m-dimensional rectangular domain that envelops the vector response process. Figure 3.1a shows a representation of this rectangular domain in the two-dimensional space of responses x_1 and x_2. This rectangular envelope is the one used when the maxima of individual response quantities are combined to evaluate the adequacy of a given design.

Now consider an arbitrary vector α that is not aligned with any of the response axes. The projection of the response vector along this direction is bounded by $x_\alpha(t) \le X_\alpha$, with X_α given by (3.4). This bound defines a hyperplane that is perpendicular to α and is at a distance X_α from the origin of the response space. Obviously, the response vector should be contained within the intersection of the half-space $\alpha^T \mathbf{x} \le X_\alpha$ defined by this hyperplane and the rectangular domain defined earlier. This intersection is shown in Figure 3.1b in the two-dimensional space of x_1 and x_2. This procedure can be repeated for many directions α, thus gradually tightening the envelope. Figure 3.1c shows the resulting envelope in the plane of x_1 and x_2. In the following, we show that this envelope is an ellipsoid that is completely defined by the response matrix $\mathbf{X}$.

Consider the bounding hyperplane defined by the unit normal vector α and distance X_α from the origin of the response space and a unit vector β having an acute angle γ with α. Let

$s_\beta(\alpha)$ denote the distance from the origin to the hyperplane in the direction of β and S_β denote the distance to the envelope in the same direction. Figure 3.2 shows these distances in the plane defined by vectors α and β. One can write

$$s_\beta(\alpha) = \frac{X_\alpha}{\cos\gamma} = \frac{(\alpha^T \mathbf{X}\alpha)^{1/2}}{\beta^T \alpha}. \tag{3.5}$$

For a given β, the distance to the envelope S_β is the minimum of $s_\beta(\alpha)$ with respect to α. To obtain this distance, we solve

$$\frac{ds_\beta}{d\alpha} = \frac{\frac{1}{2}(\alpha^T \mathbf{X}\alpha)^{-1/2}\, 2\alpha^T \mathbf{X}(\beta^T\alpha) - (\alpha^T \mathbf{X}\alpha)^{1/2}\beta^T}{(\beta^T\alpha)^2} = 0 \tag{3.6}$$

for α and substitute into (3.5). Upon rearranging (3.6) and using (3.5), one has

$$\alpha^T \mathbf{X}(\beta^T\alpha) = (\alpha^T \mathbf{X}\alpha)\beta^T = [(\beta^T\alpha)s_\beta]^2 \beta^T. \tag{3.7}$$

Hence,

$$\alpha^T \mathbf{X} = (\beta^T\alpha)s_\beta^2 \beta^T \tag{3.8}$$

and, provided $\mathbf{X}$ is not singular,

$$\alpha^T = (\beta^T\alpha)s_\beta^2 \beta^T \mathbf{X}^{-1}. \tag{3.9}$$

Substituting this result into (3.5) for α yields

$$s_\beta = \frac{[(\beta^T\alpha)s_\beta^2\, \beta^T \mathbf{X}^{-1}\mathbf{X}\mathbf{X}^{-1}\beta\, s_\beta^2 (\beta^T\alpha)]^{1/2}}{\beta^T\alpha}$$

$$= s_\beta^2 (\beta^T \mathbf{X}^{-1}\beta)^{1/2}, \tag{3.10}$$

or, since s_β in (3.10) is a minimum,

$$S_\beta = (\beta^T \mathbf{X}^{-1}\beta)^{-1/2}. \tag{3.11}$$

This equation defines an ellipsoid in the polar coordinate system. It can be used to determine the distance S_β from the origin of the response space to the envelope in any direction specified by the unit vector β.

An alternative and more convenient expression for developing the elliptical envelope is as follows: Consider Figure 3.3, which shows the orientation of α that minimizes $s_\beta(\alpha)$. It is clear that the point $\mathbf{x} = S_\beta \beta$ on the envelope satisfies the relation $\alpha^T \mathbf{x} = X_\alpha$. Using (3.4), one has

$$\alpha^T \mathbf{x} = \left(\alpha^T \mathbf{X} \alpha\right)^{1/2}$$

$$= \frac{\left(\alpha^T \mathbf{X} \alpha\right)}{\left(\alpha^T \mathbf{X} \alpha\right)^{1/2}}. \tag{3.12}$$

Since α is arbitrary,

$$\mathbf{x} = \frac{\mathbf{X}\alpha}{\left(\alpha^T \mathbf{X} \alpha\right)^{1/2}}. \tag{3.13}$$

This expression provides the Cartesian coordinates of a point on the envelope corresponding to a selected α. Note that the expression does not require inverting $\mathbf{X}$. Furthermore, due to the scaling involved, the vector α need not have a unit length. These properties prove to be useful when computing the envelope in design applications, as is done in Chapter 6.

We now examine properties of matrix $\mathbf{X}$ that are helpful in understanding the geometry of the envelope defined by (3.11). First, we rewrite (3.11) by squaring both sides of the expression and multiplying through by $\beta^T \mathbf{X}^{-1} \beta$ to obtain

$$\left(S_\beta \beta\right)^T \mathbf{X}^{-1} \left(S_\beta \beta\right) = 1. \tag{3.14}$$

As mentioned earlier, the point $\mathbf{x} = S_\beta \beta$ is located on the envelope in direction β from the origin. Hence, the envelope is defined by the locus of points $\mathbf{x}$ in the response space that satisfy

$$\mathbf{x}^T \mathbf{X}^{-1} \mathbf{x} = 1. \tag{3.15}$$

Because $\mathbf{X}$ is symmetric and real-valued, it can be expressed as

$$\mathbf{X} = \Psi \Lambda \Psi^T, \tag{3.16}$$

where Λ is an $m \times m$ diagonal matrix whose elements $\Lambda_{rr} = \lambda_r^2$, $r = 1,2,\ldots,m$ are the eigenvalues of $\mathbf{X}$ and Ψ is an $m \times m$ orthogonal matrix whose rth column is the eigenvector associated with the eigenvalue λ_r^2. The columns of Ψ form a basis for the response space that can be adopted as a new coordinate system. We designate these coordinate axes x_r', $r = 1,2,\ldots,m$, and note that, in general, they are rotated with respect to the coordinates x_r, $r = 1,2,\ldots,m$. Any point $\mathbf{x}$ in the response space can be specified by $\mathbf{x}'$ in the rotated coordinate system through the transformation

$$\mathbf{x}' = \Psi^T \mathbf{x}. \tag{3.17}$$

Substituting (3.16) into (3.15) and making use of (3.17) and the identity $\Psi^{-1} = \Psi^T$ yields

$$(\mathbf{x}')^T \Lambda^{-1} (\mathbf{x}') = 1 \tag{3.18}$$

as an expression that defines the envelope in the coordinate system formed by the columns of Ψ. Expanding (3.18), we see that the envelope is the locus of points in the response space that satisfy

$$\frac{(x_1')^2}{\lambda_1^2} + \frac{(x_2')^2}{\lambda_2^2} + \cdots + \frac{(x_m')^2}{\lambda_m^2} = 1. \tag{3.19}$$

It is clear from the preceding equation that the envelope is an ellipsoid as we asserted earlier. Moreover, the principal axes of this ellipsoid coincide with the coordinate system defined by the columns of Ψ, which were identified as the eigenvectors of $\mathbf{X}$, i.e., the eigenvectors of $\mathbf{X}$ are the principal axes of the envelope. In addition, the length of the rth semi-axis is λ_r, which is the square root of the rth eigenvalue of $\mathbf{X}$.

It is useful to examine special cases of the response vector. We consider the following cases: (1) a two-component response vector, (2) statistically independent responses, and (3) linearly dependent responses.

3.2.1 Two-component Vector Process

When $m = 2$, a convenient closed-form solution for the eigenvectors and eigenvalues of $\mathbf{X}$ can be derived and used to define the envelope. Let ψ denote the counterclockwise angle between the coordinate axes (x_1, x_2) and the principal axes (x_1', x_2') of the ellipse, as shown in Figure 3.4. It follows that

$$\Psi = \begin{bmatrix} \cos\psi & -\sin\psi \\ \sin\psi & \cos\psi \end{bmatrix}. \tag{3.20}$$

Using $\Psi^{-1} = \Psi^T$ and (3.16) we have

$$\Lambda = \Psi^T \mathbf{X} \Psi \tag{3.21}$$

for the diagonal matrix of eigenvalues. Expanding (3.21) yields

$$\lambda_1^2 = X_1^2 \cos^2\psi + X_2^2 \sin^2\psi + 2X_{12} \sin\psi \cos\psi \tag{3.22a}$$

$$\lambda_2^2 = X_1^2 \sin^2\psi + X_2^2 \cos^2\psi - 2X_{12} \sin\psi \cos\psi . \tag{3.22b}$$

As noted earlier, λ_1 and λ_2 are the lengths of the semi-axes of the ellipse. To obtain the angle ψ, we substitute (3.20), (3.22a) and (3.22b) into the eigenvalue equation

$$(\mathbf{X} - \Lambda)\Psi = 0 \tag{3.23}$$

and solve for ψ. The result is

$$\psi = \frac{1}{2} \tan^{-1}\left(\frac{2X_{12}}{X_1^2 - X_2^2} \right). \tag{3.24}$$

Hence, the size and orientation of the elliptical envelope in a two-dimensional response space are completely defined by (3.22a), (3.22b) and (3.24) in terms of the elements of the 2×2 response matrix $\mathbf{X}$.

As an example, the envelope associated with

$$\mathbf{X} = \begin{bmatrix} X_1^2 & X_{12} \\ X_{12} & X_2^2 \end{bmatrix} = \begin{bmatrix} 4 & 2 \\ 2 & 2 \end{bmatrix} \tag{3.25}$$

is shown in Figure 3.5a. This figure shows that the resulting ellipse is inscribed within the rectangular envelope specified by the peak values $X_1 = E[\max x_1(t)]$ and $X_2 = E[\max x_2(t)]$.

3.2.2 Statistically Independent Response Components

When response components are mutually statistically independent, the cross terms $X_{rs}, r \neq s$, are zero and $\mathbf{X}$ is a diagonal matrix. It follows from (3.16) and (3.17) that Ψ is an $m \times m$ identity matrix, $\Lambda = \mathbf{X}$ and $\mathbf{x}' = \mathbf{x}$. Consequently, the principal axes of the elliptical envelope coincide with the coordinate axes defined by the response quantities x_r, $r = 1,2,\ldots,m$, and the lengths of the semi-axes are identical to the individual peak responses X_r, $r = 1,2,\ldots,m$. As an example, Figure 3.5b shows the envelope for the two-dimensional response matrix

$$\mathbf{X} = \begin{bmatrix} X_1^2 & X_{12} \\ X_{12} & X_2^2 \end{bmatrix} = \begin{bmatrix} 4 & 0 \\ 0 & 2 \end{bmatrix}. \tag{3.26}$$

Note that the matrices defined in (3.25) and (3.26) differ only in the value of the cross term X_{12}. It is clear that the cross terms in the response matrix $\mathbf{X}$, which are related to the covariances between responses, carry the information on the orientation of the elliptical envelope.

3.2.3 Linearly Dependent Response Components

In the presence of linearly dependent response components, $\mathbf{X}$ is singular and has one or more zero eigenvalues. The lengths of the corresponding semi-axes of the ellipsoid vanish and, hence, the envelope has zero distance from the origin in these directions. It follows that in determining the envelope one needs only consider directions α that are orthogonal to all principal axes having zero eigenvalues. As an example, consider the two-dimensional response matrix

$$\mathbf{X} = \begin{bmatrix} X_1^2 & X_{12} \\ X_{12} & X_2^2 \end{bmatrix} = \begin{bmatrix} 4 & 2\sqrt{2} \\ 2\sqrt{2} & 2 \end{bmatrix}, \tag{3.27}$$

in which $X_{12} = X_1 X_2$. One can easily verify that the above matrix is singular having the eigenvalues 0 and 6. The ellipse has now degenerated into a line, as shown in Figure 3.5c, implying that the responses $x_1(t)$ and $x_2(t)$ are perfectly and positively correlated. Note again that the

matrix in (3.27) differs from those in (3.25) and (3.26) only in the value of the cross term X_{12}. As previously observed in Figures 3.5a and 3.5b, the envelope shown in Figure 3.5c (i.e., the diagonal line) is also inscribed within the rectangle defined by the peak values X_1 and X_2. However, unlike the cases in Figures 3.5a and 3.5b, the envelope here predicts that these peak responses occur simultaneously. We note that if the cross terms in (3.27) were replaced by $X_{12} = -2\sqrt{2}$, then the ellipse would degenerate into a line having a negative slope; i.e., $x_1(t)$ and $x_2(t)$ would be perfectly and negatively correlated.

3.3 THE SUPREME ENVELOPE

It is evident from (2.30) and (3.1) that the size and orientation of the elliptical envelope are functions of the orientation of the principal axes of ground motion, θ. In the preceding derivation, θ was assumed to be known. Normally, however, this information is not available during the design phase of a structure. In such cases, it is prudent to consider all possible values that θ can assume. That is, the envelope used for design should bound all the elliptical envelopes obtained for $0 \le \theta < 2\pi$. In this section, we derive expressions for this bounding envelope, which we denote as the "supreme" envelope.

For a specified direction α in the response space and a given orientation θ of the principal axes of ground motion, the distance X_α to the hyperplane defined by α that bounds the elliptical envelope is given by (3.4). Using (2.30) and the trigonometric identities $\sin^2\theta = (1-\cos 2\theta)/2$ and $2\sin\theta\cos\theta = \sin 2\theta$, (3.4) can be rewritten as

$$X_\alpha^2 = \alpha^T \mathbf{Q}^T \left[\left(\mathbf{Z}_1 + \frac{1}{2}\mathbf{Z}_2 \right) - \frac{1}{2}\mathbf{Z}_2 \cos 2\theta + \frac{1}{2}\mathbf{Z}_3 \sin 2\theta \right] \mathbf{Q}\alpha . \tag{3.28}$$

For a specified α, the value of θ that maximizes X_α is found by solving

$$\frac{\mathrm{d}X_\alpha^2}{\mathrm{d}\theta} = \alpha^T \mathbf{Q}^T \left[\mathbf{Z}_2 \sin 2\theta + \mathbf{Z}_3 \cos 2\theta \right] \mathbf{Q}\alpha = 0 \tag{3.29}$$

such that

$$\frac{\mathrm{d}^2 X_\alpha^2}{\mathrm{d}\theta^2} = \alpha^T \mathbf{Q}^T \left[2\mathbf{Z}_2 \cos 2\theta - 2\mathbf{Z}_3 \sin 2\theta \right] \mathbf{Q}\alpha < 0 . \tag{3.30}$$

The result is

$$\cos 2\theta = -\frac{\alpha^T \mathbf{Q}^T \mathbf{Z}_2 \mathbf{Q}\alpha}{H} \tag{3.31a}$$

$$\sin 2\theta = \frac{\alpha^T \mathbf{Q}^T \mathbf{Z}_3 \mathbf{Q}\alpha}{H} \tag{3.31b}$$

where

$$H = \left[\left(\alpha^T \mathbf{Q}^T \mathbf{Z}_2 \mathbf{Q}\alpha\right)^2 + \left(\alpha^T \mathbf{Q}^T \mathbf{Z}_3 \mathbf{Q}\alpha\right)^2\right]^{1/2}. \tag{3.32}$$

Substituting (3.31a) and (3.31b) into (3.28) yields

$$X_\alpha^2 = \alpha^T \mathbf{Q}^T \left[\left(\mathbf{Z}_1 + \frac{1}{2}\mathbf{Z}_2\right) - \frac{1}{2}\mathbf{Z}_2\left(-\frac{\alpha^T \mathbf{Q}^T \mathbf{Z}_2 \mathbf{Q}\alpha}{H}\right) + \frac{1}{2}\mathbf{Z}_3\left(\frac{\alpha^T \mathbf{Q}^T \mathbf{Z}_3 \mathbf{Q}\alpha}{H}\right)\right] \mathbf{Q}\alpha .$$

$$= \alpha^T \mathbf{X}_S \alpha , \tag{3.33}$$

where

$$\mathbf{X}_S = \mathbf{Q}^T \left[\left(\mathbf{Z}_1 + \frac{1}{2}\mathbf{Z}_2\right) - \frac{1}{2}\mathbf{Z}_2\left(-\frac{\alpha^T \mathbf{Q}^T \mathbf{Z}_2 \mathbf{Q}\alpha}{H}\right) + \frac{1}{2}\mathbf{Z}_3\left(\frac{\alpha^T \mathbf{Q}^T \mathbf{Z}_3 \mathbf{Q}\alpha}{H}\right)\right] \mathbf{Q} . \tag{3.34}$$

Equation (3.33) defines the distance to the hyperplane tangent to the supreme envelope and having α as its unit normal vector. This expression is analogous to (3.4) derived earlier for the elliptical envelope. However, the matrix $\mathbf{X}_S$ here is dependent upon α and, as a result, the supreme envelope is not an ellipsoid. It is evident that the supreme envelope is a union of all elliptical envelopes obtained for $0 \le \theta < 2\pi$. Furthermore, the bounding hyperplane in a given direction α is tangent to that ellipsoid in the union that is defined by $\mathbf{X}_S$ evaluated at α. It follows, from a derivation similar to that used to derive (3.13), that points $\mathbf{x}$ on the supreme envelope satisfy the relation

$$\mathbf{x} = \frac{\mathbf{X}_S \alpha}{\left(\alpha^T \mathbf{X}_S \alpha\right)^{1/2}} . \tag{3.35}$$

One can use this relation to compute points on the supreme envelope by varying α. Each such point corresponds to a value of θ that can be computed in terms of α by either (3.31a) or (3.31b).

As a two-dimensional example, consider the case with

$$\mathbf{Q}^T\mathbf{Z}_1\mathbf{Q} = \begin{bmatrix} 4 & 2 \\ 2 & 2 \end{bmatrix}, \qquad \mathbf{Q}^T\mathbf{Z}_2\mathbf{Q} = -\frac{1}{4}\begin{bmatrix} 5 & 4 \\ 4 & 1 \end{bmatrix}, \qquad \mathbf{Q}^T\mathbf{Z}_3\mathbf{Q} = \frac{1}{2}\begin{bmatrix} 5 & 4 \\ 4 & 1 \end{bmatrix}. \tag{3.36}$$

The resulting supreme envelope is shown in Figure 3.6. As discussed above, this envelope bounds the elliptical envelopes for all θ values. For reference, the elliptical and rectangular envelopes corresponding to $\theta = 0$ and $\theta = \pi/2$ radians are also shown in Figure 3.6. The case of $\theta = 0$ is identical to the example case (3.25) studied earlier. It is important to note that the supreme envelope exceeds the rectangular envelope for certain values of θ. Hence, designing by use of the rectangular envelope for a prescribed θ value can be unconservative when θ is unknown.

The preceding derivation of the supreme envelope assumed that $0 \le \theta < 2\pi$. One can generalize this result for the case where θ varies over a subset of the interval $[0, 2\pi)$. This would be the case, for example, when the earthquakes affecting the structure originate in a well-defined extended source near the site. In this case, the distance to the hyperplane bounding the supreme envelope in direction α is the maximum value of X_α in (3.28) over the range of θ that defines the location of the extended source relative to the structure. A closed-form expression for the supreme envelope for this case does not exist. Instead, the envelope can be constructed in a manner similar to that illustrated in Figure 3.1c, with the distances that define the bounding hyperplanes computed numerically. Alternatively, the envelope can be constructed by superimposing the elliptical envelopes for all θ values in the interval of interest.

3.4 CONTRIBUTION OF STATIC FORCES

In the preceding derivations of the elliptical and supreme envelopes, only time-varying responses arising from seismic excitation of the base were considered. In general, however, static loads are present that cause time-invariant components $\mathbf{x}_0 = [x_{01}, x_{02}, \ldots, x_{0m}]^T$ to act concurrently with $\mathbf{x}(t)$. Because the structure is linear, $\mathbf{x}(t)$ and $\mathbf{x}_0$ can be added to yield a total response vector

that varies in time about point $\mathbf{x}_0$ in the response space. The size and orientation of the two envelopes are unaffected by the presence of these static responses. The center of each envelope is simply translated from the origin of the response space to $\mathbf{x}_0$. Modifying (3.15) for this translation, we can mathematically define the elliptical envelope as the locus of points in the response space that satisfy

$$(\mathbf{x}-\mathbf{x}_0)^T \mathbf{X}^{-1}(\mathbf{x}-\mathbf{x}_0)=1. \tag{3.37}$$

However, for use with capacity interaction charts commonly encountered in practice, e.g., moment-axial interaction diagrams used for column design, it is more convenient to use (3.13) to compute the envelope bounding $\mathbf{x}(t)$ and superimpose it on to the capacity chart so that it is centered on $\mathbf{x}_0$. Mathematically, (3.13) becomes

$$\mathbf{x}=\frac{\mathbf{X}\alpha}{\left(\alpha^T \mathbf{X}\alpha\right)^{1/2}}+\mathbf{x}_0. \tag{3.38}$$

The same procedure is applicable to the supreme envelope by modifying (3.35) so that

$$\mathbf{x}=\frac{\mathbf{X}_S\alpha}{\left(\alpha^T \mathbf{X}_S\alpha\right)^{1/2}}+\mathbf{x}_0. \tag{3.39}$$

The adequacy of the structure can then be determined by comparing these demand envelopes with the capacity curves. Algorithms for this procedure are described in Chapter 6 and applied to the design examples that are presented in Chapter 7.

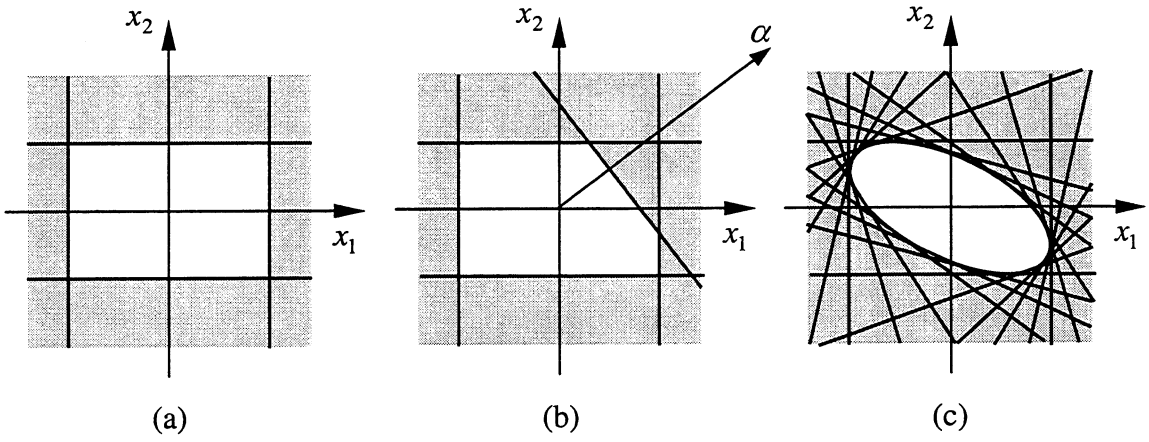

Figure 3.1. Construction of the response-spectrum-based envelope.

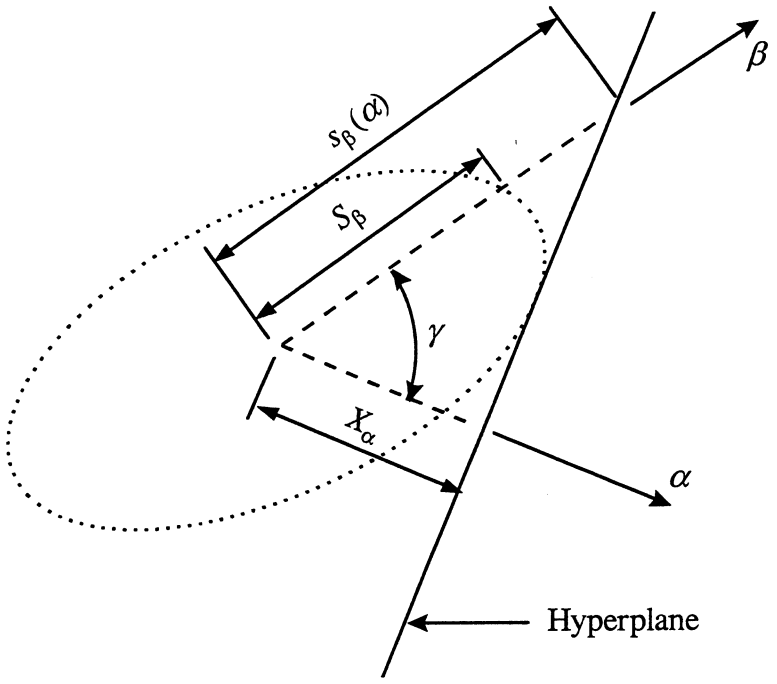

Figure 3.2. Geometry of the elliptical envelope.

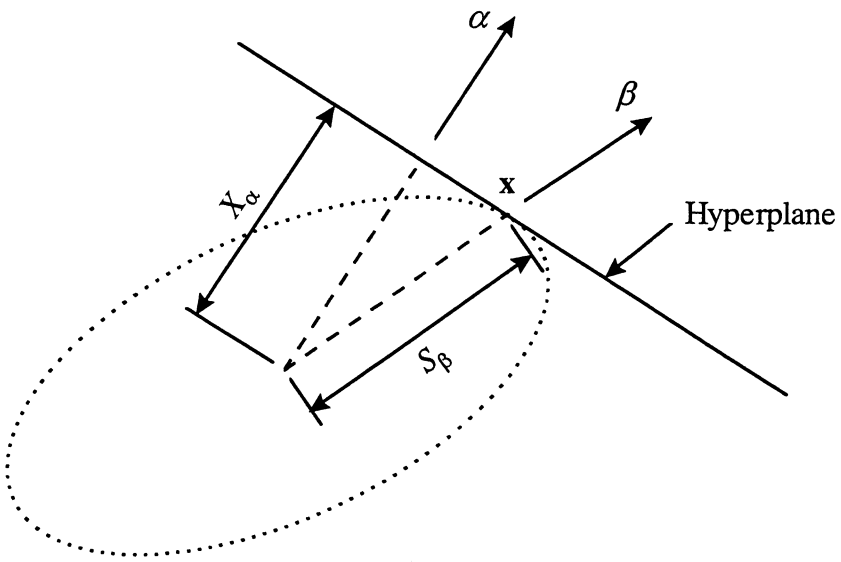

Figure 3.3. Solution α for a given β.

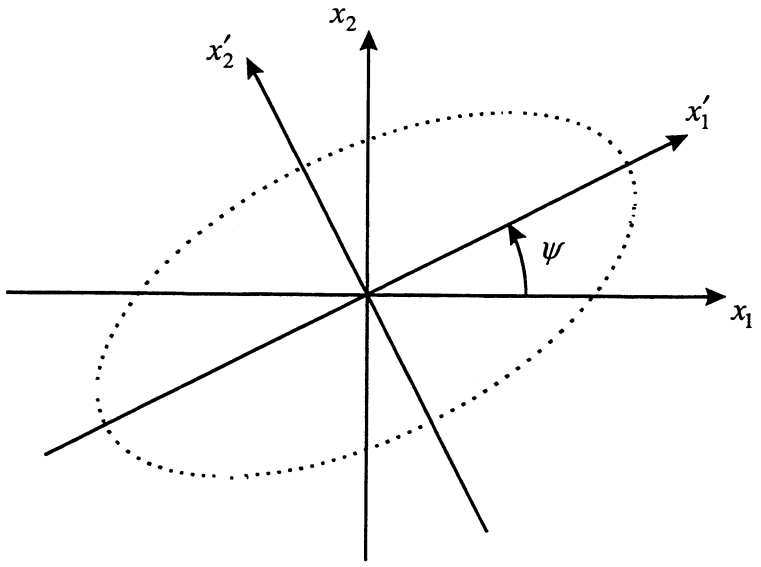

Figure 3.4. Principal axes of the response-spectrum-based envelope for a two-component vector process.

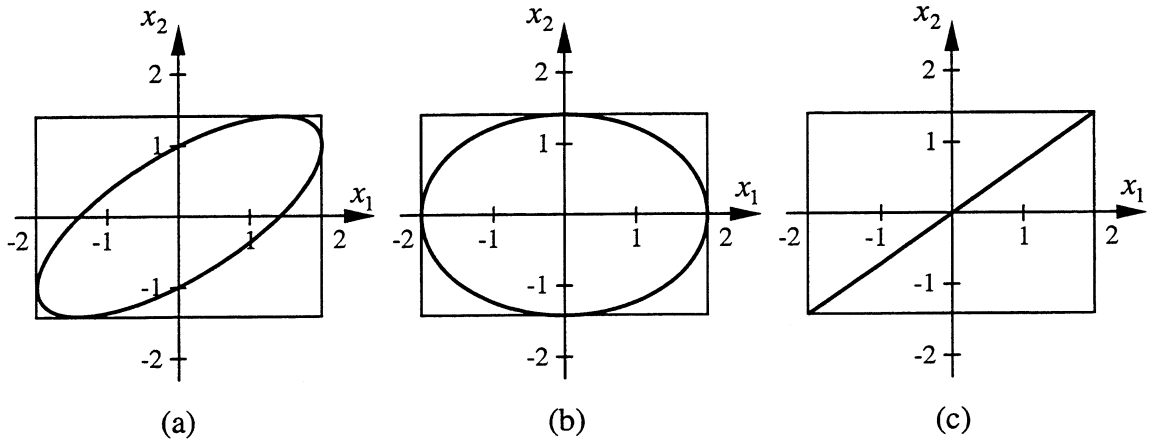

Figure 3.5. Elliptical envelopes of a two-component vector process with varying degrees of correlation.

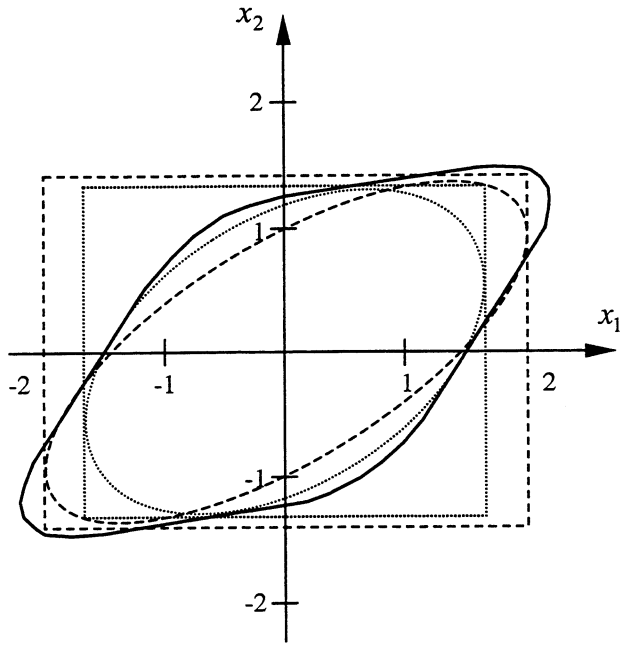

Supreme envelope

Elliptical and rectangular envelopes for $\theta = 0$

Elliptical and rectangular envelopes for $\theta = \pi/2$

Figure 3.6. Supreme envelope of a two-component vector process.

4 Example Structures and Ground Motions

4.1 INTRODUCTION

The numerical analyses employed to demonstrate the accuracy and application of the response-spectrum-based procedures developed in Chapter 3 must be carefully designed to best illustrate the possibilities and potential limitations of the method. In this chapter, we describe the example structures and the ground motions considered in these numerical investigations.

4.2 EXAMPLE STRUCTURES

The seismic responses of a three-story steel moment frame building and a reinforced concrete freeway overpass are examined in the numerical analyses. These structures were selected because they are representative of two large classes of structures that are commonly encountered in practice and, therefore, appropriate for the purposes of determining the validity and significance of the proposed procedures. The material properties, member sizes and connection details of these structures were selected, in part, to reflect current design philosophies and construction practices. Care was also taken to ensure that the responses considered had significant contributions from more than one mode so that the modal combination rules embedded within the proposed procedures make a contribution to the total computed response. DRAIN-3DX (Prakash et al., 1994) was used to model and analyze the structures.

4.2.1 Example Building

The three-story steel building shown in Figure 4.1 is the first structure that is considered in the following numerical analyses. The lateral force resisting system consists of four moment frames, each three bays in length, on the perimeter of the building. In accordance with common practice, the corner columns are not used in the moment frames. This is done primarily because steel sec-

tions, such as hollow structural tubes or built-up members composed of I-beams and plates, that are capable of resisting the bi-axial bending moments experienced by corner columns tend to be uneconomical in low-rise construction.

The beam and column sizes and material properties are listed in Figure 4.1, where E_s is the modulus of elasticity and F_y is the yield stress of the steel. All moment frame beams and columns are oriented such that their strong axes are perpendicular to the plane of the moment frame. To ensure that the lateral loads are resisted only by in-plane action of the moment frames, the columns are assigned pinned end conditions for rotations about their weak axes. The ends of the corner columns are free to rotate about both axes, so they resist only axial loads. Also, the ends of the beams spanning between the corner columns and moment frames are free to rotate about their strong axes so that elements that lie outside of the moment frames do not participate in resisting lateral loads. To approximate the in-plane stiffness of a floor diaphragm, the axial stiffness of the beams are set to large values and stiff bar elements that connect the corner nodes to a node located at the center of the floor are introduced, as shown in Figure 4.1. The section properties of the beam, column and diaphragm elements used as input for the DRAIN-3DX analyses are summarized in Table 4.1.

The moment connections at the ends of the beams and at the column bases of the moment frames are modeled using zero-length elements that have rotational stiffnesses

$$k_b = 25\frac{E_s I_b}{L} \tag{4.1a}$$

$$k_c = 100\frac{E_s I_c}{h} \tag{4.1b}$$

respectively, where I_b and I_c are the moments of inertia about the strong axes of the beams and columns, respectively, and L and h are the moment frame bay width and story height, respectively, as indicated in Figure 4.1. The stiffness values in (4.1a) and (4.1b) are typical of "fully restrained" connections defined in (AISC, 1994). For the nonlinear analyses conducted in Chapter 8, these connection elements are the only locations within the structure where yielding is assumed to occur. Each connection is modeled as an elastic-perfectly-plastic hysteretic element that has a plastic moment capacity

$$M_p = \eta F_y Z, \tag{4.2}$$

where Z is the plastic section modulus of the member that the connection supports and η is a prescribed strength ratio. The positive and negative moment capacities of the connection are equal. For the stiffnesses given in (4.1a) and (4.1b), connections modeled in this manner are described as "rigid" when $\eta \geq 1.0$, "stiff semi-rigid" when $0.2 \leq \eta \leq 1.0$ and "pinned" when $\eta < 0.2$. In the current practice, stiff semi-rigid connections are commonly used with $\eta \geq 0.7$ recognized as a practical lower limit when seismic loads govern the design. The nonlinear analyses in Chapter 8 are performed assuming $\eta = 1.0$, 0.7 and 0.4. For the linear analyses presented in Chapter 5, η is set to a large value that prevents any yielding from occurring in the structure. The properties of the connection elements used as input for the DRAIN-3DX analyses are summarized in Table 4.2. For shear and axial loads, these connection elements are modeled such that they have infinite stiffness (by setting each translational degree of freedom at one end of the element equal to the corresponding degree of freedom at the other end) and unlimited capacity.

For the dynamic analyses, the weight of the building is modeled in DRAIN-3DX by assigning lumped masses at the column locations and at the center of the floor plate as specified in Table 4.3. The resulting weight and center of mass of each floor is indicated in Figure 4.1. The center of mass is offset from the center of the floor plate by 5% of the building dimension along both horizontal structure axes.

The $N \times N$ damping matrix, $\mathbf{C}$, for the model is defined by

$$\mathbf{C} = \alpha \mathbf{M} + \sum_{i=1}^{n_e} \beta_i \mathbf{K}_i \tag{4.3}$$

where n_e is the number of elements in the model, $\mathbf{M}$ is the $N \times N$ mass matrix, $\mathbf{K}_i$ is the $N \times N$ contribution to the global stiffness matrix from the ith element and α and β_i, $i = 1, 2, \ldots, n_e$, are coefficients chosen such that the resulting modal damping ratios are reasonable for the type of structure considered. For the numerical analyses of the building, $\alpha = 0.5$ and $\beta_i = 0.001$ are used for all elements except those elements that model the beam and column connections. For these zero-length elements, $\beta_i = 0$ is used. However, these connection elements naturally introduce hysteretic damping in the nonlinear analyses.

Using the above stiffness, mass and damping values, the structural model has the modal periods and damping ratios listed in Table 4.4, for the modes of vibration included in the analy-

ses. The response of the building to vertical ground motions is not considered. Due to the rigidity of the floor diaphragms, the first 9 modes account for over 99% of the participating mass.

The response of the building due to gravity loads is computed by applying the loads shown in Figure 4.2 to the perimeter frames. The load patterns in Figure 4.2 correspond to the floor framing plan shown. The application of gravity loads is performed prior to every dynamic analysis. While this is not necessary for the linear time-history analyses presented in Chapter 5, for which the responses of the building due to gravity and seismic loads can be superimposed, it must be done for the nonlinear analyses in Chapter 8, for which the principal of superposition does not hold. The resulting responses due to these gravity loads are the static components of the response vectors considered in the investigation.

4.2.2 Example Bridge

The reinforced concrete bridge shown in Figure 4.3 is the second structure considered in this study. The seismic forces are resisted by the three bents aligned with the freeway that passes under the structure and a moment frame parallel to the longitudinal axis of the bridge that incorporates a box girder as its horizontal member. The top face of the box girder serves as the bridge deck. From Figure 4.3 we see that due to the angle at which the bridge crosses the freeway, the lateral force resisting elements are not orthogonal to each other. However, we recognize this as a common configuration. This skewness of the overpass is introduced in order that the response vectors considered in the following numerical analyses receive significant contributions from more than one mode of vibration.

The dimensions of the bridge girders and columns are shown in Figure 4.3 along with the assumed material properties, where E_c and f_c' are the modulus of elasticity and compressive strength of the concrete, respectively, and f_y is the yield strength of the reinforcing steel. All girders are post-tensioned elements. Due to the compressive forces present in all members of the overpass (resulting from either post-tensioning or gravity loads), the gross section properties of the members are assumed when calculating their stiffnesses.

A cross section of the longitudinal box girder is shown in Figure 4.4. As shown in this figure, this girder is modeled by three parallel lines of elastic beam-column elements that span between the transverse girders located along gridlines 'A', 'B', 'D', 'F' and 'G'. Stiff bar ele-

ments that lie in the horizontal plane are used to connect these beam-column elements together. The section properties of the individual members used to model the box girder, which are listed in Table 4.5, were selected such that the flexural and axial stiffness of the resulting truss-like assembly of elements matches that of the actual box girder. The bar elements have pinned end conditions. All other connections are fixed.

Also shown in Figure 4.4 are sets of six springs at each end of the bridge that represent the horizontal stiffness of the abutments. The assumed stiffness values of these springs are listed in Figure 4.4. The transverse girders at the abutments are fixed for translation in the vertical direction at gridlines '1', '2' and '3'. No restraints are placed on the rotations of the ends of the bridge, apart from what is provided by the abutment springs and girders.

The seismic mass of the bridge is modeled in DRAIN-3DX by assigning the lumped masses listed in Table 4.6 at the nodes used to define the box girder shown in Figure 4.4. The resulting weight of the bridge is indicated in Figure 4.3.

The damping matrix, $\mathbf{C}$, for the model is defined by

$$\mathbf{C} = \alpha\mathbf{M} + \beta\mathbf{K} \tag{4.4}$$

where $\mathbf{M}$ and $\mathbf{K}$ are the mass and stiffness matrices, respectively, and α and β are coefficients chosen such that the resulting modal damping ratios are reasonable for the type of structure and level of seismic loading considered. For the linear time-history analyses performed using this structure, $\alpha = 0.5$ and $\beta = 0.001$ are used.

Using the above stiffness, mass and damping values, the structural model of the bridge has the modal periods and damping ratios listed in Table 4.7 for the modes of vibration included in the analyses. In order to compute the response of the bridge to vertical ground motions accurately, it is necessary to include 15 modes.

The computed axial force and bending moments about the z_1 and z_2 axes due to gravity loads at the bases of columns 'B1', 'B2', 'D1' and 'D2' in Figure 4.3 are listed in Table 4.8. These responses are the static components of the response vectors considered in this investigation.

4.3 GROUND MOTIONS

Six ensembles of ground motions are used in the numerical analyses. Two sets consist entirely of artificially generated accelerograms that satisfy the basic assumptions behind the response spectrum method and the Penzien-Watabe characterization of multi-component ground motions described in Chapter 2. Thus, these ensembles are appropriate for evaluating the accuracy of the elliptical envelope in the context of the response spectrum method. However, as we will see shortly, these ground motions are generated in a purely numerical manner by use of a stochastic model for the ground motion. As such, they may not adequately characterize real earthquake ground motions. The other four ensembles of ground motions considered were originally compiled for Phase 2 of the SAC[1] Joint Venture Steel Project (Somerville et al., 1997). Two of these ensembles consist mostly of recorded accelerograms, but also include some synthetic records. The remaining two ensembles consist entirely of synthetic ground motions. Unlike the artificial records mentioned above, the synthetic ground motions in these ensembles were generated using seismologically based methods, i.e., propagating seismic waves through soil strata from an artificially generated extended source model (Somerville et al., 1997). Consequently, they are believed to be more realistic than ground motions generated in a purely numerical manner by direct use of a stochastic model of the ground motion. In this study, we denote ground motions generated using a seismological model as "synthetic" and those generated in a purely numerical manner as "artificial" in order to distinguish them. The SAC ensembles of ground motions are primarily used for the nonlinear analyses presented in Chapter 8. Details of the four ensembles are given in the following sections.

4.3.1 Artificially Generated Ground Motions

Two sets of 50 statistically independent artificial ground motions are generated as described below. The statistical properties of the resulting ensembles satisfy the assumptions employed in the development of the response spectrum method; namely, the ground accelerations are samples of a wide-band, zero-mean Gaussian process having a stationary duration that is several times longer than the fundamental period of the structure. One ensemble consists of records that have

[1] Structural Engineers Association of California, Applied Technology Council and California Universities for Research in Earthquake Engineering.

intensities and durations that are representative of a "serviceability" level earthquake, during which the structure is expected to remain elastic and, consequently, the response spectrum method remains valid. This ensemble is used in Chapter 5 for the purposes of establishing the accuracy of the elliptical envelope. The mean response spectrum of this ensemble is used in Chapter 7 for the application examples. The second set of artificial records have intensities and durations that are representative of an "ultimate" level event, for which life safety must be assured but the structure is expected to be severely damaged, possibly beyond repair. This ensemble is used primarily in the nonlinear analyses presented in Chapter 8.

When the power spectral density function $G_{\ddot{u}_g\ddot{u}_g}(\omega)$ of the strong motion phase of an earthquake accelerogram is specified, a realization of the process $\ddot{u}_g(t)$ can be generated using the formula (Wung and Der Kiureghian, 1989)

$$\ddot{u}_g(t) = A(t)\sum_{i=1}^{n_\omega}\sqrt{2G_{\ddot{u}_g\ddot{u}_g}(\omega_i)\Delta\omega}\cos(\omega_i t + \vartheta_i) \tag{4.5}$$

where ϑ_i are uniformly distributed random phase angles over $[0, 2\pi)$, ω_i, $i = 1,2,\ldots,n_\omega$, are a set of equally spaced frequencies at intervals $\Delta\omega$ that are included in the sinusoidal superposition, and $A(t)$ is a time modulation function that characterizes the temporal variation in the intensity of the ground motion. For this study, $n_\omega = 1000$ frequencies in the range $\pi/2$ rad/s $\le \omega_i \le 40\pi$ rad/s ($0.25\,\text{Hz} \le f \le 20\,\text{Hz}$) are used and

$$A(t) = \begin{cases} \sqrt{t} & t \le t_1 \\ 1 & t_1 < t \le t_2 \\ \exp[-c(t-t_2)] & t_2 < t \end{cases} \tag{4.6}$$

where t_1 and t_2 are prescribed times that define the strong motion phase of the ground motion and c is a coefficient that controls the rate of decay in the ground motion intensity after the strong motion phase. The form of $A(t)$ in (4.6) is due to Ruiz and Penzien (1969). The parameters t_1, t_2 and c in (4.6) must be selected to match the duration of the strong motion phase and the variation in ground motion intensity expected for the type of seismic event considered. For the serviceability level earthquake, $t_1 = 1.0$ sec, $t_2 = 2.7$ sec and $c = 0.55$ are assumed. For the ultimate level earthquakes, $t_1 = 1.0$ sec, $t_2 = 12.5$ sec and $c = 0.155$ are used. Plots of $A(t)$ for

the two types of events are shown in Figure 4.5. Note that the strong motion phase of the serviceability event is considerably shorter than that of the ultimate event. The effect of this shorter strong motion phase of the serviceability event on the accuracy of the response-spectrum-based envelope is examined in Chapter 5.

To generate the ensemble of artificial ground motions used in this study, we choose not to specify $G_{\ddot{u}_g\ddot{u}_g}(\omega)$ in (4.5) but, instead, define the coefficients

$$B_i = \sqrt{2G_{\ddot{u}_g\ddot{u}_g}(\omega_i)\Delta\omega} \quad , \quad i = 1, 2, \ldots, n_\omega \tag{4.7}$$

so that (4.5) becomes

$$\ddot{u}_g(t) = A(t)\sum_{i=1}^{n_\omega} B_i \cos(\omega_i t + \vartheta_i) \, . \tag{4.8}$$

The coefficients B_i are then determined such that the mean displacement response spectrum of the ensemble of artificial ground motions, denoted $\overline{D}(\omega,\zeta)$, approximately matches a target displacement response spectrum $D^*(\omega,\zeta)$ that is representative of the type of seismic event under consideration for a prescribed damping ratio ζ. We do this in an effort to properly capture the intensity and frequency content of the target event. The following iterative procedure, which is roughly based on the *SIMQKE* algorithm developed by Gasparini and Vanmarcke (1976), is used to find the coefficients.

Denote the displacement response spectrum of the *k*th sample of ground motion obtained using (4.8) as $D_k(\omega,\zeta)$. The mean response spectrum of the ensemble of artificial ground motions can thus be calculated as

$$\overline{D}(\omega,\zeta) = \frac{1}{n_g}\sum_{k=1}^{n_g} D_k(\omega,\zeta) \, , \tag{4.9}$$

where n_g is the desired number of ground motions in the ensemble. Let $B_i^{(j)}$ and $\overline{D}^{(j)}(\omega,\zeta)$ denote the values of B_i and $\overline{D}(\omega,\zeta)$ at the *j*th iteration, $j = 1, 2, \ldots$, and initialize $B_i^{(1)} = 1$, $i = 1, 2, \ldots, n_\omega$. At the *j*th iteration, (4.8) is used to generate the desired number of

ground motions in the ensemble and $\overline{D}^{(j)}(\omega,\zeta)$ is computed using (4.9). The estimates of the coefficients are then updated using

$$B_i^{(j+1)} = B_i^{(j)} \frac{D^*(\omega_i,\zeta)}{\overline{D}^{(j)}(\omega_i,\zeta)} . \tag{4.10}$$

The coefficients $B_i^{(j+1)}$ are now used to carry out the next iteration.

We note that because ϑ_i in (4.8) are random, $\overline{D}(\omega,\zeta)$ is also random. Furthermore, as noted by Gasparini and Vanmarcke (1976), the response spectrum ordinate $\overline{D}(\omega_i,\zeta)$ depends not only on the frequency amplitude B_i but also on frequency amplitudes close to ω_i. Consequently, we do not expect the mean response spectrum of the ensemble to converge exactly to the target spectrum. There will always be some deviation between these two spectra, which will converge to some unknown value. Therefore, a possible convergence criterion for this algorithm might involve the amount by which the root mean square difference between the mean response spectrum of the ensemble and the target spectrum changes between successive iterations, i.e., convergence is said to occur when

$$\left| \sqrt{\frac{1}{n_\omega}\sum_{i=1}^{n_\omega}\left[\overline{D}^{(j+1)}(\omega_i,\zeta)-D^*(\omega_i,\zeta)\right]^2} - \sqrt{\frac{1}{n_\omega}\sum_{i=1}^{n_\omega}\left[\overline{D}^{(j)}(\omega_i,\zeta)-D^*(\omega_i,\zeta)\right]^2} \right| \le \varepsilon , \tag{4.11}$$

where ε is a suitably small tolerance. However, this convergence criterion is not invoked in this study. It was observed in a series of trial applications of the algorithm that the mean response spectrum of the ensemble always matched the target response spectrum with sufficient accuracy after only two or three iterations. Based on this observation, rather than using the convergence criterion (4.11) to terminate the algorithm, the number of iterations to be used was simply specified *a priori*. We note that Gasparini and Vanmarcke (1976) make a similar recommendation. In this study, the coefficients B_i obtained after three iterations are used.

The target response spectra are obtained from the Abrahamson and Silva (1997) attenuation relationship for rock sites and strike-slip events. For the serviceability level earthquake, the site is assumed to be 8 km from the closest point on the rupture plane of a moment magnitude $M_w = 5.5$ event. For the ultimate level earthquake, an $M_w = 7.5$ event whose rupture plane comes within 2 km of the site is assumed. The target pseudo-acceleration response spectra,

$A^*(\omega,\zeta) = \omega^2 D^*(\omega,\zeta)$, are plotted in Figure 4.6. We note that the above attenuation relationship yields the conventional two-sided response spectrum, i.e., the response spectrum corresponding to the maximum absolute value of the response. Consequently, the response spectra plotted in Figure 4.6 and in subsequent figures in this chapter correspond to this definition. Furthermore, the algorithm used to determine the coefficients B_i in (4.8) must also employ this two-sided definition. However, for the response spectrum analyses performed in the following chapters, the one-sided definition of the response spectrum, i.e., the response spectrum corresponding to the maximum positive value of the response, is assumed. These one-sided response spectra are computed directly from the ensembles of ground motions generated by (4.8).

Sample accelerograms from the two ensembles and the corresponding pseudo-acceleration response spectra, together with the target response spectra are plotted in Figure 4.7. Naturally, the target response spectra are much smoother than the response spectra of the individual motions. In Figure 4.8, the target response spectra are plotted along with the mean response spectra of the two ensembles. Also plotted in Figure 4.8 are the mean-plus-or-minus-one-standard-deviation response spectra predicted by the attenuation relationship and computed from the ensembles of ground motions. It is clear from Figure 4.8 that the mean response spectra of the generated ensembles closely match the target response spectra. However, the variability in the response spectra of the artificial motions is much less than that predicted by the attenuation relationship. There are two reasons for this discrepancy in the variability of the spectra. First, in (4.8) only the phase angles ϑ_i are random; a more realistic model would include uncertainty in the frequency amplitudes B_i as well as in the parameters that define $A(t)$. These additional sources of uncertainty would obviously increase the variability in the two ensembles of simulated response spectra. However, to the authors' knowledge, there are no established models for these random quantities. Second, because the attenuation relationship is based on regression of ground motions recorded at a variety of sites for a variety of earthquake mechanisms, the variability predicted by the attenuation relationship is greater than what one would expect for any given site. The actual variability of the response spectra for a given site probably lies somewhere between that computed using the ensemble of generated motions and that predicted by the attenuation relationship. In this study, we do not adjust the variability of the artificial records, since any attempt would be somewhat arbitrary in nature and could produce misleading results. Instead, we simply acknowledge this reduced variability in the response spectra of the artificial

ground motions and exercise caution when drawing inferences from the time-history data that may be affected by this apparent shortcoming.

4.3.2 Recorded Ground Motions

It is well known that the response of nonlinear structures can be sensitive to the time-dependent variations in the intensity, frequency content and phasing of the input ground motions. Consequently, time-history analyses conducted with the artificial ground motions described in the previous section may not yield a realistic representation of the nonlinear response of a structure subjected to a large magnitude event. For this reason, several ensembles of recorded and synthetic accelerograms that are representative of a variety of seismic events are also considered in this study. These ensembles of ground motions, which are described below, were originally commissioned for Phase 2 of the SAC Joint Venture Steel Project (Somerville et al., 1997).

4.3.2.1 Seattle ground motions

The first ensemble of recorded and synthetic accelerograms used in this study contains pairs of horizontal ground motion components that are representative of a broad range of seismic events near Seattle, Washington, which have a probability of occurrence of 2% in 50 years. The source of each accelerogram included in the ensemble is listed in Table A.1 of Appendix A. Additional details of the events and the ways in which they were modified are described by Somerville et al. (1997).

This ensemble was compiled "to provide a statistical sample of the variability in phasing and spectra through a set of time histories that are realistic not only in their average properties but in their individual characteristics" (Somerville et al., 1997). However, each pair of original accelerograms was scaled by a single factor that was chosen to minimize the weighted sum of the squared errors between a target spectrum and the average response spectrum of the two components at four prescribed control periods (Somerville et al., 1997). The periods used to match the response spectra were 0.3, 1.0, 2.0 and 4.0 sec. The weights assigned to these periods were 0.1, 0.3, 0.3 and 0.3, respectively. We note that due to the ragged nature of actual response spectra, this approach can result in unrealistic levels of variability in the response of structures whose predominant periods lie away from the more heavily weighted control periods. This is the case

for both structures considered in this study. Furthermore, recall that an implicit assumption of the response spectrum method is that the ground motions are realizations of a common underlying stochastic process. Consequently, due to the variety of fault mechanisms, geographical locations, distances and durations described by Somerville et al. (1997) for the Seattle records, this collection of ground motions does not constitute a "true" ensemble for the purposes of applying the response spectrum method. We must exercise caution when examining the statistical measures of the time-history results generated using this ensemble in the following chapters.

For this study, each pair of accelerograms in this ensemble was decomposed into uncorrelated components through the rotational transformation

$$\begin{Bmatrix} \ddot{u}'_{g1}(t) \\ \ddot{u}'_{g2}(t) \end{Bmatrix} = \begin{bmatrix} \cos\phi & \sin\phi \\ -\sin\phi & \cos\phi \end{bmatrix} \begin{Bmatrix} \ddot{u}_{g1}(t) \\ \ddot{u}_{g2}(t) \end{Bmatrix} \tag{4.12}$$

where $\ddot{u}_{g1}(t)$ and $\ddot{u}_{g2}(t)$ are the scaled ground motions in the original ensemble, $\ddot{u}'_{g1}(t)$ and $\ddot{u}'_{g2}(t)$ are the uncorrelated components and ϕ is the required rotation. To determine ϕ, we first compute the combined Arias intensity of the event, defined as

$$I_A = \int_0^{t_r} \left\{ [\ddot{u}_{g1}(t)]^2 + [\ddot{u}_{g2}(t)]^2 \right\} dt \tag{4.13}$$

where t_r is the length of the record. The times at which 5% and 95% of the Arias intensity is realized, denoted t_5 and t_{95} respectively, are then determined by solving

$$\begin{aligned} 0.05 I_A &= \int_0^{t_5} \left\{ [\ddot{u}_{g1}(t)]^2 + [\ddot{u}_{g2}(t)]^2 \right\} dt \\ 0.95 I_A &= \int_0^{t_{95}} \left\{ [\ddot{u}_{g1}(t)]^2 + [\ddot{u}_{g2}(t)]^2 \right\} dt . \end{aligned} \tag{4.14}$$

The length of the record spanning from t_5 to t_{95} (known as the Arias duration) is then used to compute ϕ such that

$$\left\langle \ddot{u}'_{g1} \ddot{u}'_{g2} \right\rangle = \frac{1}{t_{95} - t_5} \int_{t_5}^{t_{95}} \ddot{u}'_{g1}(t) \; \ddot{u}'_{g2}(t) \; dt = 0 \tag{4.15}$$

where we assume $\ddot{u}'_{g1}(t)$ and $\ddot{u}'_{g2}(t)$ are zero-mean processes for $t_5 < t < t_{95}$ and $\langle\cdot\rangle$ denotes the temporal average. Substituting (4.12) into (4.15) and solving for ϕ yields

$$\phi = \tan^{-1}\left[\frac{\left\langle \ddot{u}_{g2}^2(t)\right\rangle - \left\langle \ddot{u}_{g1}^2(t)\right\rangle \pm \sqrt{\left(\left\langle \ddot{u}_{g2}^2(t)\right\rangle - \left\langle \ddot{u}_{g1}^2(t)\right\rangle\right)^2 + 4\left\langle \ddot{u}_{g1}(t)\,\ddot{u}_{g2}(t)\right\rangle^2}}{2\left\langle \ddot{u}_{g1}(t)\ddot{u}_{g2}(t)\right\rangle}\right] \tag{4.16}$$

where the sign in the numerator of the argument of (4.16) is chosen such that $\left\langle \ddot{u}'^2_{g1}(t)\right\rangle > \left\langle \ddot{u}'^2_{g2}(t)\right\rangle$, assuming that the magnitudes of $\left\langle \ddot{u}'^2_{g1}(t)\right\rangle$ and $\left\langle \ddot{u}'^2_{g2}(t)\right\rangle$ are sufficient to determine the relative intensities of the two uncorrelated components.

The values of t_5, t_{95} and ϕ for each event included in this ensemble are listed in Table A.1 of Appendix A. Plots of each pair of uncorrelated ground acceleration records along with the corresponding ground velocity and displacement records and the pseudo-acceleration response spectra are also presented in Appendix A. The mean and mean-plus-or-minus-one-standard-deviation response spectra for the major ($\ddot{u}'_{g1}$) and minor ($\ddot{u}'_{g2}$) components of these ground motions are plotted in Figure 4.9. A comparison of Figure 4.9 with Figure 4.8 reveals that variability in the response spectra of these uncorrelated ground motion components is comparable to that predicted by the Abrahamson and Silva attenuation relationship for the ultimate level event, which we argued earlier may be excessive for a given site.

4.3.2.2 Near-fault ground motions

Three ensembles of near-fault records are used in this study. All three ensembles contain pairs of fault-normal and fault-parallel ground motions that are representative of the seismic environment near Los Angeles, California. One ensemble consists entirely of recorded accelerograms. The other two ensembles each contain five pairs of synthetic records. These ensembles are included in response to the recent attention directed by the engineering community at the behavior of structures subjected to near-fault motions. The source of each recorded ground motion is listed in Table B.1 of Appendix B and the target events used to generate the synthetic records are listed in Table C.1 of Appendix C. Plots of each pair of near-fault ground accelerations along with the corresponding ground velocity and displacement records and the pseudo-acceleration response

spectra are presented in Appendices B and C for the recorded and synthetic ensembles, respectively. Additional details of the events included in these ensembles can be found in (Somerville et al., 1997).

Unlike the ensemble of ground motions compiled for Seattle, no attempt was made to scale the recorded near-fault accelerograms to a target spectrum and the ensemble does not represent a statistical sample of such ground motions (Somerville et al., 1997). As a result, caution must be exercised when examining the statistical measures of the ensemble of structural responses that are obtained using these ground motions in the following chapters. Each of the synthetic ensembles though appear to consist of closely related ground motions that can be considered as realizations of a common underlying stochastic process. This attribute makes them attractive for the purposes of testing the response-spectrum-based procedures developed in Chapter 3. Unfortunately, the small size of these ensembles limits their use in providing statistically significant results and conclusions.

It is possible to decompose each pair of accelerograms in these ensembles into uncorrelated components, as was done for the Seattle ensemble. However, such a decomposition may not be appropriate for these records, which do not have pronounced phases of stationarity and, therefore, cannot be adequately described by second moment statistical measures such as correlation. By convention, components of near-field motions are generally provided for directions normal and parallel to the strike of the fault. This is the case for the ensemble used in this study. It is assumed that the motions in these two directions are statistically independent.

Studying the figures in Appendices B and C, we note that many of the near-fault records do not have a pronounced near-stationary strong motion phase. Thus, these ground motions violate one of the underlying assumptions of the response spectrum method. The mean and mean-plus-or-minus-one-standard-deviation response spectra for the fault-normal and fault-parallel components are plotted in Figures 4.10, 4.11 and 4.12 for the recorded and two synthetic ensembles, respectively. Comparing Figure 4.10 to Figures 4.8 and 4.9, we see that the variability in the response spectra of the recorded near-fault ground motions is comparable to that predicted by the Abrahamson and Silva attenuation relationship for the ultimate level event and the ensemble of Seattle ground motions. Conversely, for the period range of interest for the example structures considered, the synthetic ensembles shown in Figures 4.11 and 4.12 display a level of variability closer to that of the artificial ground motions generated for this study.

Table 4.1. Section properties of the elements in example building.

Element	Level	Section designation	Area (mm^2)	Moment of inertia (mm^4)	Plastic section modulus (mm^3)
Columns	All	W14 × 398	7.55×10^4	2.50×10^9	1.31×10^7
Beams	2	W36 × 160	6.45×10^8	4.06×10^9	1.02×10^7
	3	W33 × 152	6.45×10^8	3.40×10^9	9.16×10^6
	4	W30 × 99	6.45×10^8	1.66×10^9	5.11×10^6
Diaphragms	All	—	6.45×10^{10}	—	—

Table 4.2. Section properties of the connection elements in example building.

Supported element	Level	Initial stiffness (kN·m/rad)	Plastic moment capacity (kN·m)		
			$\eta = 0.4$	$\eta = 0.7$	$\eta = 1.0$
Columns	Base	1.22×10^7	1.30×10^3	2.27×10^3	3.25×10^3
Beams	2	2.66×10^6	1.01×10^3	1.77×10^3	2.53×10^3
	3	2.23×10^6	0.91×10^3	1.59×10^3	2.27×10^3
	4	1.09×10^6	0.51×10^3	0.89×10^3	1.27×10^3

Table 4.3. Lumped masses assigned at each level of the example building.

Node[1]	Mass (kg)	
	z_1 loading	z_2 loading
A2	—	1.86×10^4
A3	—	1.86×10^4
A5	—	1.86×10^4
A6	—	1.86×10^4
G2	—	3.46×10^4
G3	—	3.46×10^4
G5	—	3.46×10^4
G6	—	3.46×10^4

Node[1]	Mass (kg)	
	z_1 loading	z_2 loading
B1	1.86×10^4	—
C1	1.86×10^4	—
E1	1.86×10^4	—
F1	1.86×10^4	—
B7	3.46×10^4	—
C7	3.46×10^4	—
E7	3.46×10^4	—
F7	3.46×10^4	—
D4	4.26×10^5	4.26×10^5

[1] Refer to Figure 4.1

Table 4.4. Modal properties of the example building.

Mode	Period (sec)	Damping ratio
1	0.6755	0.03102
2	0.6706	0.03086
3	0.3785	0.02246
4	0.2196	0.02192
5	0.2180	0.02195
6	0.1231	0.02841
7	0.1193	0.03044
8	0.1185	0.03059
9	0.0669	0.04851

Table 4.5. Section properties of the elements used to model the box girder of the example bridge.

Element [2]	Area (mm^2)	Moment of inertia about horizontal axis (mm^4)	Moment of inertia about vertical axis (mm^4)	Polar moment of inertia (mm^4)
Box girder elements	2.26×10^6	8.17×10^8	5.54×10^{12}	2.69×10^{12}
Transverse girders	1.86×10^6	3.60×10^8	2.30×10^8	5.49×10^7
Bar elements	1.60×10^{12}	—	—	—

[2] Refer to Figure 4.4

Table 4.6. Lumped masses assigned at the nodes of the bridge model.

Node[3]	Mass (kg)
A1	5.50×10^4
A2	5.50×10^4
A3	5.50×10^4
B1	1.24×10^5
B2	1.24×10^5
B3	1.24×10^5
C1	9.63×10^4

Node[3]	Mass (kg)
C2	9.63×10^4
C3	9.63×10^4
D1	1.18×10^5
D2	1.18×10^5
D3	1.18×10^5
E1	9.63×10^4
E2	9.63×10^4

Node[3]	Mass (kg)
E3	9.63×10^4
F1	1.24×10^5
F2	1.24×10^5
F3	1.24×10^5
G1	5.50×10^4
G2	5.50×10^4
G3	5.50×10^4

[3] Refer to Figure 4.4

Table 4.7. Modal properties of the example bridge.

Mode	Period (sec)	Damping ratio
1	0.2593	0.02243
2	0.2386	0.02266
3	0.2118	0.02326
4	0.2115	0.02327
5	0.2079	0.02338
6	0.1997	0.02368
7	0.1691	0.02531
8	0.1689	0.02532
9	0.1679	0.02539
10	0.0665	0.04991
11	0.0321	0.09910
12	0.0321	0.09912
13	0.0314	0.10136
14	0.0314	0.10136
15	0.0311	0.10241

Table 4.8. Axial loads and bending moments in selected bridge columns due to gravity loads.

Column [4]	Axial load (kN)	Moment about z_1 axis (kN m)	Moment about z_2 axis (kN m)
B1	1550	-47.2	25.2
B2	2500	-11.4	36.4
D1	1860	-55.1	-5.9
D2	3080	0.0	0.0

[4] Refer to Figure 4.4

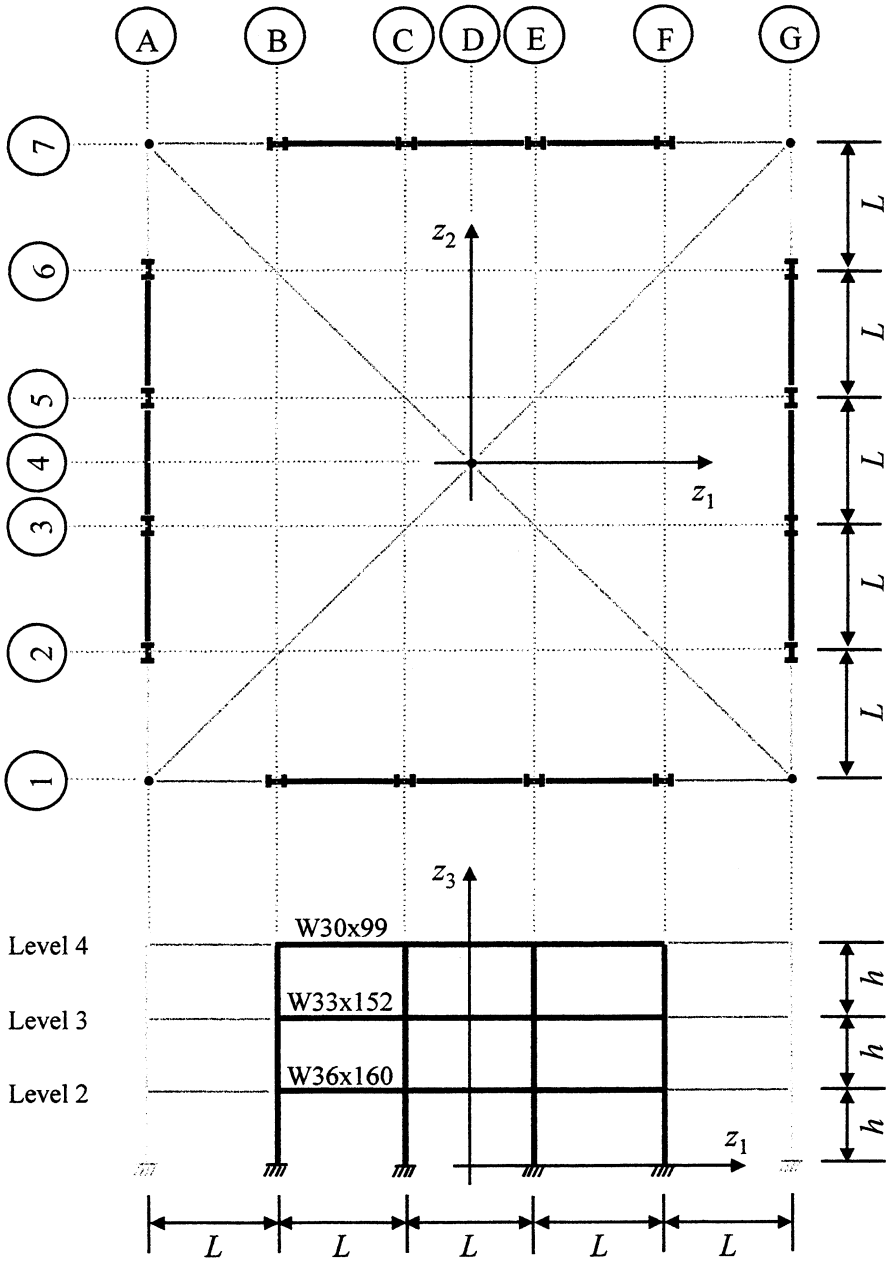

All columns W14x398

E_s = 200,000 MPa	L = 7,620 mm	Weight = 6,250 kN / level
F_y = 248 MPa	h = 4,115 mm	Center of mass at (z_1, z_2) = (1905 mm, 1905 mm)

Figure 4.1. Example three-story steel moment frame building.

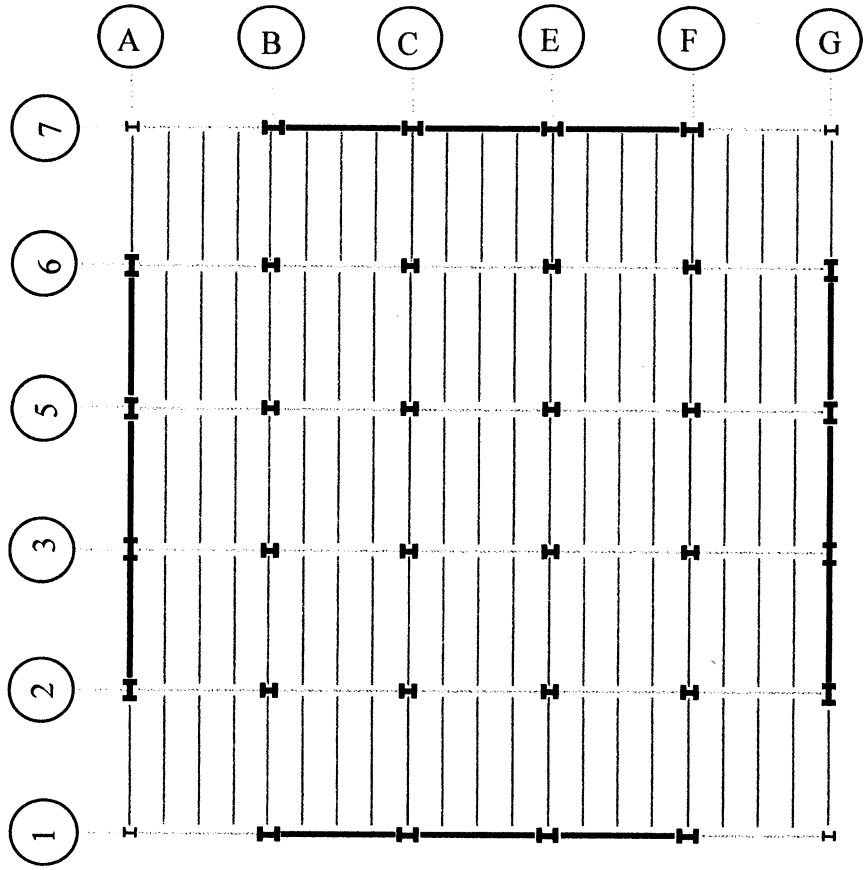

Framing Plan

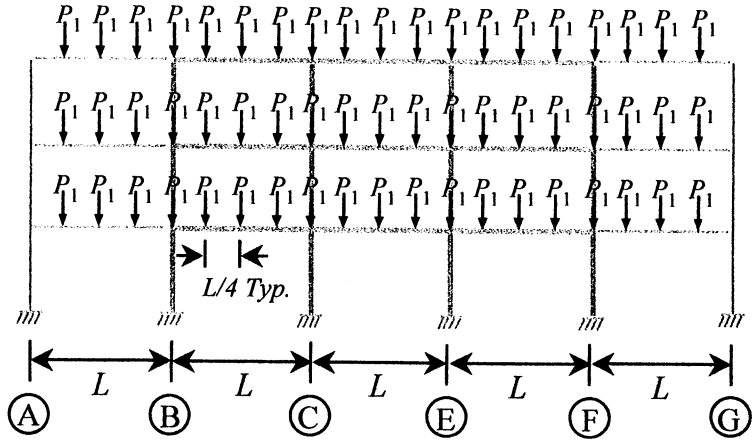

Frames along gridlines 1 and 7

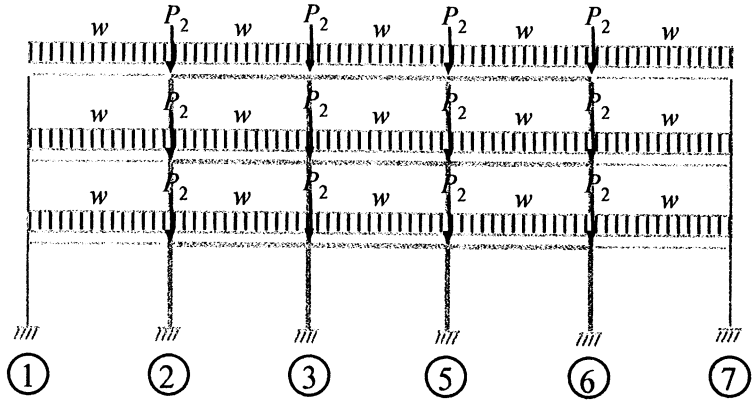

Frames along gridlines A and G

$P_1 = 41.7$ kN $\quad P_2 = 125.1$ kN $\quad w = 5.47$ kN/m

Figure 4.2. Gravity loads acting on example building.

Plan

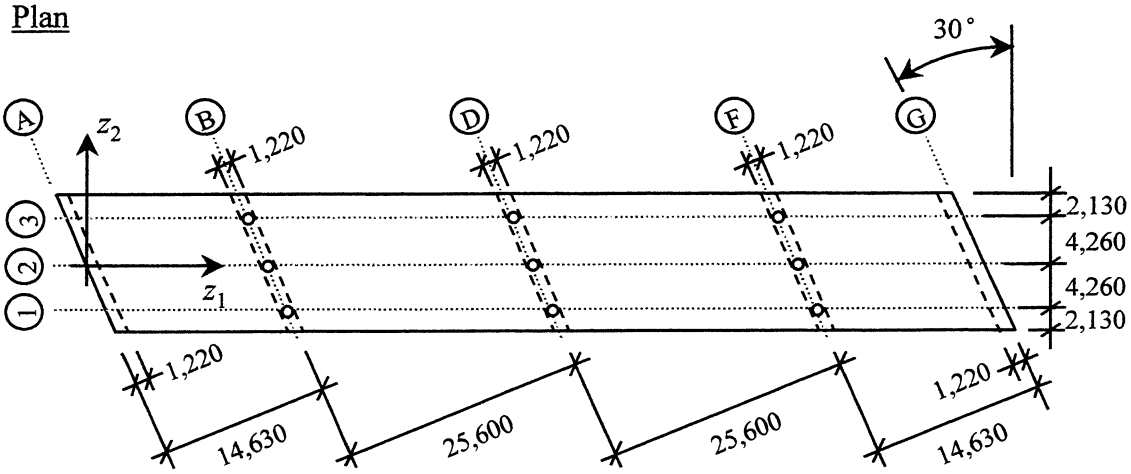

Elevation

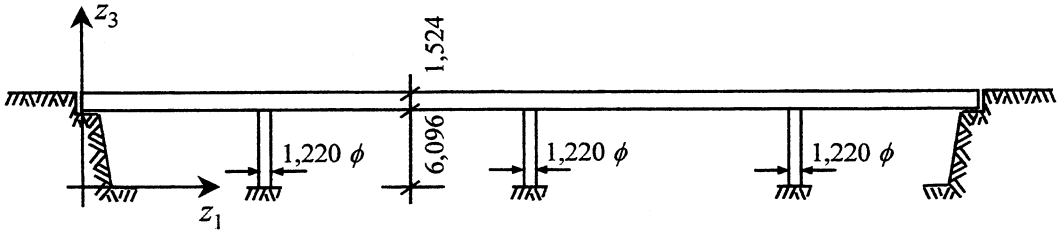

Columns : 1,220 ϕ

Girders along Ⓐ Ⓑ Ⓓ Ⓕ and Ⓖ : 1,220 x 1,524

See Figure 4.4 for cross section of bridge deck.

All dimensions in mm

E_c = 27,600 MPa

f_c' = 30 MPa

f_y = 400 MPa

Weight = 19,700 kN

Figure 4.3. Example reinforced concrete bridge.

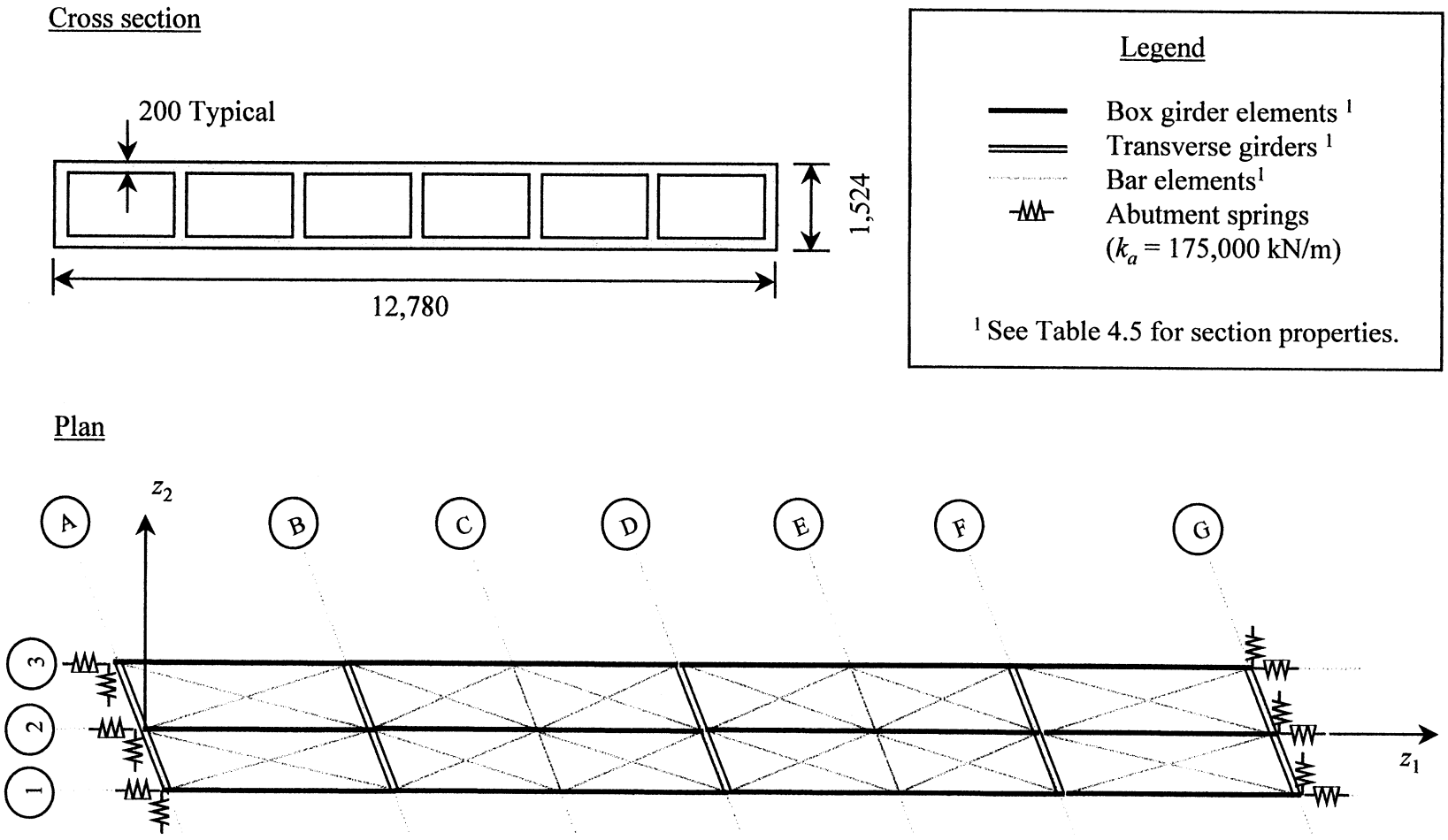

Figure 4.4. Cross section and structural model of post-tensioned concrete bridge deck.

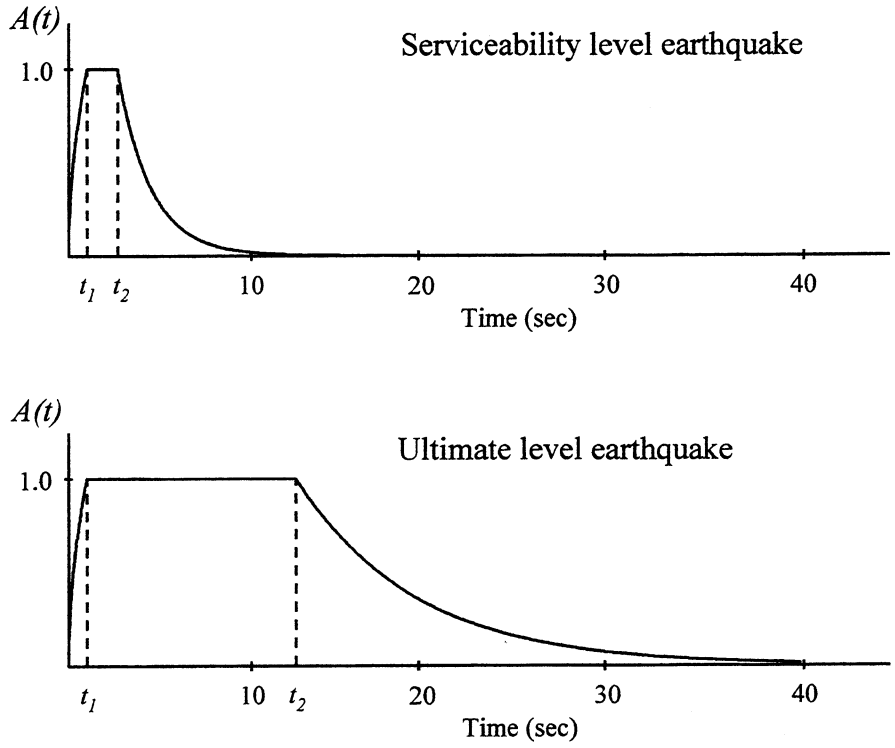

Figure 4.5. Time modulation functions for artificial ground motions.

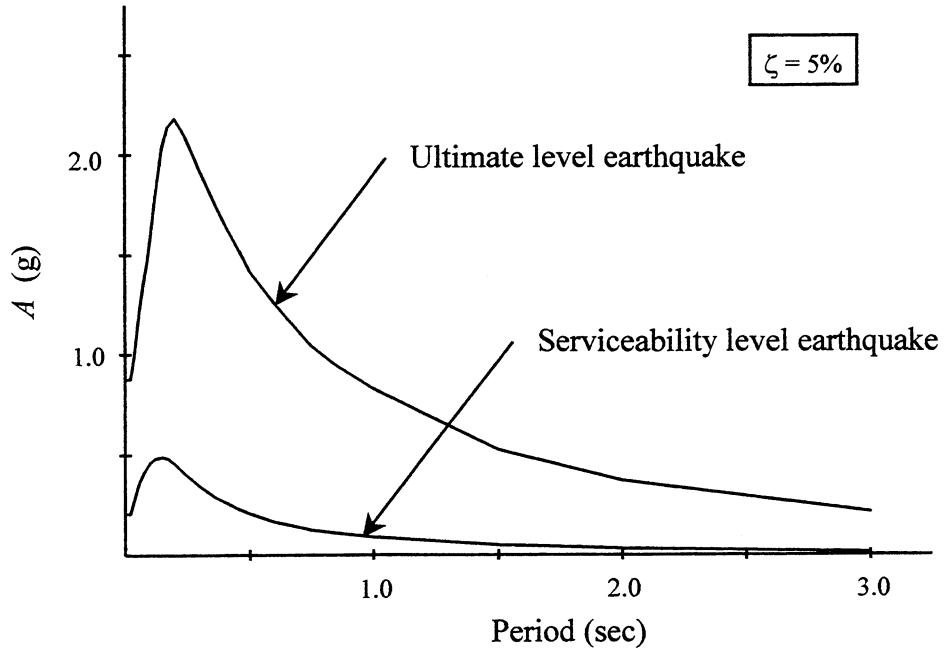

Figure 4.6. Target pseudo-acceleration response spectra for artificial ground motions.

Serviceability level earthquake

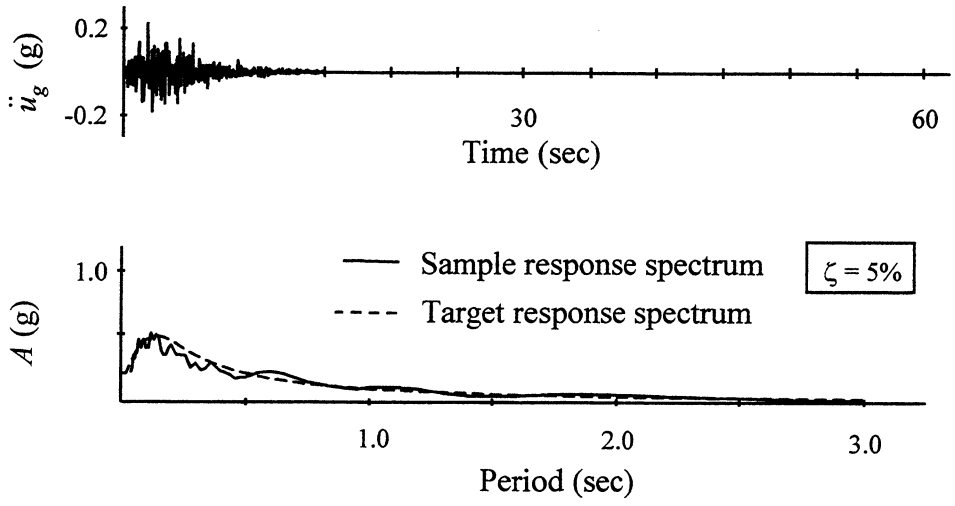

Ultimate level earthquake

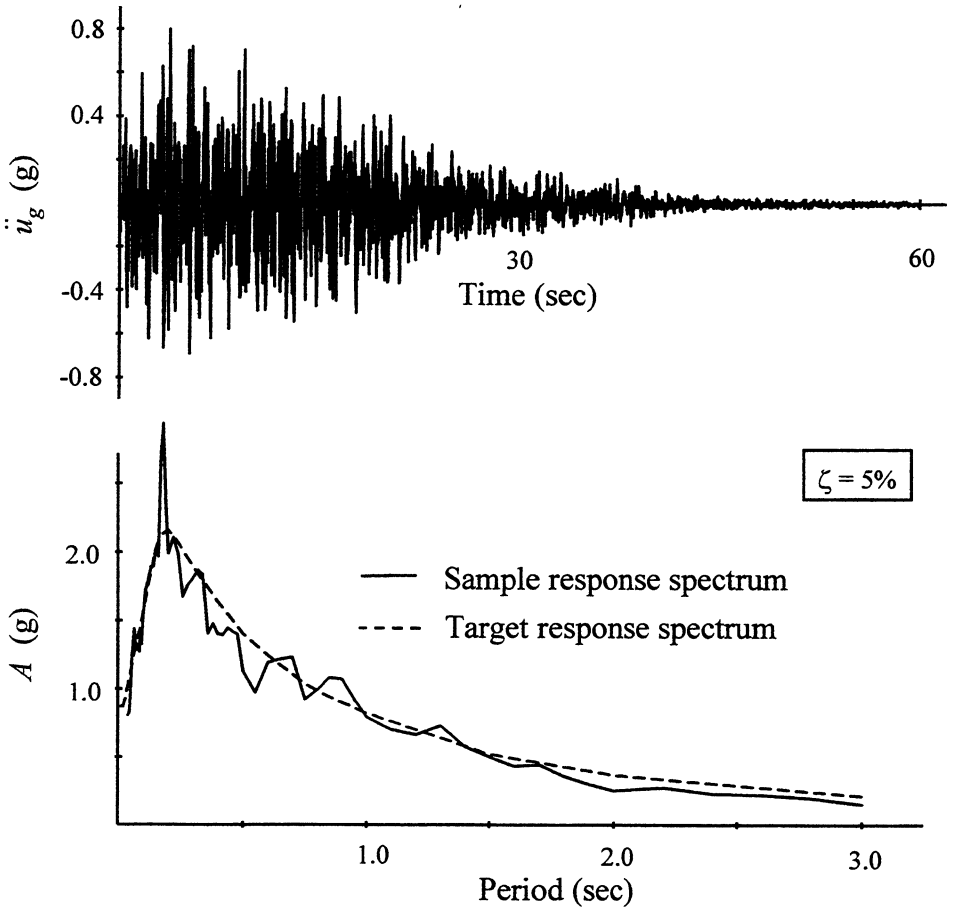

Figure 4.7. Sample accelerograms and corresponding pseudo-acceleration response spectra for artificial ground motions.

Serviceability level earthquake

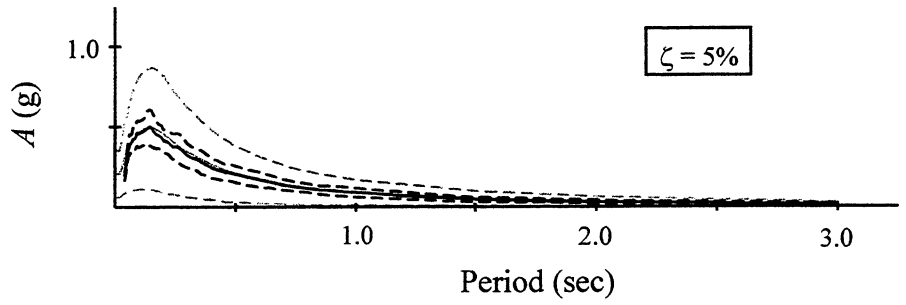

Ultimate level earthquake

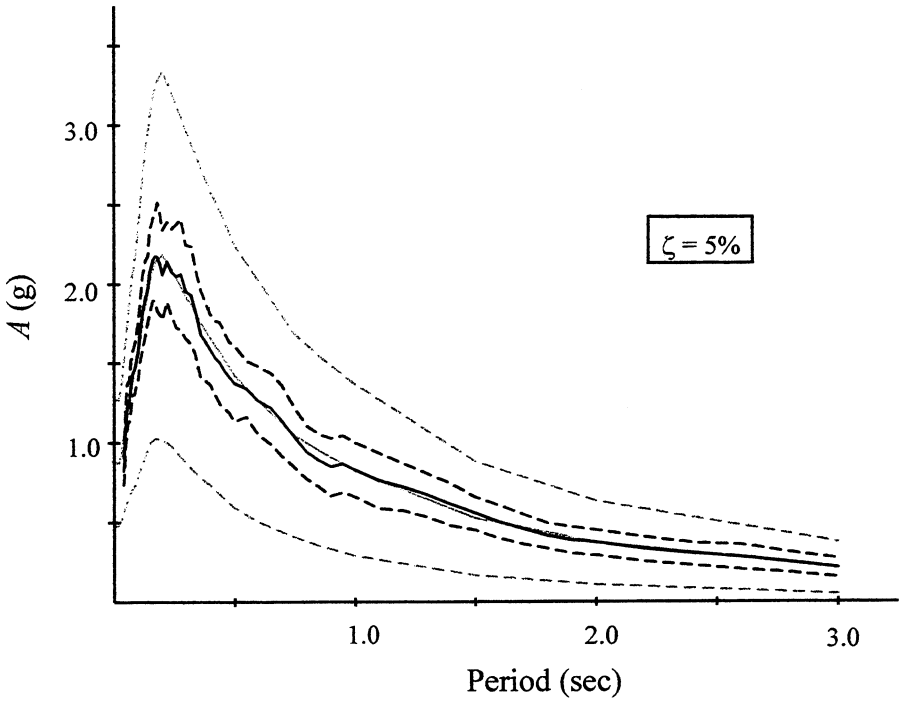

—— Ensemble mean response spectrum
- - - - Ensemble mean-plus-or-minus-one-standard-deviation response spectrum
—— Target response spectrum
- - - - Target mean-plus-or-minus-one-standard-deviation response spectrum

Figure 4.8. Target and ensemble mean and mean-plus-or-minus-one-standard-deviation pseudo-acceleration response spectra for artificial ground motions.

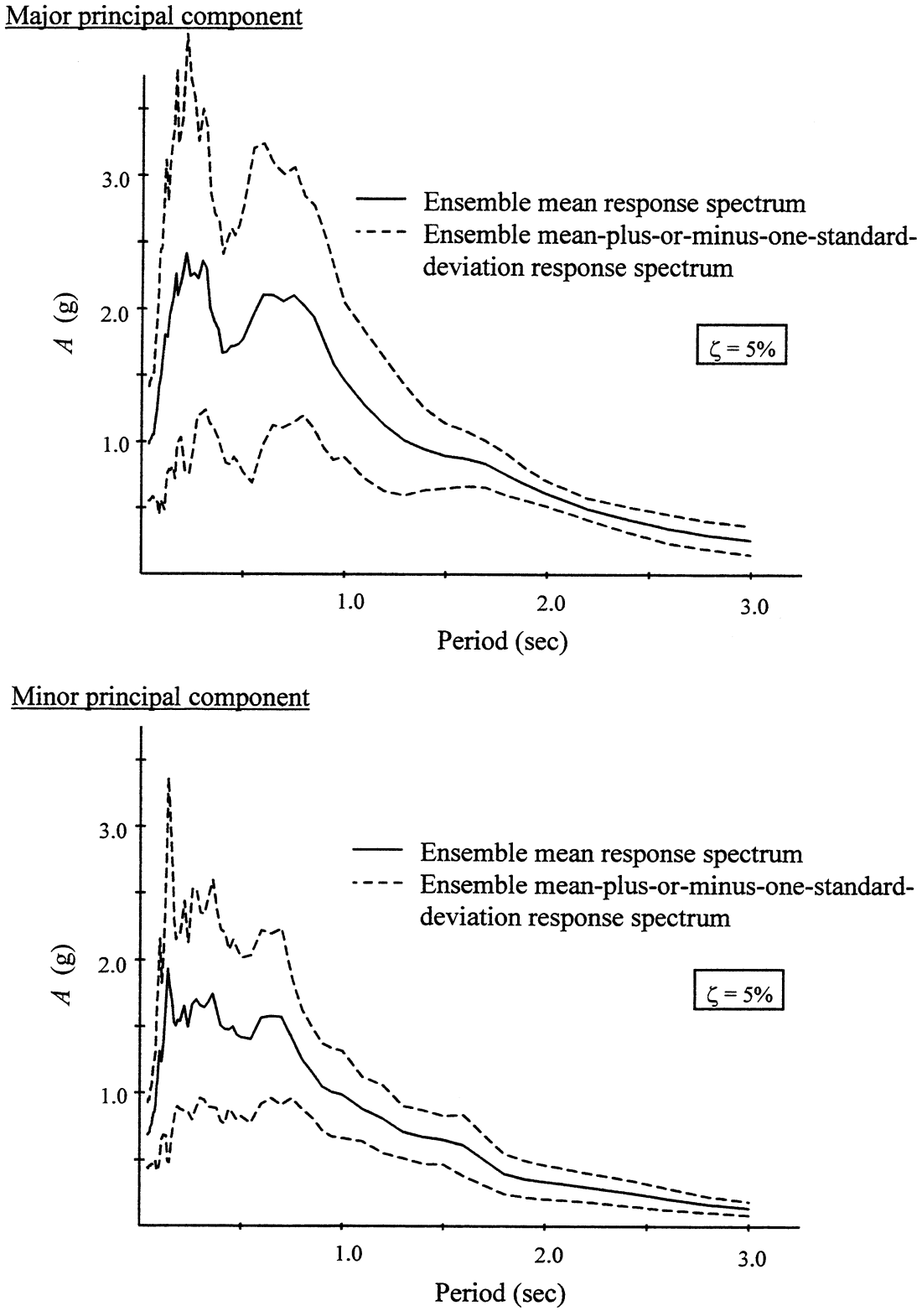

Figure 4.9. Mean and mean-plus-or-minus-one-standard-deviation pseudo-acceleration response spectra for ensemble of Seattle ground motions.

Fault-normal component

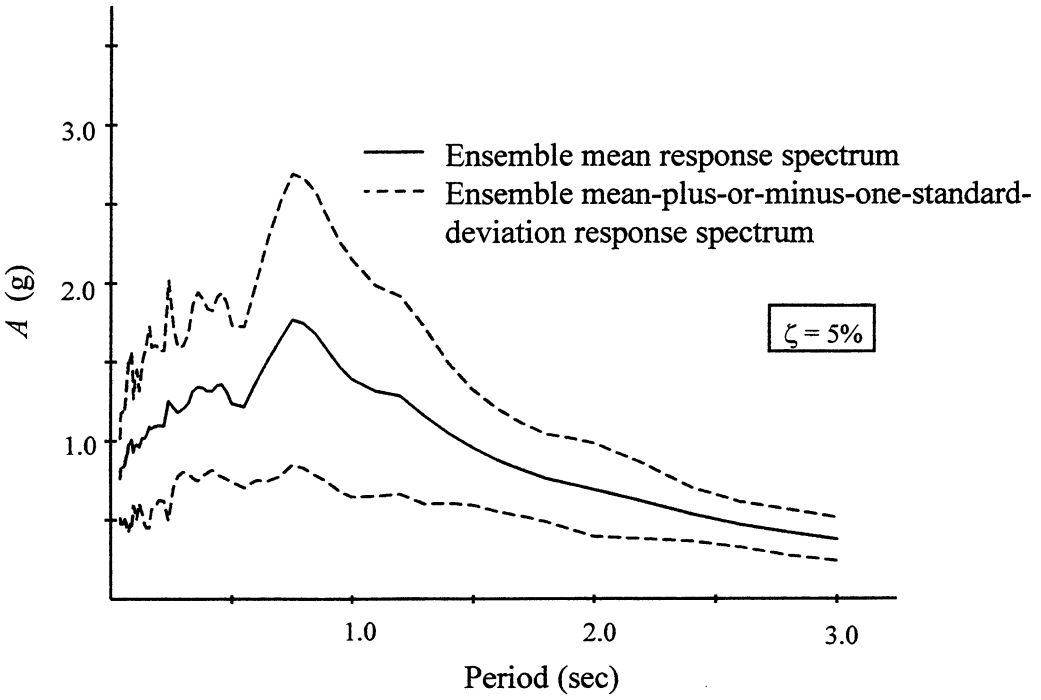

Fault-parallel component

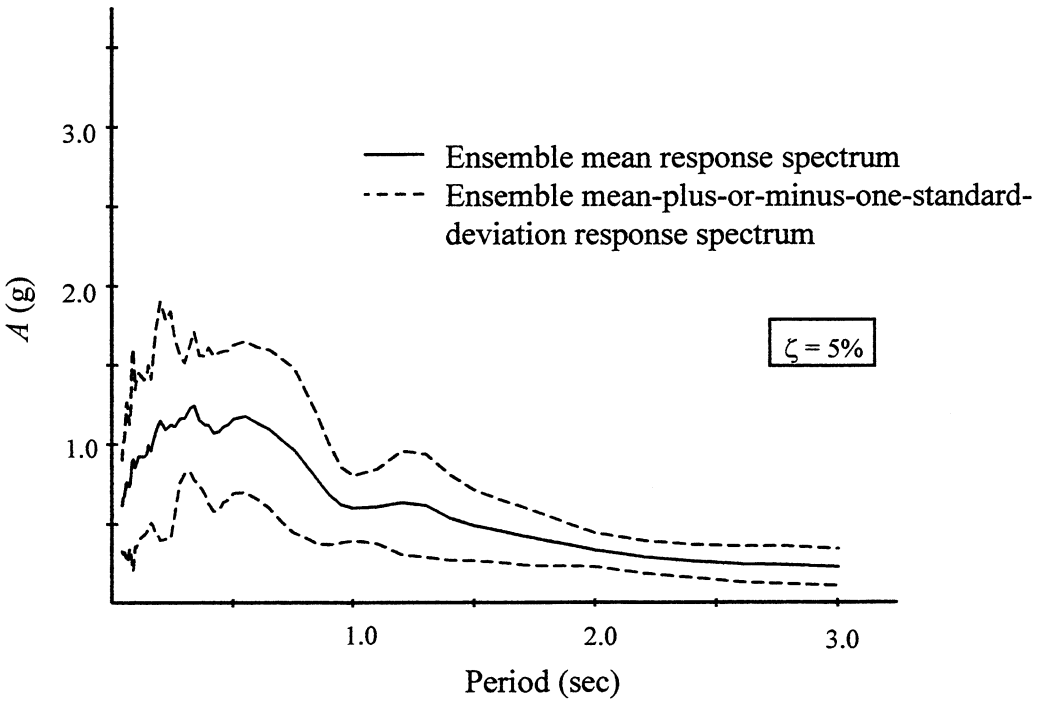

Figure 4.10. Mean and mean-plus-or-minus-one-standard-deviation pseudo-acceleration response spectra for ensemble of recorded near-fault ground motions.

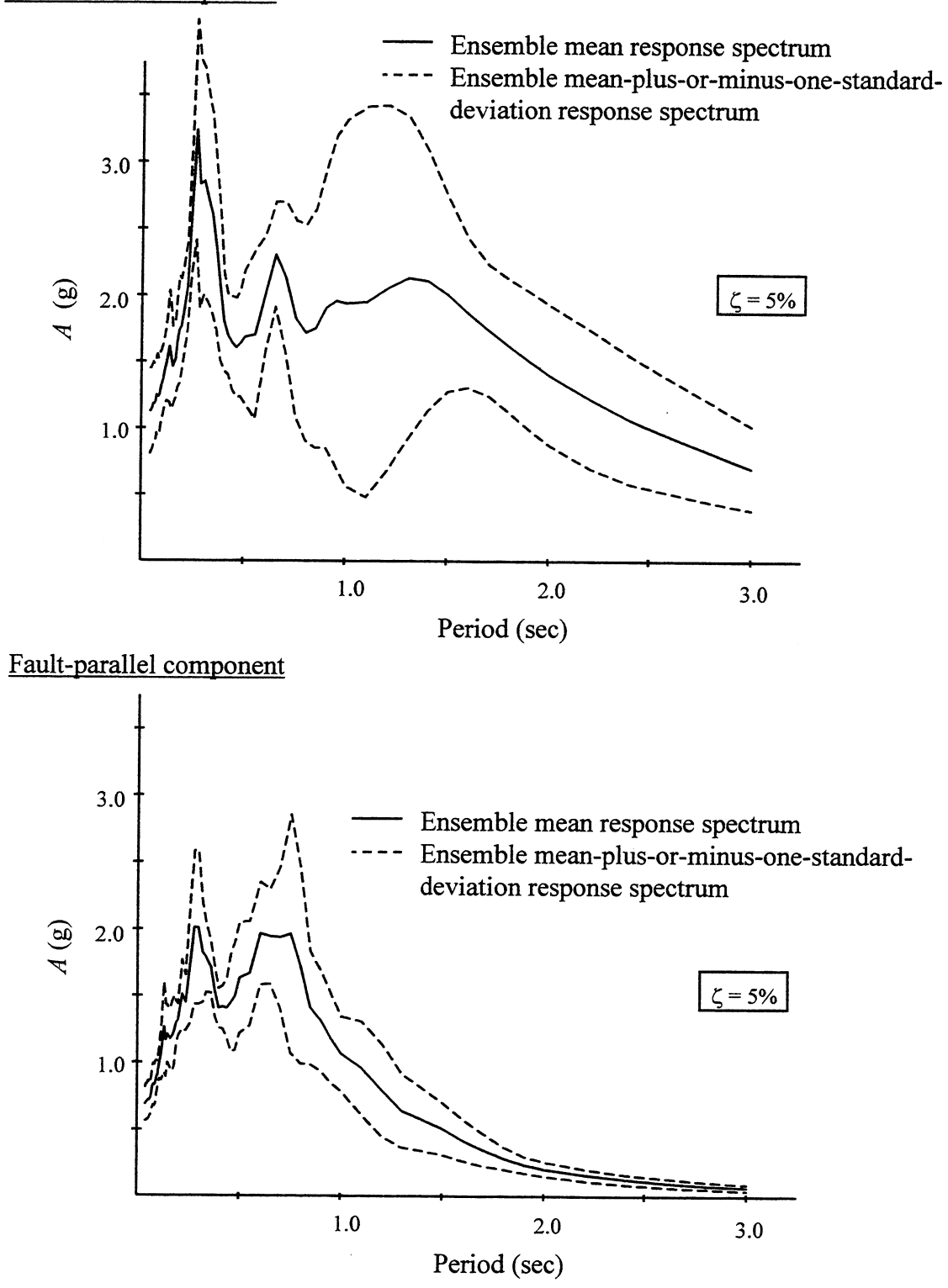

Figure 4.11. Mean and mean-plus-or-minus-one-standard-deviation pseudo-acceleration response spectra for synthetic near-fault ground motion ensemble #1.

Fault-normal component

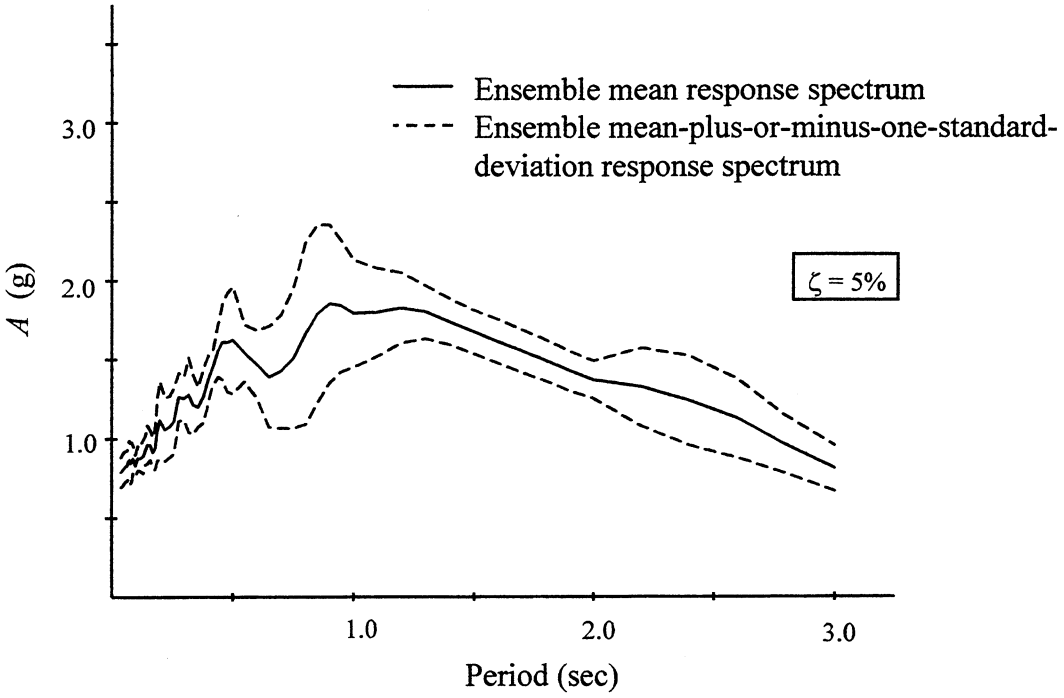

Fault-parallel component

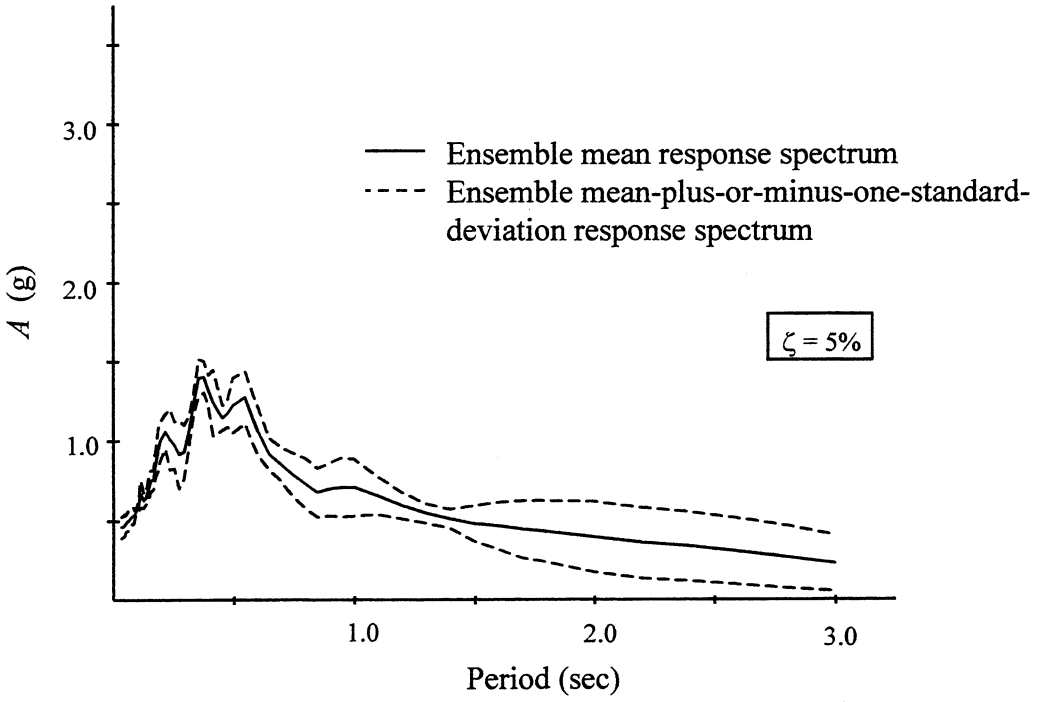

Figure 4.12. Mean and mean-plus-or-minus-one-standard-deviation pseudo-acceleration response spectra for synthetic near-fault ground motion ensemble #2.

5 Verification of the Elliptical Envelope

5.1 INTRODUCTION

The procedure developed in Chapter 3 is based upon the response spectrum method and the Penzien-Watabe (1975) characterization of multi-component ground motions. Consequently, it inherits a number of assumptions and approximations implicit in these methods. In particular, as discussed in Chapter 2, the response spectrum method is based on notions of stationary random vibrations and entails approximations involving peak factors, while the Penzien-Watabe idealization assumes that the directions of the ground motion remain fixed for the duration of the strong motion. In essence, the motion is assumed to have a nearly stationary strong motion phase that has a broad frequency content and a duration several times longer than the fundamental period of the structure. Naturally, these assumptions and approximations affect the accuracy of the procedure for actual earthquakes.

In this chapter, we examine the accuracy of the response-spectrum-based envelope by means of comparison to "exact" results obtained by time-history analyses for the two structures described in Chapter 4. For the steel building, the horizontal roof displacements are studied. For the reinforced concrete bridge, attention is focused on the axial load and bending moments acting in one of the columns.

The first set of the numerical analyses compares the mean elliptical and simulated envelopes predicted and obtained, respectively, for the ensembles of artificial ground motions described in the previous chapter. In light of the assumptions used to develop the response spectrum method in Chapter 2 and the statistical nature of the peak value estimates provided by the method, we argue that this comparison is a fair test of the validity of the response-spectrum-based procedure developed in Chapter 3. A selected number of orientations of the principal axes of ground motion, defined by the angle θ in Chapters 2 and 3, are considered. Because the supreme envelope is constructed by superimposing elliptical envelopes for $0 \leq \theta < 2\pi$, its accu-

racy is comparable to that observed for the elliptical envelopes for varying θ. For this reason, no attempt is made to simulate the supreme envelope.

Having established the accuracy of the elliptical envelope for the ensembles of artificial ground motions, we then examine the ability of the method to predict the envelopes that arise when the example structures are subjected to the synthetic near-fault motions. While the results obtained from this part of the numerical investigation cannot be regarded as conclusive due to the limited sizes of the ensembles, they do suggest that the response-spectrum-based procedure developed in Chapter 3 can be used with these near-fault motions with some degree of confidence.

Finally, in the last section of this chapter, we examine the ability of the method to predict the envelope of a time-varying response vector resulting from a specified ground motion. We note that this is a misuse of the procedure because the response spectrum method has a statistical basis that enables it only to correctly predict expected peak values over ensembles of time-history results. As such, the observations made in this part of the numerical analyses cannot be used to either validate or refute the accuracy of the elliptical envelope; however, they do provide additional insight into the probabilistic nature of the response-spectrum-based estimates obtained from the proposed procedure.

5.2 COMPARISON OF MEAN ENVELOPES — ARTIFICIAL GROUND MOTIONS

To assess the ability of the proposed method to accurately predict the envelope of a vector of seismic responses, the set of 50 serviceability level artificial ground motions was randomly divided into 25 sets of two. For each of these pairs of accelerograms, time-history analyses were conducted by applying them as orthogonal, statistically independent components of horizontal ground motion acting on the two example structures. Vertical accelerations were not applied. The time-history results are used to compute the mean envelopes bounding the response vectors considered. These simulated envelopes are then compared to the elliptical envelopes predicted by the response-spectrum-based procedure developed in Chapter 3 using the mean of the ensemble response spectra, as described below.

We denote the one-sided displacement response spectrum of the major principal direction of ground motion D_1 and assume it is the mean one-sided displacement response spectrum of the ensemble of 50 artificial ground motions. The ordinates of this response spectrum corresponding

to the periods and damping ratios of the modes included in the analyses are tabulated in Tables 5.1 and 5.2 for the example building and bridge, respectively. As is common in practice, the response spectrum of the intermediate principal direction of ground motion, i.e., the horizontal component orthogonal to the major axis, is assumed to be proportional to D_1. However, we note that the procedure is not restricted to this special case. Based on the observations made by Penzien and Watabe (1975), we assume $D_2 = 0.85\, D_1$ for the intermediate principal direction of ground motion. In the time-history analyses that follow, the artificially generated ground motions applied along the intermediate principal axis are scaled by 0.85 to be consistent with the assumed response spectra.

Four orientations of the principal axes of ground motion, relative to the structure axes, are considered: $\theta = 0$, $\pi/8$, $\pi/4$ and $3\pi/8$ radians. Due to the symmetry of the example building, these values of θ provide a nearly complete description of the influence of θ on the computed envelope for this structure. For the example bridge, values of $\pi/2 \leq \theta < \pi$ should be included for completeness; however, preliminary investigations indicated that the nature of results obtained for this range of θ do not differ in any significant way from what is presented below. Therefore, results for this range are not presented. The major principal component of ground motion is applied along an axis that is rotated by the angle θ in the counterclockwise direction from the z_1 axis of the structures shown in Figures 4.1 and 4.2.

For the building example, we consider the horizontal roof displacements, $\Delta_1(t)$ and $\Delta_2(t)$ in the z_1 and z_2 directions, respectively, at corner 'G7' in Figure 4.1 (located at the intersection of gridlines G and 7). For the bridge, attention is focused on the axial load, $P(t)$, and the bending moments, $M_1(t)$ and $M_2(t)$ about the z_1 and z_2 axes, respectively, acting in column 'B1' of Figure 4.3 (located at the intersection of gridlines B and 1). Apart from the fact that these response quantities are of engineering interest, they are considered in the following numerical investigation because they each receive significant contributions from more than one mode of vibration for some directions of loading, as is evident in Tables 5.3 and 5.4. Thus, the modal combination rule embedded in the response spectrum procedure contributes to the observed results. We note from the results presented in Table 5.3 that the peak values $\Delta_1(t)$ and $\Delta_2(t)$ are strongly dependent upon the direction in which the horizontal ground motion is applied. However, the results tabulated in Table 5.4 indicate that the peak bridge column responses are compa-

rable for ground motions directed along any of the horizontal axes considered. This unusual characteristic of the example bridge is due to the fact that its lateral force resisting elements are not orthogonal to each other.

For each time-history analysis, the response quantities were recorded as they evolved in time. Hence, for each orientation of the principal axes of ground motion considered, 25 realizations of the response vector $\mathbf{x}(t) = [\Delta_1(t), \Delta_2(t)]^T$ for the building example and $\mathbf{x}(t) = [P(t), M_1(t), M_2(t)]^T$ for the bridge example were obtained. These realizations of $\mathbf{x}(t)$ were used to estimate the mean bounding envelope on the corresponding vector process as follows: The peak value of the projection of the response vector along a specified direction α in the response space was computed for each time history. For a given time history, this peak value defines a plane perpendicular to α that the response vector touches but does not cross, i.e., this plane defines the upper bound of the response in direction α for the particular realization. The mean of the 25 peak values obtained for a given direction α thus defines a plane that, in an average sense, bounds the vector process in that direction. This calculation was repeated for a large number of directions in the response space, each yielding a plane that bounds the vector process in an average sense. A mean envelope for the vector process was developed using this ensemble of planes in a way analogous to that illustrated in Figure 3.1c.

The simulated mean envelopes bounding the building response $\mathbf{x}(t) = [\Delta_1(t), \Delta_2(t)]^T$ are shown in Figure 5.1 along with the elliptical envelopes computed using the mean response spectra. In Figure 5.2, the simulated mean envelopes and the corresponding elliptical envelopes bounding the bridge column response are projected onto the three planes defined by the response pairs (P, M_1), (P, M_2) and (M_1, M_2). For both structures, the static components of the response vectors due to gravity loads were calculated and the envelopes were shifted accordingly in the response space as described in Section 3.4. The results obtained for the four orientations of the principal directions of ground motion are presented in Figures 5.1 and 5.2. These figures show excellent agreement between the simulated and predicted mean envelopes.

Also indicated in Figures 5.1 and 5.2 are the simulated and predicted mean-plus-one-standard-deviation envelopes for the response vectors. These envelopes are obtained in a manner similar to that described above for the mean envelopes. While the agreement between the simulated and predicted mean-plus-one-standard-deviation envelopes is good, it is not as good as that found for the mean envelopes. This observation is a consequence of the well-known fact that, for

a fixed number of data points (in this case, the 25 realizations of the distance to the bounding hyperplane in any give direction), the mean of the data can be estimated more accurately than the standard deviation.

We note that the sizes and orientations of the envelopes in Figures 5.1 and 5.2 appear to be relatively insensitive to the value of θ. This result is primarily due to the assumed ratio, $S_2/S_1 = 0.85$, between the response spectra of the two principal components of ground motion. As originally noted by Smeby and Der Kiureghian (1985), as S_2/S_1 increases to unity, the contributions to the total response made by the terms in (2.28a) that are functions of θ decrease to zero. In fact, for $S_2/S_1 = 1$, the elliptical envelope is independent of θ and there would be no difference between the theoretical results predicted for the different orientations. Had we used a smaller value for S_2/S_1 in these numerical analyses, the results would have shown greater sensitivity to θ. As an extreme example, the mean elliptical envelopes bounding the responses in bridge column B1 are plotted for the case of a single component of ground motion, i.e., $S_2/S_1 = 0$, in Figure 5.3. We note that the correlation structure between $P(t)$, $M_1(t)$ and $M_2(t)$ changes significantly with θ in Figure 5.3, but the peak values of these responses change only slightly. This insensitivity of the peak values to changes in θ stems from the fact that the peak column responses are comparable for ground motions directed along any horizontal axis, as can be deduced from the modal contributions listed in Table 5.4.

The symmetric appearance of the deviations between the simulated and predicted envelopes in Figures 5.1 and 5.2 suggests that they are primarily due to the approximations inherent in the response spectrum method and the Penzien-Watabe characterization of the ground motions. If a significant component of these deviations were due to the limited number of realizations of $\mathbf{x}(t)$ used to determine the simulated envelope, we would have observed more chaotic deviations in Figures 5.1 and 5.2. We note, however, that the differences are relatively small. Among all directions in the response space, the maximum difference between the simulated and predicted mean envelopes is approximately 10%. For most directions, the difference is much less than this worst case.

Some of the discrepancy between the elliptical and simulated envelopes appearing in Figures 5.1 and 5.2 may be due to the short duration of the serviceability level event assumed in the analyses. Recall that one of the assumptions of the response spectrum method is that the

strong motion phase of the earthquake is several times longer than the fundamental period of the structure. This condition is imposed to ensure that the response of the structure reaches an approximate state of stationarity. Comparing the sample accelerogram for the serviceability event shown in Figure 4.7 to the natural period of the bridge listed in Table 4.7, one can argue that this condition is satisfied for the bridge. However, for the analyses involving the building, which has a longer natural period (see Table 4.4), the assumption that the response of the structure reaches a state of stationarity for this short-duration event is questionable. To further explore this effect, the above analyses were repeated using the ensemble of artificial ground motions for the ultimate level earthquake. As can be seen in Figure 4.7, this event has a much longer strong motion phase than the serviceability level earthquake. Therefore, we should expect an improvement in the agreement between the predicted and simulated envelopes, especially for the building example. The results of these analyses are presented in Figure 5.4 for the building example and Figure 5.5 for the bridge example. Due to the apparent insensitivity of the accuracy of the predicted envelopes to θ observed in Figures 5.1 and 5.2, only the results for $\theta = 0$ are shown. As we speculated, the agreement between the predicted and simulated envelopes for the building example shown in Figure 5.4 is better than that shown in Figure 5.1. For the mean envelopes shown in Figure 5.4, the maximum difference in any direction is less than 4%. For the bridge example, the agreement between the predicted and simulated results shown in Figure 5.5 is only marginally better than that shown in Figure 5.2, as we predicted.

5.3 COMPARISON OF MEAN ENVELOPES — SYNTHETIC NEAR-FAULT GROUND MOTIONS

In this section, we repeat the analyses performed in the previous section with the two ensembles of synthetic near-fault ground motions. As mentioned in Chapter 2, impulsive, short duration events that are commonly recorded in the near-field of an earthquake do not properly satisfy some of the assumptions invoked in the development of the response spectrum method. The objective of the following analyses is to investigate the possibility of using the response-spectrum-based procedure developed in Chapter 3 with ground motions of this type. Unfortunately, due to the limited size of the synthetic ensembles, conclusive results cannot be expected.

For both ensembles of synthetic near-fault motions, the simulated and predicted mean envelopes bounding the vectors of responses considered above were computed as described for

the artificial motions. However, unlike the analyses done above, a scale factor is not applied to either component of these ground motions for obvious reasons. Furthermore, in light of the results in Figures 5.1 and 5.2, only the case of $\theta = 0$ is considered. Finally, for reasons that will be explained shortly, the simulated mean-plus-or-minus-one-standard-deviation envelopes are also shown for the building displacements. The results are plotted in Figures 5.6 and 5.7 for the building and bridge responses, respectively.

Studying Figures 5.6 and 5.7, we first remark on the relative magnitudes of the events contained in the two ensembles. It is obvious from the figures that the first ensemble of synthetic near-fault motions is stronger than the second one. Furthermore, a comparison of the mean-minus-one-standard-deviation envelope of the first ensemble to the mean-plus-one-standard-deviation envelope of the second ensemble in Figure 5.6 suggests that it is not reasonable to combine these ensembles. The statistical measures of the combined ensemble would be meaningless due to the "clumping" of the two sets of data evident in Figures 5.6 and 5.7.

Overall, the agreement between the simulated and elliptical mean envelopes plotted in Figures 5.6 and 5.7 is good, considering the limited number of the ground motions used in the computations. Except for the building response due to the second ensemble, the differences between the simulated and theoretical envelopes in Figures 5.6 and 5.7 have a symmetric appearance similar to that noted in Figures 5.1 and 5.2. As we argued earlier, this observation suggests that the discrepancies between the simulated and elliptical envelopes are primarily due to the approximations inherent in the procedure and not due to a lack of data. On the other hand, in contrast to the simulated envelopes plotted in Figures 5.1 and 5.2, the simulated envelopes in Figures 5.6 and 5.7 have sharp "corners" in some directions. Each of these corners is due to a single ground motion dominating the time-history results in that direction, which suggests that more data is required to properly resolve any differences between the mean simulated and predicted envelopes for the near-fault motions. The result obtained for the building response to the second ensemble also suggests that larger ensembles should be used. In spite of this apparent lack of data, the differences between the simulated and elliptical mean envelopes are relatively small, particularly when one considers the spread in the data indicated by the mean-plus-or-minus-one-standard-deviation envelopes. The maximum difference between the simulated and predicted envelopes in some directions of the response space is approximately 15%. While this difference is larger than what was observed for the envelopes obtained using the artificial far-field motions above, it is not excessive. For most directions, the difference is much less than this worst case.

Moreover, it is evident from Figures 5.6 and 5.7 that the response-spectrum-based procedure correctly predicts the correlation between the various responses.

Unfortunately, we cannot draw any strong conclusions from the numerical analyses performed with these synthetic near-fault ground motions. The results presented in Figures 5.6 and 5.7 suggest that the response-spectrum-based procedure may be able to predict the mean envelopes that bound seismic response vectors resulting from near-fault motions with reasonable accuracy. However, the limited sizes of the available ensembles do not provide sufficient resolution of the simulated envelopes necessary to either validate or refute the use of the procedure for ground motions of this type. This problem should be revisited with larger ensembles of near-fault motions designed to provide conclusive, statistically sound results.

5.4 COMPARISON OF TIME HISTORIES WITH ELLIPTICAL ENVELOPES

Due to the probabilistic basis of the response spectrum method, the procedure developed in Chapter 3 should be used to predict the envelope that bounds a response vector in a statistical sense, i.e., the mean or mean-plus-one-standard-deviation over an ensemble of ground motions. Our attention thus far has focused on the agreement between the simulated and elliptical mean envelopes obtained for what are believed to be "true" ensembles of ground motions in the context of the response spectrum method. However, it is also interesting and insightful to examine the relationship between individual time histories and the elliptical envelopes predicted using the actual response spectra of the input ground motions. In particular, these comparisons will help reveal the probabilistic nature of the response spectrum procedure developed in Chapter 3. Also, it is interesting to compare the qualitative nature of the results obtained for the artificial ground motions, which satisfy the assumptions of the response spectrum method, to that of the ensembles of more realistic records. Recall that these ensembles of recorded ground motions are not "true" ensembles in the context of the response spectrum method; hence, we can only indirectly evaluate the procedure for these ground motions by making these qualitative comparisons. Before proceeding, we stress that comparisons made between individual time histories and response-spectrum-based estimates are, strictly speaking, a misuse of the response spectrum method. Thus, the results reported in this section cannot be used to either validate or refute the accuracy of the response spectrum procedure. Our objective is simply to examine the relationship

between the response-spectrum-based envelope and realizations of the time-varying response vector it is supposed to bound.

Cataloged in Figures 5.8 through 5.12 are the trajectories of the building roof displacement corresponding to $\theta = 0$ for the ensembles of artificial ground motions, the ensembles of synthetic and recorded near-fault motions, and the ensemble of Seattle ground motions. Plotted with every trajectory is the elliptical envelope computed using the actual response spectra of the input ground motions. For the artificial ground motions and the synthetic near-fault motions, the mean and mean-plus-one-standard-deviation elliptical envelopes computed using the corresponding response spectra for the ensemble are also shown. Naturally, the elliptical envelopes computed using the ensemble response spectra are the same for every time history. Preliminary analyses revealed that the qualitative nature of the results obtained for the bridge example do not differ from that observed for the building. Therefore, the time histories recorded for the bridge are not cataloged.

We first examine the time-history results obtained for the ensembles of artificial ground motions. These are recorded in Figures 5.8 and 5.9 for the serviceability and ultimate level earthquakes, respectively. For the majority of the time histories plotted in these figures, the envelope predicted using the actual response spectra of the input ground motions bounds the trajectory of the response vector with reasonable accuracy. In general, the trajectories recorded for the ultimate earthquakes appear to "fill in" the corresponding elliptical envelopes better than the trajectories recorded for the shorter duration serviceability level events. While nearly every response vector trajectory crosses the envelope computed using the actual response spectra, none of the observed excursions appears to be excessive. However, for time histories #2, #13 and #16 in Figure 5.8, the orientation of this envelope, which is related to the correlation between the elements of the response vector, does not appear to match the orientation along which the response vector trajectory evolves. Similar discrepancies, although not as pronounced, are evident in some of the results plotted for the ultimate level events in Figure 5.9. Time history #5 in Figure 5.9 appears to have at least two distinct phases during which the orientation suggested by the trajectory of the response vector is different from that predicted by the elliptical envelope. We should not be surprised nor alarmed by these discrepancies between the predicted orientation of the envelope and the orientation of the response trajectory for a given ground motion. The correlation predicted by the response spectrum method is statistical in nature and should not be expected to agree with the orientation of any given realization of the response vector it is supposed to bound.

As an analogy, we do not expect every sample drawn from a random population to be equal to the mean of the population. There are many factors that contribute to the correlation between the elements of a sample response vector, e.g., the frequency content and relative intensities of the components of ground motion as well as the existence (or non-existence) of time intervals during which the components are in or out of phase. For recorded ground motions, temporal variations in the frequency content and intensities can also contribute. We note, however, that for artificial records such as those used in this study, these effects should cancel each other out as the length of the record increases. This most likely explains the better agreement that is observed in the results obtained for the ultimate level events plotted in Figure 5.9, compared to the results plotted for the shorter duration serviceability events in Figure 5.8.

For some of the time histories in Figures 5.8 and 5.9, the envelope computed using the actual response spectra is notably different in size and/or orientation from the envelope computed using the mean response spectra of the ensemble. These differences are an indication of the probabilistic nature of the response spectrum method. Of course, we should expect to see some variation between the envelopes predicted using the actual and the mean response spectra, because, by definition, the mean response spectrum is an average of the actual response spectra over the ensemble of ground motions. Recall from Figures 5.1 and 5.4 that the simulated and elliptical mean envelopes agree very well for these ensembles of motions, in spite of these observed differences in Figures 5.8 and 5.9. It is noted that the envelopes based on the actual response spectra are in better agreement with the response trajectories than the envelopes based on the mean response spectra

It is also interesting to compare the response vector trajectories to the mean-plus-one-standard-deviation envelopes shown in Figures 5.8 and 5.9. In any given direction in the response space, the projection of the response vector exceeds the projection of this envelope in approximately 10% – 15% of the time histories, which is a reasonable rate for the probability level associated with this bound. However, in 44% of the time histories plotted in Figure 5.8 and in 40% of the time histories plotted in Figure 5.9, the response vector crosses the mean-plus-one-standard-deviation envelope at least once. This increased rate arises from the simple fact that the response vector does not cross the envelope in the same direction for all realizations. It is obvious from Figures 5.8 and 5.9 that the response vector crosses the mean envelope much more often. In light of these observations, it may be prudent to adopt at least the mean-plus-one-standard-deviation envelope for design purposes. We note however that this choice, which is

usually specified by the building codes in an implicit manner, also depends upon the load factors applied to the seismic responses and any performance factors applied to the limit state surface that defines the boundary between acceptable and unacceptable behaviors.

We now turn our attention to the time histories obtained for the ensembles of synthetic near-fault ground motions, which are catalogued in Figure 5.10. It is evident from the results presented in this figure that there are two distinct sub-ensembles of ground motions in this collection, which supports our decision in Section 5.3 to examine the mean envelopes of these two groups separately. Also, note that in the second group (time histories #6 – #10), the response vector trajectories obtained using ground motions #6 and #7 have noticeably longer excursions in the $-\Delta_1$ direction than in the $+\Delta_1$ direction. This bias is the cause of the offset between the simulated and elliptical mean envelopes observed for this ensemble of ground motions in Figure 5.6.

The qualitative relationship between the response vector trajectories and the elliptical envelopes plotted in Figure 5.10 appears to be similar to that observed for the artificial ground motions in Figures 5.8 and 5.9. Based on this comparison, there is no evidence in Figure 5.10 that suggests that the response-spectrum-based procedure developed in Chapter 3 cannot be used with ground motions of this type. Of the ten time histories plotted in Figure 5.10, only time history #5 exhibits a pronounced difference between the apparent orientation of the response trajectory and that predicted by the response-spectrum-based envelopes. However, we note that the disagreement is no worse than what was observed in Figure 5.8 for time histories # 2 and #16.

The time-history results obtained for the recorded near-fault motions and the ensemble of ground motions compiled for Seattle, Washington, are plotted in Figures 5.11 and 5.12, respectively. Unlike what was observed in Figures 5.8, 5.9 and 5.10, the magnitude of the response vectors and envelopes cataloged in Figures 5.11 and 5.12 vary significantly between events. Thus, these figures suggest that neither of these ensembles are composed of ground motions that are realizations of a common underlying stochastic process. As we pointed out in Chapter 4, these ensembles are not suitable for testing the response spectrum procedure developed in Chapter 3. For this reason, we have not plotted the elliptical envelopes computed using the mean and mean-plus-one-standard-deviation response spectra of these ensembles. Nevertheless, we can examine the qualitative relationship between the response vector trajectories and elliptical enve-

lopes based on the actual response spectra obtained for these ground motions and make comparisons with similar results presented in Figures 5.8 and 5.9.

For all records plotted in Figures 5.11 and 5.12, the magnitudes of the individual components of the response vectors appear to be well predicted by the response-spectrum-based envelopes. Among the near-fault records plotted in Figure 5.11, only two (#2 and #5) exhibit significant differences between the trajectory of the response vector and the elliptical envelope computed using the actual response spectra of the input ground motions. These differences, however, are similar to those observed in Figure 5.8 for time histories #2, #13 and #16. For the Seattle ensemble plotted in Figure 5.12, only trajectories #7 and #8 appear to be correlated differently from what is predicted by the response-spectrum-based elliptical envelopes associated with these records. Also of interest in this ensemble is time history #9, which exhibits two distinct phases during which the correlation of the response vector is different. This result is comparable to that observed for time history #5 in Figure 5.9. Overall, the qualitative nature of the results presented in Figures 5.11 and 5.12 is comparable to what was observed in Figures 5.8 and 5.9 for the artificial ground motions. There are no trends apparent in these results for recorded ground motions that suggest that the response-spectrum-based envelope developed in Chapter 3 cannot be used with ground motions of this type.

Table 5.1. Mean one-sided displacement response spectrum ordinates of the serviceability level event corresponding to the modes of the example building.

Mode	Period (sec)	Damping ratio	D_1 (mm)
1	0.6755	0.03102	18.329
2	0.6706	0.03086	18.309
3	0.3785	0.02246	11.632
4	0.2196	0.02192	6.205
5	0.2180	0.02195	6.129
6	0.1231	0.02841	2.098
7	0.1193	0.03044	1.881
8	0.1185	0.03059	1.854
9	0.0669	0.04851	0.421

Table 5.2. Mean one-sided displacement response spectrum ordinates of the serviceability level event corresponding to the modes of the example bridge.

Mode	Period (sec)	Damping ratio	D_1 (mm)
1	0.2593	0.02243	7.981
2	0.2386	0.02266	6.822
3	0.2118	0.02326	5.746
4	0.2115	0.02327	5.732
5	0.2079	0.02338	5.562
6	0.1997	0.02368	5.184
7	0.1691	0.02531	4.000
8	0.1689	0.02532	3.994
9	0.1679	0.02539	3.959
10	0.0665	0.04991	0.409
11	0.0321	0.09910	0.057
12	0.0321	0.09912	0.057
13	0.0314	0.10136	0.056
14	0.0314	0.10136	0.056
15	0.0311	0.10241	0.055

Table 5.3. Modal contributions to roof displacements of the example building.

Direction of loading θ [1] (radians)	Mode(s)	Δ_1 (mm)	Δ_2 (mm)
0	1	13.1	13.1
	2	11.6	11.6
	1 and 2	24.6	2.5
	all	24.7	2.7
$\pi / 8$	1	7.1	7.1
	2	15.2	15.2
	1 and 2	22.2	8.3
	all	22.3	8.4
$\pi / 4$	1	0.0	0.0
	2	16.5	16.5
	1 and 2	16.5	16.5
	all	16.5	16.5
$3\pi / 8$	1	7.1	7.1
	2	15.2	15.2
	1 and 2	8.3	22.2
	all	8.4	22.3
$\pi /2$	1	13.1	13.1
	2	11.6	11.6
	1 and 2	2.5	24.6
	all	2.7	24.7

[1] Refer to Figure 2.1

Table 5.4. Modal contributions to response of column B1 of the example bridge.

Direction of loading θ [1] (radians)	Mode(s)	P (kN)	M_1 (kN m)	M_2 (kN m)
0	1	306	1302	1533
	2	396	1175	1076
	1 and 2	442	1543	2063
	all	441	1543	2063
$\pi / 8$	1	388	1652	1954
	2	198	588	539
	1 and 2	394	1623	2133
	all	394	1623	2132
$\pi / 4$	1	411	1751	2061
	2	30	88	81
	1 and 2	419	1773	2044
	all	418	1773	2043
$3\pi / 8$	1	372	1583	1863
	2	253	751	688
	1 and 2	495	1899	1834
	all	493	1899	1834
$\pi /2$	1	276	1174	1381
	2	438	1299	1190
	1 and 2	568	1939	1606
	all	564	1938	1607

[1] Refer to Figure 2.1

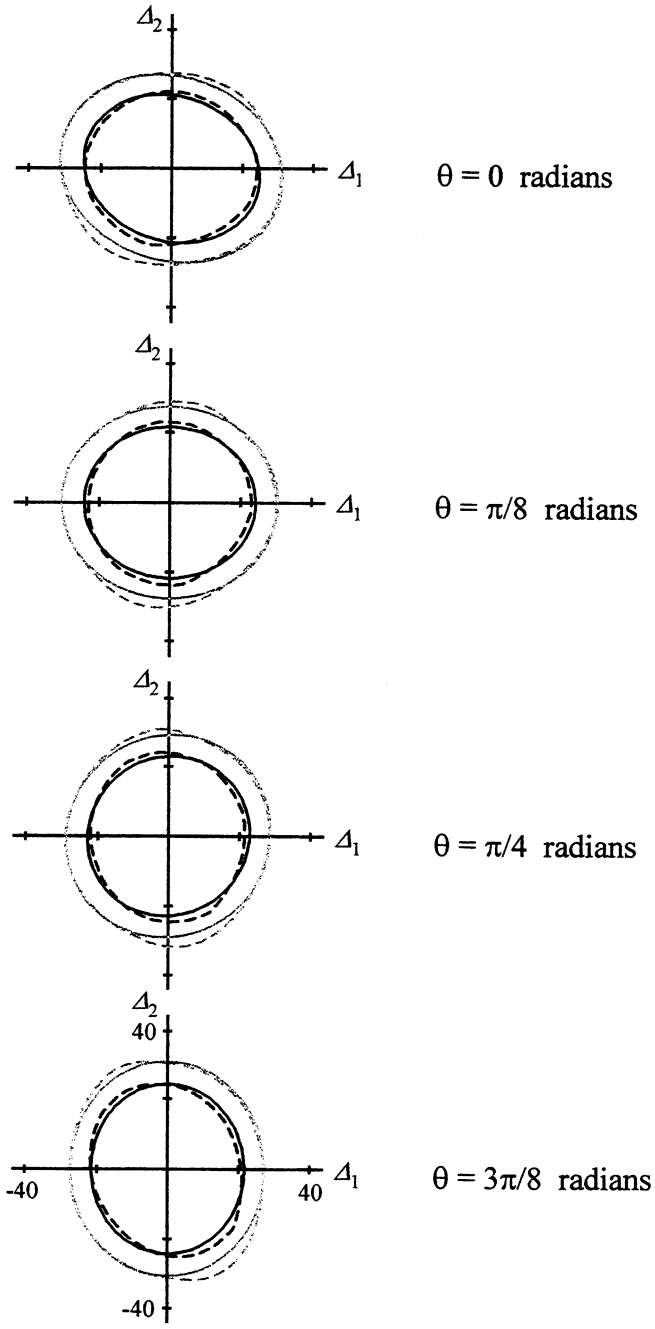

—— Elliptical envelope based on mean response spectrum
- - - - Simulated mean envelope
—— Elliptical envelope based on mean-plus-one-standard-deviation response spectrum
- - - - Simulated mean-plus-one-standard-deviation envelope

Displacements in mm
Scale for all plots as shown for $\theta = 3\pi/8$ radians.

Figure 5.1. Comparison of simulated and predicted envelopes for building roof displacements due to the serviceability level event.

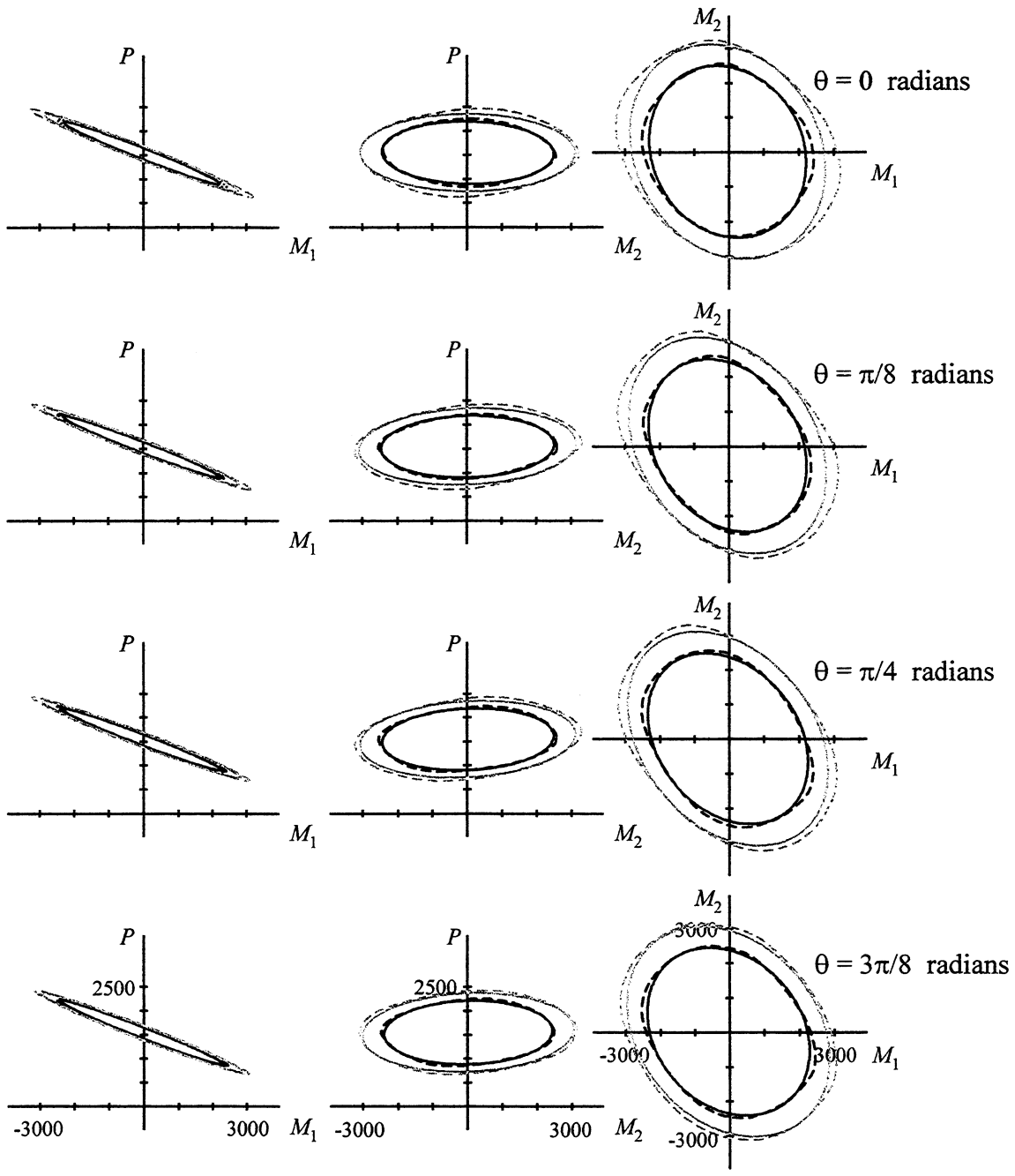

—— Elliptical envelope based on mean response spectrum

- - - - Simulated mean envelope

—— Elliptical envelope based on mean-plus-one-standard-deviation response spectrum

- - - - Simulated mean-plus-one-standard-deviation envelope

Axial load P in kN

Bending moments M_1 and M_2 in kN m

Scale for all plots as shown for $\theta = 3\pi/8$ radians.

Figure 5.2. Comparison of simulated and predicted envelopes for bridge column responses due to the serviceability level event.

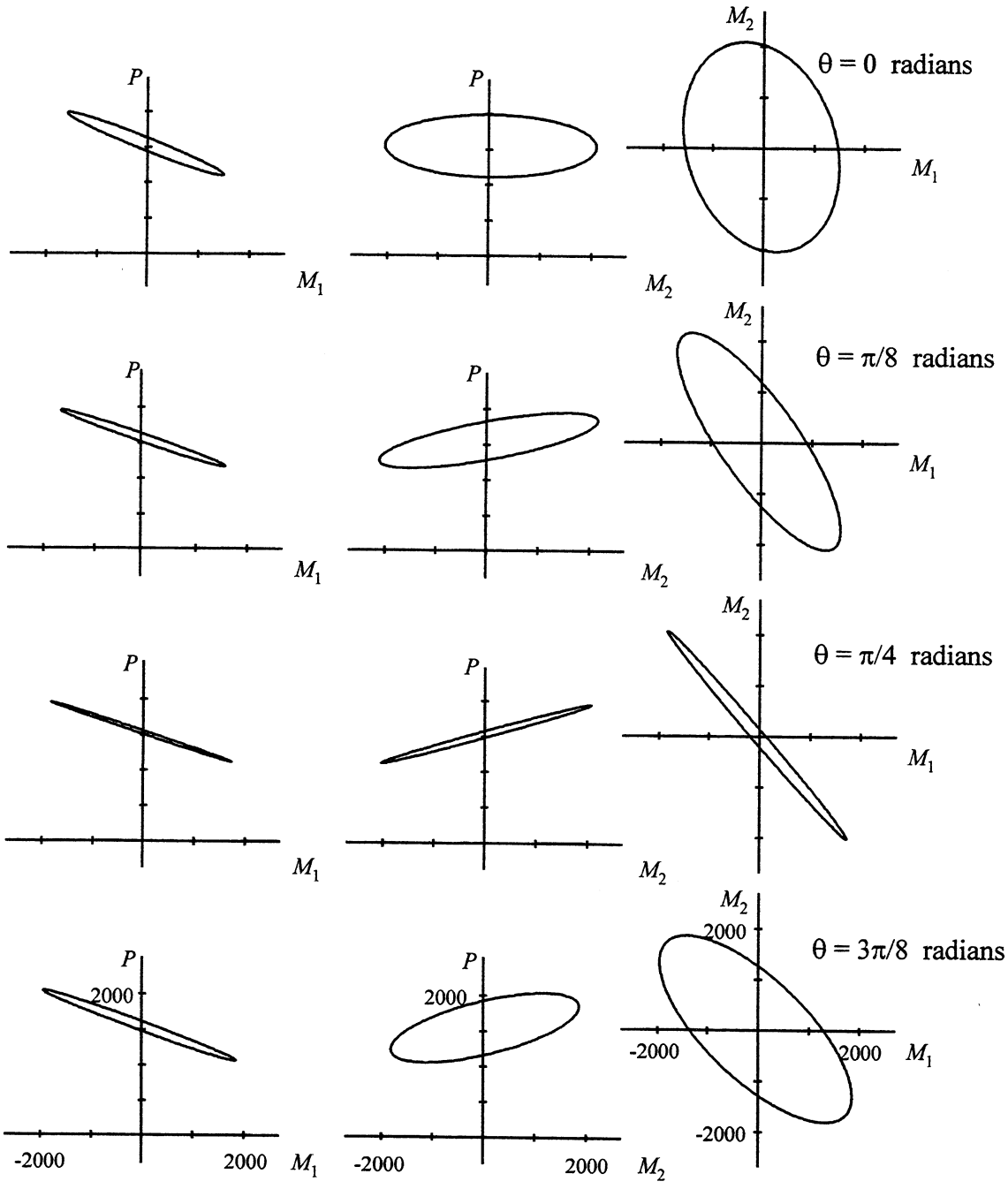

—— Elliptical envelope based on mean response spectrum

Axial load P in kN
Bending moments M_1 and M_2 in kN m

Scale for all plots as shown for $\theta = 3\pi/8$ radians.

Figure 5.3. Elliptical envelopes for bridge column responses when $S_2 / S_1 = 0$.

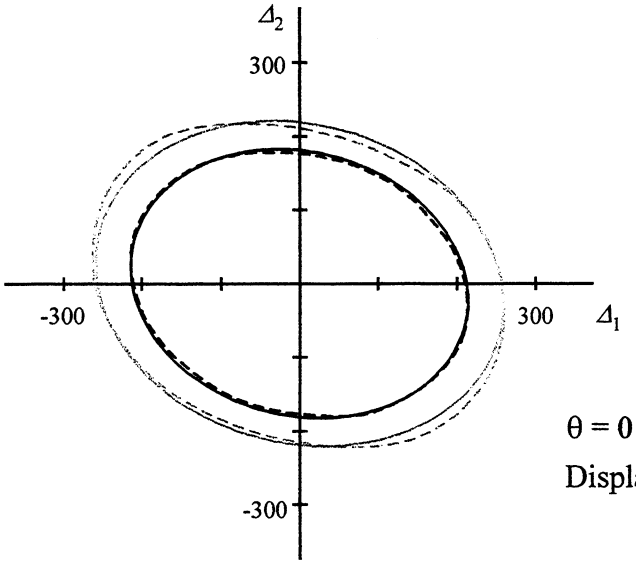

θ = 0 radians

Displacements in mm

—— Elliptical envelope based on mean response spectrum

---- Simulated mean envelope

—— Elliptical envelope based on mean-plus-one-standard-deviation response spectrum

---- Simulated mean-plus-one-standard-deviation envelope

Figure 5.4. Comparison of simulated and predicted envelopes for building roof displacements due to the ultimate level event.

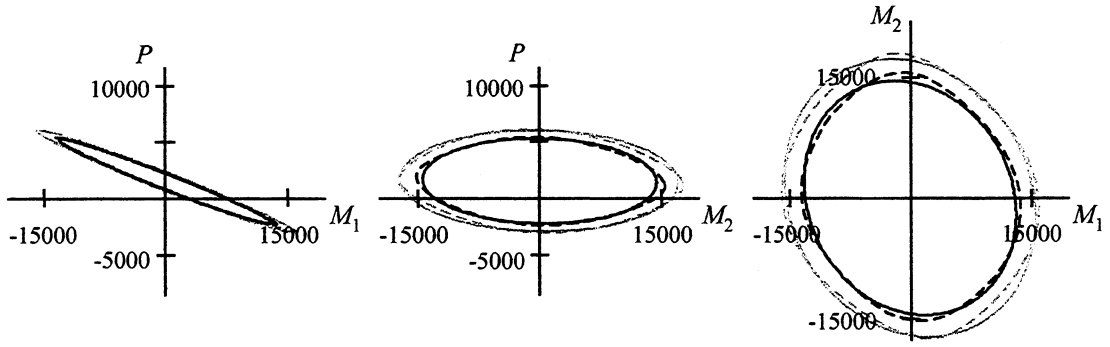

—— Elliptical envelope based on mean response spectrum

---- Simulated mean envelope

—— Elliptical envelope based on mean-plus-one-standard-deviation response spectrum

---- Simulated mean-plus-one-standard-deviation envelope

θ = 0 radians

Axial load P in kN

Bending moments M_1 and M_2 in kN m

Figure 5.5. Comparison of simulated and predicted envelopes for bridge column responses due to the ultimate level event.

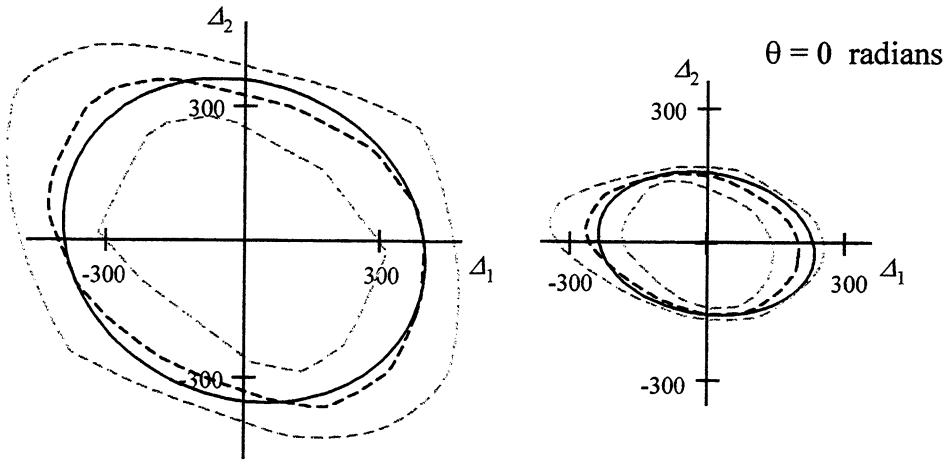

Near-fault ensemble #1 Near-fault ensemble #2

—— Elliptical envelope based on mean response spectrum
- - - - Simulated mean envelope
- - - Simulated mean-plus-or-minus-one-standard-deviation response spectrum

Displacements in mm

Figure 5.6. Comparison of simulated and predicted envelopes for building roof displacements due to the synthetic near-fault ensembles.

Near-fault ensemble #1

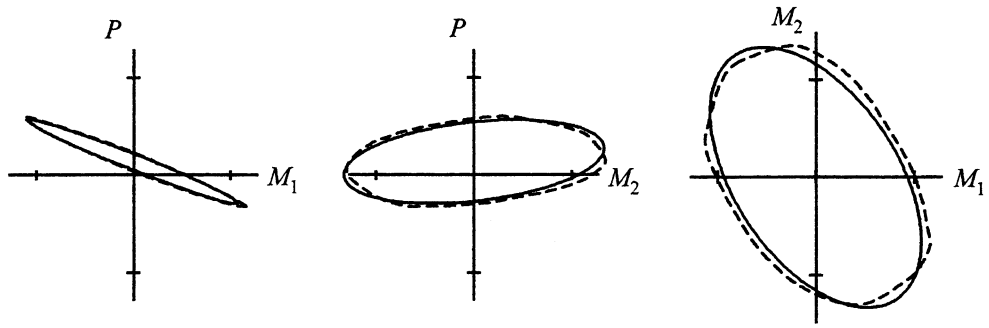

Near-fault ensemble #2

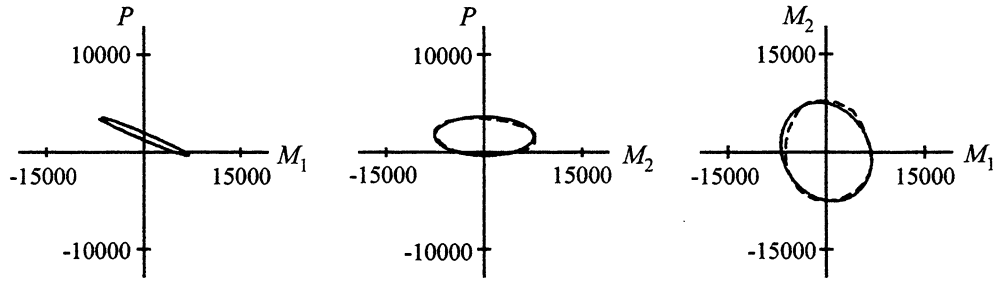

—— Elliptical envelope based on mean response spectrum $\theta = 0$ radians

---- Simulated mean envelope

Axial load P in kN

Bending moments M_1 and M_2 in kN m

Scale for ensemble #1 same as that shown for ensemble #2

Figure 5.7. Comparison of simulated and predicted envelopes for bridge column responses due to the synthetic near-fault ensembles.

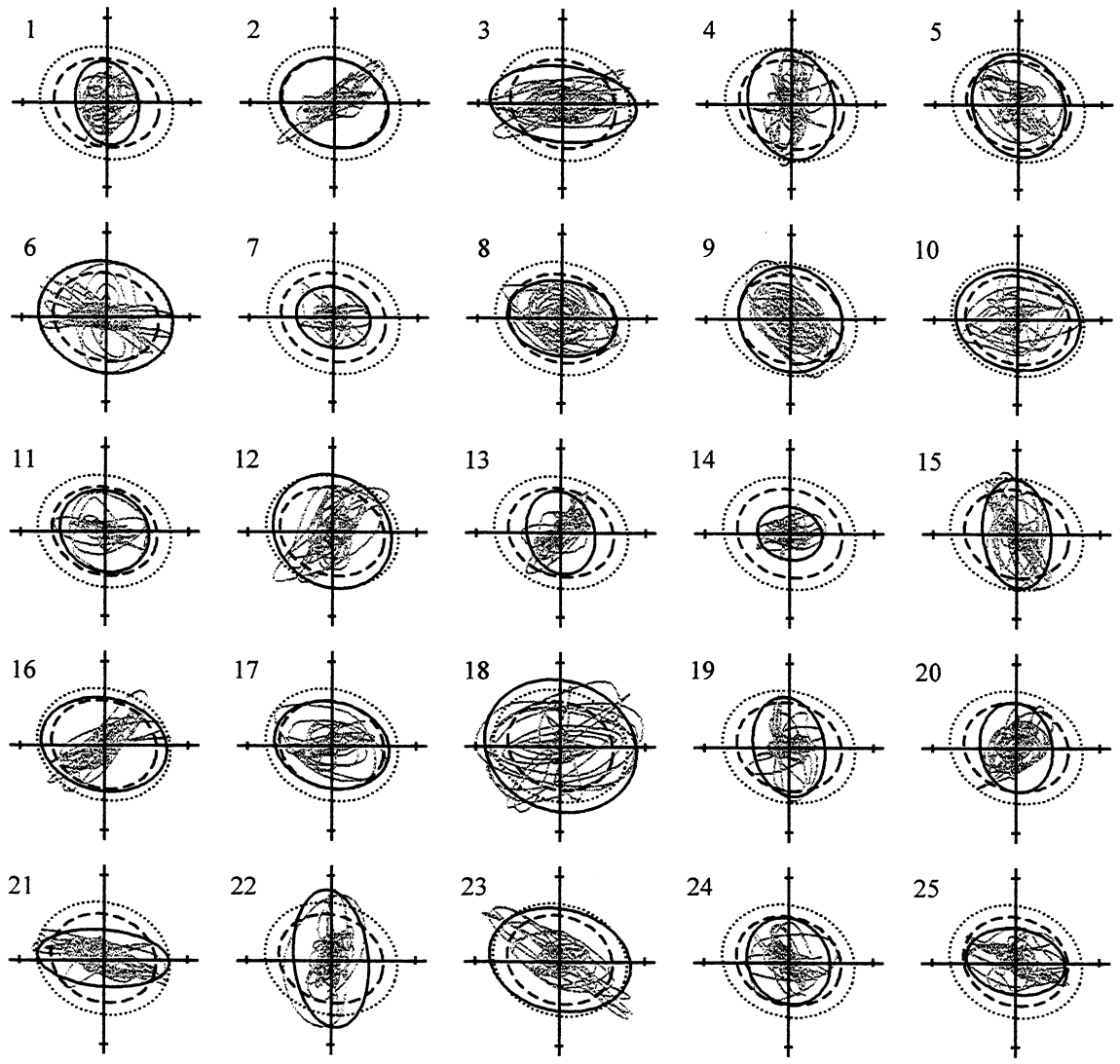

Response trajectory

Elliptical envelope computed using actual response spectrum

Elliptical envelope computed using mean response spectrum

Elliptical envelope computed using mean-plus-one-standard-deviation response spectrum

Scale for all plots as shown
Displacements in mm

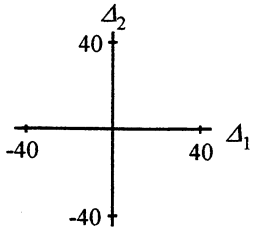

Figure 5.8. Response trajectories for the building roof displacements due to the serviceability level events.

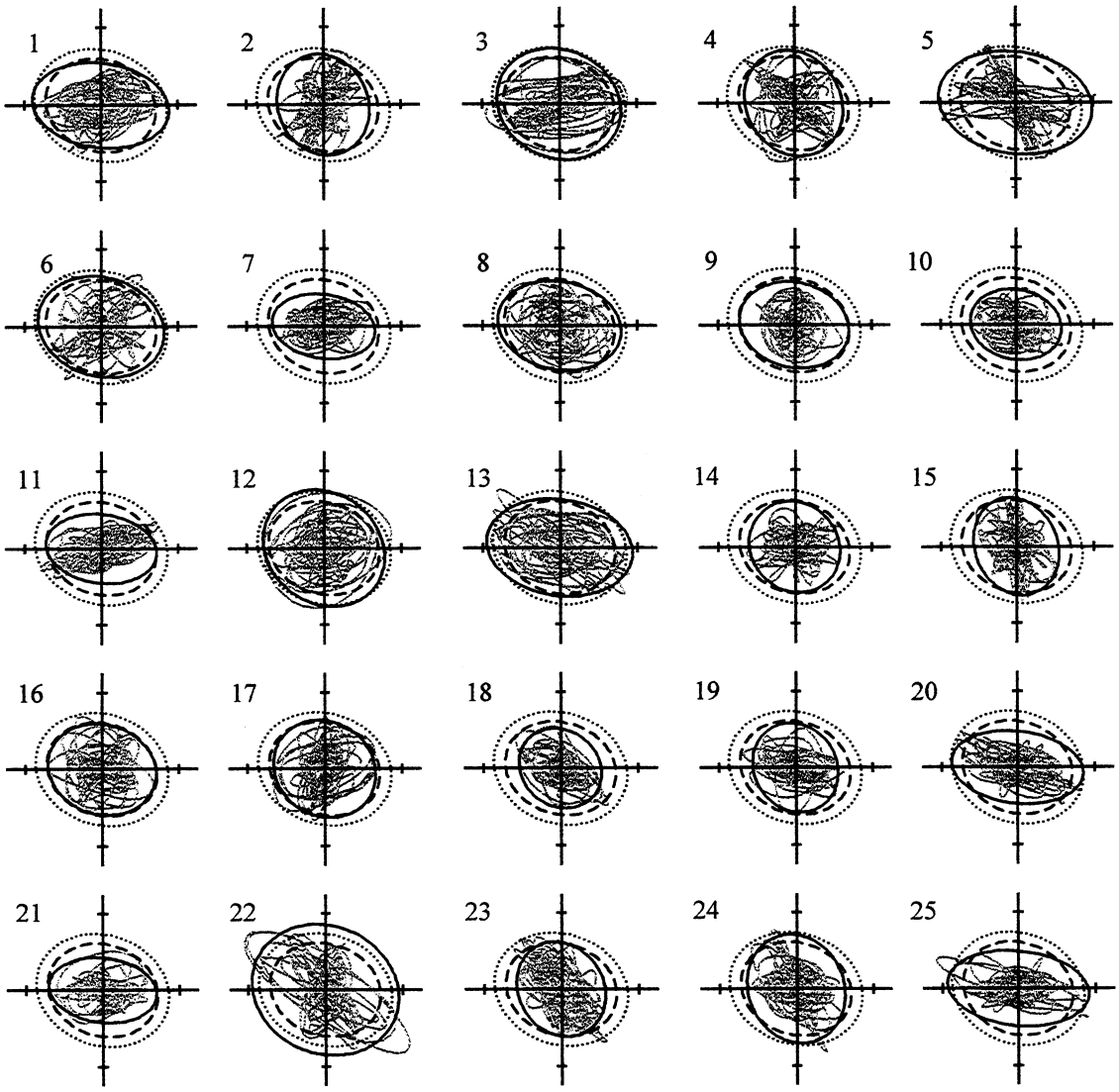

—— Response trajectory

—— Elliptical envelope computed using actual response spectrum

- - - - Elliptical envelope computed using mean response spectrum

····· Elliptical envelope computed using mean-plus-one-standard-deviation response spectrum

Scale for all plots as shown
Displacements in mm

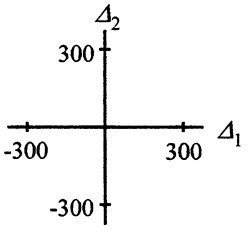

Figure 5.9. Response trajectories for the building roof displacements due to the ultimate level events.

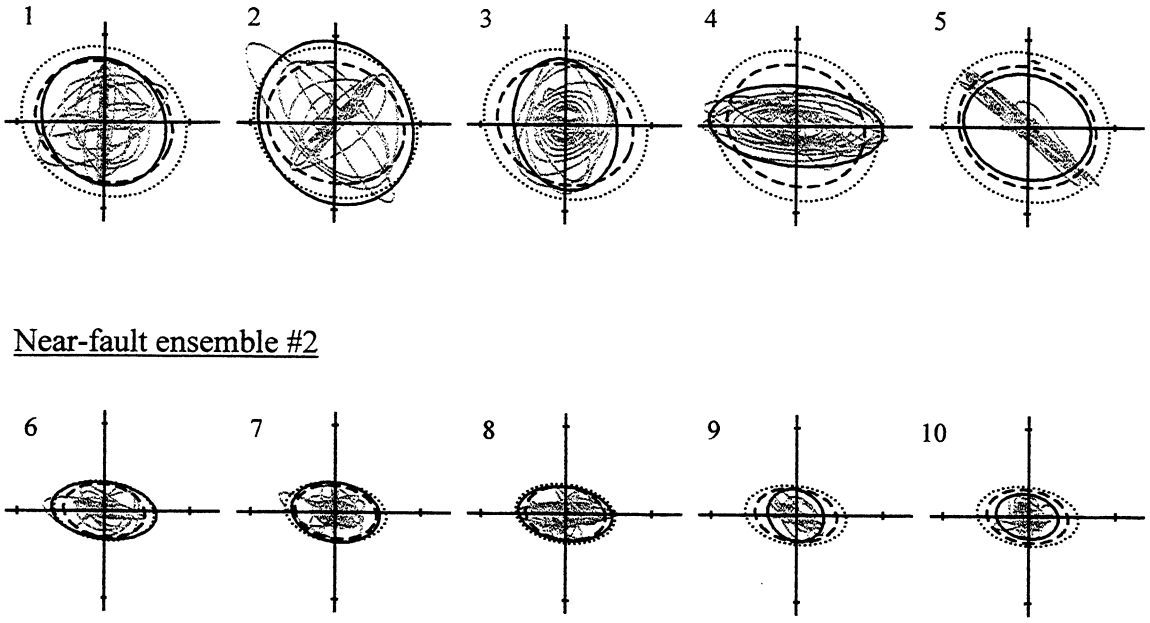

Figure 5.10. Response trajectories for the building roof displacements due to the synthetic near-fault ground motions.

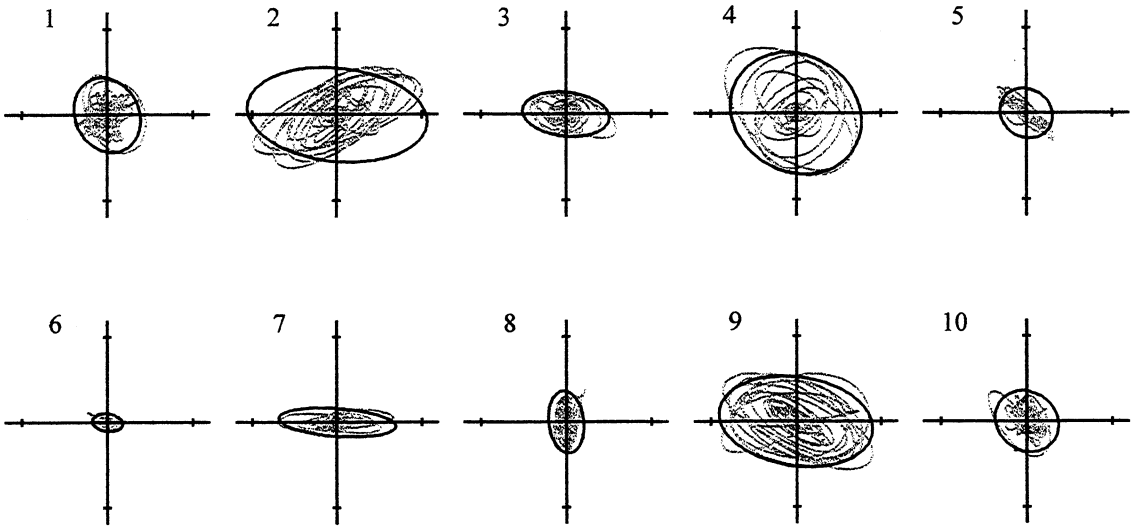

—— Response trajectory

—— Elliptical envelope computed using actual response spectrum

Scale for all plots as shown
Displacements in mm

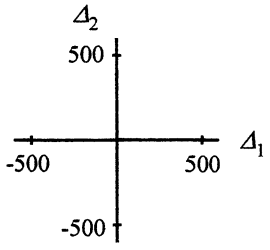

Figure 5.11. Response trajectories for the building roof displacements due to the recorded near-fault ground motions.

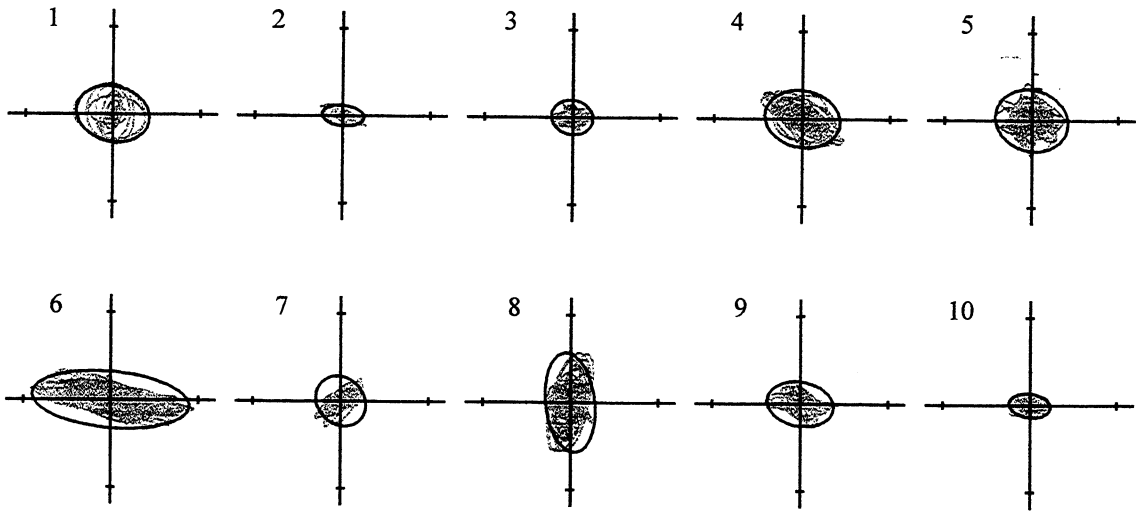

—— Response trajectory

—— Elliptical envelope computed using actual response spectrum

Scale for all plots as shown
Displacements in mm

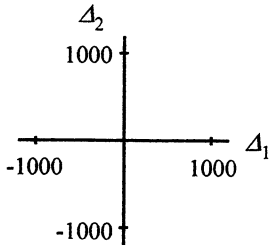

Figure 5.12. Response trajectories for the building roof displacements due to the Seattle ground motions.

6 Use of the Response Envelopes for Analysis and Design

6.1 INTRODUCTION

Having established the accuracy of the response-spectrum-based envelope, we now turn our attention to the question of how to use the envelope in the practice of seismic analysis and design. In particular, in this chapter we examine the ways in which the envelope can be used in conjunction with a capacity surface (commonly known as an interaction diagram) to either determine the adequacy of a design or to determine the required value of a design parameter. In the first case, the analyst must determine whether the envelope bounding the response vector lies entirely within a prescribed capacity surface. In the second case, the value of a design parameter, which controls the position of the capacity surface in the response space, must be determined such that the capacity surface completely encompasses the envelope. We examine both of these problems in this chapter and provide generic algorithms for their solution. The algorithms are developed for the supreme envelope because we maintain that, due to the uncertainty in the orientation of the principal directions of ground motion θ, this is the appropriate envelope to use for the purpose of assessing the adequacy of a design. However, due to the similarity between the expressions (3.38) and (3.39) used to define points on the supreme and elliptical envelopes, respectively, the same algorithms are applicable to the elliptical envelope.

Before proceeding to the discussion and development of the algorithms described above, we review the classical structural reliability approach to this problem and its relationship to the response envelopes developed in this study.

6.2 THE VECTOR OUT-CROSSING PROBLEM

Consider a capacity surface associated with a set of responses that is fixed in the response space. To determine the adequacy of a design with respect to the type of failure associated with this capacity surface, it is necessary to determine whether the response vector, as it evolves in time, out-crosses the capacity surface. If it does, then the system is said to have "failed"; otherwise, the system is said to be "safe."

Due to the probabilistic nature of seismic excitation and response, there is almost always a finite probability that a system will fail. Recognizing this fact, in a reliability-based approach, a design is considered adequate if the associated probability of failure does not exceed a prescribed threshold. The determination of the probability of the failure event described above is the well-known vector out-crossing problem in the field of structural reliability. This problem unfortunately does not have an exact solution. However, an upper bound on the probability can be obtained as described below.

Referring to Figure 6.1, an upper bound on the probability p_f that the response vector $\mathbf{x}(t)$ out-crosses the capacity surface ∂S in time interval $0 \le t \le T$ is given by (Shinozuka, 1964)

$$p_f \le p_f(0) + \int_0^T \upsilon(\partial S, t)\, dt\,, \tag{6.1}$$

where $p_f(0)$ is the probability that the response vector originates in the failure domain (usually $p_f(0) = 0$ for applications of seismic design) and $\upsilon(\partial S, t)$ is the mean rate at which $\mathbf{x}(t)$ out-crosses ∂S per unit time. In general, the solution of $\upsilon(\partial S, t)$ is difficult, as it involves the joint distribution of the response vector and its time derivative and an integration over the capacity surface (Belyaev, 1968). Consequently, there are only a few closed-form solutions available for the mean out-crossing rate for restricted classes of processes and capacity surfaces (e.g., Veneziano, et al., 1977). It should be noted that the above approach effectively couples the computation of the response vector statistics and the capacity surface, which is not convenient for practical design.

The response-spectrum-based envelope developed in this study provides an alternative means of addressing the question of whether a given design is adequate. In particular, we con-

sider a design adequate when the envelope bounding the response vector under consideration is completely encompassed by the capacity surface. This is in fact the traditional approach taken in structural engineering, namely to predict the critical combination of responses acting in a structural element and to compare this combination to the capacity of the element. An important advantage of this approach, over that based on the out-crossing formula (6.1), is that the demand and capacity evaluations are effectively uncoupled, i.e., one simply computes the response envelope and capacity surface and compares them. Naturally, an important consideration when making such a comparison is the probability level associated with the envelope (e.g., mean, mean-plus-one-standard-deviation, etc.). Usually, however, this aspect is implicitly controlled by building codes through prescribed design response spectra and load factors. For the remainder of this chapter and the next, the mean bounding envelope is assumed. However, we stress that the algorithms developed in this chapter and the qualitative nature of the results and conclusions presented here and in the Chapter 7 are not affected by this choice.

When there are only two response quantities, the adequacy of the system can be determined by simply plotting the response envelope and the capacity curve and visually confirming that the capacity curve completely encompasses the envelope. This approach can be extended to analyses involving three response quantities by plotting cross sections of the response envelope and capacity surface at several values of one response. However, this approach clearly becomes cumbersome for problems that involve more than three responses. For such cases, a numerical algorithm for determining whether the capacity surface completely encompasses the m-dimensional response envelope is necessary. The remainder of this chapter focuses on the development of such algorithms.

6.3 COMPARISON WITH A PRESCRIBED CAPACITY SURFACE

Consider Figure 6.2, in which we show the cross section of the supreme envelope bounding response vector $\mathbf{x}(t)$ centered at $\mathbf{x}_0$, a unit vector α, which defines a hyperplane that is tangent to the envelope at $\mathbf{x}_\alpha$, and the corresponding unit vector $\beta = (\mathbf{x}_\alpha - \mathbf{x}_0)/\| \mathbf{x}_\alpha - \mathbf{x}_0 \|$ in the plane defined by α and β. Also indicated in this figure is the cross section of the capacity surface in this plane, which is defined by the limit state function $g(\mathbf{x}) = 0$, and the distance R_β from $\mathbf{x}_0$ to the capacity surface along the direction β. Let S_β denote the distance to the envelope in the

same direction. It is assumed that $g(\mathbf{x}) > 0$ on the safe side of the capacity surface. The following development is restricted to concave safe domains, such as that shown in Figure 6.2. Furthermore, we assume the safe domain is closed (i.e., it does not extend to infinity in any direction) and does not contain any failure subregions. Capacity surfaces commonly encountered in structural engineering applications have these properties. Clearly, the capacity surface completely encompasses the response envelope when $R_\beta / S_\beta \geq 1$ for all directions β. Thus, our objective is to determine the minimum value of $\lambda = R_\beta / S_\beta$ for all β, which we denote as λ^*, and check whether $\lambda^* \geq 1$. If this inequality is satisfied, then the system is said to be safe. We note that the ratio λ^* is commonly called a "safety factor" in engineering practice. In the present case, it can be interpreted as the factor by which the response spectra of the components of ground motion must be scaled so that the response envelope touches, but does not cross, the capacity surface. Thus, λ^* is a measure of the safety of the design.

Ideally, we would like to work only with β and avoid involving α in the minimization procedure. This is possible for the elliptical envelope through use of (3.11), but not for the supreme envelope because the matrix $\mathbf{X}_S$ defined in (3.34), which is central to the definition of the supreme envelope, is a complicated function of α. Thus, we must resort to expressing S_β and β in terms of α and find α^* corresponding to λ^*. The required criteria for λ to be a minimum are

$$\nabla \lambda^* = \left. \frac{\partial \lambda}{\partial \alpha} \right|_{\alpha = \alpha^*} = \{0\} \tag{6.2}$$

$$\det\left[\nabla^2 \lambda^*\right] < 0 \tag{6.3}$$

where $\{0\}$ is an m-vector of zeros and

$$\nabla^2 \lambda^* = \left[\frac{\partial \lambda^2}{\partial \alpha_i \partial \alpha_j} \right]_{\alpha = \alpha^*} \qquad i, j = 1, 2, \ldots, m \tag{6.4}$$

is the $m \times m$ Hessian matrix. Recognizing machine precision limits, the convergence criterion (6.2) is considered satisfied when

$$\left\| \nabla \lambda^* \right\| < \varepsilon \tag{6.5}$$

where ε is a suitably small tolerance. We note that the evaluation of (6.2) and (6.4) require that the limit state surface $g(\mathbf{x}) = 0$ be differentiable, which may not be the case, e.g., at points 'a', 'b' and 'c' in Figure 6.2. A practical approach to avoiding this problem is to locally smoothen the limit state surface at those points where $g(\mathbf{x}) = 0$ is not differentiable. In engineering applications, this can usually be done with negligible loss in the accuracy of the limit state surface.

Due to the obvious nonlinear nature of this optimization problem, its solution must be found by iteration. However, before starting the iterative portion of the solution scheme, it is computationally advantageous to check that $g(\mathbf{x}_0) > 0$. Obviously, if the center of the envelope is not in the safe domain, then the capacity surface does not encompass the response envelope and there is no reason to proceed to the iterative portion of the algorithm. In fact, if $g(\mathbf{x}_0) \leq 0$, then the system is unsafe under the static loads acting on it. Let $\alpha^{(i)}$, $\beta^{(i)}$, $\mathbf{x}_\alpha^{(i)}$, $R_\beta^{(i)}$, $S_\beta^{(i)}$ and $\lambda^{(i)}$ denote the values of α, β, $\mathbf{x}_\alpha$, R_β, S_β and λ at iteration i, respectively. To start the algorithm, an initial direction vector $\alpha^{(0)}$ is specified. The ith iteration of the algorithm involves the following computational steps.

(1) Compute the point $\mathbf{x}_\alpha^{(i)}$ on the response envelope for $\alpha^{(i)}$ using (3.38) or (3.39), depending on the envelope considered.

(2) Compute $S_\beta^{(i)}$ and $\beta^{(i)}$ from

$$S_\beta^{(i)} = \left\| \mathbf{x}_\alpha^{(i)} - \mathbf{x}_0 \right\| \tag{6.6}$$

and

$$\beta^{(i)} = \frac{\left(\mathbf{x}_\alpha^{(i)} - \mathbf{x}_0\right)}{S_\beta^{(i)}}. \tag{6.7}$$

(3) Determine the distance $R_\beta^{(i)}$ from $\mathbf{x}_0$ to the capacity surface in direction $\beta^{(i)}$. Referring to Figure 6.2, this distance is the positive value of $R_\beta^{(i)}$ that satisfies $g(R_\beta^{(i)}\beta^{(i)} + \mathbf{x}_0) = 0$. A hypothetical plot of $g(R_\beta^{(i)}\beta^{(i)} + \mathbf{x}_0)$ as a function of $R_\beta^{(i)}$, which corresponds to the situation illustrated in Figure 6.2, is shown in Figure 6.3. Note that, because the safe domain is closed and we checked that $g(\mathbf{x}_0) > 0$ before entering the iterative portion of the

algorithm, a unique positive value of $R_\beta^{(i)}$ that satisfies $g(R_\beta^{(i)}\beta^{(i)}+\mathbf{x}_0)=0$ must exist. This root can be found most efficiently by means of the Newton-Raphson algorithm. We denote the value of $R_\beta^{(i)}$ at the jth iteration of this root-finding algorithm as $R_\beta^{(i)(j)}$ and note that the initial value $R_\beta^{(i)(0)}$ must be chosen so that the procedure converges to the desired positive root. It can be seen from Figure 6.3 that this corresponds to the case when

$$\left.\frac{dg\left(R_\beta^{(i)}\beta^{(i)}+\mathbf{x}_0\right)}{dR_\beta^{(i)}}\right|_{R_\beta^{(i)}=R_\beta^{(i)(0)}}<0. \tag{6.8}$$

(4) Compute the gradient vector $\nabla\lambda^{(i)}$ and the Hessian matrix $\nabla^2\lambda^{(i)}$ by finite differences.

(5) Check the convergence criterion

$$\left\|\nabla\lambda^{(i)}\right\|<\varepsilon. \tag{6.9}$$

If (6.9) is satisfied, the sign of $\det[\nabla^2\lambda^{(i)}]$ is checked to determine whether $\lambda^{(i)}$ represents a maximum or a minimum; otherwise, the direction vector is updated using the Newton-Raphson rule

$$\alpha^{(i+1)}=\alpha^{(i)}+\Delta\alpha^{(i)}, \tag{6.10}$$

where the step size is

$$\Delta\alpha^{(i)}=-\left[\nabla^2\lambda^{(i)}\right]^{-1}\nabla\lambda^{(i)}, \tag{6.11}$$

and the next iteration of the algorithm is started.

As for any nonlinear optimization routine, there is no guarantee that the above algorithm will converge. For convergence, one may have to reduce the step size in (6.10) by multiplying $\Delta\alpha^{(i)}$ by a factor that is less than unity. This was not necessary though for any of the numerical analyses performed in Chapter 7 using this algorithm. However, we caution that if the convergence criterion (6.9) is satisfied and $\det[\nabla^2\lambda^{(i)}]<0$, then $\lambda^{(i)}$ is a minimum but not necessarily λ^*, since the algorithm cannot distinguish between global and local minima. This is also a well-known shortcoming of all nonlinear optimization routines. One way to address this problem is to

restart the above algorithm with several different initial vectors $\alpha^{(0)}$ in an effort to sample all regions of the response space surrounding the envelope. Initial vectors directed along each response axis in both the positive and negative directions are reasonable choices for this purpose.

6.4 COMPARISON WITH A PARAMETERIZED CAPACITY SURFACE

The algorithm developed in the previous section assumed that the capacity surface was fixed in the response space. This condition usually reflects an analysis situation in which the adequacy of a structure is being assessed. In this section, we consider a related problem that arises primarily in design situations, in which the position of the capacity surface in the response space is variable, but uniquely determined by k design parameters $\mathbf{y} = [y_1, y_2, \ldots, y_k]^T$; i.e., the limit state function that defines the safe domain is of the form $g(\mathbf{x}, \mathbf{y}) = 0$. To ensure the safety of the system, the engineer must select the parameters such that no point on the response envelope under consideration exceeds the resulting capacity surface. Obviously, when there is more than one design parameter, an objective function is necessary to guide the choice. A common approach used in practice, however, is to prescribe all but one parameter, which is then determined such that the capacity surface completely encompasses the response envelope. If required, the prescribed parameters can then be varied and the free parameter re-evaluated to find the most suitable design. To illustrate this approach, we present in this section an algorithm for finding the required reinforcement ratio of a reinforced concrete column that has a prescribed size and steel and concrete strengths. The algorithm is used for the bridge design examples presented in Chapter 7. While the details of the procedure presented in this section are particular to our needs in Chapter 7, the algorithm can be easily modified for use with any response interaction problem involving any number of responses and a single design parameter.

Suppose for the example bridge in Figure 4.2, the column sizes and material strengths are fixed at the values listed in the figure. The column reinforcement is assumed to be uniformly distributed around the perimeter of the section with the centerline of the reinforcing steel located 75 mm from the column face. Under these conditions, the only variable controlling the capacity of the column in the design examples presented in Chapter 7 is the reinforcement ratio ρ_s. Thus, the limit state function can be expressed in the form $g(\mathbf{x}, \rho_s) = 0$. This assumes that the limit state function monotonically increases with ρ_s, which is correct for realistic values of ρ_s. It is

assumed that ρ_s can be determined for any point $\mathbf{x} = [P, M_1, M_2]^T$ on the capacity surface, where P is the axial load in the column and M_1 and M_2 are the bending moments about the z_1 and z_2 axes shown in Figure 4.2, respectively. Each value of ρ_s corresponds to a bending moment / axial force capacity surface in the response space. For this study, the capacity surface is based on the provisions of ACI 318-95 (ACI, 1995). Capacity surfaces for the circular columns considered in this study are rotationally symmetric about the axial force axis. Cross sections of the capacity surfaces corresponding to selected values of ρ_s are shown in Figure 6.4. For a given response envelope (rectangular, elliptical or supreme), the required reinforcement ratio, ρ_s^*, corresponds to a capacity surface that completely encompasses the response envelope and touches it at a point that we denote as $\mathbf{x}^*$.

For the rectangular envelope, owing to the convexity of the capacity surfaces plotted in Figure 6.4, $\mathbf{x}^*$ always coincides with one of the corners of the rectangle. However, $\mathbf{x}^*$ is not as obvious for the elliptical and supreme envelopes. When there are only two response quantities, e.g., axial force and a bending moment about one axis, $\mathbf{x}^*$ can be found by simply plotting the response envelope on a set of capacity curves corresponding to a range of ρ_s and selecting that ρ_s for which the capacity surface completely encompasses the response envelope. This approach can be extended to analyses involving three response quantities (the present case) by plotting cross sections of the response envelope and capacity surfaces at several values of one response, e.g., the axial load. The maximum required reinforcement ratio found from this ensemble of cross sections is approximately ρ_s^*. Naturally, the accuracy of this estimate is dependent upon the number of cross sections considered. While this approach is sound, it can be cumbersome. Furthermore, it is not practical for problems that involve more than three responses. In such cases, a numerical algorithm for determining $\mathbf{x}^*$ is required.

For the elliptical and supreme envelopes, the capacity surface defined by ρ_s^* must be tangent to the envelope at $\mathbf{x}^*$. Hence, the gradient vector,

$$\nabla \rho_s^* = \left. \frac{\partial \rho_s}{\partial \mathbf{x}} \right|_{\mathbf{x}=\mathbf{x}^*}, \tag{6.12}$$

which is normal to the capacity surface, must be parallel to the normal vector α^* that defines the bounding hyperplane tangent to the envelope at $\mathbf{x}^*$; i.e.,

$$\nabla\rho_s^* \propto \alpha^* \,. \tag{6.13}$$

A point on the envelope at which (6.13) is satisfied can be found by iteration. Let $\alpha^{(i)}$, $\mathbf{x}^{(i)}$ and $\nabla\rho_s^{(i)}$ denote the values of α, $\mathbf{x}$ and $\nabla\rho_s$ at the ith step and start the algorithm with an initial direction vector $\alpha^{(0)}$. The ith iteration of the algorithm proceeds as follows.

(1) Compute $\mathbf{x}^{(i)}$ on the response envelope corresponding to $\alpha^{(i)}$ using (3.38) or (3.39), depending on the type of envelope used.

(2) Compute $\nabla\rho_s^{(i)}$ of the capacity surface at $\mathbf{x}^{(i)}$ by finite differences. Note that the evaluation of $\nabla\rho_s^{(i)}$ requires that the capacity surface be differentiable at $\mathbf{x}^{(i)}$, which cannot be guaranteed; e.g., see Figure 6.4. As suggested in Section 6.3, a practical solution to this problem is to locally smoothen the capacity surface at those points where it is not differentiable.

(3) Update the direction vector using the recursive formula

$$\alpha^{(i+1)} = \nabla\rho_s^{(i)} \,. \tag{6.14}$$

Recall that when using (3.38) or (3.39), α need not be a unit vector. A slight computational advantage is gained from this property by not normalizing the vector $\alpha^{(i+1)}$ obtained from (6.14).

(4) Check the convergence criterion

$$\frac{\left\| \alpha^{(i+1)} - \alpha^{(i)} \right\|}{\left\| \alpha^{(i)} \right\|} < \varepsilon \tag{6.15}$$

where ε is a suitably small tolerance. If (6.15) is satisfied, the algorithm is terminated, otherwise the next iteration is started. As we discussed in the previous section, due to the nonlinear nature of the preceding algorithm, we cannot guarantee that it will converge to a solution that satisfies (6.15). Nevertheless, for all numerical cases investigated in Chapter 7 using this algorithm, rapid convergence was achieved.

Upon convergence of the algorithm, the corresponding values of $\mathbf{x}$ and ρ_s are recorded. These values, however, are not necessarily $\mathbf{x}^*$ and ρ_s^*, since the algorithm cannot distinguish between global and local maxima or minima. To address this problem, the algorithm can be re-started with several different initial directions $\alpha^{(0)}$. For the analyses presented in Chapter 7, $\alpha^{(0)}$ was taken to be a unit vector directed along one of the three response axes in either the positive or negative directions. Hence, six realizations of $\alpha^{(0)}$ were used. From the six trials, the maximum value of ρ_s was considered to be the required reinforcement ratio, ρ_s^*. For the present investigation, the accuracy of the reported results was confirmed by studying three-dimensional plots of the envelope and capacity surface in the response space. In all cases, at least one of the six trials converged to the true critical point $\mathbf{x}^*$ and corresponding ρ_s^*. This was visually verified by observing that the capacity surface defined by ρ_s^* encompassed the response envelope and was tangent to it at $\mathbf{x}^*$.

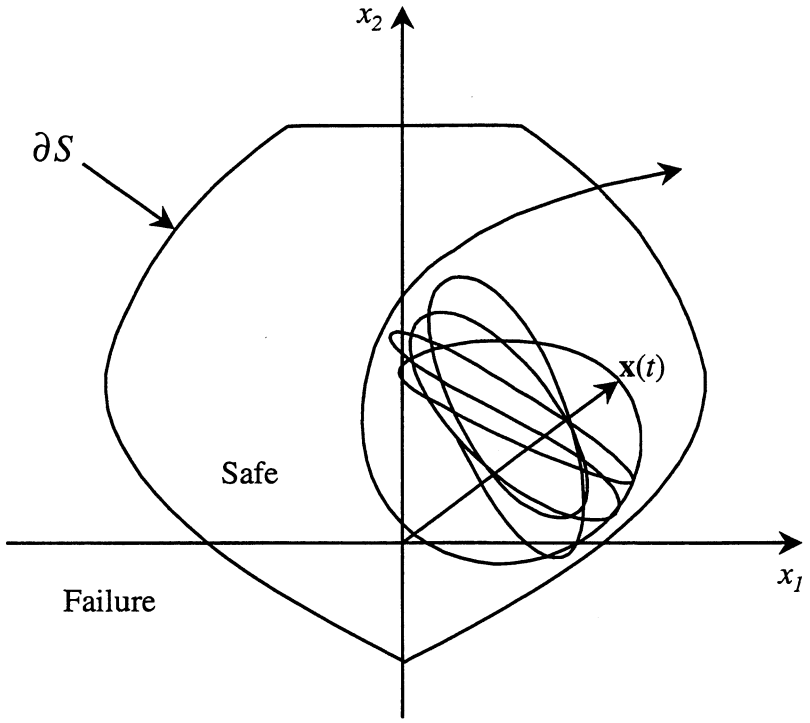

Figure 6.1. The vector out-crossing problem.

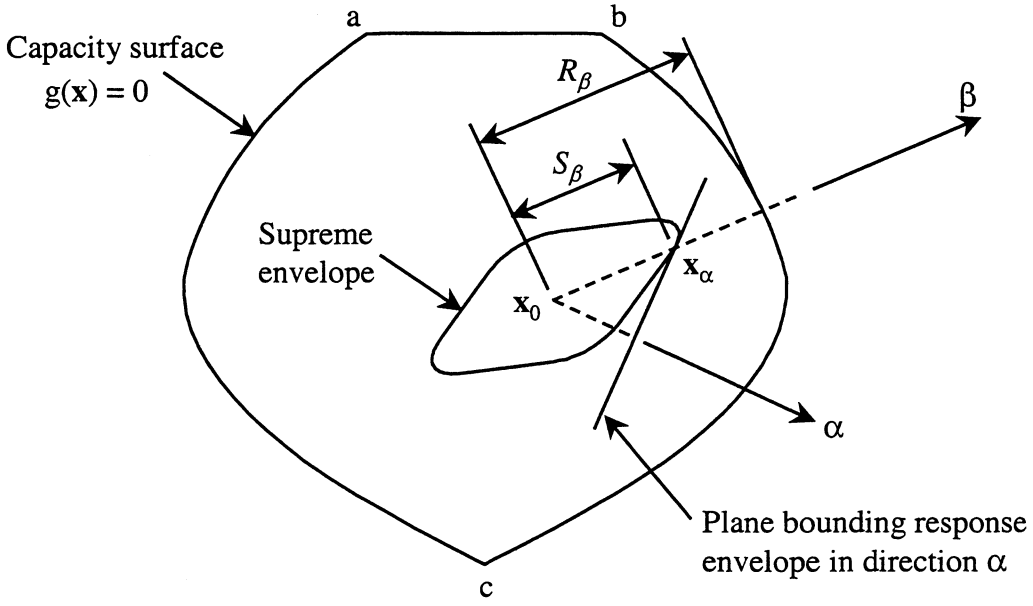

Figure 6.2. The geometry of the response envelope in relation to the capacity surface.

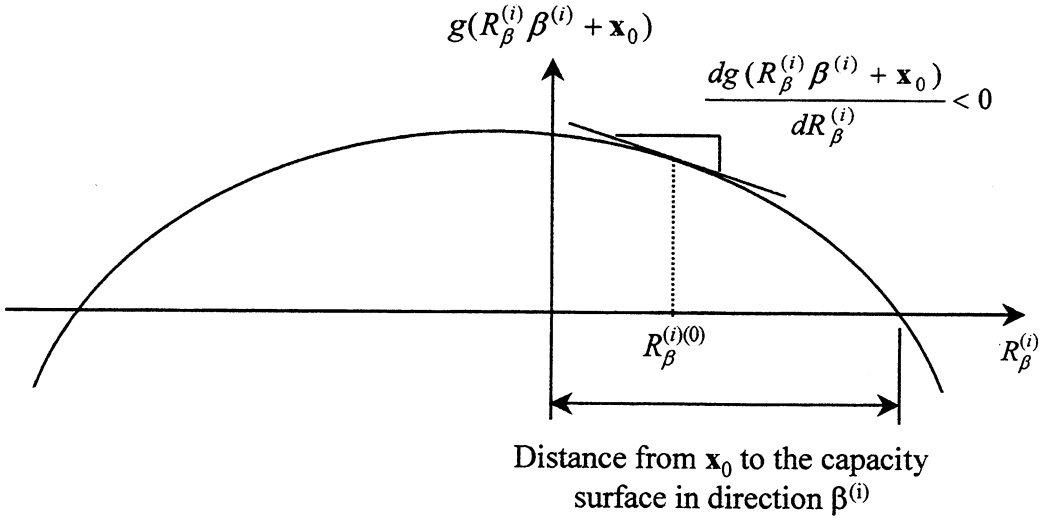

Figure 6.3. Distance to the capacity surface in direction $\beta^{(i)}$.

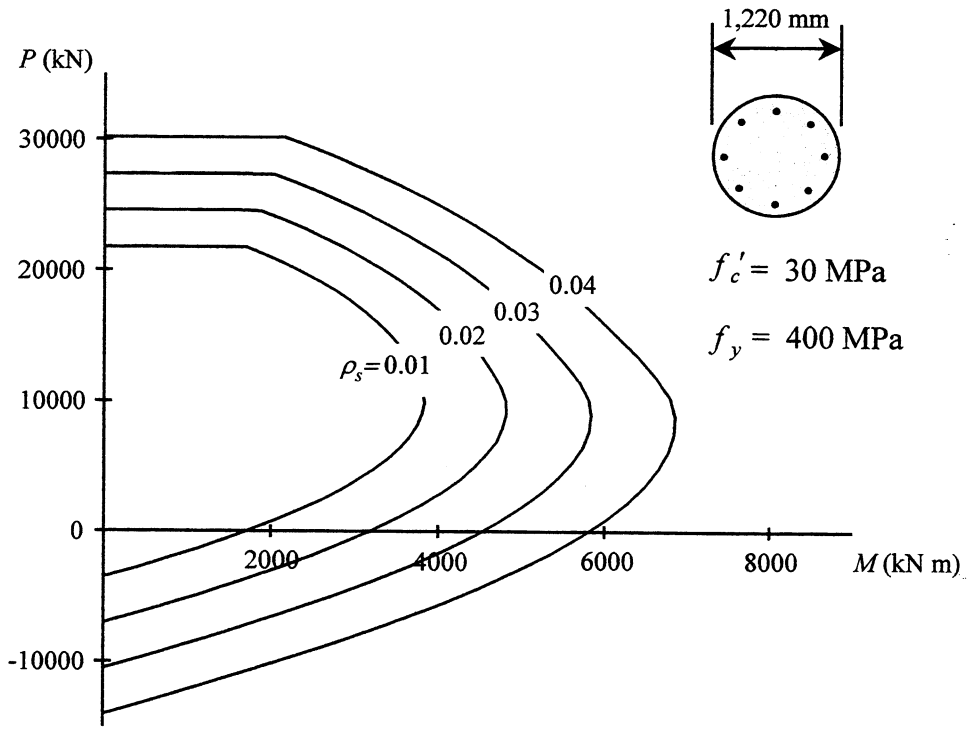

Figure 6.4. Cross sections of the rotationally symmetric moment-axial capacity surfaces for the example bridge columns.

7 Analysis and Design Applications

7.1 INTRODUCTION

The results presented in Chapter 5 demonstrate that for a prescribed value of θ, the proposed elliptical envelope accurately bounds the vector response process as it evolves in time. This result also carries over to the supreme envelope, as the latter is the union of the elliptical envelopes for all values of θ. In this chapter, we address the question of whether the use of the elliptical and/or supreme envelope, rather than the rectangular envelope commonly used in the current practice, has any significant effect on the analysis or design of structural elements subjected to seismic loads.

To answer this question, we consider selected columns of the reinforced concrete bridge shown in Figure 4.3, which must resist the axial forces and bending moments that act concurrently in them. The chapter is divided into three sections. In Sections 7.2 and 7.3, comparisons are made between the results obtained using the elliptical and rectangular envelopes for a specified orientation of the principal components of ground motion. This corresponds to the case in which the principal directions of the earthquake are known in advance, which could occur when there is a single, well-defined potential source for the earthquake. In Section 7.2, a situation commonly encountered in the analysis of existing structures is considered; specifically, the dimensions, material properties and reinforcement ratios of the columns are prescribed and their adequacy to resist the seismic loads imposed on them is evaluated. The algorithm developed in Section 6.3 is used for this purpose. In Section 7.3, only the dimensions and material properties of the columns are specified and the algorithm developed in Section 6.4 is used to determine the required reinforcement ratios. The calculations performed in Section 7.3 are typical of those routinely done in the design of new structures. Finally, in Section 7.4, the assumption that the principal directions of ground motion are known is relaxed and the required column reinforcement ratios that correspond to the elliptical and rectangular envelopes for all possible values of θ are

computed. These results are compared to those obtained using the supreme envelope in order to understand its significance on the seismic design of structures. The comparisons made in this chapter reveal the benefits that can be derived by using the elliptical or supreme envelope, rather than the conventional rectangular envelope used in the current practice.

7.2 SIGNIFICANCE OF THE ELLIPTICAL ENVELOPE ON THE EVALUATION OF EXISTING STRUCTURES

Consider columns B1, B2, D1 and D2 of the reinforced concrete bridge shown in Figure 4.3. During an earthquake, each of these columns must resist the axial force $P(t)$ and bending moments $M_1(t)$ and $M_2(t)$ about the z_1 and z_2 axes, respectively, that act at their bases. For the following analyses, the dimensions and material properties of these columns are as specified in Figure 4.3 and each column has a reinforcement ratio $\rho_s = 0.015$. Hence, the capacity surfaces for the columns are completely defined, as might be the case for an existing structure. In this section, we demonstrate the significance of using the elliptical envelope, instead of the conventional rectangular envelope, in the evaluation of the adequacy of these columns to resist the demands imposed on them by an earthquake.

The analyses are performed for the three load cases listed in Table 7.1. The displacement response spectrum of the major principal component of the ground motion, denoted D_1 in Table 7.1, corresponds to the mean pseudo-acceleration response spectrum of the ensemble of serviceability level earthquakes shown in Figure 4.8. This component is directed along the z_1 axis of the bridge shown in Figure 4.3, i.e., $\theta = 0$. As is common in practice, the response spectra associated with the intermediate and minor principal components of ground motion are assumed to be proportional to D_1, as indicated in Table 7.1. The scale factors applied to these components are based on the observations made by Penzien and Watabe (1975). Strictly speaking, it is not correct to refer to the principal components of ground motion for load case 1, as there is only one component of ground motion acting on the structure. However, no confusion should arise from denoting this single component of ground motion as the major principal component. The contributions of the static forces arising from dead loads are included in the analyses. The static components of the axial forces and bending moments acting at the bases of the columns considered are listed in Table 4.8.

Using the moment-axial capacity surfaces in Figure 6.4, which are in accordance with the provisions of ACI 318-95 (ACI, 1995), the adequacy of each column is evaluated using the algorithm described in Section 6.3. Recall that this algorithm computes a factor λ^* that is a measure of how much the response spectra must be scaled so that the response envelope touches, but does not exceed, the prescribed capacity surface. When $\lambda^* \geq 1$, the capacity surface completely encompasses the response envelope and the system is said to be "safe." Conversely, when $\lambda^* < 1$, there are points on the response envelope that exceed the capacity surface and the system is said to be "unsafe." The value of λ^* obtained using the elliptical envelope is compared to that obtained when the rectangular envelope is assumed. Due to the convexity of the column capacity surface, λ^* for the rectangular envelope can be determined by computing the required scale factor at each corner of the envelope and selecting the minimum value. However, such a comparison could be unfair. Often the behavior of a structure under lateral loads is simple enough that an experienced engineer can rule out improbable combinations of responses predicted by the rectangular envelope. In effect, the engineer would be making a subjective prediction about the correlation structure of the response vector. However, it would not be prudent of the engineer to assume a response combination that did not lie on a corner of the rectangular envelope. To approximately account for this effect, in addition to computing the minimum scale factor for the rectangular envelope, λ^*_{worst}, by considering all corners of the envelope, the scale factor, $\lambda^*_{\text{nearest}}$, of that corner that lies nearest to the critical point on the elliptical envelope (corresponding to λ^*) is also computed. Presumably, if the engineer's judgment is sound, this is the corner of the rectangular envelope that he or she would use in the assessment.

The scale factors obtained for each column, load case and type of envelope are summarized in Table 7.2. Also listed in this table are the critical combinations of axial force and bending moments $[P^*, M_1^*, M_2^*]^T$ for each case. The results summarized in Table 7.2 indicate that the use of the elliptical envelope, rather than the rectangular envelope, can have a significant effect on the seismic evaluation of an existing structure. As expected, the scale factors λ^*_{worst} and $\lambda^*_{\text{nearest}}$ obtained using the rectangular envelope are smaller than λ^* obtained using the elliptical envelope in all cases. Thus, by adopting the rectangular envelope, one obtains a conservative estimate of the adequacy of the bridge columns. However, the results in Table 7.2 suggest that the rectangular envelope can be overly conservative. For all columns and load cases listed in Table

7.2, $\lambda^* > 1$ for the elliptical envelope. This suggests that the columns are safe and do not need to be improved. In contrast, the results obtained using the rectangular envelope indicate that the columns are safe only for load case #1, in which the bridge is subjected to a single component of ground motion. For the more realistic load cases #2 and #3, the scale factors obtained using the rectangular envelope lie in the ranges $0.75 \leq \lambda^*_{\text{worst}} \leq 0.88$ and $0.77 \leq \lambda^*_{\text{nearest}} \leq 0.88$ for the "worst" and "nearest" corners, respectively. Based on these values of the scale factor, one would conclude that the columns are inadequate and should be improved. For an existing structure, such improvements can be expensive. Thus, this example demonstrates the economic benefit that may be derived from use of the elliptical envelope rather than the rectangular envelope in such analyses. Namely, unnecessary and potentially expensive renovations might be avoided by using the elliptical envelope.

The substantial difference between the scale factors recorded for the elliptical and rectangular envelopes in Table 7.2 is primarily due to the weak correlation that exists between the bending moments M_1 and M_2 (e.g., see Figure 5.2 for column B1). Consequently, as can be seen in Table 7.2, the critical point on the elliptical envelope corresponding to λ^* lies away from the corners of the rectangular envelope. Due to the convexity of the capacity surface, the corners of the rectangular envelope can therefore lie much closer to the capacity surface than the critical point on the elliptical envelope, leading to the observed differences between the scale factors. The weak correlation between M_1 and M_2 is also responsible for the small difference between λ^*_{worst} and $\lambda^*_{\text{nearest}}$ recorded for each load case, since the nearest corner of the rectangular envelope tends to be only marginally closer to the critical point on the elliptical envelope than the worst corner. In fact, for column D2, the worst and nearest corners of the rectangular envelope are the same. We note that if the critical point on the elliptical envelope were located near one of the corners of the rectangular envelope (e.g., see the envelope corresponding to $\theta = \pi/4$ radians in Figure 5.3), then the scale factors λ^* and $\lambda^*_{\text{nearest}}$ would be comparable. Moreover, λ^*_{worst} in this case could be significantly larger than λ^* and $\lambda^*_{\text{nearest}}$, depending on the location of the response envelope relative to the capacity surface.

The results presented in Table 7.2 indicate that the scale factors computed using load cases #2 and #3 differ only slightly, if at all. To understand this observation, consider Table 7.3, which lists the peak seismic axial forces and bending moments due to load cases #2 and #3 along

with the difference between these values. The differences, which are due to the vertical component of ground motion, indicate that the vertical ground accelerations significantly increase the seismic axial forces but not the bending moments acting in the bridge columns, as we might expect. However, for each column, the increase in the axial load due to vertical ground motions listed in Table 7.3 is small relative to the scale of the capacity surface plotted in Figure 6.4. Hence, large differences between the scale factors obtained for load cases #2 and #3 are not expected. In general, for a given envelope, the scale factor decreases or does not change upon the introduction of the vertical component of ground motion. One exception, however, is column B2. For this column, the scale factor computed using the nearest corner of the rectangular envelope increases, i.e., the adequacy of the column improves, when the vertical accelerations are included in the analyses. This counterintuitive result occurs because (1) the axial load associated with the nearest corner of the rectangular envelope for this column increases when vertical ground motions are included (see Table 7.2) and (2) the envelope lies in a region of the response space where an increase in the axial load increases the capacity of the column; i.e., the column capacity is controlled by the yield strength of the reinforcing steel rather than the compressive strength of the concrete.

7.3 SIGNIFICANCE OF THE ELLIPTICAL ENVELOPE ON THE SEISMIC DESIGN OF NEW STRUCTURES

To evaluate the potential significance of using the elliptical envelope rather than the conventional rectangular envelope in design calculations, bridge columns B1, B2, D1 and D2 shown in Figure 4.3 are designed for the axial force and bending moments that act at their bases. In particular, we assume that the column sizes and material properties are fixed at the values listed in Figure 4.3 and we compute the required reinforcement ratios of these columns using the algorithm formulated in Section 6.4 of the previous chapter. The design calculations are performed for the three load cases listed in Table 7.1, with the contributions of the static forces arising from dead loads included in the analyses.

Assuming the elliptical envelope and using the moment-axial capacity surfaces in Figure 6.4, the required reinforcement ratio, ρ_s^*, and corresponding point $\mathbf{x}^*$ on the envelope are computed. The reinforcement ratio is compared to the maximum reinforcement ratio required when the rectangular envelope is used to design the column. This approach, namely to apply the

ground motions along the assumed structure axes and to use the most critical combination of responses obtained for design, is common in the current practice. It essentially requires checking the eight corners of the rectangular envelope and determining the maximum reinforcement ratio. However, as we discussed in Section 7.2, such a comparison could be unfair as the behavior of a structure under lateral loads is often simple enough that an experienced engineer can rule out improbable combinations of responses predicted by the rectangular envelope. Thus, in addition to computing the maximum required reinforcement ratio, $\rho_{s,\text{worst}}$, by considering all corners of the rectangular envelope, we compute the required reinforcement ratio, $\rho_{s,\text{nearest}}$, of that corner that lies nearest to $\mathbf{x}^*$.

The required reinforcement ratios for each column and load case assuming the different envelopes and load conditions described above are summarized in Table 7.4. The amount of additional reinforcement required when the rectangular envelope is used is expressed as the percentage

$$e_{\text{worst}} = \frac{\rho_{s,\text{worst}} - \rho_s^*}{\rho_s^*} \times 100\ \% \tag{7.1}$$

or

$$e_{\text{nearest}} = \frac{\rho_{s,\text{nearest}} - \rho_s^*}{\rho_s^*} \times 100\ \% \tag{7.2}$$

for the worst and nearest corners of the rectangular envelopes, respectively. These percentages can be interpreted as the amount of over-design incurred when the rectangular envelope is used to compute the required reinforcement ratio.

The results presented in Table 7.4 are similar to those presented in Table 7.2 in many respects. As can be seen in Table 7.4, use of the elliptical envelope can lead to significant reductions in the required reinforcement ratios for all load cases considered. With one exception, columns B1, B2 and D1 require approximately 50% to 60% more reinforcement when designed using the "nearest" corner of the rectangular envelope rather than the elliptical envelope. The effect is even more pronounced in column D2 where use of the rectangular envelope results in approximately 80% to 90% more reinforcement than that found using the elliptical envelope. As discussed in Section 7.2, these results stem from the fact that there is weak correlation between

the bending moments M_1 and M_2. Consequently, the critical design point $\mathbf{x}^*$ is far from the corners of the rectangular envelope, leading to the observed differences between the required reinforcement ratios. We also note that, while we expect the corner of the rectangular envelope nearest $\mathbf{x}^*$ to yield a smaller value for the required reinforcement ratio than the worst corner, the difference between the values obtained using these different corners is small compared to the difference between the elliptical and rectangular envelope results. Again, this observation is similar to that made in Section 7.2 with respect to the scale factors computed using the worst and nearest corners of the rectangular envelope.

The results in Table 7.4 obtained upon introducing the third component of ground motion directed vertically along the z_3 axis (load case 3) differ only marginally from the results obtained for load case 2. This is because the vertical component of ground motion does not contribute substantially to the response of the bridge. This observation agrees with the recommendations contained in most building codes that stipulate that vertical accelerations need not be considered in the design of conventional structures. It is interesting to note, however, that the required column reinforcement ratio for column B2 decreases slightly when the vertical component of ground motion is included in the analyses. This result and its cause are similar to what was observed and discussed in Section 7.2 for this column and load case.

As expected, when the bridge is subjected to one component of ground motion (i.e., load case 1) the required reinforcement ratios computed using either of the envelopes are smaller than the corresponding values computed for load cases 2 or 3. This difference is approximately 40% in all cases, thus illustrating the importance of including all components of ground motion in the analyses. However, for all columns, the reinforcement ratio calculated using the rectangular envelope for load case 1 is comparable to that found using the elliptical envelope for load cases 2 and 3. This observation may suggest that the conventional approach for analyzing a structure for a single component of ground motion and proportioning its elements based on the results obtained using the rectangular envelope is acceptable. However, this is an incorrect conclusion. The apparent agreement between the rectangular envelope results obtained for load case 1 and the elliptical envelope results obtained for load cases 2 and 3 is incidental. It arises from a combination of effects particular to this example, including the relative intensity of the horizontal components of ground motion, the correlation structure of the response vector and the shape of the capacity surface.

7.4 EFFECT OF UNKNOWN θ ON DESIGN

The elliptical envelope should be used for design only when the orientation of the principal directions of ground motion is known in advance. This is not the case in most applications. When θ is unknown, it is prudent to use the supreme envelope derived in Chapter 3 for design. In this section, we again consider bridge columns B1, B2, D1 and D2 shown in Figure 4.3 and the load cases listed in Table 7.1. As noted earlier, load case 1 in Table 7.1 corresponds to a single component of ground motion acting on the structure; hence, for this load case, the counterclockwise angle θ defines the direction in the horizontal plane with respect to the z_1 axis along which the single component of ground motion acts. For each combination of column and load case, the reinforcement ratios predicted by the supreme, elliptical and rectangular envelopes are compared. The implications of the results on the design of the columns when θ is not known in advance are then examined.

In Figure 7.1 the required column reinforcement ratios predicted by the supreme envelope are plotted with those obtained using the elliptical and rectangular envelopes for $0 \le \theta < \pi$. Naturally, for each column and load case, the supreme envelope result coincides with the maximum of the elliptical envelope results. Also, note that the reinforcement ratios shown for $\theta = 0$ are the same as those presented in Table 7.3. Because the contribution to the total response from the vertical component of ground motion is small relative to the contributions from the horizontal components, the reinforcement ratios computed for load cases 2 and 3 differ only slightly. Therefore, the results of load case 3 are not plotted with the understanding that they are adequately represented by those shown for load case 2. Note that the results for $\pi \le \theta < 2\pi$ are identical to those for $0 \le \theta < \pi$; hence, the data presented in Figure 7.1 effectively covers the complete range of orientations that the principal directions of ground motion can assume.

As expected, the results based on the elliptical envelope lie below the rectangular envelope results in Figure 7.1. Furthermore, for each value of θ, the required reinforcement ratio computed using the corner of the rectangular envelope nearest $\mathbf{x}^*$ on the elliptical envelope is less than or equal to that computed using the worst corner of the rectangular envelope. We can see from the plots in Figure 7.1 that, while the required reinforcement ratios computed using the elliptical envelope and the worst corner of the rectangular envelope vary relatively smoothly with θ, the reinforcement ratio computed using the "nearest" corner of the rectangular envelope

exhibits some sharp and sudden changes, e.g., see column B2, load case 2. These abrupt changes are not unexpected; they arise from the fact that as θ is varied, the corner of the rectangular envelope nearest $\mathbf{x}^*$ on the elliptical envelope changes quadrants. Such changes are discontinuous in nature and thus may involve sudden changes in the corresponding reinforcement ratio.

Further examining the load case 1 results in Figure 7.1, we see that the reinforcement ratio predicted by the rectangular envelope is approximately constant for the entire range of θ, while the reinforcement ratio predicted by the elliptical envelope fluctuates noticeably. This interesting trend is due to the fact that as θ is varied, the peak values of P, M_1 and M_2 remain relatively constant but the correlation between these responses changes markedly. This is clearly seen in Figure 5.3, in which projections of the elliptical envelope for column B1 are plotted for several values of θ. As discussed in Chapter 5, the geometry of the bridge is primarily responsible for the insensitivity of the peak values of P, M_1 and M_2 to θ that is apparent in Figure 5.3. In particular, recall the results summarized in Table 5.4, which indicate that the peak values of P, M_1 and M_2 are comparable for ground motions oriented in any horizontal direction.

Considering load case 2, we again see that the rectangular envelope results are relatively constant for the entire range of θ; however, the fluctuations in the elliptical envelope results are less than that observed for load case 1. This observation arises from the fact that upon introducing a second component of ground motion, the correlation structure between any two responses naturally weakens (unless the responses are perfectly correlated). While this does not affect the rectangular envelope results, it does affect the elliptical envelope results, particularly at those values of θ at which the envelope obtained for load case 1 displays strong correlation between M_1 and M_2. A plot of the column B1 envelopes for various values of θ for load case 2 can be found in Figure 5.2. A comparison of the projections onto the (M_1, M_2) plane found in Figures 5.2 and 5.3 clearly shows that by introducing a second component of ground motion, the correlation between M_1 and M_2 weakens.

The results presented in Figure 7.1 have the following significant implications on the choice of the envelope to be used for design.

(1) Use of the rectangular envelope, which is common in the current practice, is not necessarily a conservative approach. We can see from the load case 1 plots in Figure 7.1 that when the rectangular envelope is adopted, an unconservative estimate of the required re-

inforcement ratio relative to the supreme envelope may be obtained if θ is selected arbitrarily. We note that this approach, in which a structure is designed for a single component of ground motion applied in an arbitrary direction, is common in the current practice, typically with $\theta = 0$ and/or $\theta = \pi/2$ radians. Even when the worst corner of the rectangular envelope is used, the reinforcement ratio based on the rectangular envelope can be smaller than that based on the supreme envelope by as much as 15% for column B2.

(2) Adopting the rectangular envelope for realistic load cases involving more than one component of ground motion (load cases 2 and 3) can yield overly conservative estimates for the required reinforcement ratio. From Figure 7.1, we can see that by using a rectangular envelope for these load cases, columns B1, B2, D1 and D2 will be over-reinforced by at least 35%, 40%, 40% and 55%, respectively.

(3) Any elliptical envelope is unconservative relative to the corresponding supreme envelope. Naturally, when θ is unknown in advance, assuming an arbitrary value for θ and using the corresponding elliptical envelope for design will always result in a smaller estimate for the required reinforcement ratio than that predicted by the supreme envelope. For load case 1, the estimates made using the supreme and elliptical envelopes can differ by as much as 50%. For load case 2, the difference between the required reinforcement ratios based on the supreme and elliptical envelopes is approximately 15% to 20% for all columns considered.

In light of these observations, we conclude that the rectangular envelope, which can be unconservative in some situations but overly conservative in others, should not be used for design. If θ can be confidently predicted, as might be the case when there is a single, well-defined source of seismic activity near the structure, then the elliptical envelope may be used to produce a safe and economical design. However, when θ is unknown in advance, as is often the case, it is prudent to use the supreme envelope.

Table 7.1. Load cases considered in design example.

Load Case	Response spectra in the principal directions		
	major	intermediate	minor
1	D_1	0.0	0.0
2	D_1	0.85 D_1	0.0
3	D_1	0.85 D_1	0.67 D_1

Table 7.2. Scale factors and critical response combinations obtained using the elliptical and rectangular envelopes corresponding to $\theta = 0$.

Column[1]	Load case	Elliptical envelope				Rectangular envelope							
						Worst corner				Nearest corner			
		λ^*	P^* (kN)	M_1^* (kN m)	M_2^* (kN m)	λ^*_{worst}	P^* (kN)	M_1^* (kN m)	M_2^* (kN m)	$\lambda^*_{nearest}$	P^* (kN)	M_1^* (kN m)	M_2^* (kN m)
B1	1	1.29	1402	806	-2126	0.99	1062	-1745	2295	1.02	1062	1650	-2244
	2	1.05	1138	1715	-2137	0.76	830	-2530	2747	0.78	830	2436	-2696
	3	1.04	1098	1733	-2121	0.75	732	-2532	2750	0.77	732	2439	-2699
B2	1	1.39	2507	-735	2258	1.12	2501	-1830	2323	1.12	2508	-1830	2323
	2	1.15	2508	-1653	2356	0.85	2482	-2673	2781	0.85	2527	-2674	2781
	3	1.15	2513	-1690	2335	0.83	2203	-2678	2784	0.87	2807	-2678	2784
D1	1	1.33	1681	678	-2183	1.02	1330	-1767	-2280	1.04	1330	1657	-2280
	2	1.08	1396	1592	-2201	0.77	1077	-2564	-2736	0.79	1077	2454	-2736
	3	1.08	1366	1606	-2184	0.77	932	-2564	-2736	0.78	932	2454	-2736
D2	1	1.49	3084	-717	2198	1.17	3084	-1898	2272	1.17	3084	-1898	2272
	2	1.21	3084	-2302	1674	0.88	3084	-2784	2729	0.88	3084	-2784	2729
	3	1.21	3064	-2300	1673	0.86	2590	-2784	2729	0.86	2590	-2784	2729

[1] Refer to Figure 4.3

Table 7.3. Peak seismic column responses due to load cases #2 and #3.

Column[1]	Load case	P (kN)	M_1 (kN m)	M_2 (kN m)
B1	2	717	2483	2721
	3	816	2486	2724
	difference	99	3	3
B2	2	22	2663	2745
	3	302	2666	2747
	difference	280	3	2
D1	2	783	2509	2730
	3	928	2509	2730
	difference	145	0	0
D2	2	0	2784	2729
	3	0	2784	2729
	difference	494	0	0

[1] Refer to Figure 4.3

Table 7.4. Comparison of required column reinforcement ratios based on the elliptical and rectangular envelopes corresponding to $\theta = 0$.

Column[2]	Load case	Elliptical envelope ρ_s^*	Rectangular envelope			
			Worst corner		Nearest corner	
			$\rho_{s,\text{worst}}^*$	% overdesign e_{worst}	$\rho_{s,\text{nearest}}^*$	% overdesign e_{nearest}
B1	1	0.01012	0.01523	50.4	0.01293	27.7
	2	0.01401	0.02206	57.5	0.02130	52.1
	3	0.01410	0.02231	58.2	0.02156	52.9
B2	1	0.00806	0.01242	54.1	0.01241	53.9
	2	0.01181	0.01946	64.8	0.01937	64.1
	3	0.01183	0.02007	69.7	0.01885	59.4
D1	1	0.00944	0.01459	54.6	0.01411	49.5
	2	0.01322	0.02162	63.5	0.02106	59.3
	3	0.01325	0.02195	65.6	0.02139	61.4
D2	1	0.00625	0.01116	78.6	0.01116	78.6
	2	0.01028	0.01859	80.8	0.01859	80.8
	3	0.01031	0.01957	89.8	0.01957	89.8

[2] Refer to Figure 4.3

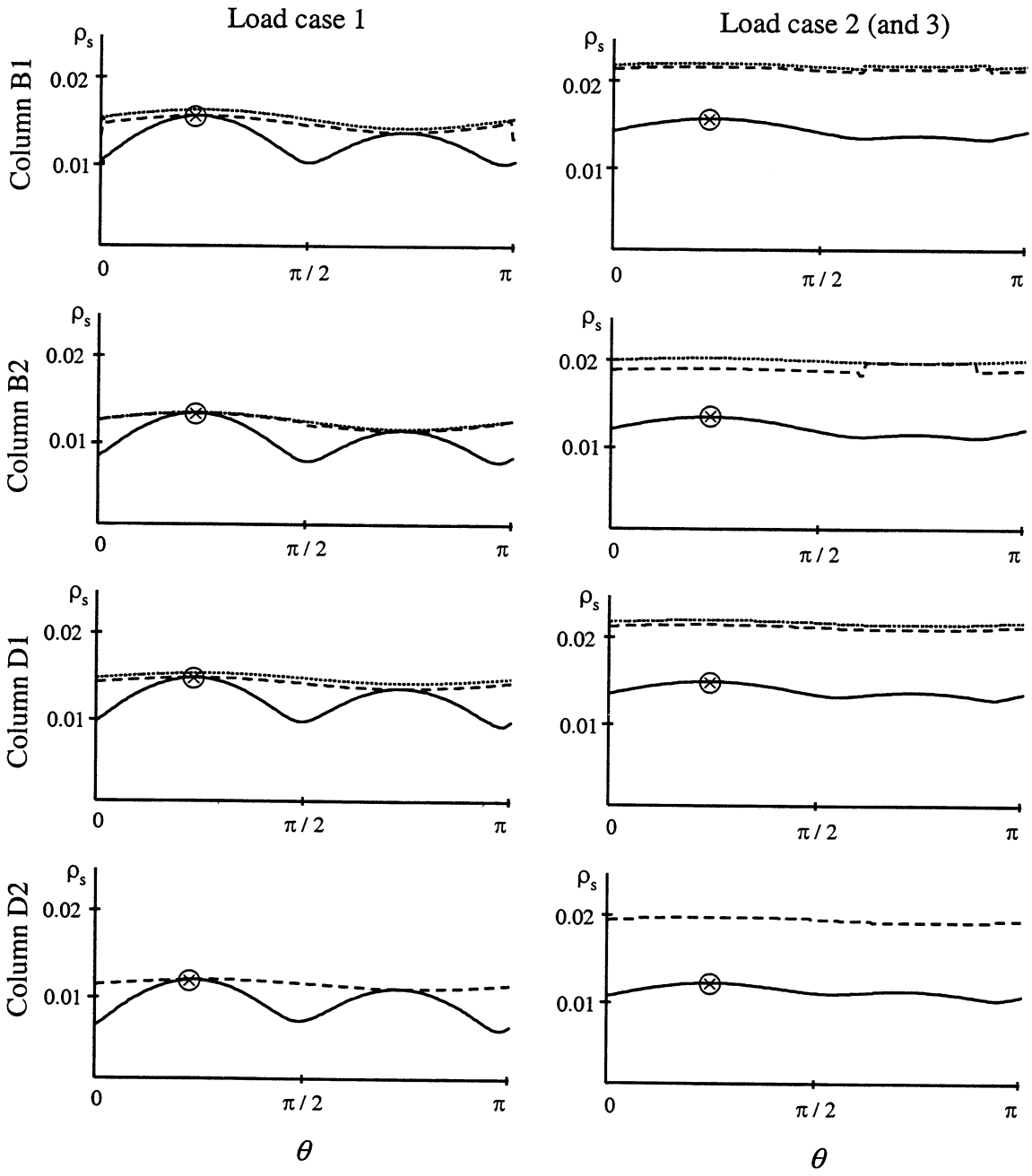

Figure 7.1. Comparison of required reinforcement ratios predicted by the supreme, elliptical and rectangular envelopes.

8 Response Envelopes for Nonlinear Structures

8.1 INTRODUCTION

As evidenced by the results presented in Chapter 7, the response-spectrum-based procedure developed in Chapter 3 is a valuable tool for the seismic design of structures subjected to serviceability level earthquakes, during which they are expected to remain linear. However, it is usually uneconomical to proportion structures to remain linear during large magnitude earthquakes. For such events, the effects of nonlinear behavior must be considered in the evaluation of structural response. The objective of this chapter is to examine how the introduction of nonlinear elements into a structure affect the size, shape and variability of the envelopes that bound selected response vectors. We will see that additional and practical insight into the nonlinear behavior of structures can be gained by studying these response envelopes.

To the authors' knowledge, all research conducted to date on the nonlinear seismic behavior of structures has focused on scalar quantities. Thus, the approach taken in this chapter, namely to examine the envelopes bounding vectors of nonlinear responses, is unprecedented. Furthermore, most of the research conducted to date has considered single-degree-of-freedom (SDOF) systems. Only recently have realistic multiple-degree-of-freedom (MDOF) structures, such as the building considered here, been studied (e.g., Krawinkler and Gupta, 1998; Biddah and Heidebrecht, 1998; Shome and Cornell, 1999). As the speed of computers increases and structural analysis programs improve, future research in this field will undoubtedly concentrate on MDOF systems. In addition, nonlinear time-history analyses will probably be used more routinely by practicing engineers for design. Consequently, a secondary objective of this chapter is to demonstrate how the information provided by response envelopes can be used to better understand the nonlinear seismic response of MDOF structures. The results presented below suggest

potentially valuable lines of research that can be explored in the future and possible applications of the response envelope in the design of nonlinear structures.

The steel building described in Chapter 4 is considered in the nonlinear analyses presented below. The amount of nonlinear behavior experienced by the building is controlled by the parameter η introduced in Chapter 4, which defines the strength of the elastic-perfectly-plastic moment connections at the ends of the beams and at the column bases. Recall that the plastic moment capacity of a connection is

$$M_p = \eta F_y Z, \tag{8.1}$$

where F_y is the yield stress of the steel and Z is the plastic section modulus of the beam or column that the connection supports. Hence, as η is decreased, the amount of nonlinear behavior experienced by the building increases. For all but the last two sets of analyses, every connection element in the model is assigned the same value of η. However, η is varied between the ensembles of time-history results in an effort to examine how the level of nonlinearity present in the model affects the response envelope. In the analyses that follow, η = 0.4, 0.7, 1.0 and ∞ are used, with $\eta = \infty$ representing the case in which the structure remains linear.

Except for the ensemble of serviceability level earthquakes, which do not cause nonlinear response in this building, all ground motions described in Chapter 4 are considered. For the ultimate level earthquakes and the ensemble of Seattle ground motions, the major principal component of ground motion is directed along the z_1 axis of the building shown in Figure 4.1, i.e., $\theta = 0$ radians. For the near-fault ground motions, the fault-normal component is directed along the z_1 axis. The response of nonlinear structures can be sensitive to the time-dependent variations in the intensity, phasing and frequency content of the input ground motions. Consequently, we will see that the size, shape and variability of the nonlinear response envelopes described below are, in some cases, strongly dependent upon the ground motions used.

Three response vectors are considered. First, the roof displacements, which were considered in Chapter 5 for the linear system, are examined. The observations made with respect to this response vector provide insight into the global nonlinear deformation of the building. Second, we study the envelope that bounds the axial force and bending moments acting in one of the ground floor columns. This envelope is considered in an effort to assess the effectiveness of the conventional design approach for structures of this type, which is to limit the forces acting in

critical structural elements by forcing nonlinear behavior to occur at only selected locations. Finally, we consider the envelope that bounds the horizontal roof displacement and the plastic hinge rotation at the base of a column. We will see that a simple geometric interpretation of this envelope provides useful information about the performance of the building that might otherwise be difficult to infer from time-history results alone.

8.2 ENVELOPES BOUNDING ROOF DISPLACEMENTS

The effects of nonlinear behavior on the size and shape of the envelope bounding the horizontal roof displacements at corner G7 of the steel building shown in Figure 4.1 are considered first. We denote the roof displacements as Δ_1 and Δ_2 in the z_1 and z_2 directions, respectively, as we did in Chapter 5. Displacements are often used to characterize the performance of structures subjected to intense ground motions, thus the envelope that bounds such response quantities is of practical interest.

The results obtained using the ensemble of artificial ground motions representative of the ultimate level earthquake are plotted in Figure 8.1. Shown in this figure are the mean and mean-plus-one-standard-deviation simulated envelopes for the three levels of nonlinearity listed above and the corresponding elliptical envelopes for the linear structure ($\eta = \infty$). The scale for all plots is the same as that shown for the elliptical envelopes.

It is interesting to note in Figure 8.1 that, for all values of η, the mean nonlinear envelope is significantly smaller than the elliptical envelope obtained under the assumption that the structure remains linear. This observation does not agree with the "equal displacements" rule that is often assumed for structures like the one considered here. However, similar results can be inferred from data compiled for nonlinear SDOF systems studied by Miranda (1993) and Nassar and Krawinkler (1991), although neither study discusses these results. This behavior is thought to be the result of the following trade-off between increased effective period and increased effective damping ratio of the structure as it yields. Consider an SDOF system that has initial period T and damping ratio ζ. If the yield strength of the system is set at a sufficiently high value, then the system does not yield and its displacement is given by the ordinate of the displacement response spectrum corresponding to T and ζ, which is denoted by $D(T,\zeta)$ in Figure 8.2. For the yielding structure, we consider an equivalent linear system to represent its response. This com-

mon technique was originally proposed by Caughey (1963) as a means of solving nonlinear problems in structural dynamics. The effective period and damping ratio of this equivalent system, denoted T_{eff} and ζ_{eff} respectively, can be found by the method of statistical linearization (Roberts and Spanos, 1990). They are greater than the initial period and damping ratio of the linear system. The effective period lengthens by an amount controlled by the post-yield stiffness of the system and the damping ratio increases due to the hysteretic dissipation of energy. Depending on the values of T_{eff} and ζ_{eff} relative to T and ζ, the displacement of the nonlinear system, denoted by $D(T_{eff}, \zeta_{eff})$ can be less than that of the linear system as indicated in Figure 8.2. Naturally, this effect is controlled by the details of the structure and the ground motion. We expect the behavior described above to be most pronounced when (1) ζ is small, so that the effect of the hysteretic damping is significant, (2) the post-yield stiffness of the system is of similar magnitude to the initial stiffness, so that T_{eff} is nearly equal to T and (3) the period of the linear system is greater than the predominant period of the earthquake, so that, for a given damping ratio, an increase in the period from T to T_{eff} does not result in a large increase in the displacement. Considering the response spectrum of the ground motions plotted in Figure 4.8, the modal properties of the building tabulated in Table 4.4 and the fact that its post-yielding stiffness is controlled by large number of plastic hinges, it is arguable that all of the above conditions are satisfied and the reduced nonlinear displacements observed in Figure 8.1 are not unrealistic.

The plots in Figure 8.1 indicate that for $\eta = 1.0$ the variability in the envelope that bounds the roof displacements in the nonlinear structure is comparable to that predicted by the response-spectrum-based envelope for the linear structure. As η is decreased however, the variability in the envelopes for the nonlinear structure increases. Note that we are only comparing the relative degree of variability exhibited by the envelopes for the different levels of nonlinearity. As we have stressed before, no attempt has been made to accurately represent the true variability of seismic motions in the ensemble of artificial motions used in Figure 8.1. Consequently, the absolute variability observed in these plots may not be representative of the variability in actual ground motions. The artificial ground motions generated for this study probably have a reduced level of variability compared to true seismic motions generated by similar earthquakes at a site. Hence, we expect the variability exhibited by a more realistic ensemble of ground motions to be somewhat larger than that suggested in Figure 8.1.

It is well known that the response of nonlinear structures can be sensitive to the time-dependent variations in the intensity, frequency content and phasing of the input ground motions. Some of these characteristics, e.g., temporal variability in the frequency content, were not included in the artificial ground motions. Consequently, the time-history analyses conducted above may not yield a realistic representation of the nonlinear response of a structure subjected to a large magnitude event. For this reason, the analyses were repeated using the ensemble of ground motions compiled for large magnitude events near Seattle, Washington. The mean and mean-plus-one-standard-deviation envelopes obtained from this second set of analyses are plotted in Figure 8.3.

The trends that were observed in Figure 8.1 are also apparent in Figure 8.3. For all values of η considered, the mean nonlinear envelope bounding the displacements is significantly smaller than the elliptical envelope predicted for the linear case. The variability of the envelopes obtained for the nonlinear structures, relative to that predicted by the response-spectrum-based envelopes, is also comparable to that observed in Figure 8.1; although, the increase in the variability clearly seen in Figure 8.1 when η is decreased is not as obvious in Figure 8.3. We note that the coefficient of variation of the envelopes plotted in Figure 8.3 is greater than what is seen in Figure 8.1 for the envelopes obtained using the artificial records. This is expected, based on the discussion of these ground motions in Chapter 4. Recall that we argued in Chapter 4 that the variability of the ground motions contained in the Seattle ensemble may be excessive for a given site.

Plotted in Figures 8.4 and 8.5 are the envelopes obtained when the nonlinear structure is subjected to the ensembles of synthetic near-fault ground motions. These figures are organized in the same way as Figures 8.1 and 8.3. It is evident in Figures 8.4 and 8.5 that these near-fault motions cause severe nonlinear behavior in the structure. While the displacement Δ_2 experienced by the nonlinear structure is less than or equal to that predicted for the linear system by the elliptical envelope, Δ_1 is several times larger in some cases. In addition to this increased mean displacement in the z_1 direction, the simulated mean-plus-one-standard-deviation envelopes plotted in Figures 8.4 and 8.5 indicate an increased amount of variability, relative to that of the linear structure. The relative variability in Δ_2 also appears to have increased but not to the same extent as that observed for Δ_1. For both ensembles, the fault-normal component, which contains a velocity pulse and is more intense than the fault-parallel component (see Figures 4.11, 4.12 and

Appendix C), is directed along the z_1 axis of the structure, thus explaining the substantially larger values observed for the mean and standard deviation of Δ_1. It is interesting to note that these adverse effects of the fault-normal component are not apparent in envelopes for the linear structure in Figures 8.4 and 8.5. We caution however that the synthetic near-fault ensembles used in Figures 8.4 and 8.5 are small in number, consisting of only five records each. Consequently, the amplified response in the fault-parallel direction apparent in these figures may be exaggerated by virtue of the fact that the database is small and therefore sensitive to extreme values.

The analyses were also repeated using the ensemble of recorded near-fault ground motions. The simulated envelopes, which are plotted in Figure 8.6, are similar to those obtained using the synthetic records. However, the increase in the mean and standard deviation of displacement Δ_1 seen in Figure 8.6 is not as pronounced as in Figures 8.4 and 8.5.

8.3 ENVELOPES BOUNDING COLUMN RESPONSES

In this section we examine the effects of nonlinear behavior on the size and shape of the envelopes that bound the axial load and bending moment at the top and bottom of the ground floor column located at node B7 in Figure 4.1. We denote the axial load P and the bending moments about the z_2 axis at the top and bottom of the column M_{top} and M_{bot}, respectively. Note that the building is designed such that the moment frame columns are subjected to uni-axial bending only. This is common in the current practice because steel sections that are capable of resisting bi-axial bending moments tend to be uneconomical in low-rise construction.

For seismic loading, the currently accepted design philosophy is to restrict any nonlinear action, such as yielding, to predefined locations distributed evenly throughout the structure. During an intense earthquake, these locations of yielding act as fuses and limit the amount of shear force and bending moment that can be transmitted to members in the structure that are intended to remain undamaged. The design of conventional buildings usually forces plastic hinges to form in the beams and prevents inelastic action in the columns, except at their bases. Given the location and moment capacity of the plastic hinges, reasonable estimates of the maximum forces that can be experienced by the structural elements of the building can be made and used to size the elements properly. Thus, in nonlinear seismic design and analysis, attention is usually focused on deformation quantities, rather than forces or bending moments, since the designer has

less control over these response quantities. Nevertheless, it is interesting to examine the envelopes that bound responses such as axial loads and bending moments in columns for nonlinear and linear structures to better understand the benefits of the current design philosophy and its potential shortcomings.

The simulated mean and mean-plus-one-standard-deviation envelopes that bound the axial load and bending moment at the top and bottom of column B7 for the different ensembles of ground motions are plotted in Figures 8.7 through 8.11 inclusive. Each figure presents the results obtained for the four values of η listed in the introduction to this chapter. The scale for all plots is the same as that shown for the linear case ($\eta = \infty$).

An examination of Figures 8.7 through 8.11 reveals that, in general, the column responses in the nonlinear structure are similar regardless of the ensemble of ground motions considered. This, of course, is the chief benefit of the design philosophy described above. By restricting the structure to yield at predefined locations, the designer can remove almost all of the uncertainty in the axial loads, bending moments and shear forces that the structural elements must resist. This effect can be seen in Figures 8.7 and 8.8 for the artificial ground motions and the Seattle ensemble respectively. Referring to these figures, we can see distinct bounds on the axial force and bending moment acting at the base of the column. The upper bound on the bending moment is obviously the plastic capacity of the column base assumed in the structural model. The bounds on the axial load in this column are given by

$$P_{\max} = P_0 + \frac{2}{L} \sum_{i=1}^{3} M_{pi} \tag{8.2}$$

and

$$P_{\min} = P_0 - \frac{2}{L} \sum_{i=1}^{3} M_{pi}, \tag{8.3}$$

where P_0 is the gravity load acting in the column, M_{pi} is the plastic hinge capacity of the beam framing into the column at level i (assuming identical plastic hinges at either end of the beam) and L is the length of the beam. Note that $P_{\max}$ and $P_{\min}$ are realized only when all beams framing into the column yield at both ends simultaneously. At the top of the ground floor column, the axial load is again bounded by the values given in (8.2) and (8.3), but there are no strict bounds

on M_{top}. Because the columns are assumed to remain elastic in the superstructure, they can (and do) attract additional bending moments during intervals of severe yielding in the beams. Consequently, not all of the uncertainty in the forces and bending moments that the structural elements must resist can be eliminated. This undesirable effect can be seen in the results plotted in Figures 8.9, 8.10 and 8.11 for the near-fault records and is undoubtedly related to the pronounced response of the structure to the fault-normal component of ground motion. Note that the moment frame in which the column is located is aligned with the structure axis along which the fault-normal component was applied. For the two ensembles of synthetic near-fault motions, the bending moment at the top of the column exceeds the yield capacity when $\eta = 0.7$ or 1.0. Thus, these time-history results, which assume that yielding does not occur in the columns above their bases, are invalid unless we assume that the columns are sufficiently reinforced, without changing their stiffnesses, to prevent them from yielding.

8.4 ENVELOPES BOUNDING PLASTIC HINGES AND ROOF DISPLACEMENTS

To this point, we have only considered response vectors that consist of "interacting" components that can combine in an adverse way that must be guarded against, usually by comparing the envelope of the response vector to a prescribed capacity surface. However, the responses included in an analysis do not have to be related by some design criterion. Any combination of responses can be considered. In this section we consider the response vector $\mathbf{x}(t) = [\Delta_1(t), \theta_p(t)]^T$, in which Δ_1 is the roof displacement in the z_1 direction at node G7 in Figure 4.1 and θ_p is the plastic hinge rotation at the base of the column located at node B7 in the same figure. For design purposes, these deformation demands do not have to be considered together since their acceptable limits are independent of each other, i.e., the peak values of Δ_1 and θ_p can be considered separately. However, as we will see shortly, the size and shape of the envelope bounding these response quantities reveal aspects of the building's nonlinear behavior that might otherwise be difficult to infer from scalar time-history results.

Plotted in Figure 8.12 are the simulated mean and mean-plus-or-minus-one-standard-deviation envelopes bounding $\mathbf{x}(t) = [\Delta_1(t), \theta_p(t)]^T$ obtained from nonlinear time-history analyses performed using the ensemble of artificial ultimate level ground motions and the three values

of $\eta < \infty$ listed in the introduction to this chapter. The qualitative nature of the results obtained using the other ensembles of ground motions is similar to that seen in Figure 8.12; thus, they are not presented. Also plotted in Figure 8.12 is a diagonal line that passes through the origin of the response space and has a slope of $1/H$, where H is the total height of the building. The significance of this diagonal line is discussed below.

Consider Figure 8.13, which shows three idealized sketches of the moment frame along gridline 7 in Figure 4.1. Superimposed on these outlines are open circles that indicate locations of yielding when the maximum hinge rotation $\theta_{p\max}$ is realized at the base of the column at node B7. The distribution of plastic hinges in the sway mechanism shown in Figure 8.13a is considered an ideal condition since the damage is distributed throughout the moment frame and all plastic hinges participate in the dissipation of the seismic energy imparted to the building. It can be seen from the geometry of Figure 8.13a that, for this ideal condition, $\theta_{p\max}$ is related to the peak roof displacement $\Delta_{1\max}$ by

$$\frac{\theta_{p\max}}{\Delta_{1\max}} = \frac{1}{H}, \tag{8.4}$$

which we recognize as the slope of the diagonal lines plotted in Figure 8.12. Thus, if the structure reaches the ideal state depicted in Figure 8.13a, then, for a given $\theta_{p\max}$, the corresponding peak roof displacement should lie on the diagonal line. Consider the mean envelopes plotted in Figure 8.12. We can see that this situation nearly occurs for $\eta = 0.4$, but for $\eta = 0.7$ and $\eta = 1.0$ the peak roof displacement that occurs concurrently with the maximum hinge rotation is greater than that predicted by the diagonal line. Furthermore, the difference between the ideal and observed roof displacements is greater for $\eta = 1.0$ than for $\eta = 0.7$. Consider what these observations imply. For a given level of seismic input, as η increases fewer plastic hinges form on average. Consequently, the ideal condition, in which all plastic hinges are simultaneously active, is less likely to be achieved. Thus, the increased difference between the ideal and observed roof displacements seen as η is increased should be expected; it is indicative of fewer plastic hinges forming in the structure. Moreover, as we will demonstrate below, the relative magnitudes of the ideal and observed displacements, i.e., whether the observed displacement is greater than or less

than the ideal displacement, is indicative of where in the moment frame the yielding elements are located.

First consider Figure 8.13b, in which a suboptimal distribution of plastic hinges coinciding with $\theta_{p\max}$ is depicted. This condition might result if the capacities of the plastic hinges in the lower levels of the moment frame are so large that they do not yield. It can be seen from this figure that the peak roof displacement in this case is greater than that predicted by $H\theta_{p\max}$, which corresponds to the diagonal lines in Figure 8.12. Based on this observation, we can infer from the envelopes in Figure 8.12 for $\eta = 0.7$ and $\eta = 1.0$ that the plastic hinges are concentrated in the upper levels of the moment frame.

A second suboptimal condition, in which the yielding elements are concentrated in the lower levels of the moment frame, is depicted in Figure 8.13c. From this figure, we conclude that the peak roof displacements exhibited by such structures are less than those predicted by the diagonal lines in Figure 8.12. None of the cases shown in Figure 8.12 correspond to this situation. To support the claims made above, the building was reanalyzed assuming that the hinge capacities, as defined by η, are varied over the height of the building as indicated in Figure 8.14. Configuration #1 in this figure, for which the hinge capacities decrease toward the top of the building, should cause the plastic hinges to be concentrated near the top of the structure, as shown in Figure 8.13b. Conversely, configuration #3 in Figure 8.14 should cause more yielding near the base of the structure, as depicted in Figure 8.13c. The envelopes obtained from these time-history analyses, along with the case of $\eta = 0.7$ for all hinges from Figure 8.12 (configuration #2), are plotted in Figure 8.15. It is clear from these results that these envelopes can be used in the way described above to determine where in the moment frame the yielding elements are located. A practical application of this information is discussed in the following section.

8.5 SIGNIFICANCE TO NONLINEAR SEISMIC DESIGN

The previous sections have demonstrated some ways in which the simulated envelopes that bound vectors of responses in a nonlinear structure can be used to quantify the behavior of the structure when it is subjected to intense ground motions. In this section, we discuss the significance of the observations made above and suggest lines of research that can be explored in the future, and possible applications of response envelopes in the design of nonlinear structures.

8.5.1 Displacement Demands in Nonlinear Structures

The roof displacement results presented in Section 8.2 suggest that conventional empirical approaches used to estimate the nonlinear displacements of a structure, such as the "equal displacements" rule, may not be adequate. While the reduced nonlinear displacements obtained for the far-field motions are reassuring, in the sense that they suggest that the equal displacements rule is conservative, the amplified nonlinear displacements plotted in Figures 8.4, 8.5 and 8.6 for the near-fault motions should cause us to consider with caution the applicability of such rules to the design of MDOF structures subjected to realistic ground motions. In light of the results presented in Figures 8.1 and 8.3 – 8.6, the factors that control the nonlinear displacement of MDOF structures should be studied more closely. In particular, the pronounced difference between the response of the building in the fault-normal and fault-parallel directions noted in Figures 8.4 – 8.6, suggests that attention should be focused on developing rules that properly account for both the frequency content and temporal characteristics of the ground motion. Such research may lead to rules and procedures that can better predict these displacements. It would also be beneficial to see if similar results hold for more localized displacements, such as interstory drift.

Often, the peak displacement of a structure in any direction is of interest in seismic design, e.g., when the displacement is required to evaluate or design architectural components such as partition walls or cladding. In such cases, the information provided by the envelope bounding the two horizontal displacements and, possibly, the vertical displacement is more useful than the peak values of the individual components of the displacement vector. Such envelopes are plotted in Figures 8.1 and 8.3 – 8.6. As mentioned above, the near-fault results plotted in Figures 8.4 – 8.6 indicate that the temporal characteristics of the ground motion are as important to the nonlinear response of a structure as the frequency content. Therefore, it is unlikely that analytical procedures or empirical rules that relate the nonlinear envelope to the response-spectrum-based envelope of the linear system can be developed. At present, it appears that simulation is the only reliable way of predicting the envelope that bounds a vector of responses in a nonlinear structure. As computing power increases, the use of simulation in structural engineering will become practical and it is likely that in the near future nonlinear time-history analyses will be used routinely by practicing engineers for design. Therefore, there is a need to develop procedures and guidelines for the use of simulation in structural analysis. Some research in this field (Shome and Cornell, 1999) has already been undertaken. We should stress that the introduction of simulation

into structural analysis envisioned here does not discount the need for the empirical rules described in the previous paragraph. Such rules are invaluable during the preliminary stages of design when a refined model of the structure is not available and time-history analyses are therefore unwarranted.

An underlying objective of the conventional approach to seismic design is to reduce the uncertainty in the structural response, usually by allowing damage to occur at selected locations within the structure. This approach is primarily used to limit the stresses in critical structural elements. We discuss the effectiveness of this approach for the column responses considered in Section 8.3 in the next section. Here we note that there is an economical advantage to be gained by reducing the yield strength of the plastic hinges and, hence, the stresses experienced by the lateral force resisting elements. Obviously, by reducing the stresses, it may be possible to use smaller sections. However, the results plotted in Figures 8.1 and 8.3 – 8.6 indicate that this advantage is offset by increased variability in the displacement demands imposed on the structure (recall that reducing the yield strength of the plastic hinges corresponds to reducing η). This trade-off must be addressed when selecting the strength of the nonlinear elements in the structure.

8.5.2 Effectiveness of the Conventional Design Philosophy for Column Design

For all seismic events considered in Figures 8.7 – 8.11, there are strict bounds on the axial force and bending moment at the base of the column that are completely determined by the yield capacities of the plastic hinges introduced into the structure by the designer. Furthermore, these bounds are independent of the ground motions applied. Clearly, this is a desirable result, since the engineer has complete control over the stresses that the column experiences at its base. Because there is no uncertainty in the column response, the designer can select the required column section with confidence. As we discussed earlier, this is the chief advantage of the conventional approach to seismic design, in which plastic hinges are used as fuses to limit the shear forces and bending moments that can be transmitted to members in the structure that are to remain elastic.

The primary shortcoming of this design methodology can be seen in the envelopes that bound the column responses at the top of the ground floor column in Figures 8.7 – 8.11. While there are strict bounds on the axial load evident in these envelopes, for reasons described in Section 8.3, similar bounds on the bending moment do not exist. Consequently, the fundamental ob-

jective of the conventional approach to seismic design, which is to limit the demands imposed on critical elements of the structure, cannot be guaranteed. The uncertainty that is observed in the peak bending moment acting at the top of the column is undesirable. If it is not properly accounted for, it can result in the formation of a plastic hinge in the column and, possibly, a "soft-story" sway mechanism in the structure. In a soft-story sway mechanism, yielding occurs primarily at the top and bottom of the columns at one level of the building. Such mechanisms are undesirable because the damage is concentrated in the soft story, which is not only inefficient for dissipating the seismic energy imparted to the building, but can also cause the structure to become unstable. Current building codes address this problem in an approximate manner by requiring that the sum of the moment capacities of the columns that frame into a joint be greater than the sum of the moment capacities of the beams that frame into the joint. However, it is well known that this design criterion does not guarantee that yielding will not occur in the columns. Consequently, research is needed to develop reliable procedures for predicting the peak responses that can be expected in the lateral force resisting elements of a nonlinear structure.

8.5.3 Identification of Sway Mechanisms

As discussed in Section 8.4, under severe seismic loading, it is beneficial to have as many plastic hinges as possible form in a structure. The ideal sway mechanism for the moment frame considered in this study is sketched in Figure 8.13a. Suboptimal conditions are shown in Figures 8.13b and 8.13c. When proportioning the elements of a moment frame, a designer attempts to avoid sway mechanisms like those shown in Figures 8.13b and 8.13c in favor of a sway mechanism that matches that shown in Figure 8.13a as closely as possible.

The only reliable way of predicting the sway mechanism that will form as a result of intense ground shaking is by performing nonlinear time-history analyses using an appropriate ensemble of ground motions. In the current practice however, this is rarely done because computers are not yet fast enough to perform the required dynamic analyses in a reasonable amount of time. Approximate, simplified procedures that can be unreliable are used instead to select the member sizes and connection strengths of moment frames. However, as a result of the current improvements witnessed in the speed of desktop computers and the increased availability of nonlinear structural analysis software, it is anticipated that nonlinear time-history analyses will be used more routinely in the near future to identify sway mechanisms. This time-history approach is not

problem-free though. It requires that the yield events at the plastic hinge locations be recorded in time and somehow studied as a group (usually by plotting the yield events as they occur in time on an elevation of the moment frame) to confirm that a desirable sway mechanism is attained. Moreover, since an ensemble of ground motions should be considered, the analyst is also faced with the problem of incorporating the results of several time-history analyses into the evaluation procedure. The amount of data that must be recorded and stored can become unmanageable unless an efficient procedure for interpreting the time-history results is available.

The response envelope described in Section 8.4 is well suited to this problem. Recall that the responses bound by this envelope are the plastic hinge rotation at a column base and the roof displacement. As demonstrated in Section 8.4, the orientation of this envelope in the response space, with respect to a diagonal line that is defined by the height of the building, is indicative of the distribution of the plastic hinges that form in the moment frame and hence the sway mechanism. The chief advantage of using the response envelope to identify the sway mechanism is that it avoids the need to plot the yield events as they occur in time. Furthermore, the results from a number of time-history analyses can be rationally incorporated into the evaluation procedure by computing statistical envelopes such as those corresponding to the mean and mean-plus-or-minus-one-standard-deviation of the ensemble. Thus, the response envelope described in Section 8.4 has a practical application in that it provides concise information that can be used to identify the sway mechanism that is expected to form in a moment frame.

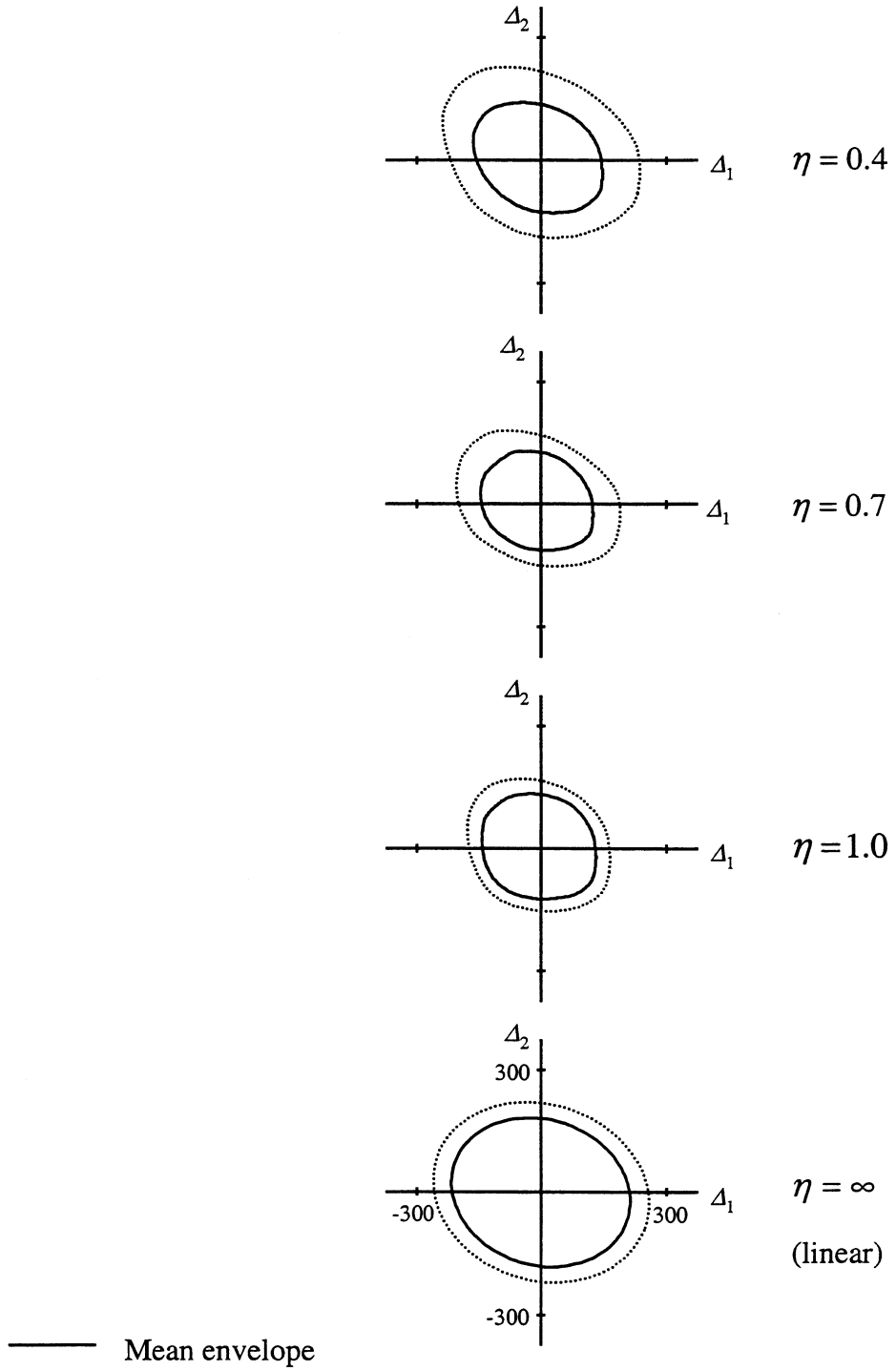

Figure 8.1. Roof displacement envelope of the nonlinear structure due to the ultimate level event.

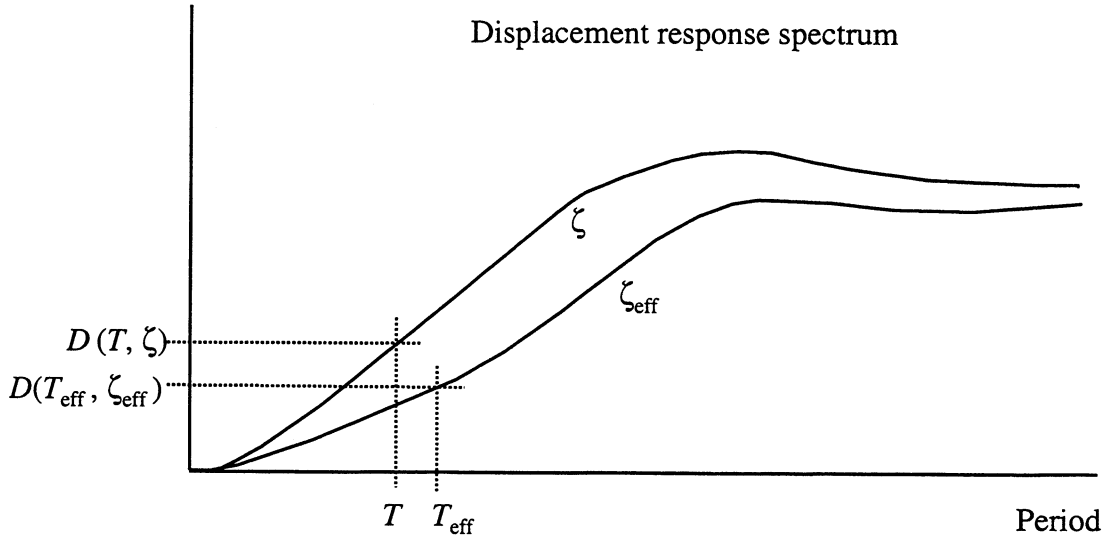

Figure 8.2. Reduction in displacement due to nonlinear behavior.

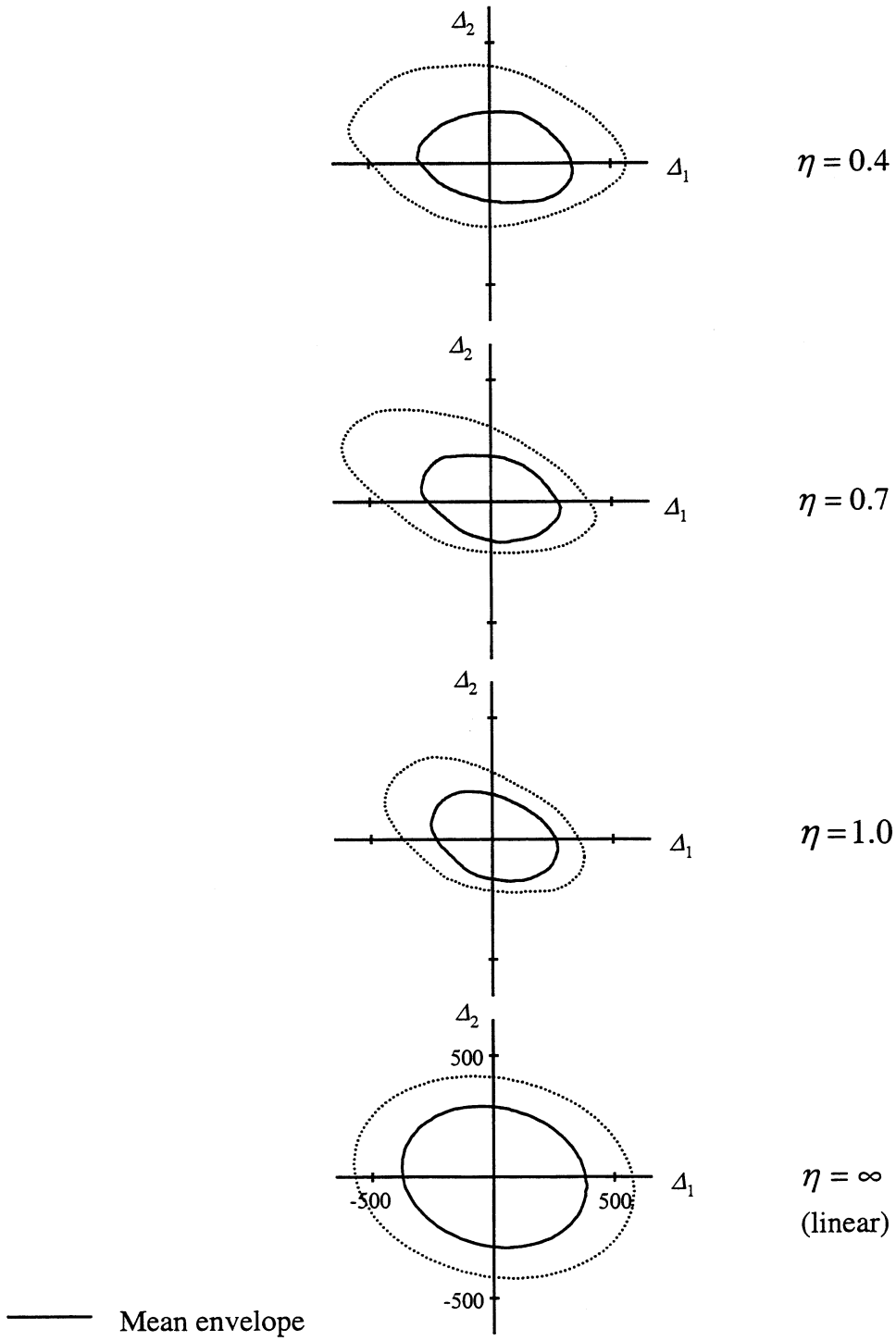

Figure 8.3. Roof displacement envelope of the nonlinear structure due to the ensemble of Seattle ground motions.

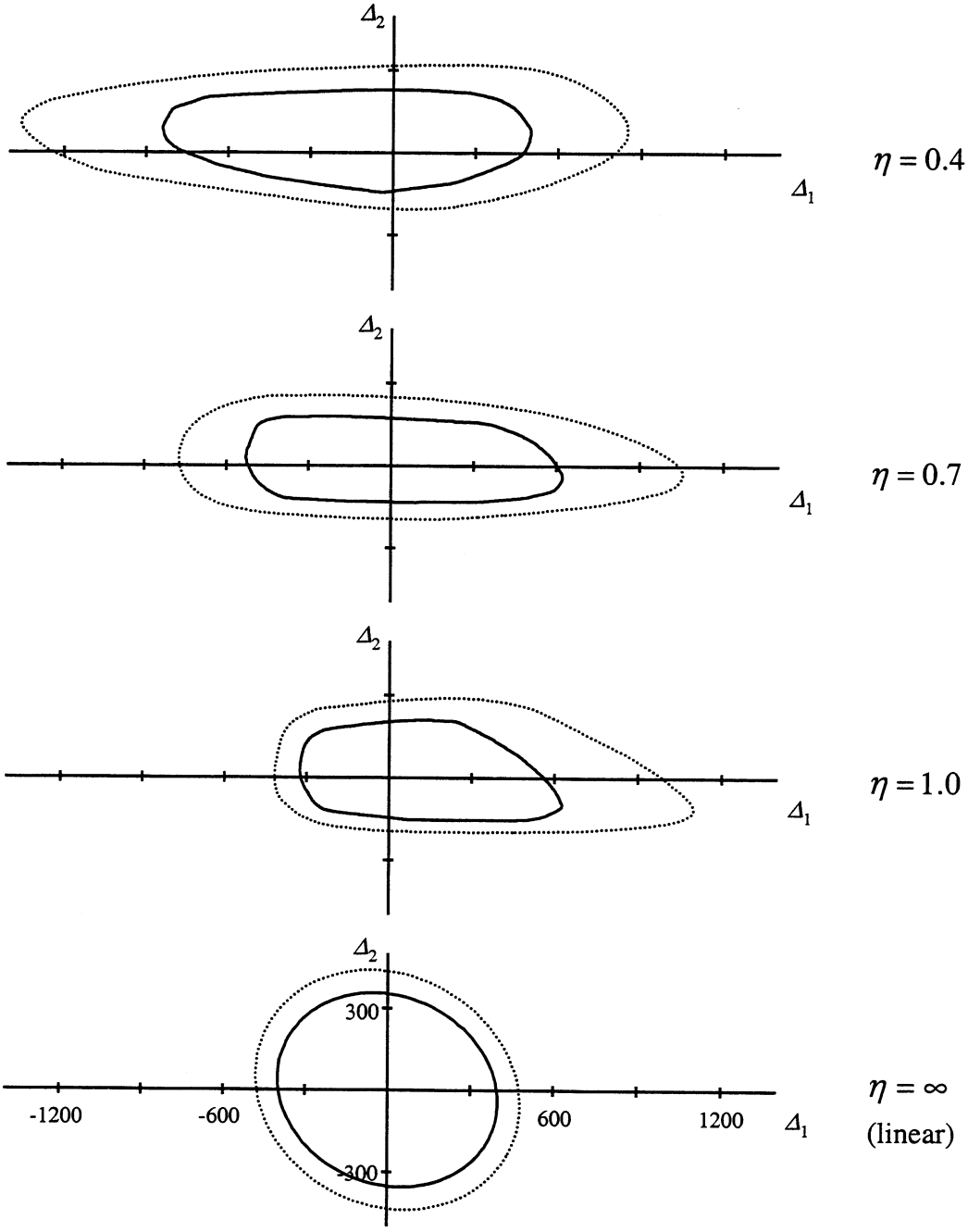

Figure 8.4. Roof displacement envelope of the nonlinear structure due to the ensemble #1 of synthetic near-fault ground motions.

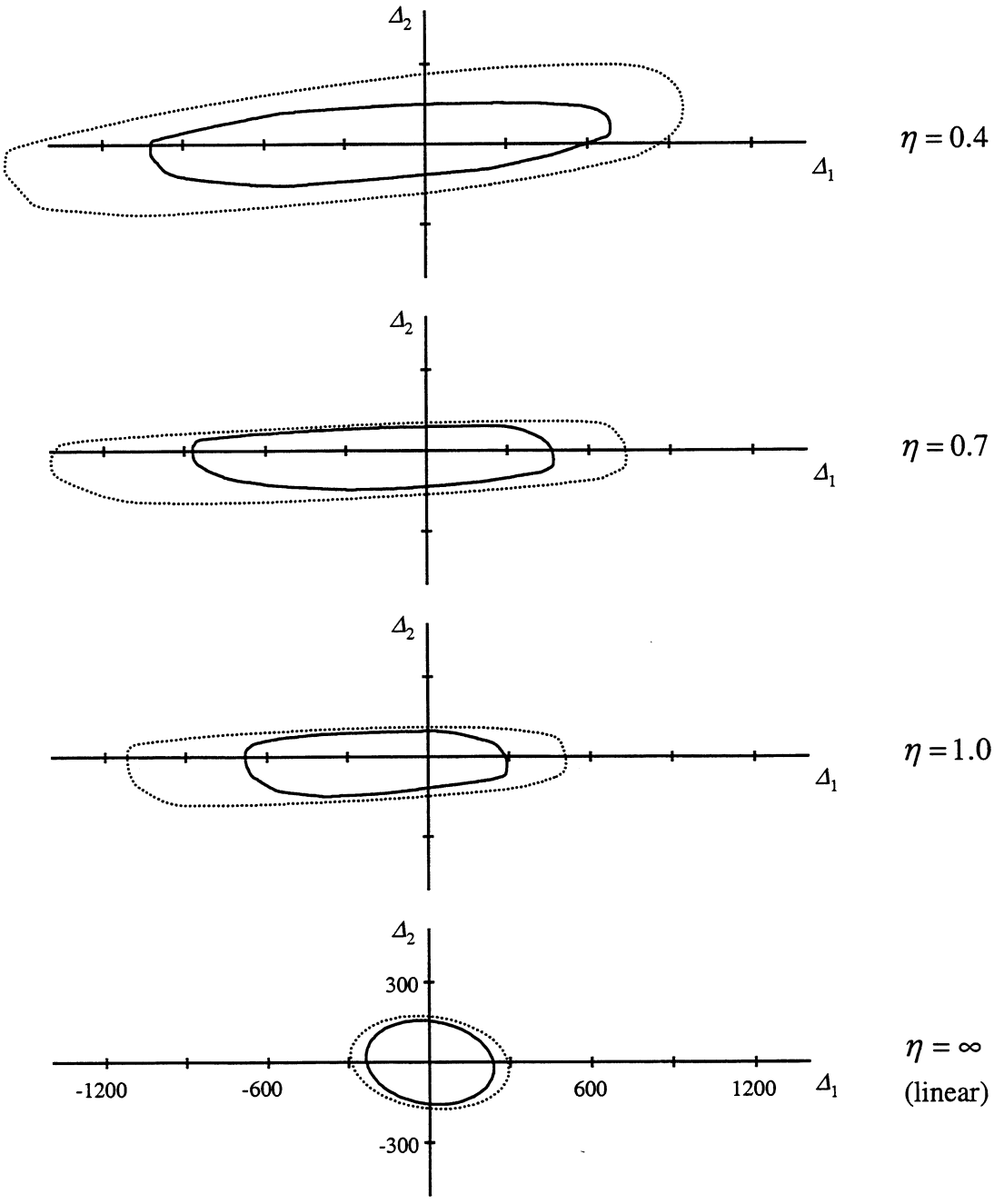

Figure 8.5. Roof displacement envelope of the nonlinear structure due to the ensemble #2 of synthetic near-fault ground motions.

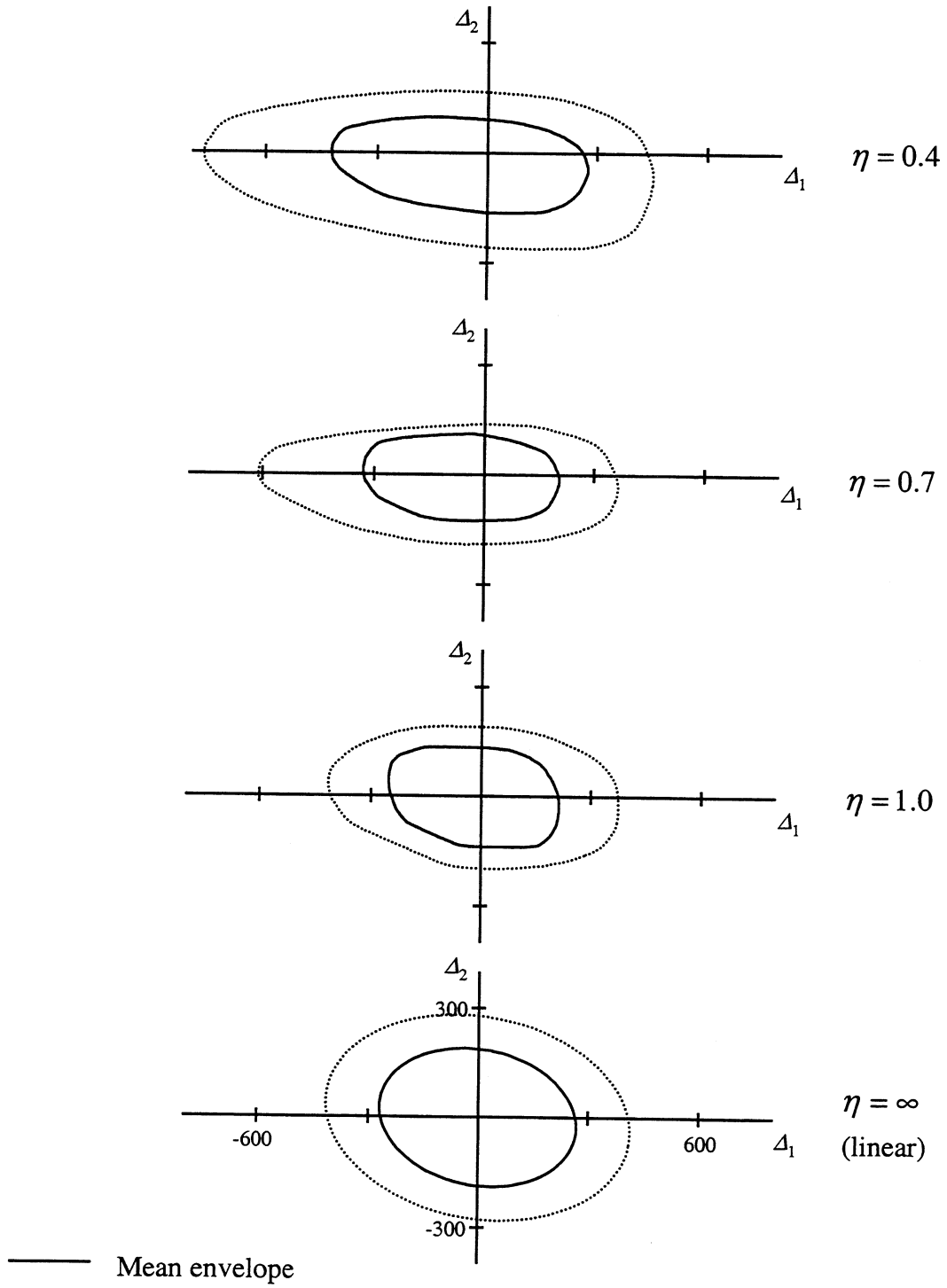

Figure 8.6. Roof displacement envelope of the nonlinear structure due to the ensemble of recorded near-fault ground motions.

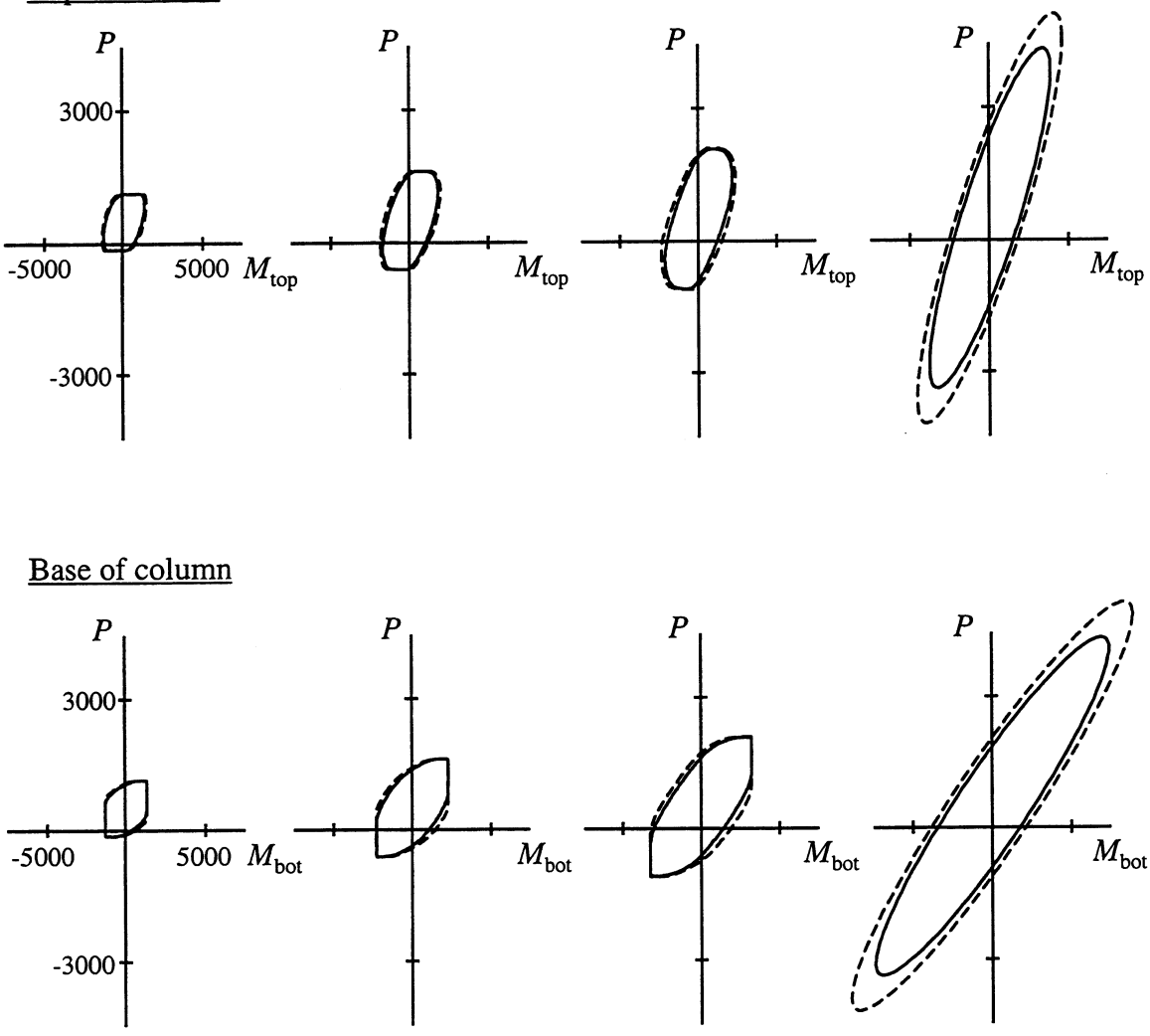

——— Mean envelope

- - - - - Mean-plus-one-standard-deviation envelope

Axial load P in kN
Bending moments M_{top} and M_{bot} in kN m
Scale for all plots as shown for $\eta = 0.4$

Figure 8.7. Column response envelope of the nonlinear structure due to the ultimate level event.

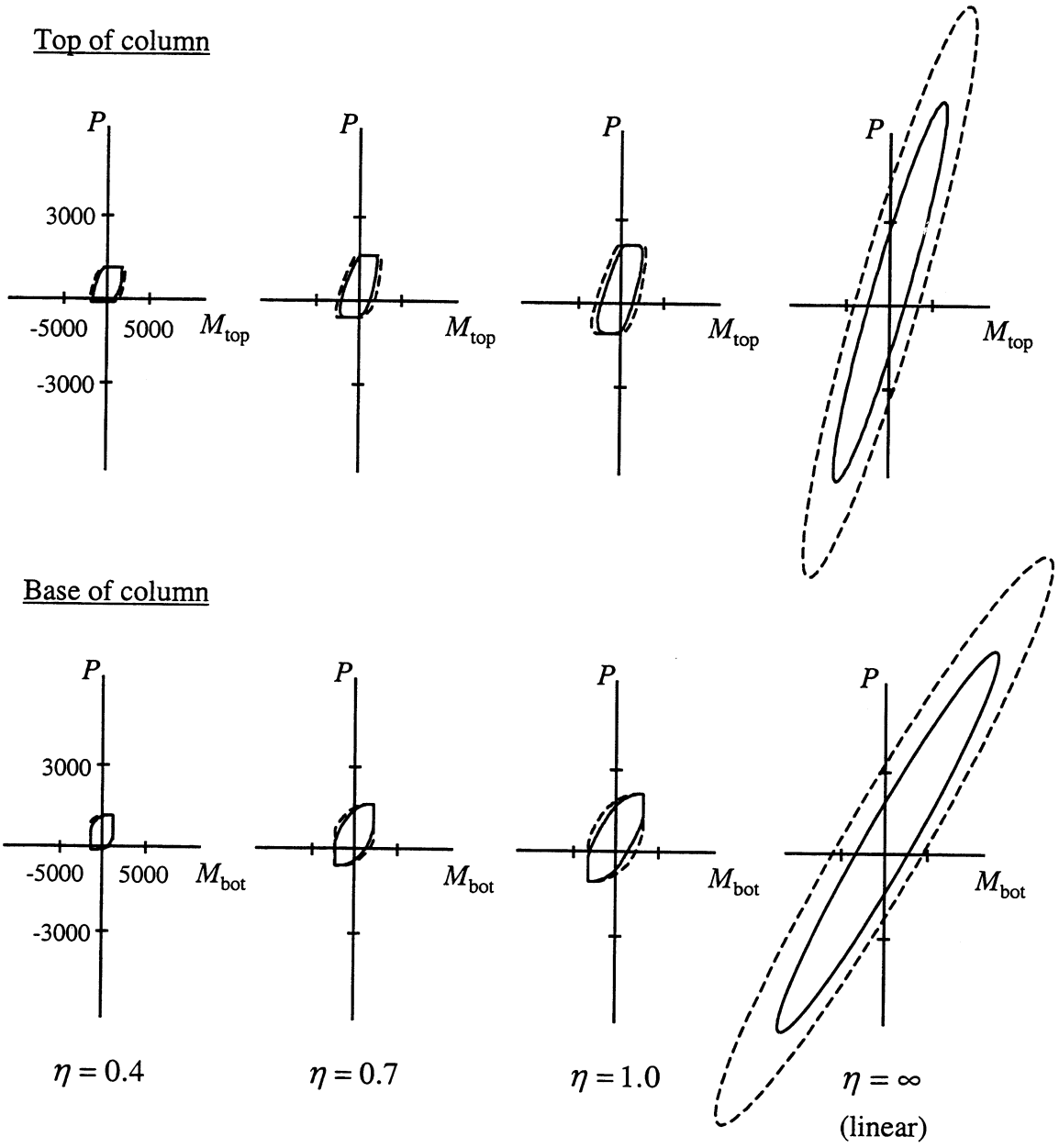

——— Mean envelope

- - - - - Mean-plus-one-standard-deviation envelope

Axial load P in kN
Bending moments M_{top} and M_{bot} in kN m
Scale for all plots as shown for $\eta = 0.4$

Figure 8.8. Column response envelope of the nonlinear structure due to the ensemble of Seattle ground motions.

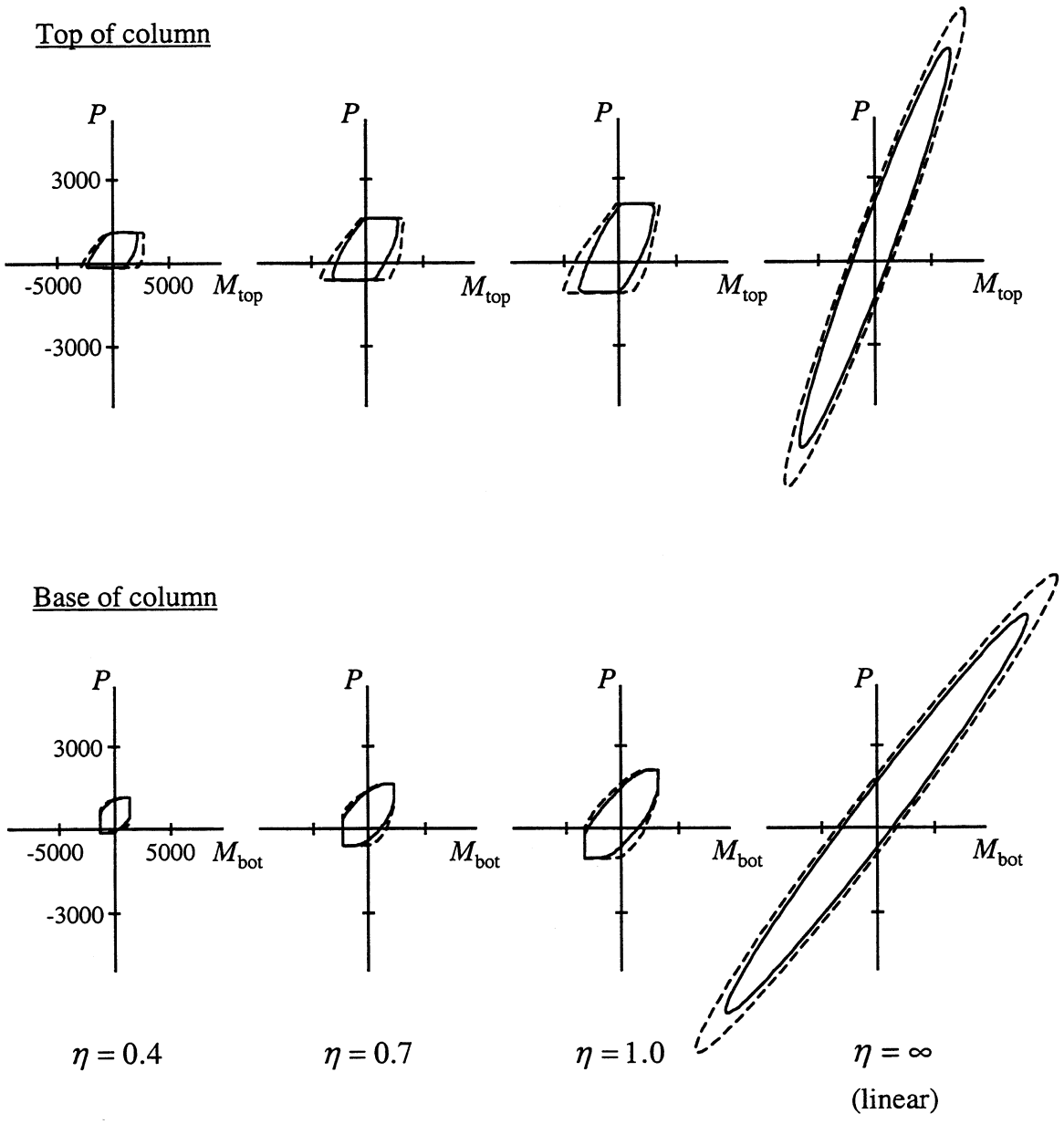

——— Mean envelope

- - - - - Mean-plus-one-standard-deviation envelope

Axial load P in kN
Bending moments M_{top} and M_{bot} in kN m
Scale for all plots as shown for $\eta = 0.4$

Figure 8.9. Column response envelope of the nonlinear structure due to the ensemble #1 of synthetic near-fault ground motions.

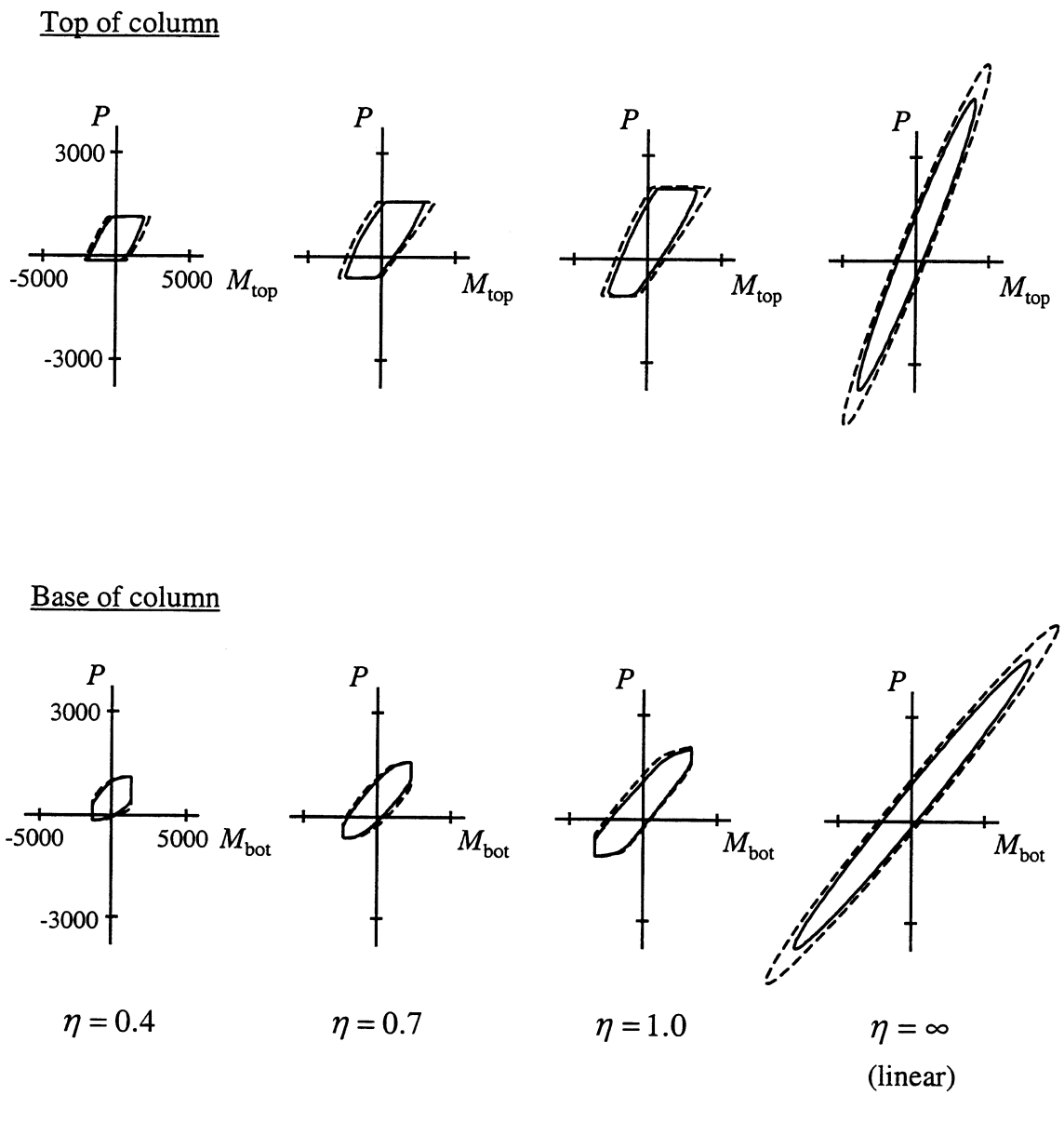

——— Mean envelope

- - - - - Mean-plus-one-standard-deviation envelope

Axial load P in kN
Bending moments M_{top} and M_{bot} in kN m
Scale for all plots as shown for $\eta = 0.4$

Figure 8.10. Column response envelope of the nonlinear structure due to the ensemble #2 of synthetic near-fault ground motions.

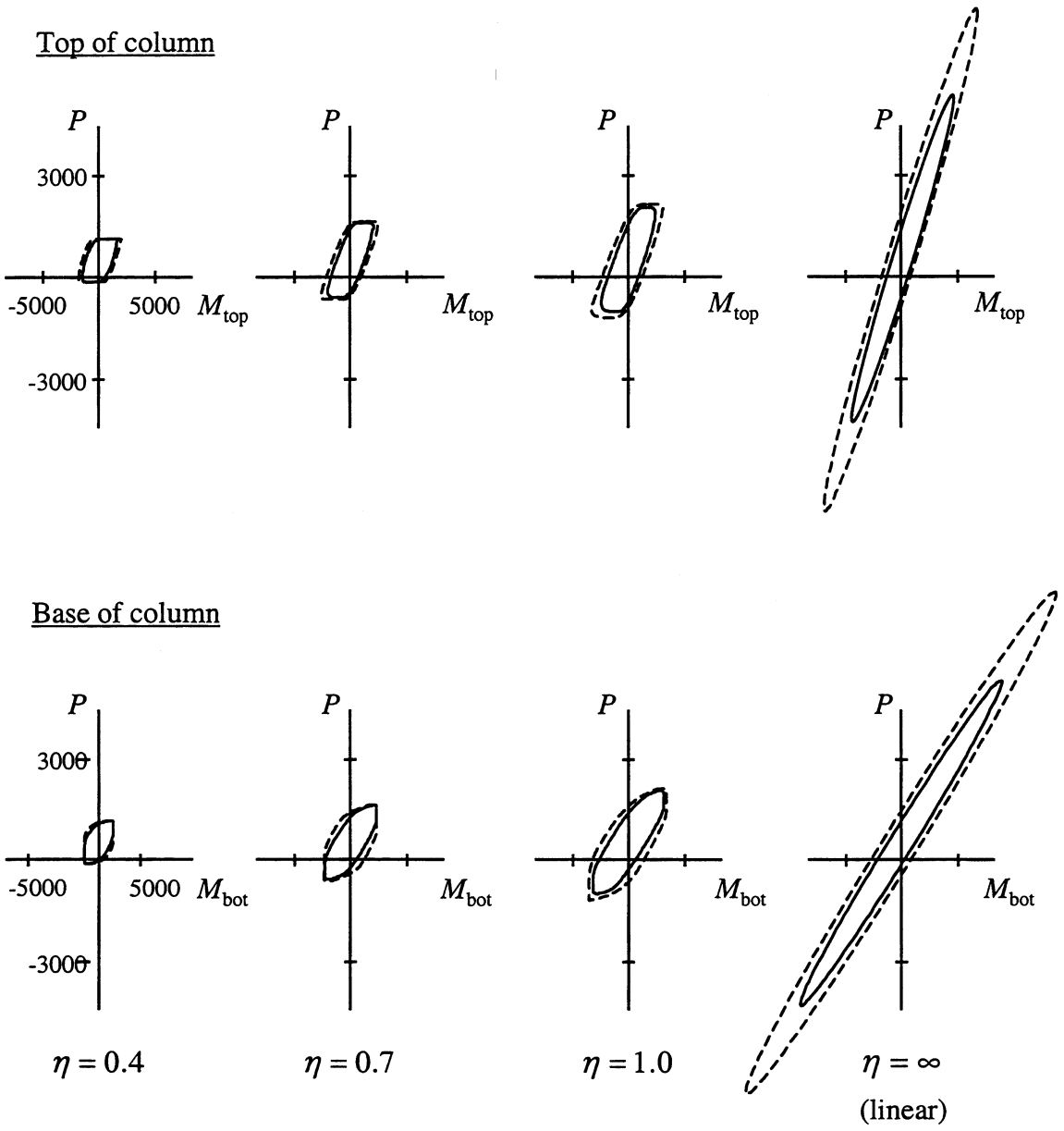

——— Mean envelope

- - - - - Mean-plus-one-standard-deviation envelope

Axial load P in kN
Bending moments M_{top} and M_{bot} in kN m
Scale for all plots as shown for $\eta = 0.4$

Figure 8.11. Column response envelope of the nonlinear structure due to the ensemble of recorded near-fault ground motions.

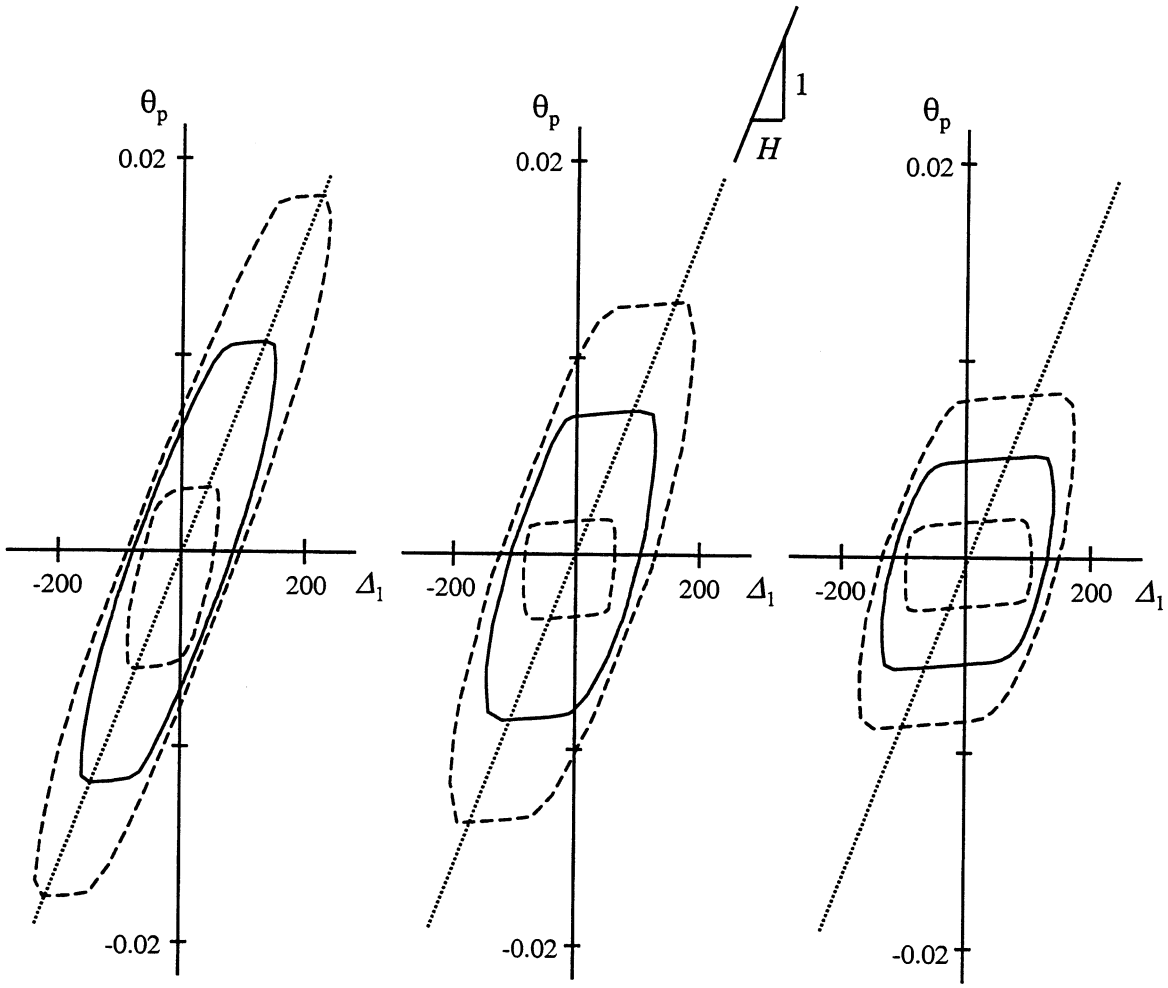

——— Mean envelope

- - - - - Mean-plus-or-minus-one-standard-deviation envelope

Roof displacement Δ_1 in mm

Hinge rotation θ_p in radians

H = total height of building (see Figure 8.13)

Figure 8.12. Envelopes bounding the roof displacement and plastic hinge rotation at the column base due to artificial ultimate level event.

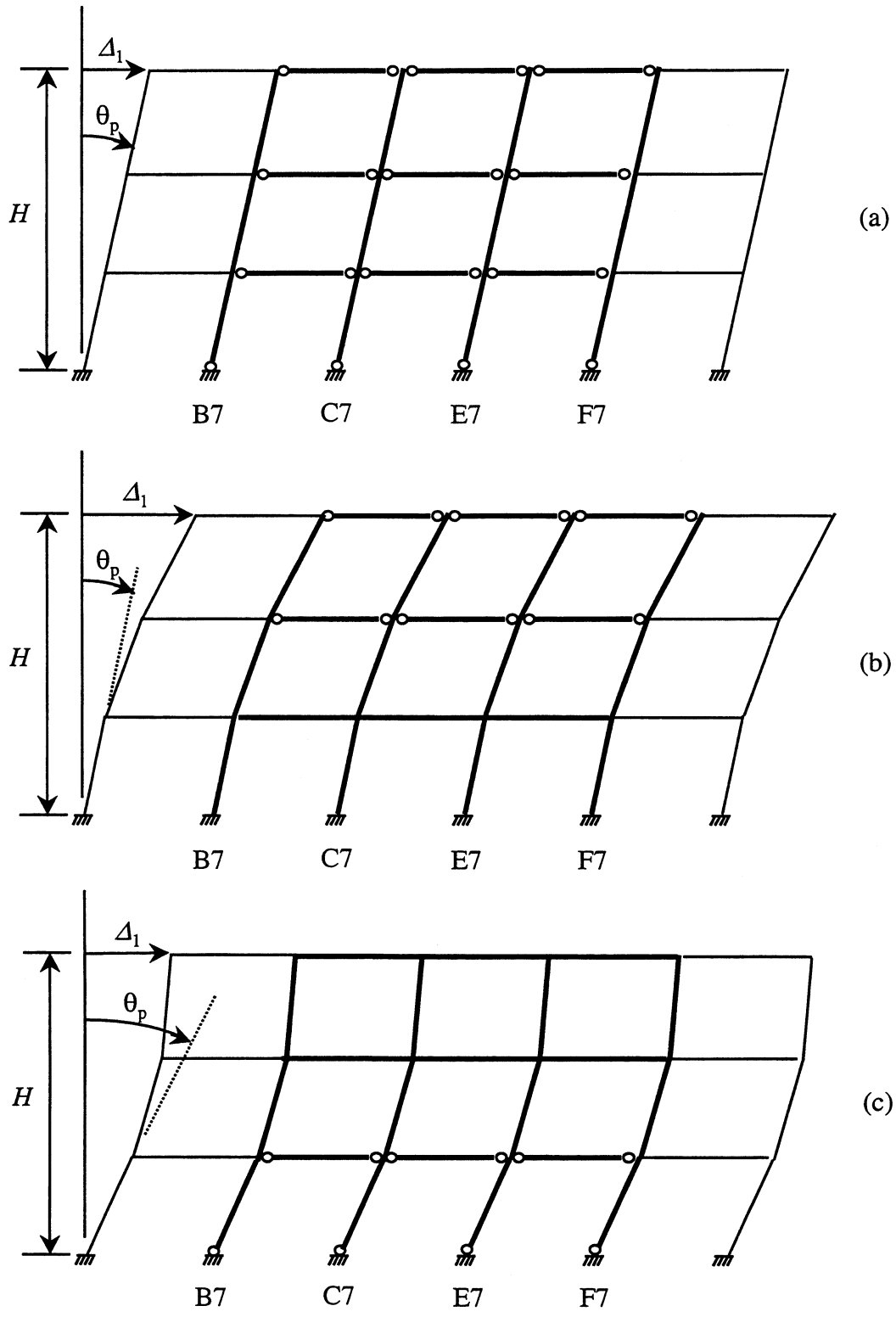

Figure 8.13. Possible sway mechanisms in the moment frame.

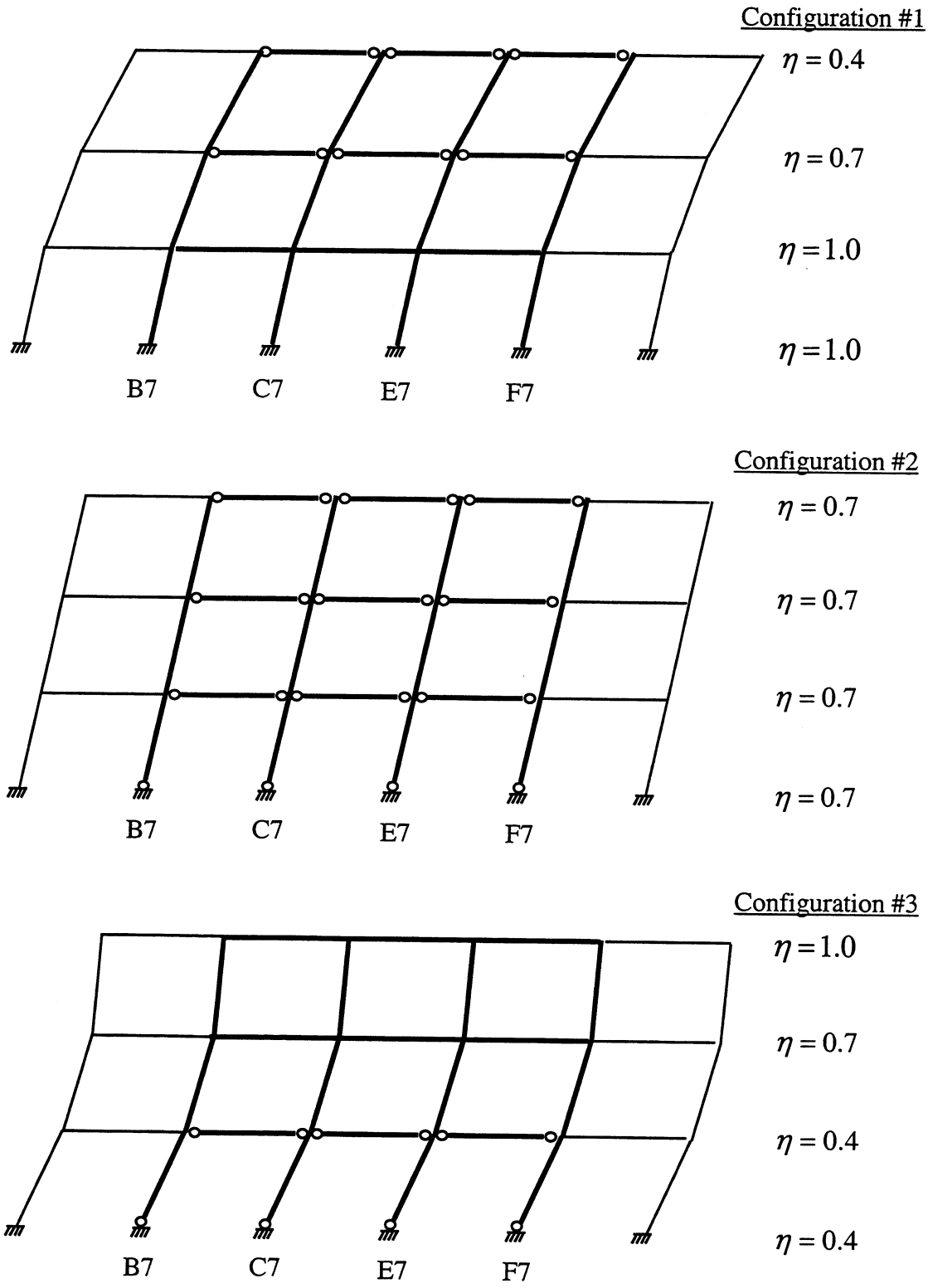

Figure 8.14. Distributions of connection strengths over height of the building.

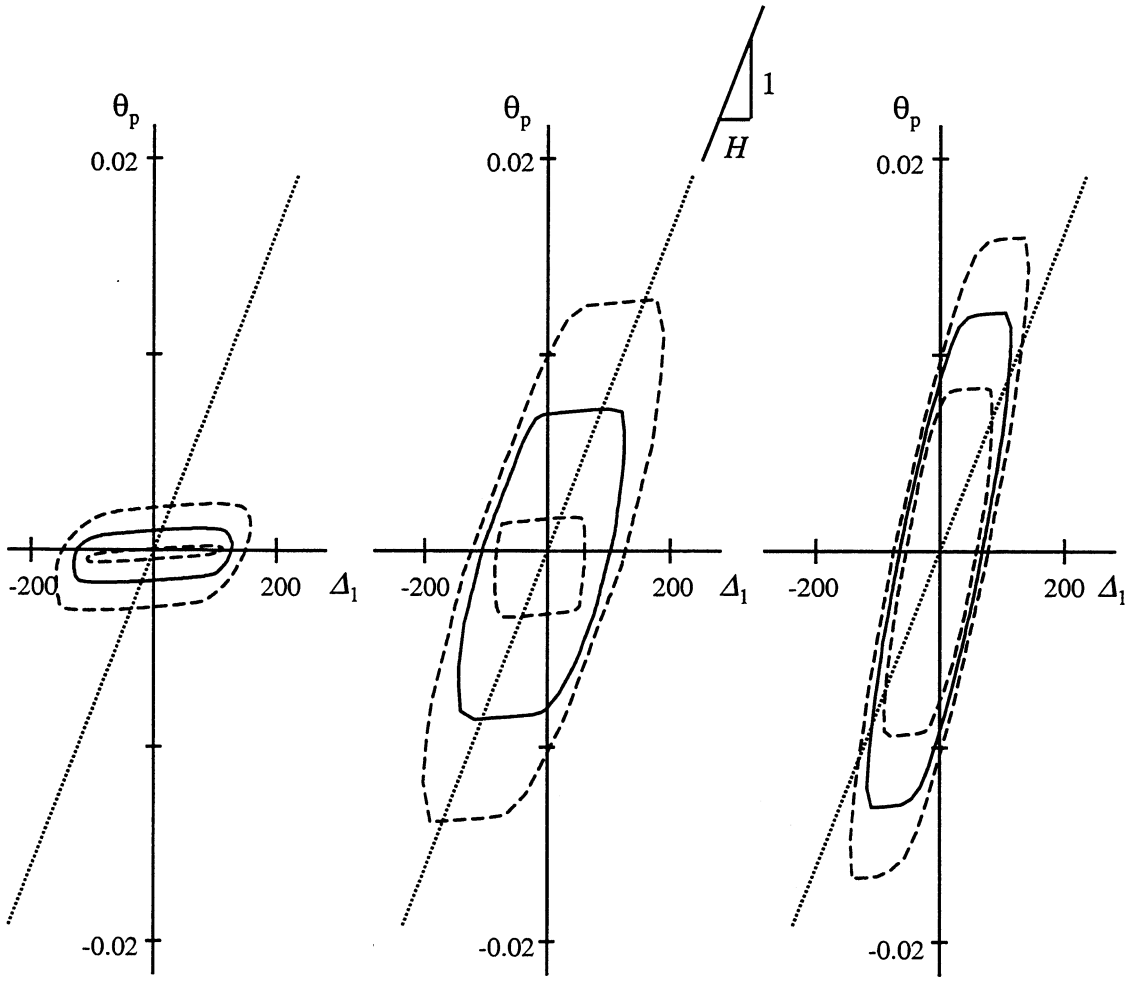

Figure 8.15. Envelopes bounding the roof displacement and plastic hinge rotation at the column base for various sway mechanisms.

9 Summary and Conclusions

Using the theory of random vibrations, a response-spectrum-based procedure for predicting the envelope of a vector of seismic responses has been developed. The envelope is completely defined by quantities available in the conventional response spectrum method. When the orientation of the principal directions along which the ground motion components are uncorrelated are known, the envelope is an ellipsoid that is inscribed within the rectangular envelope defined by the peak values of the individual response components. The size and orientation of the ellipsoid depends on the correlation between the individual response components. For the case when the principal directions are unknown, a supreme envelope is defined that bounds the union of the elliptical envelopes for all directions. A simple analytical expression for this envelope, which is not elliptical in shape, has been derived.

The accuracy of the elliptical envelope was examined through a series of time-history analyses performed on a three-story steel moment frame building and a reinforced concrete bridge using both artificial and recorded ground motions. It was shown that, consistent with the response spectrum approach, the elliptical envelope accurately bounds the response vector in an average sense. Analyses conducted with near-fault ground motions did not provide any evidence to suggest that the method could not be used with such motions.

Algorithms have been developed for applications of the elliptical and supreme envelope in seismic analysis and design. Using these algorithms, we investigated whether the use of the elliptical envelope, rather than the rectangular envelope commonly used in the current practice, has any significant effect on the analysis or design of structural elements subjected to seismic loads. For this purpose, the elliptical and rectangular envelopes bounding the moment-axial response vectors in selected columns of the example bridge were computed using a prescribed set of response spectra and assuming a specified orientation of the principal components of ground motion. Two types of analyses were performed with these response envelopes. First, the dimensions, material properties and reinforcement ratio of each column was fixed and its ability to re-

sist the prescribed seismic demands, as predicted by the elliptical and rectangular envelopes, was evaluated. Calculations of this type, which are commonly encountered when assessing the safety of an existing structure, involve a comparison of the prescribed response envelope to the capacity surface defined by the material and geometric properties of the column. It was demonstrated that the rectangular envelope can be overly conservative for such analyses. In particular, for the bridge columns considered in this example, unnecessary and potentially expensive modifications can be avoided by using the elliptical envelope rather than the rectangular envelope. Second, a design example was considered in which the required reinforcement ratios for selected columns in the example bridge were computed using the elliptical and conventional rectangular envelopes and were compared. It was found that the required reinforcement ratios of the columns could be reduced by as much as 45% when the elliptical envelope was used instead of the rectangular envelope. Comparisons were also made between the required column reinforcement ratios predicted by the supreme envelope and those obtained using the elliptical and rectangular envelopes over the entire range of orientations that the principal directions of ground motion could assume. It was shown that, when the principal directions are unknown, arbitrarily specifying the principal directions and using the corresponding elliptical envelope can yield unconservative results; using the rectangular envelope under the same circumstances can result in both unconservative and overly conservative estimates for the required column reinforcement, depending on the load condition. Based on these observations, it is recommended that the supreme envelope be used for design when the principal directions of ground motion are unknown in advance.

Recognizing that it is usually uneconomical to design a structure to remain linear during a large magnitude earthquake, we examined how the size, shape and variability of the elliptical envelope that bounds a vector of seismic responses in a linear structure change when nonlinear elements are introduced. It was found that the results of this investigation provide additional and practical insight into the nonlinear behavior of structures and the effectiveness of current seismic design methodologies. In particular, it was observed that the size, shape and variability of the nonlinear response envelopes are strongly dependent upon the characteristics of the ground motion components. For example, for the near-fault ground motions, the changes in the size and variability of the response envelopes upon the introduction of nonlinear elements into the system were more pronounced in the fault-normal direction than in the fault-parallel direction. This observation suggests that the temporal characteristics of the ground motion are as important to the nonlinear response of a structure as the frequency content. Therefore, it is unlikely that analytical

procedures or empirical rules can be developed that relate the nonlinear envelope to the response-spectrum-based envelope of the linear system. Simulation appears to be the only reliable way of predicting the envelope that bounds a vector of responses in a nonlinear structure. We also demonstrated how the information provided by a simulated nonlinear response envelope could be used to identify the sway mechanism that is expected to form in a structure subjected to intense ground shaking. Other practical applications of response envelopes of this type probably exist. Considering the current rate at which computing power and structural analysis software are improving and recognizing the value of the information provided by nonlinear time-history analyses, it is envisioned that such analyses will be used more routinely by practicing engineers for structural design in the near future. Possible areas where future research could benefit by examining response envelopes for nonlinear structures were described in the conclusion of Chapter 8.

REFERENCES

Abrahamson, N. and Silva, W.J. (1997). "Empirical response spectral attenuation relations for shallow crustal earthquakes." *Seismological Research Letters* **68**, 94-127.

American Concrete Institute (ACI) (1995). *Building code requirements for structural concrete and commentary, ACI 318-95.* Detroit, MI.

American Institute of Steel Construction (AISC) (1994). *Manual of steel construction, load and resistance factor design, volume II — Connections,* 2nd Ed. Chicago, IL.

Anastassiadis, K. (1993). "Directions sismiques défavorables et combinaisons défavorables des efforts." *Annales de l'Institut Technique du Bâtiment et des Travaux Publics* **512**, 83-97 (in French).

Belyaev, Y.K. (1968). "On the number of exits across the boundary of a region by a vector stochastic process." *Theory of Probability Applications* **13**, 320-324.

Biddah, A., and Heidebrecht, A.C. (1998). "Seismic performance of moment-resisting steel frame structures designed for different levels of seismic hazard." *Earthquake Spectra* **14**, 597-627.

Caughey, T.K. (1963). "Equivalent linearization techniques." *Journal of the Acoustical Society of America* **35**, 1706-1711.

Der Kiureghian, A. (1980). "Structural response to stationary excitation." *Journal of the Engineering Mechanics Division, ASCE* **106**, 1195-1213.

Der Kiureghian, A. (1981). "A response spectrum method for random vibration analysis of MDF systems." *Earthquake Engineering and Structural Dynamics* **9**, 419-435.

Der Kiureghian, A., and Nakamura, Y. (1993). "CQC modal combination rule for high-frequency modes." *Earthquake Engineering and Structural Dynamics* **22**, 943-956.

Gasparini, D., and Vanmarcke, E.H. (1976). "Simulated earthquake motions compatible with prescribed response spectra." *Evaluation of seismic safety of buildings report no. 2,* Department of Civil Engineering, Massachusetts Institute of Technology, Cambridge, MA.

Gupta, A.K. (1990). *Response spectrum method in seismic analysis and design of structures.* Blackwell, Cambridge, MA.

Gupta, A.K., and Singh, M.P. (1977). "Design of column sections subjected to three components of earthquake." *Nuclear Engineering and Design* **41**, 129-133.

Krawinkler, H., and Gupta, A. (1998). "Story drift demand for steel moment frame structures in different seismic regions." *Proceedings of the Sixth U.S. National Conference on Earthquake Engineering,* Earthquake Engineering Research Institute.

López, O.A., and Torres, R. (1997). "The critical angle of seismic incidence and the structural maximum response." *Earthquake Engineering and Structural Dynamics* **26**, 881-894.

Menun, C., and Der Kiureghian, A. (1998). "A replacement for the 30%, 40% and SRSS rules for multicomponent seismic analysis." *Earthquake Spectra* **14**, 153-163.

Miranda, E. (1993). "Site-dependent strength-reduction factors." *Journal of Structural Engineering, ASCE* **109**, 3503-3519.

Nassar, A. A., and Krawinkler, H. (1991). "Seismic demands for SDOF and MDOF systems." Report No. 95, John A. Blume Earthquake Engineering Center, Stanford University, Stanford, CA.

Penzien, J., and Watabe, M. (1975). "Characteristics of 3-dimensional earthquake ground motion." *Earthquake Engineering and Structural Dynamics* **3**, 365-374.

Prakash, V., Powell, G.H., and Campbell, S. (1994). "DRAIN-3DX base program description and user guide." Report No. UCB/SEMM-94/07, Department of Civil Engineering, University of California, Berkeley, CA.

Roberts, J.B., and Spanos, P.D. (1990). *Random vibration and statistical linearization.* John Wiley and Sons, New York, NY.

Rosenblueth, E., and Elorduy, J. (1969). "Responses of linear systems to certain transient disturbances." *Proceedings of the Fourth World Conference on Earthquake Engineering*, Santiago, Chile, 185-196.

Ruiz, P., and Penzien, J. (1969). "Probabilistic study of the behavior of structures during earthquakes." Report No. UCB/EERC 69-3, Earthquake Engineering Research Center, University of California, Berkeley, CA.

SEAOC (1995). *Vision 2000: Performance based seismic engineering of buildings.* San Francisco, CA.

SEAOC (1996). *Recommended lateral force requirements and commentary "blue book", 6th ed.* Seismology Committee, Structural Engineers Association of California, Sacramento, CA.

Shinozuka, M. (1964). "Probability of failure under random loading." *Journal of the Engineering Mechanics Division, ASCE* **90**, 147-171.

Singh, M.P., and Chu, S.L. (1976). "Stochastic considerations in seismic analysis of structures." *Earthquake Engineering and Structural Dynamics* **4**, 295-307.

Singh, M.P., and Maldonado, G.O. (1991). "An improved response spectrum method for calculating seismic design response. Part 1: classically damped structures." *Earthquake Engineering and Structural Dynamics* **20**, 621-635.

Smeby, W., and Der Kiureghian, A. (1985). "Modal combination rules for multicomponent earthquake excitation." *Earthquake Engineering and Structural Dynamics* **13**, 1-12.

Shome, N., and Cornell, C.A. (1999). "Probabilistic seismic demand analysis of nonlinear structures." Report No. RMS-35, Reliability of Marine Structures Program, Dept. of Civil Engineering, Stanford University, Stanford, CA.

Somerville, P., Smith, N., Punyamurthula, S., and Sun, J. (1997). "Development of ground motion time histories for phase 2 of the FEMA/SAC steel project." Report No. SAC/BD - 97/04, Sacramento, CA.

Soong, T.T., and Grigoriu, M. (1993). *Random vibration of mechanical and structural systems.* Prentice Hall, Englewood Cliffs, NJ.

Veneziano, D., Grigoriu, M., and Cornell, C.A. (1977). "Vector-process models for system reliability." *Journal of the Engineering Mechanics Division, ASCE* **103**, 441-460.

Wung, C., and Der Kiureghian, A. (1989). "STOCAL II: computer-assisted learning system for stochastic dynamic analysis of structures. Part I — theory and development." Report No. UCB/SEMM-89/10, Department of Civil Engineering, University of California, Berkeley, CA.

APPENDIX A

SEATTLE GROUND MOTIONS

Table A.1 lists the source of each accelerogram included in the ensemble of Seattle ground motions along with its original SAC identification number. Additional details of this ensemble of events, which was originally compiled for Phase 2 of the SAC Joint Venture Steel Project, are described by Somerville et al. (1997). As described in Chapter 4, for each event, the original pair of accelerograms was decomposed into uncorrelated components through the rotational transformation (4.12). The required rotation ϕ and the times t_5 and t_{95} that define the length of the records used to compute this rotation are also summarized in Table A.1.

Each pair of uncorrelated ground acceleration records along with the corresponding ground velocity and displacement records and the pseudo-acceleration response spectra are plotted in Figures A.1 through A.10. The major component of ground motion is shown on the left-hand side of all figures.

Table A.1. Events included in the ensemble of Seattle ground motions.

Event	SAC #	Description	ϕ (rad)	t_5 (sec)	t_{95} (sec)
1	SE21	Mendocino (1992)	0.133	2.8	20.6
	SE22				
2	SE23	Erizincan (1992)	0.384	2.4	11.8
	SE24				
3	SE25	Olympia (1949)	-0.759	5.7	23.3
	SE26				
4	SE27	Seattle (1965)	0.173	3.5	29.9
	SE28				
5	SE29	Valparaiso (1985)	-0.703	15.2	52.8
	SE30				
6	SE31	Valparaiso (1985)	-0.318	17.3	67.4
	SE32				
7	SE33	Synthetic (deep inter-plate event)	0.469	19.0	48.4
	SE34				
8	SE35	Miyagi-oki (1978)	1.383	10.7	28.4
	SE36				
9	SE37	Synthetic (shallow inter-plate event)	1.558	9.1	31.2
	SE38				
10	SE39	Synthetic (shallow inter-plate event)	-1.369	12.0	33.8
	SE40				

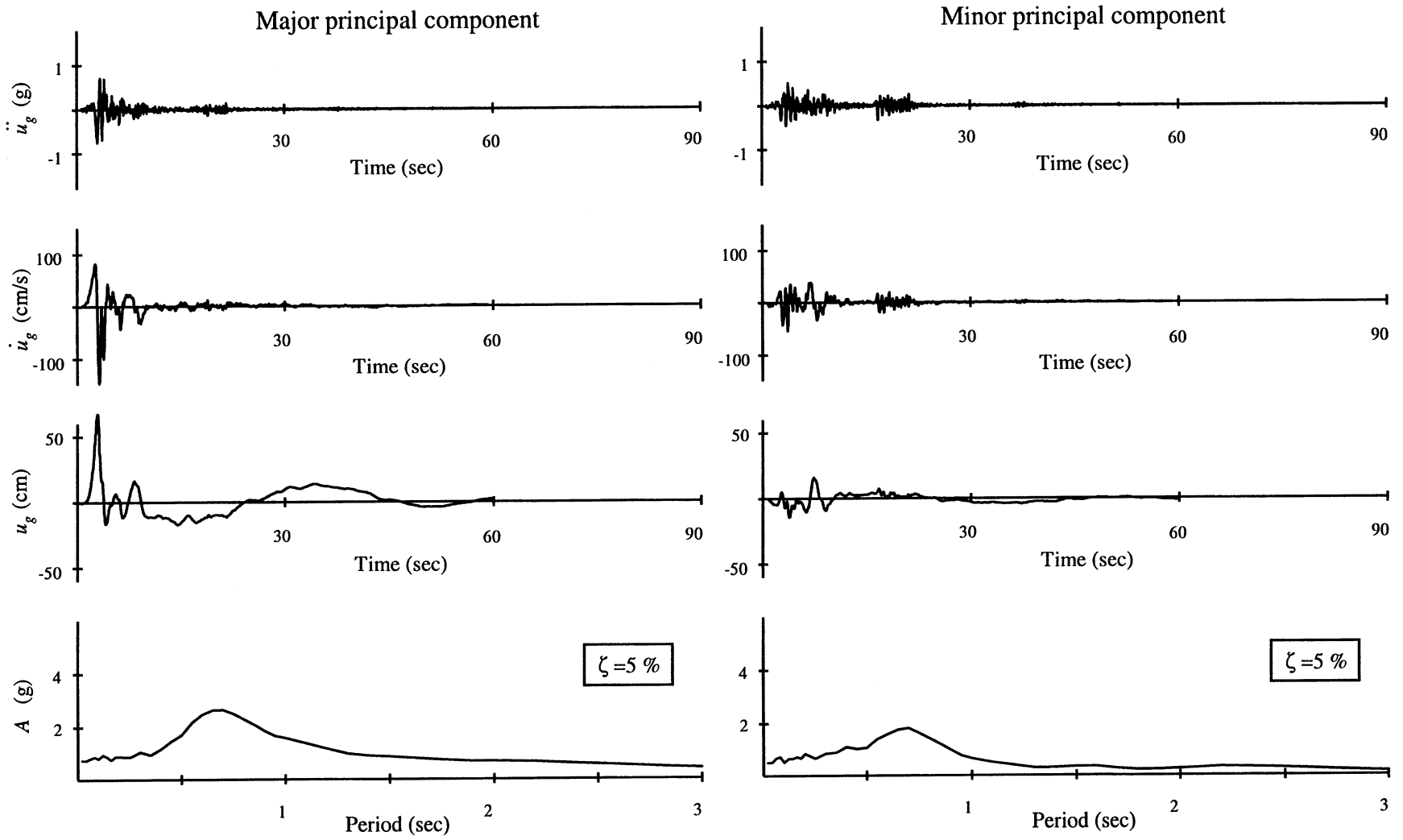

Figure A.1. Event # 1 in the ensemble of Seattle ground motions.

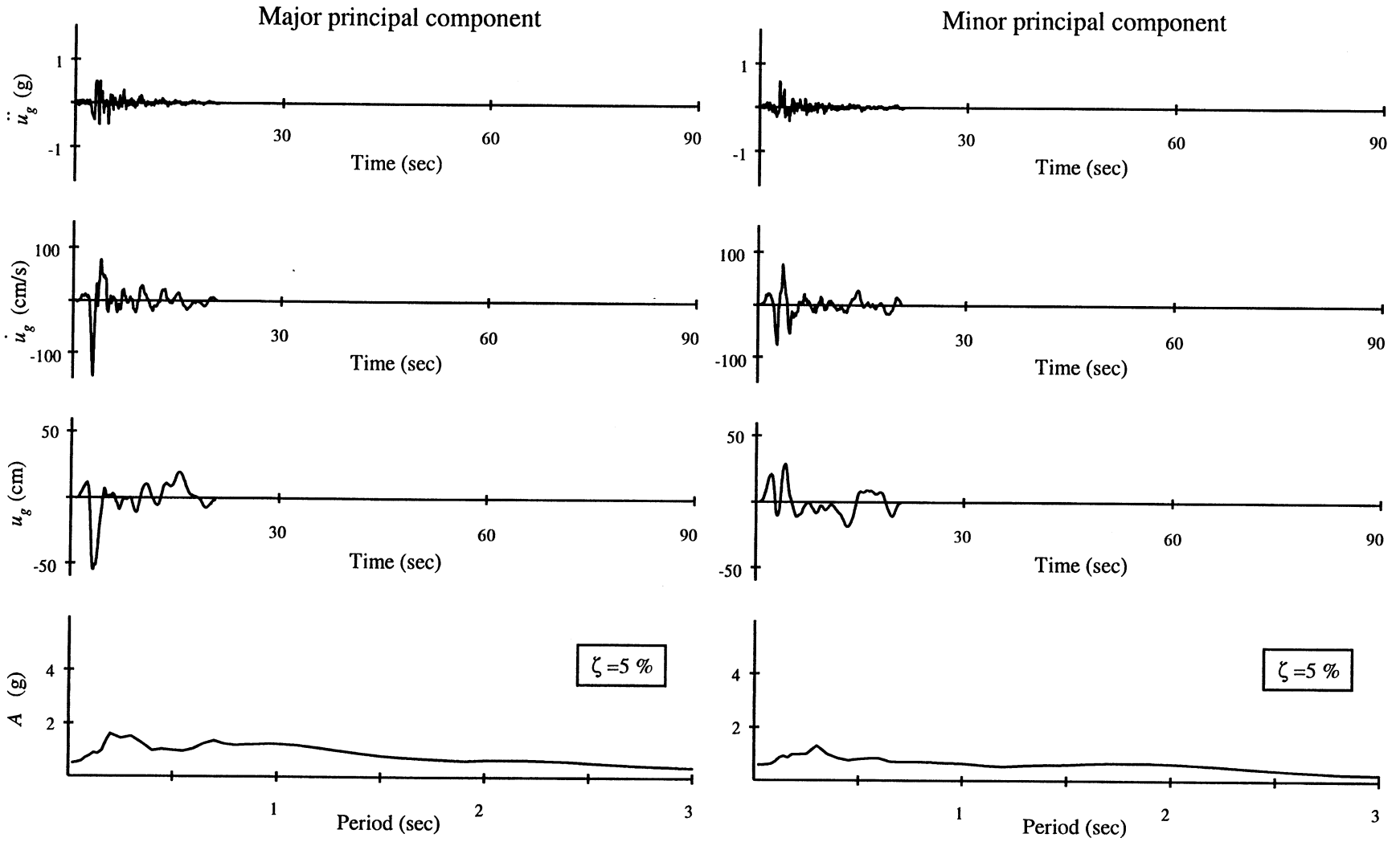

Figure A.2. Event # 2 in the ensemble of Seattle ground motions.

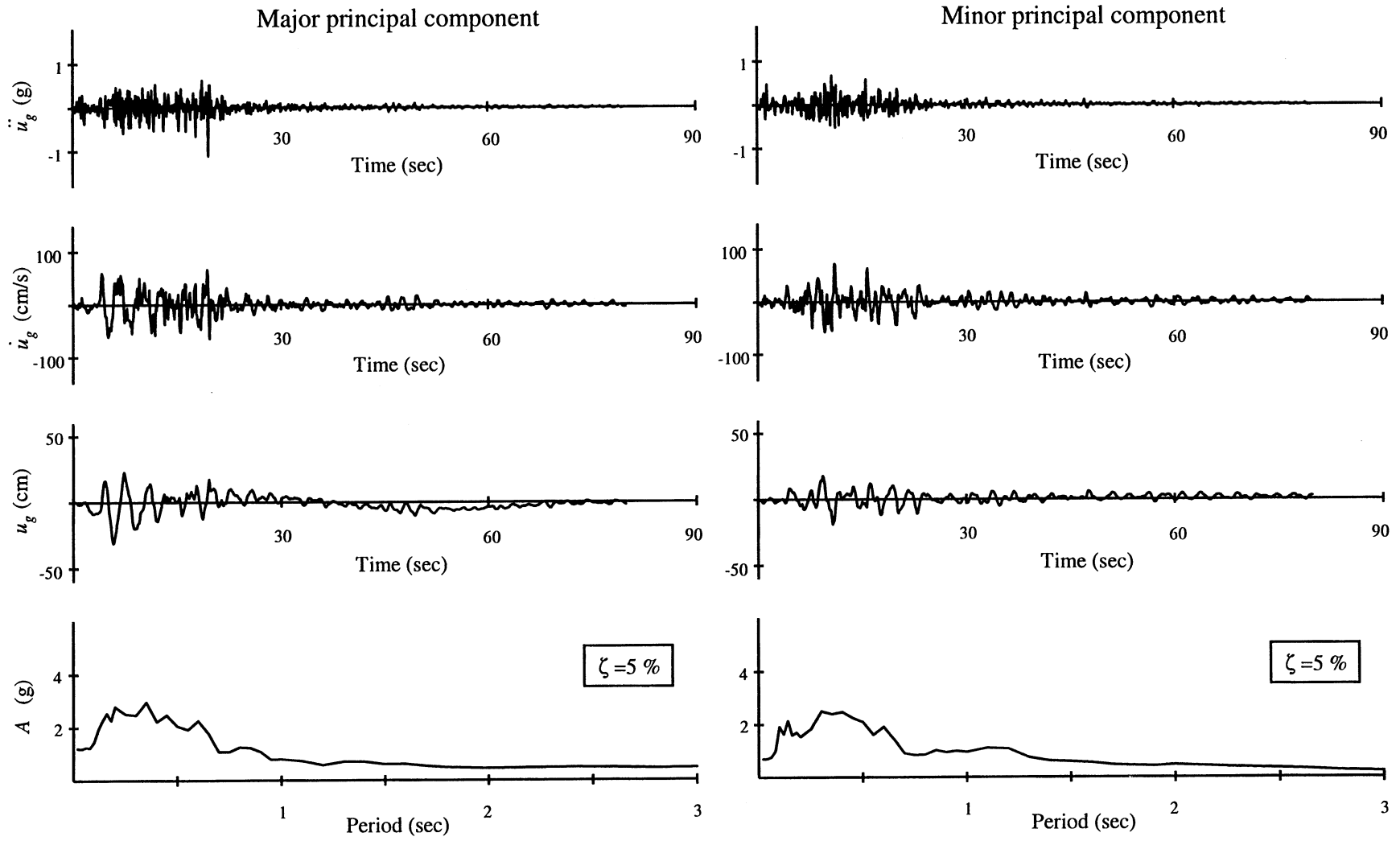

Figure A.3. Event # 3 in the ensemble of Seattle ground motions.

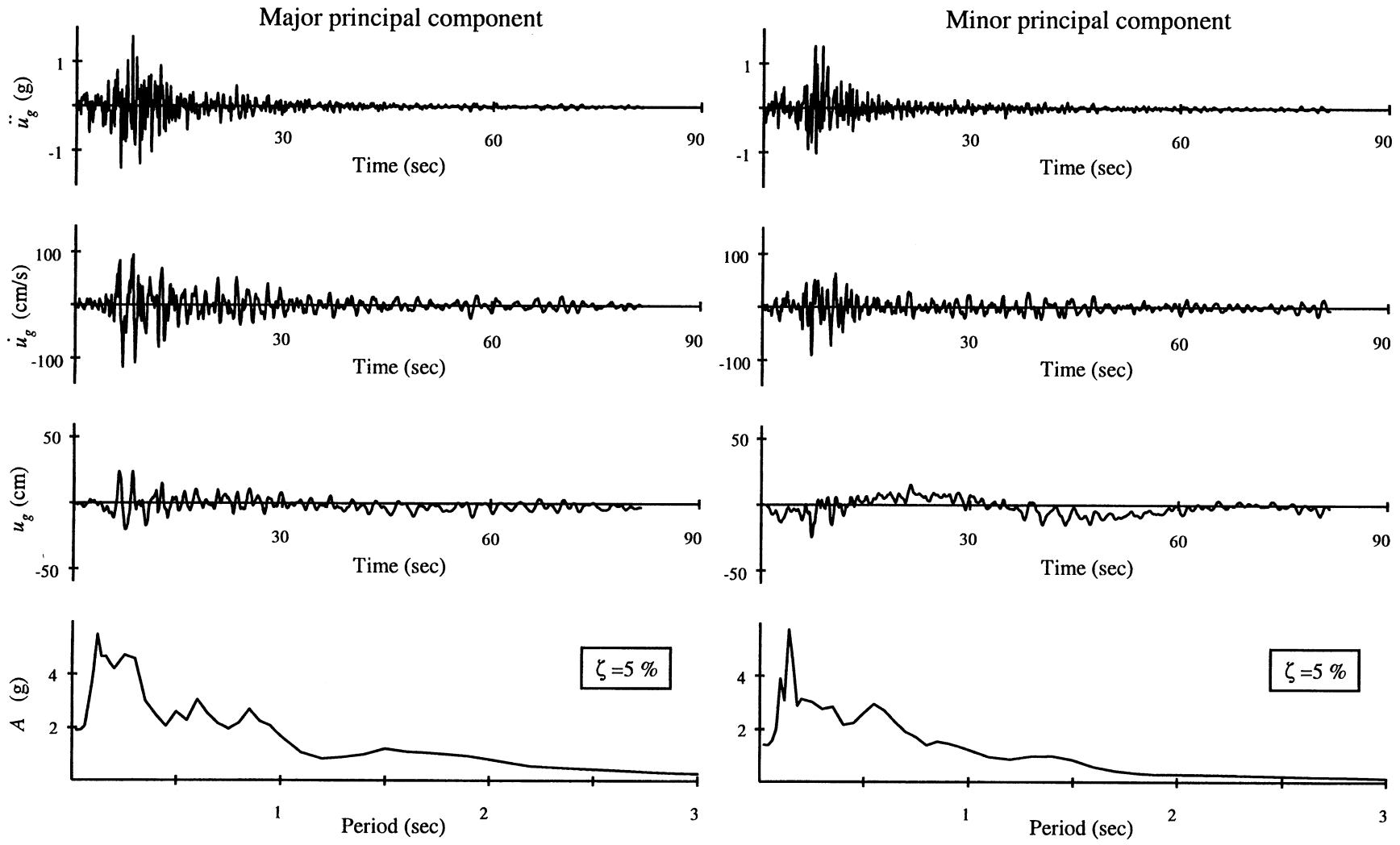

Figure A.4. Event # 4 in the ensemble of Seattle ground motions.

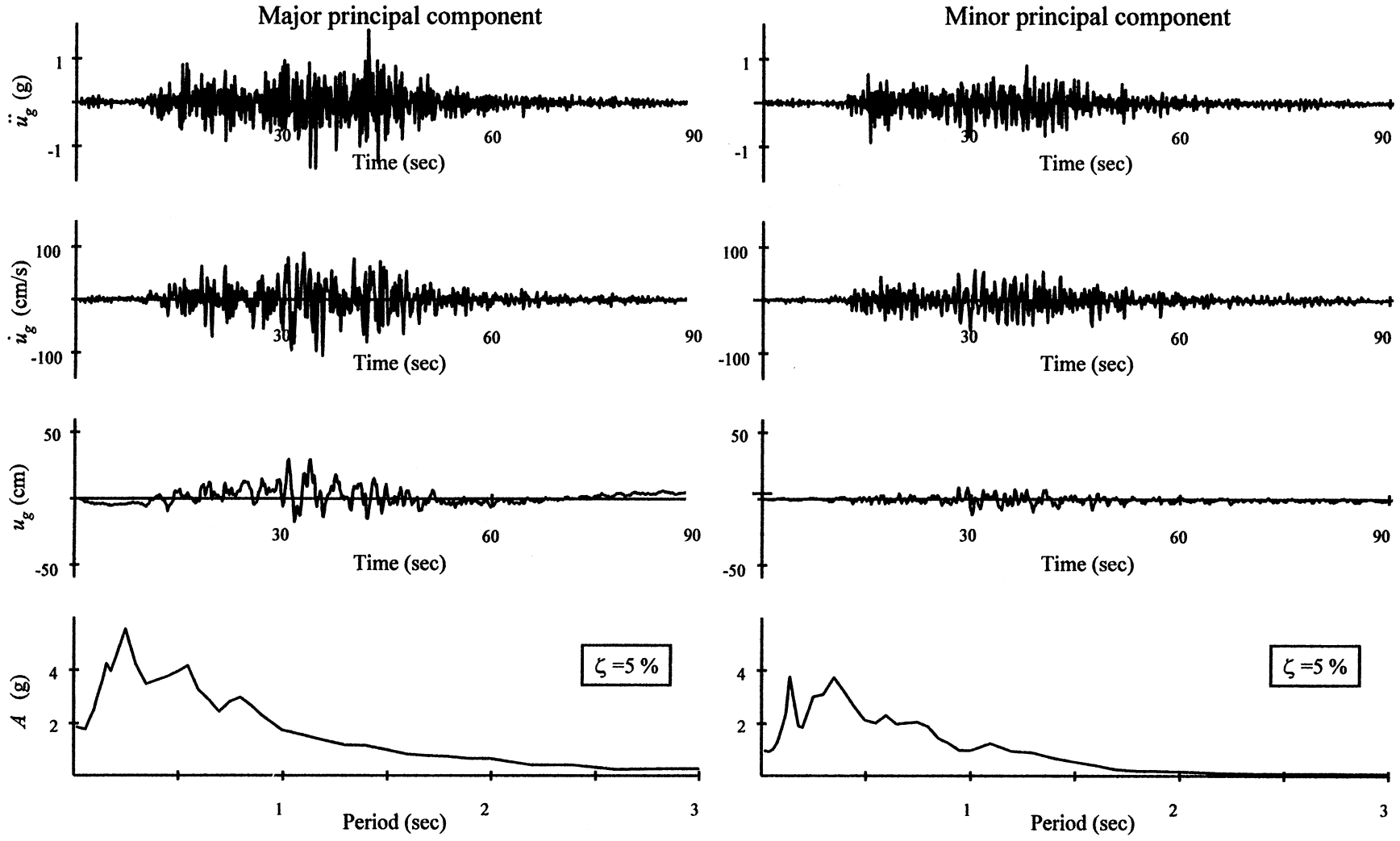

Figure A.5. Event # 5 in the ensemble of Seattle ground motions.

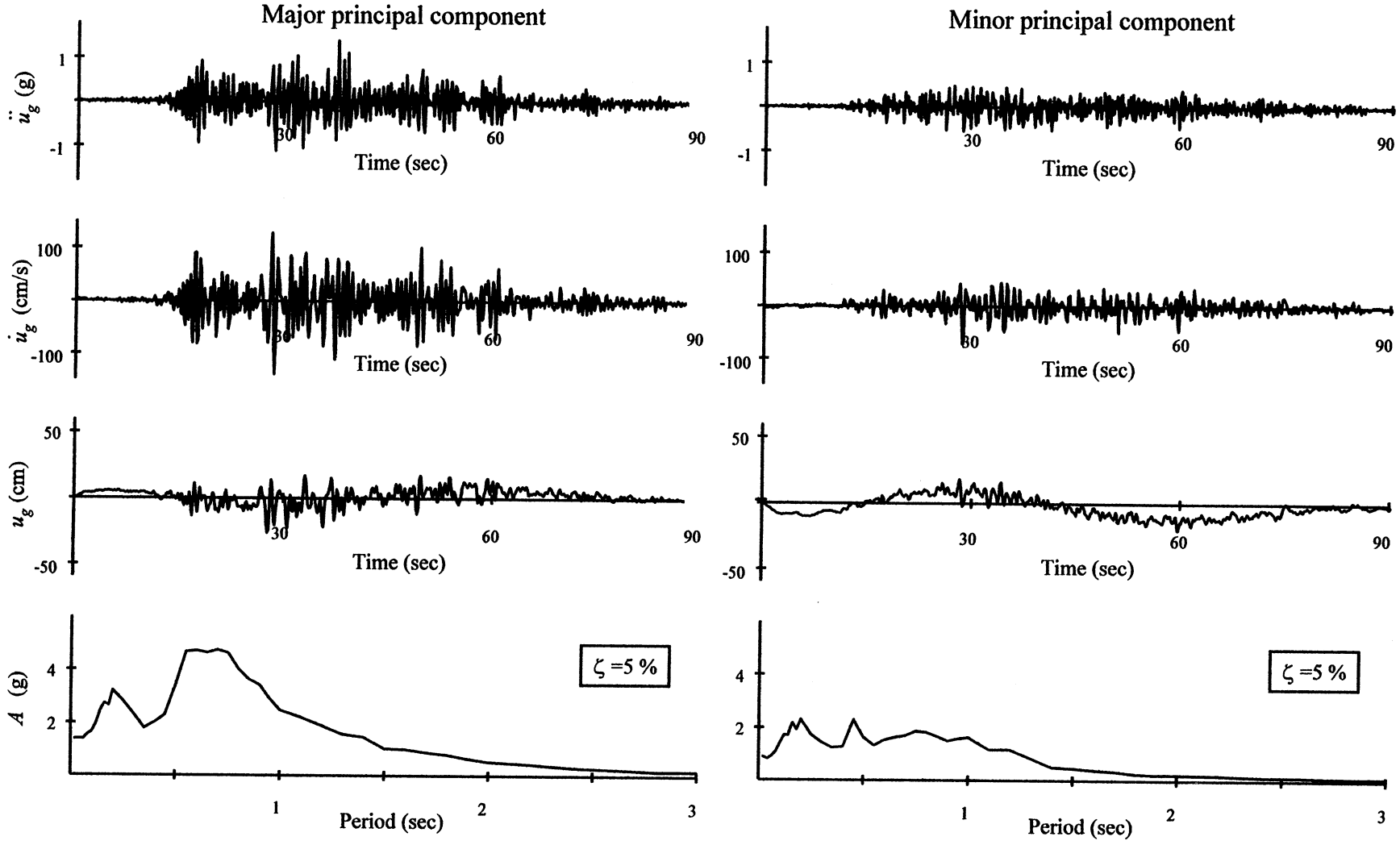

Figure A.6. Event # 6 in the ensemble of Seattle ground motions.

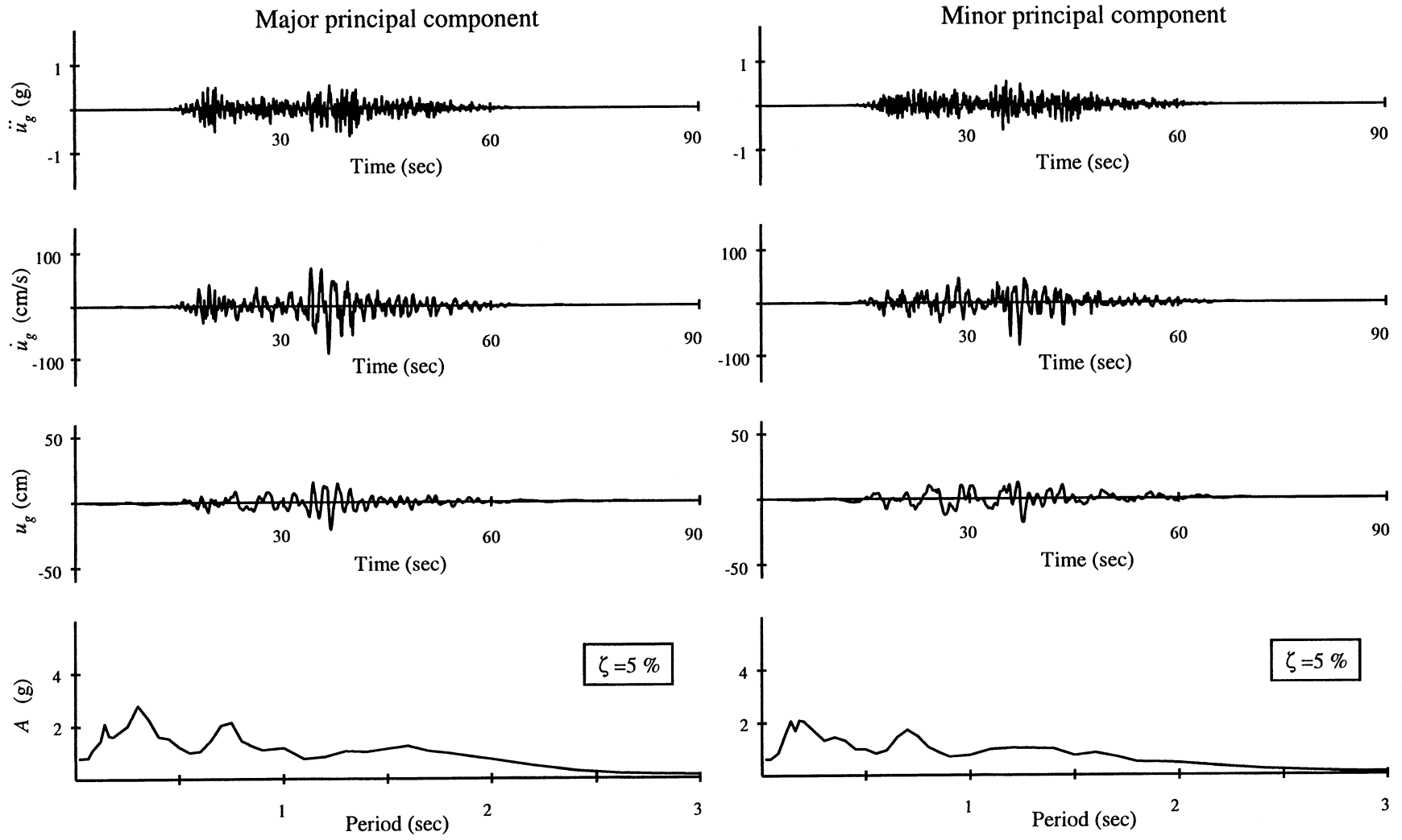

Figure A.7. Event # 7 in the ensemble of Seattle ground motions.

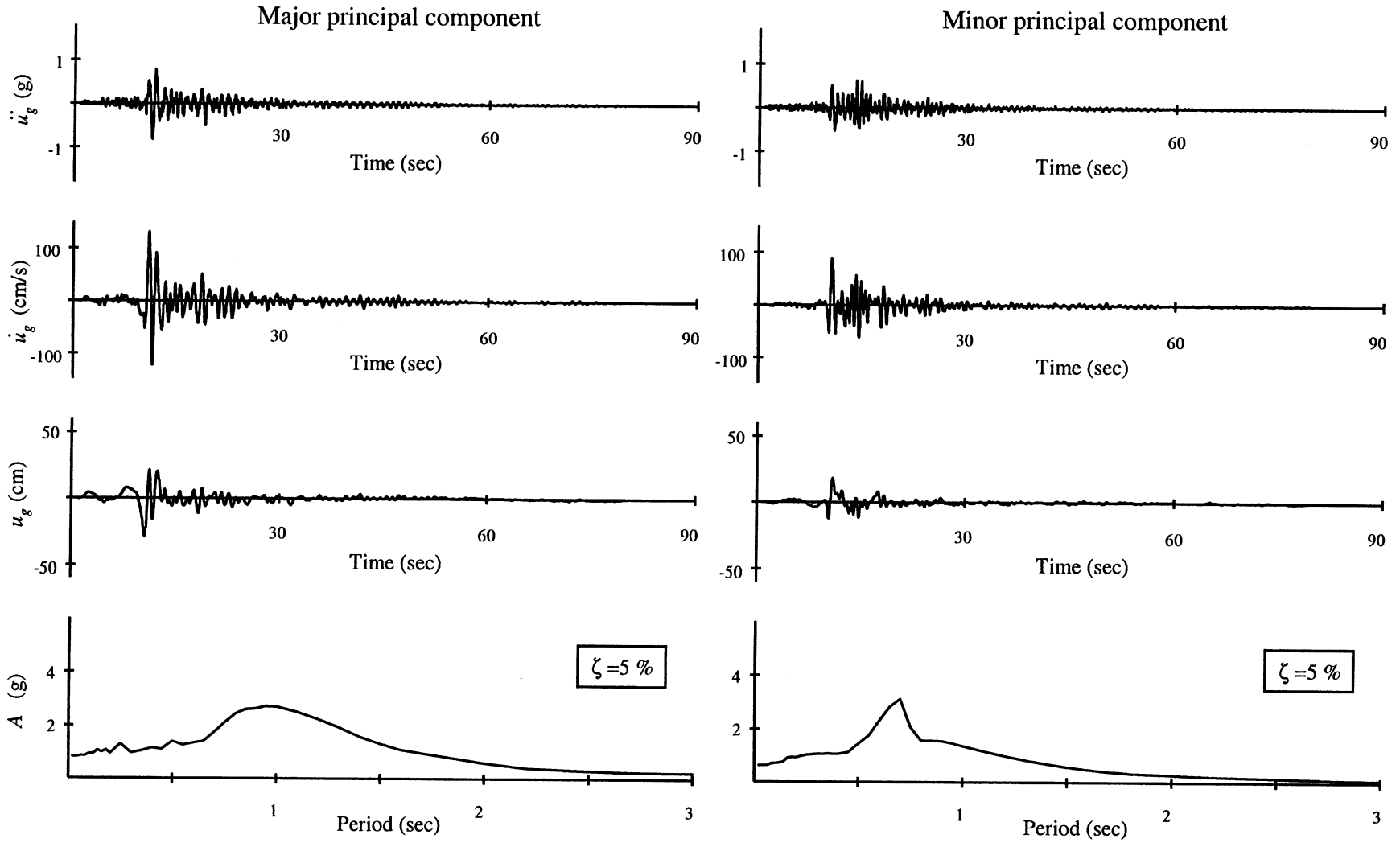

Figure A.8. Event # 8 in the ensemble of Seattle ground motions.

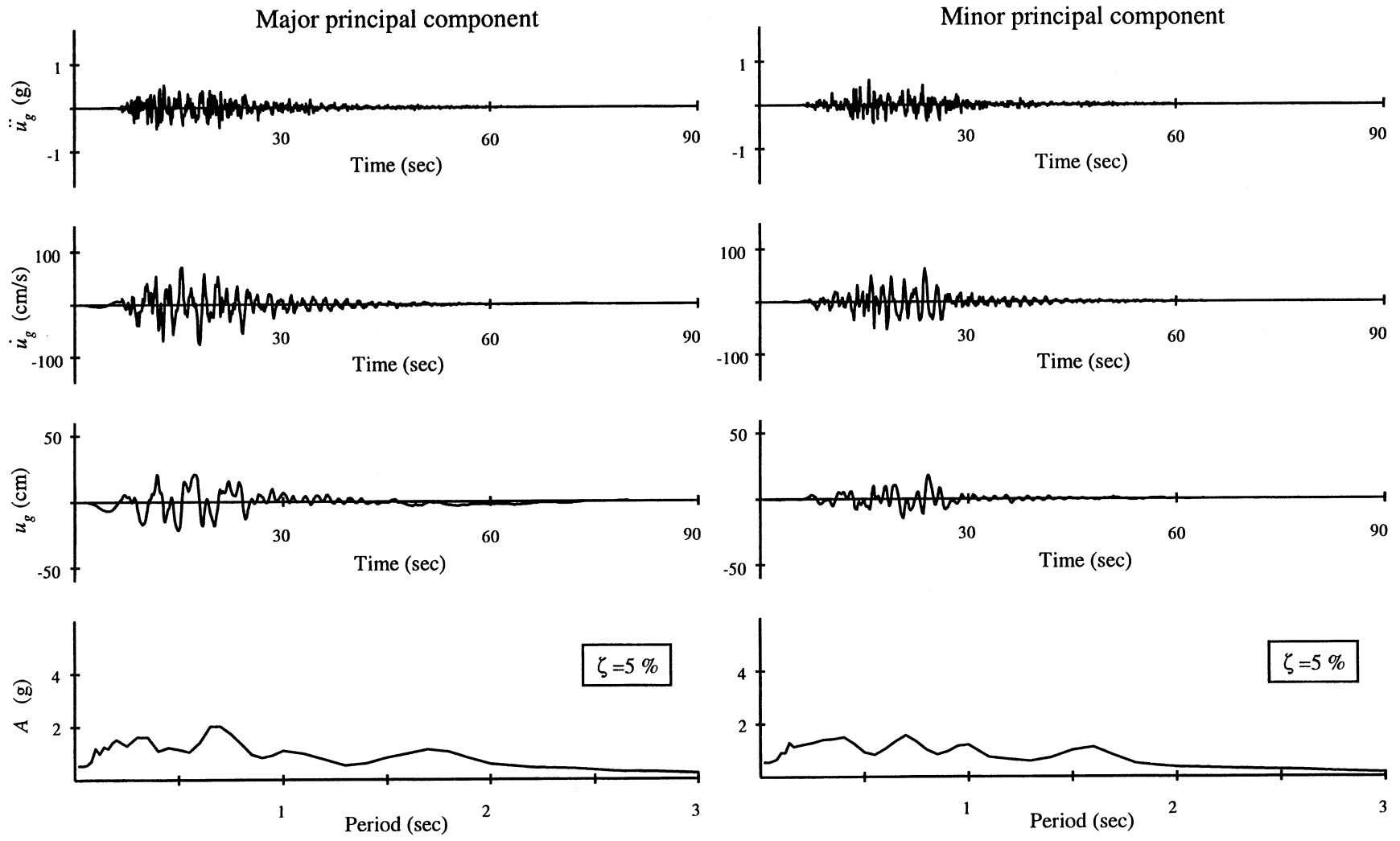

Figure A.9. Event # 9 in the ensemble of Seattle ground motions.

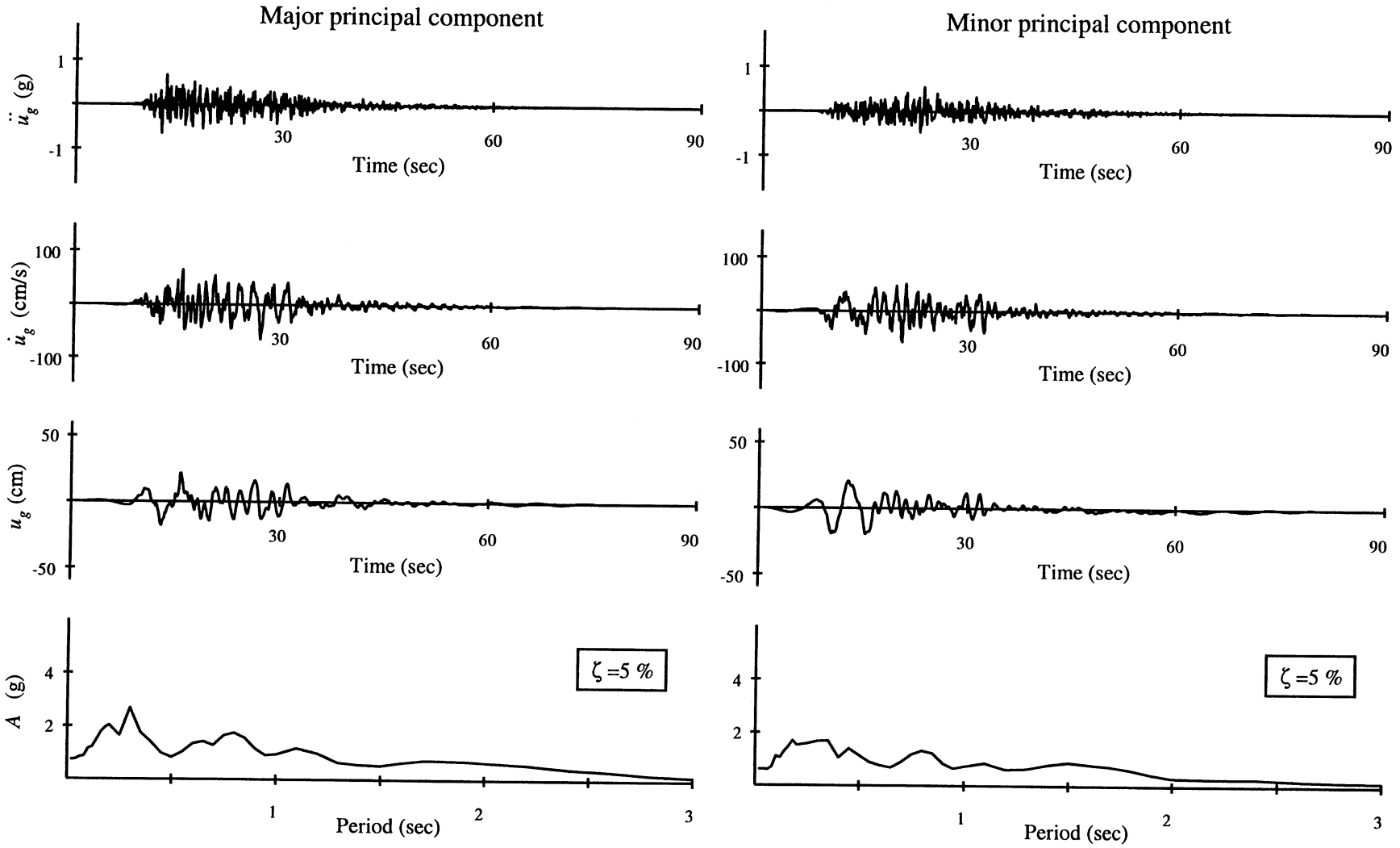

Figure A.10. Event # 10 in the ensemble of Seattle ground motions.

APPENDIX B

RECORDED NEAR-FAULT GROUND MOTIONS

Table B.1 lists the source of each accelerogram included in the ensemble of recorded near-fault ground motions along with its original SAC identification number. The ground motions are either normal or parallel to the strike of the fault, as indicated in Table B.1. Additional details of these records are described by Somerville et al. (1997).

Each pair of ground acceleration records along with the corresponding ground velocity and displacement records and the pseudo-acceleration response spectra are plotted in Figures B.1 through B.10. For each event, the fault-normal component of ground motion is shown on the left-hand side of the figure.

Table B.1. Events included in the ensemble of recorded near-fault ground motions.

Event	SAC #	Description	
1	NF01	Tabas (1978)	Fault-normal
	NF02	Tabas (1978)	Fault-parallel
2	NF03	Loma Prieta, Los Gatos (1989)	Fault-normal
	NF04	Loma Prieta, Los Gatos (1989)	Fault-parallel
3	NF05	Loma Prieta, Lex. Dam (1989)	Fault-normal
	NF06	Loma Prieta, Lex. Dam (1989)	Fault-parallel
4	NF07	Mendocino, Petrolia (1992)	Fault-normal
	NF08	Mendocino, Petrolia (1992)	Fault-parallel
5	NF09	Erzincan (1992)	Fault-normal
	NF10	Erzincan (1992)	Fault-parallel
6	NF11	Landers (1992)	Fault-normal
	NF12	Landers (1992)	Fault-parallel
7	NF13	Northridge, Rinaldi (1994)	Fault-normal
	NF14	Northridge, Rinaldi (1994)	Fault-parallel
8	NF15	Northridge, Olive View (1994)	Fault-normal
	NF16	Northridge, Olive View (1994)	Fault-parallel
9	NF17	Kobe (1995)	Fault-normal
	NF18	Kobe (1995)	Fault-parallel
10	NF19	Kobe, Takatori (1995)	Fault-normal
	NF20	Kobe, Takatori (1995)	Fault-parallel

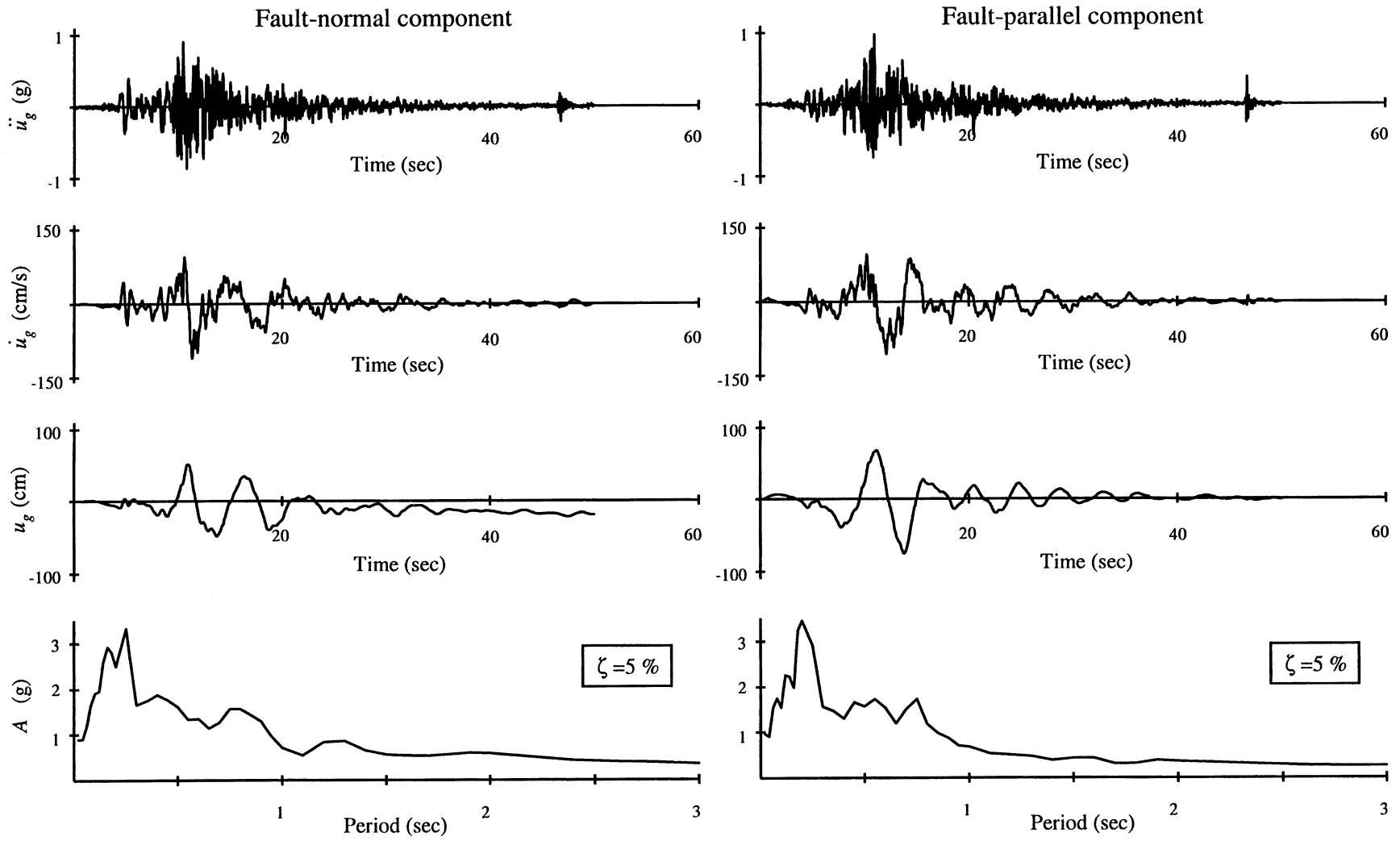

Figure B.1. Event # 1 in the ensemble of recorded near-fault ground motions.

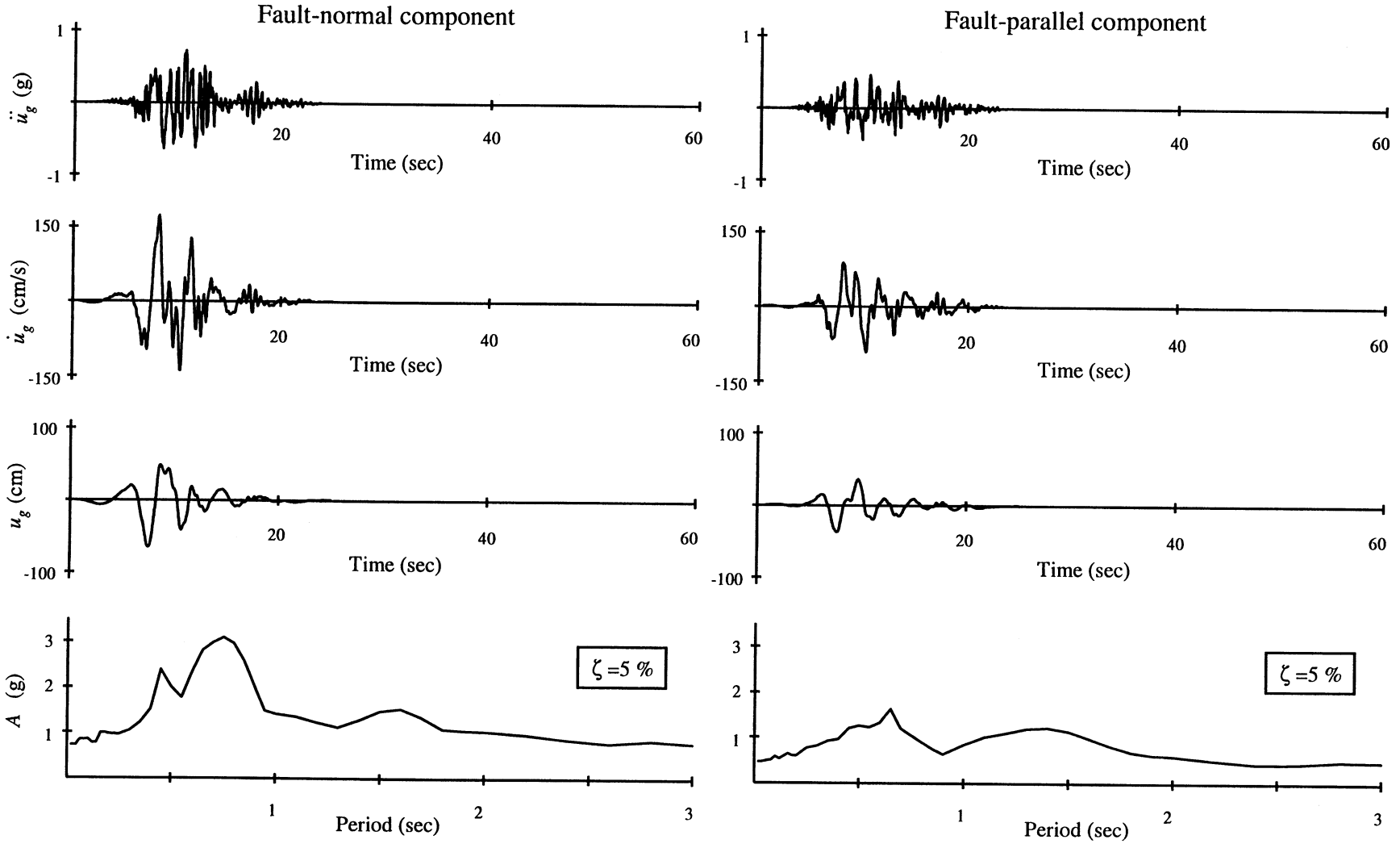

Figure B.2. Event # 2 in the ensemble of recorded near-fault ground motions.

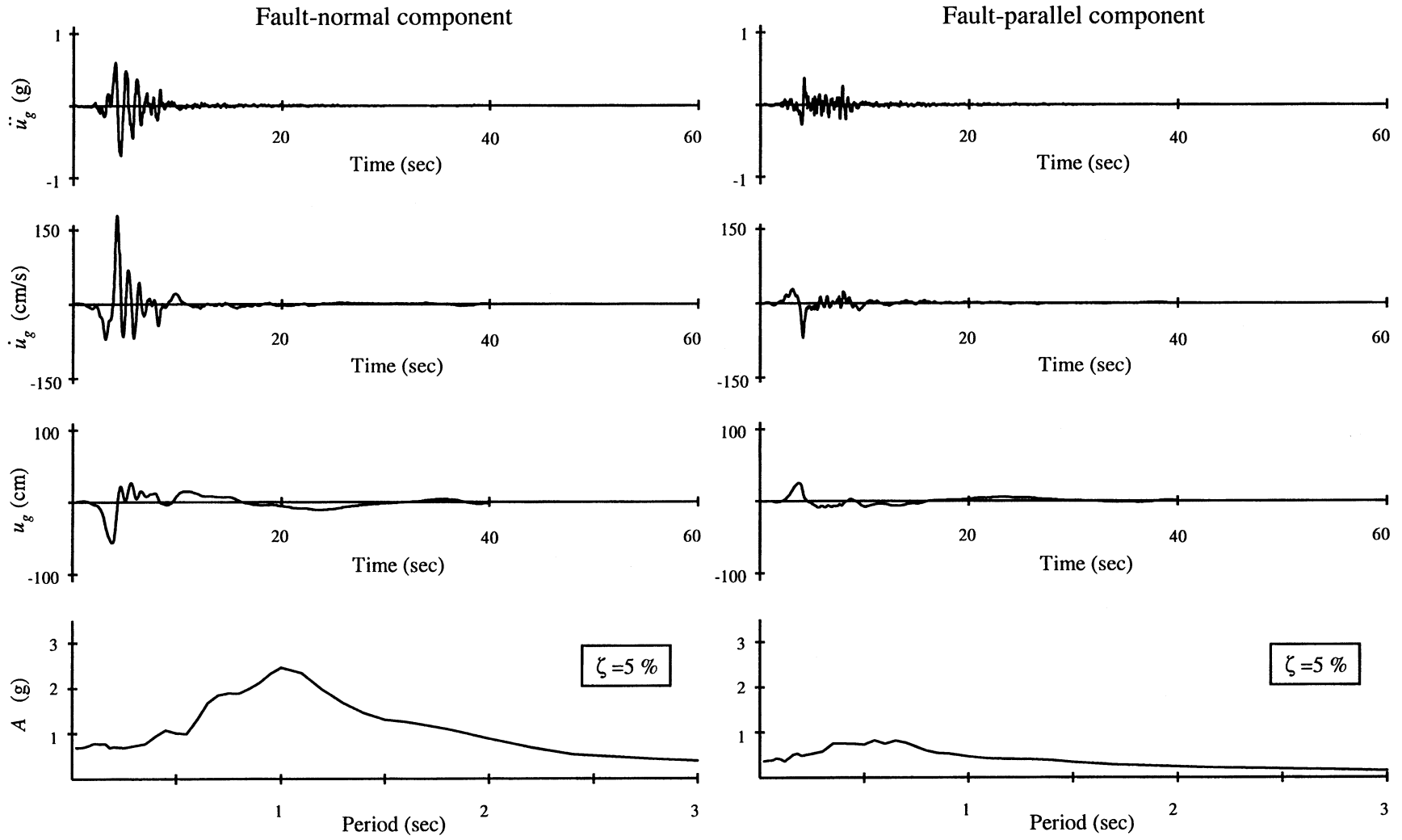

Figure B.3. Event # 3 in the ensemble of recorded near-fault ground motions.

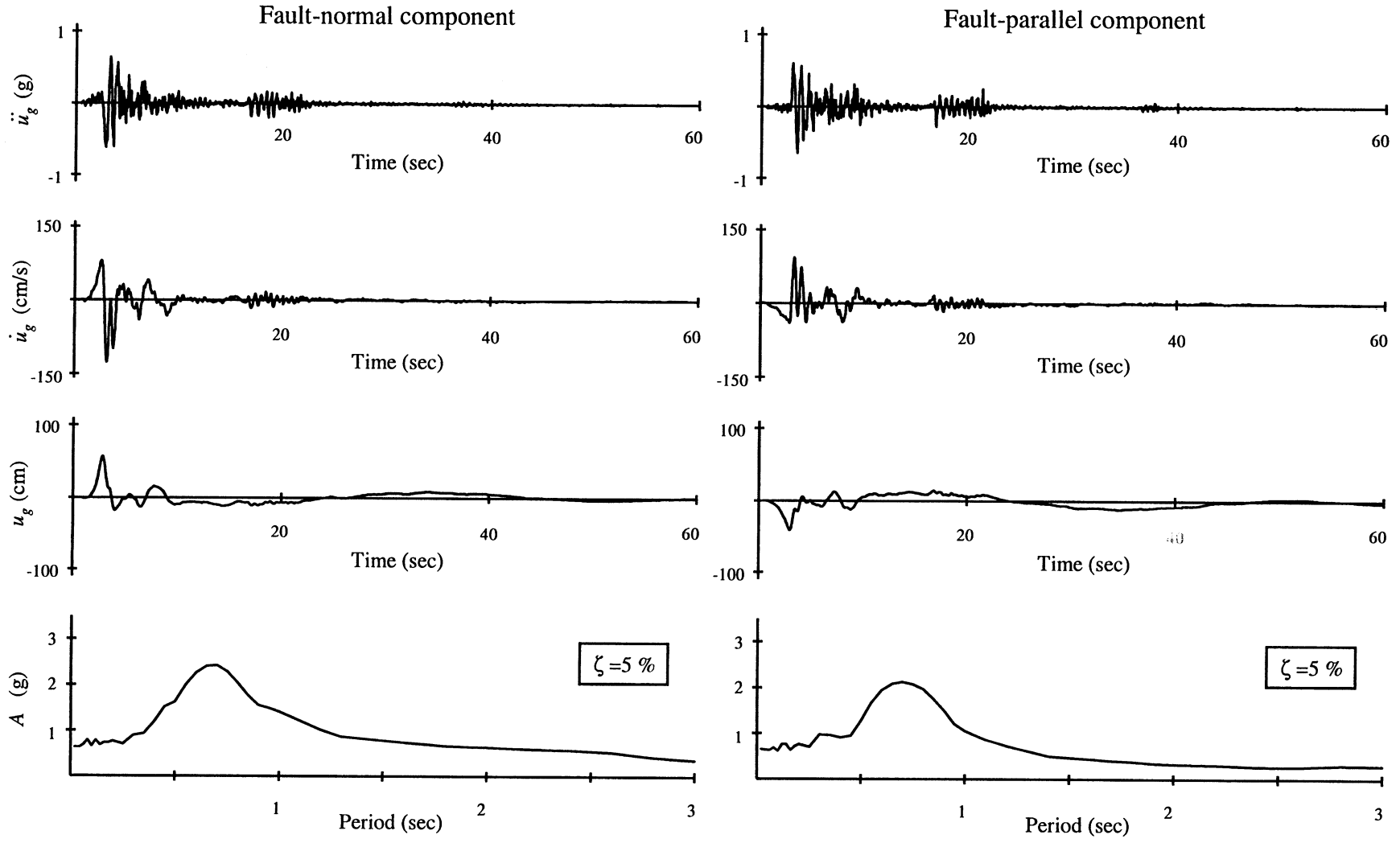

Figure B.4. Event # 4 in the ensemble of recorded near-fault ground motions.

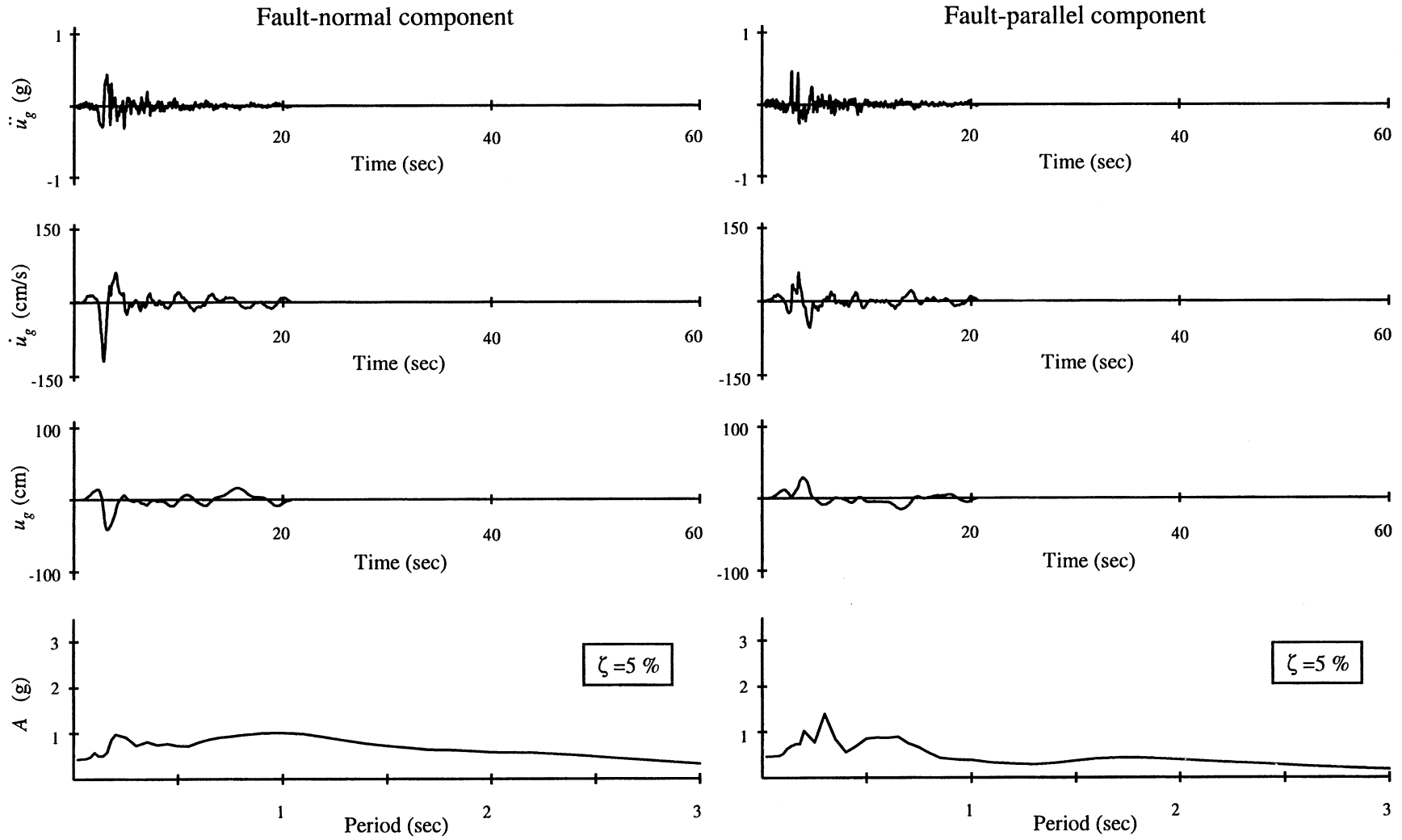

Figure B.5. Event # 5 in the ensemble of recorded near-fault ground motions.

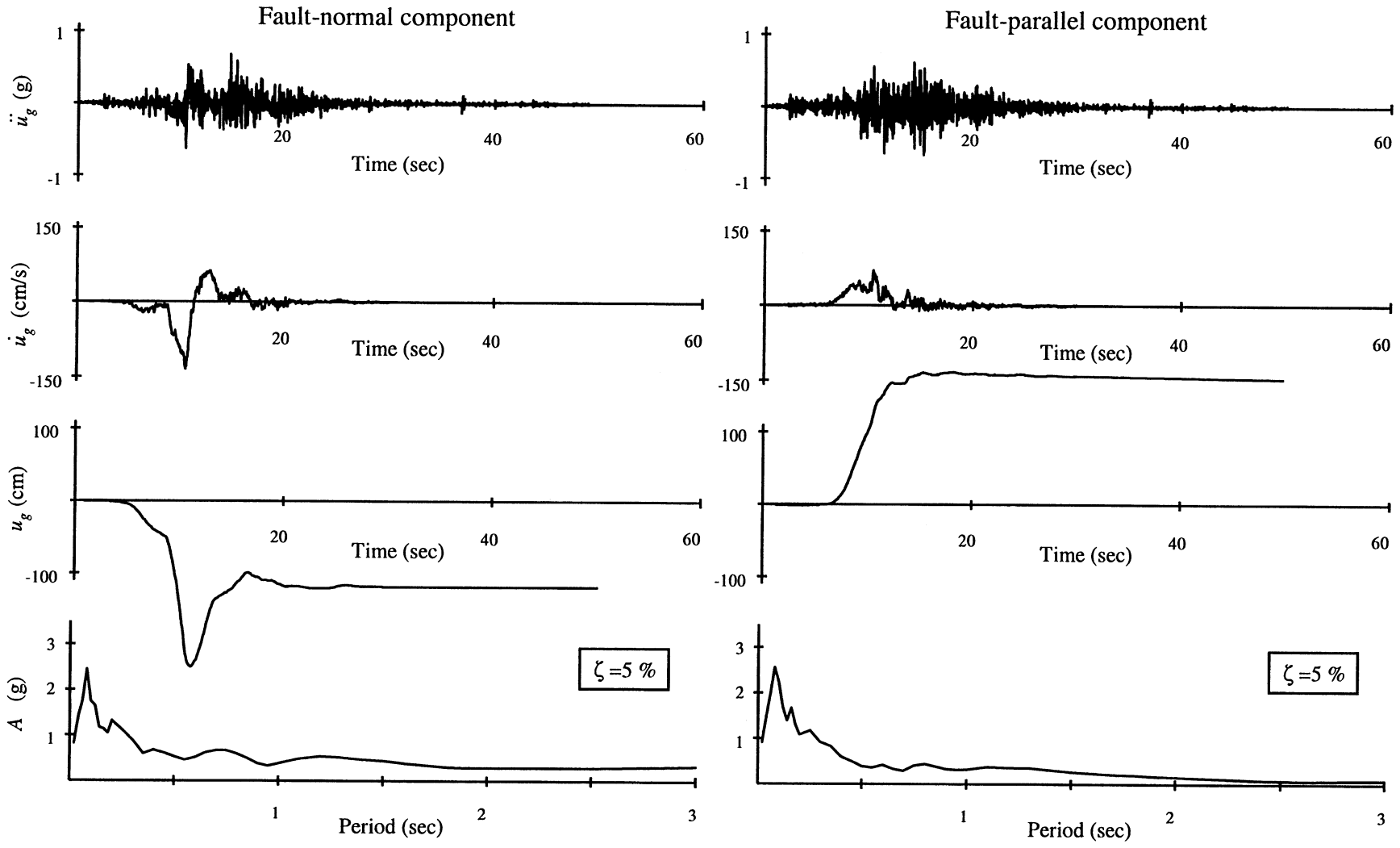

Figure B.6. Event # 6 in the ensemble of recorded near-fault ground motions.

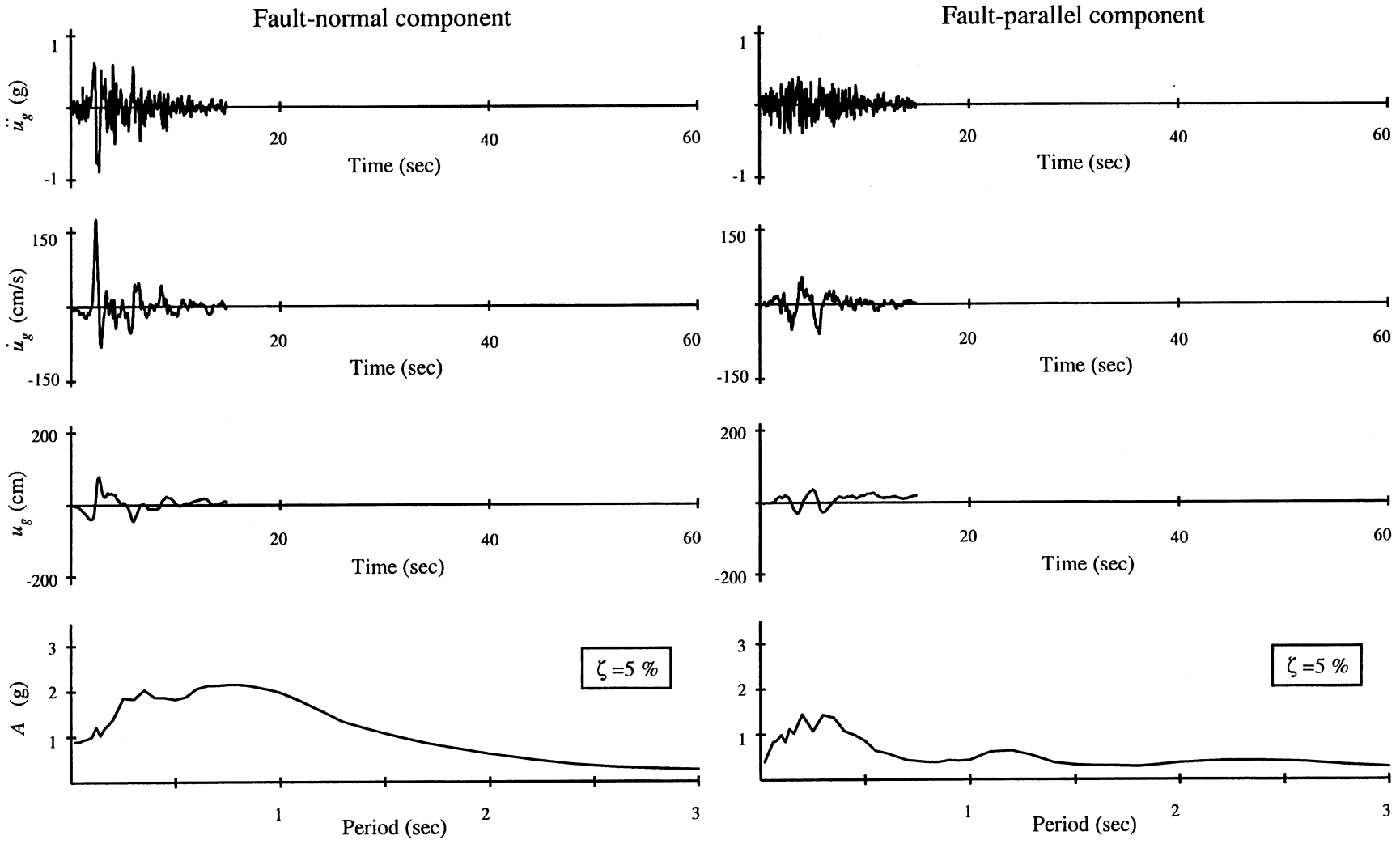

Figure B.7. Event # 7 in the ensemble of recorded near-fault ground motions.

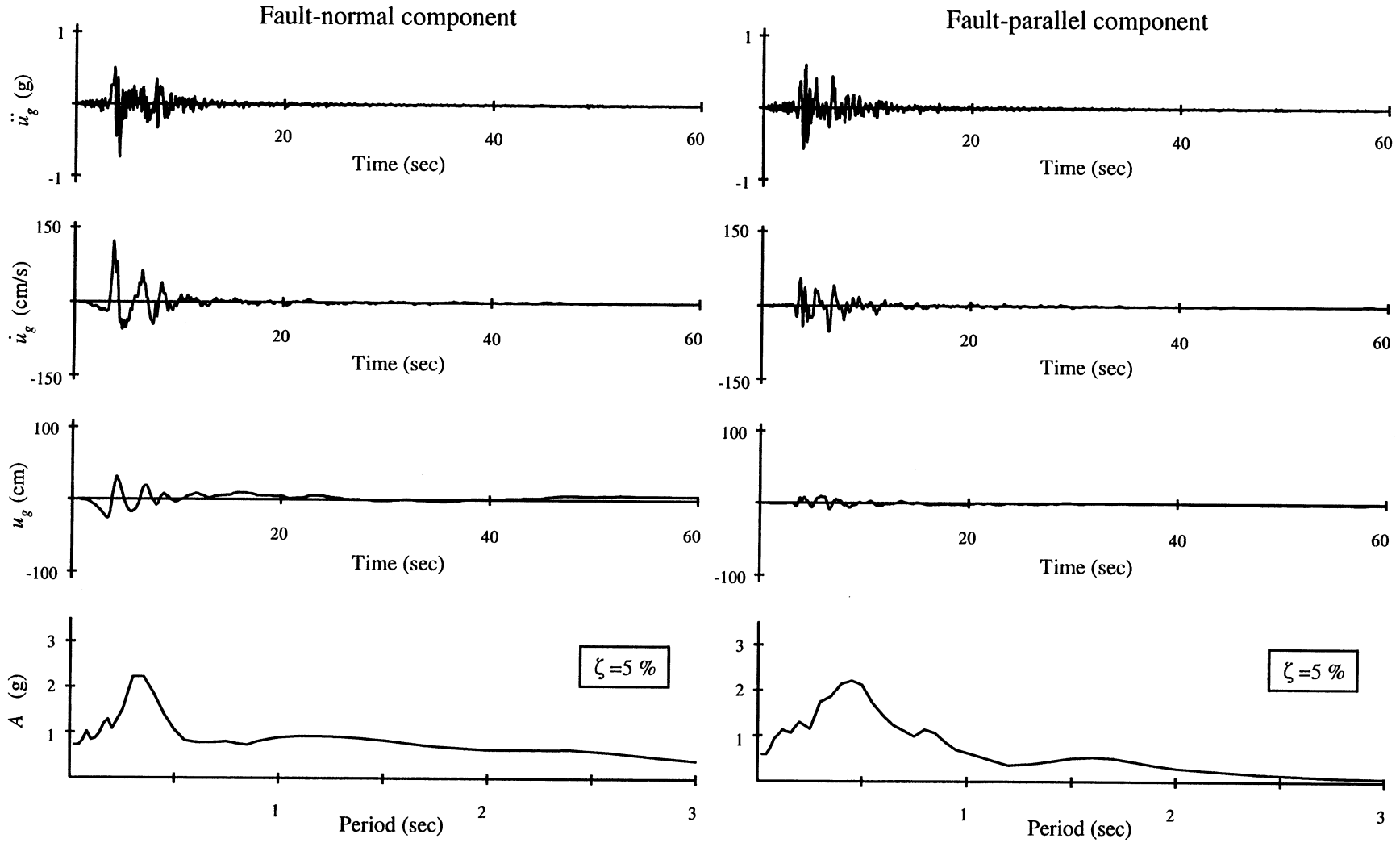

Figure B.8. Event # 8 in the ensemble of recorded near-fault ground motions.

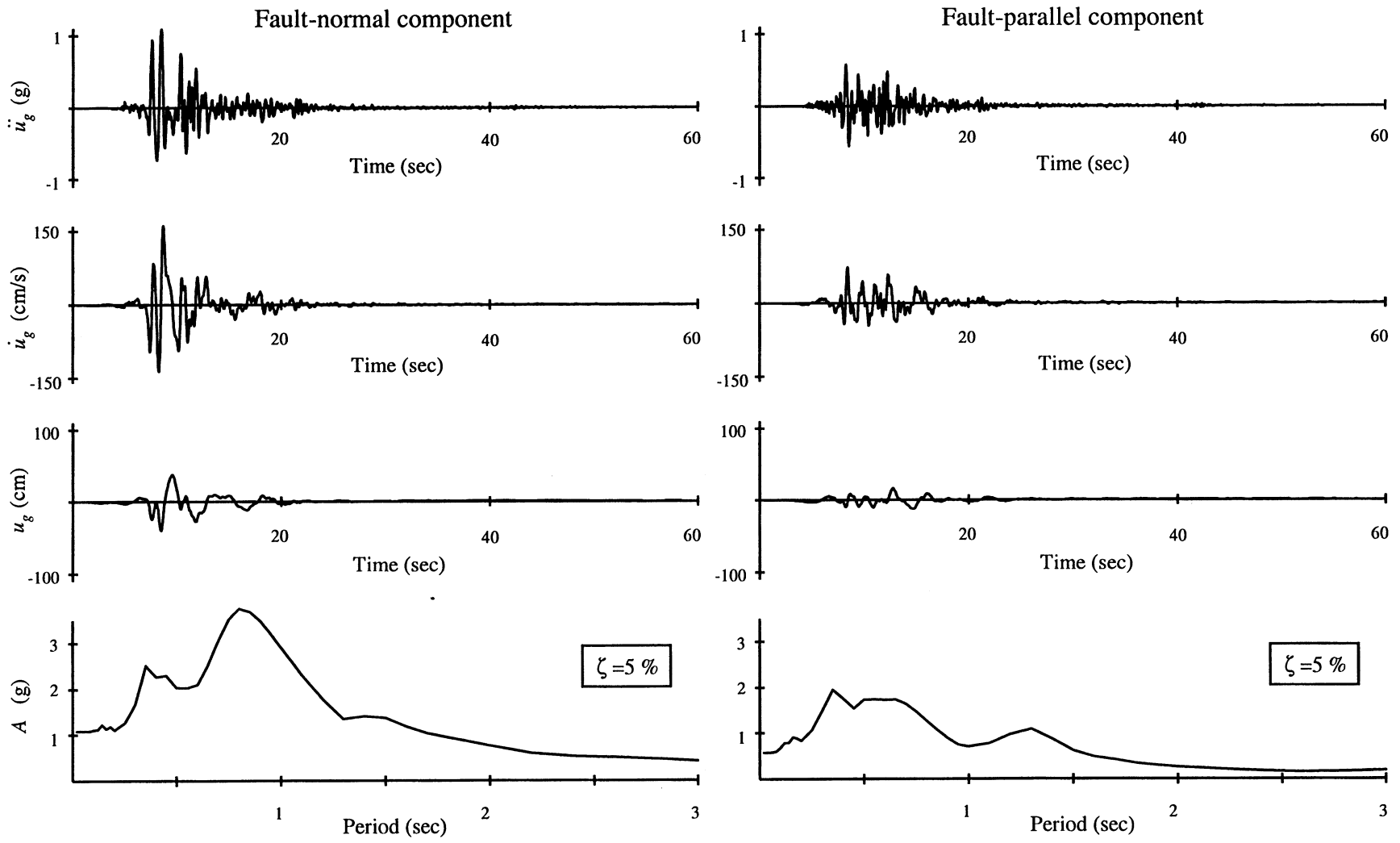

Figure B.9. Event # 9 in the ensemble of recorded near-fault ground motions.

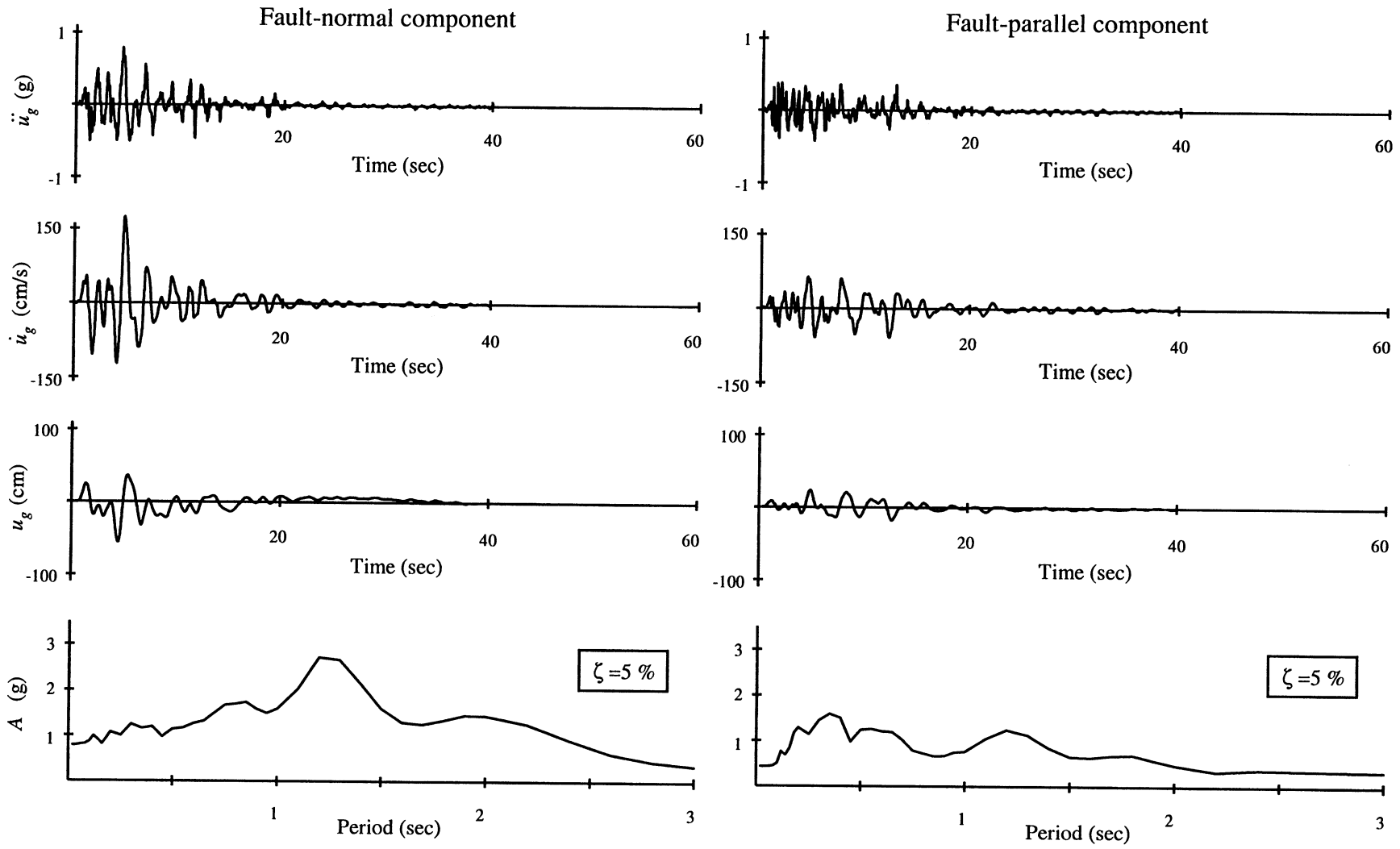

Figure B.10. Event # 10 in the ensemble of recorded near-fault ground motions.

APPENDIX C

SYNTHETIC NEAR-FAULT GROUND MOTIONS

Table C.1 lists the target events used to generate the ensembles of synthetic near-fault ground motions. Also listed in this table are the original SAC identification numbers assigned to these records. As indicated in Table C.1, all events in these ensembles are representative of magnitude $M_w = 7.1$ earthquakes. Events 1–5, which for the first ensemble of synthetic ground motions, were simulated using the Elysian Park fault as a basis. Events 6–10, which for the second ensemble, represent ground motions due to an earthquake on the Palos Verdes fault. The ground motions are either normal or parallel to the strike of the fault, as indicated in Table C.1. Additional details of these records are described by Somerville et al. (1997).

Each pair of ground acceleration records along with the corresponding ground velocity and displacement records and the pseudo-acceleration response spectra are plotted in Figures C.1 through C.10. For each event, the fault-normal component of ground motion is shown on the left-hand side of the figure.

Table C.1. Target events used to generate the ensemble of synthetic near-fault ground motions.

Event	SAC #	Description	
1	NF21	Elysian Park ($M_w = 7.1$)	Fault-normal
	NF22	Elysian Park ($M_w = 7.1$)	Fault-parallel
2	NF23	Elysian Park ($M_w = 7.1$)	Fault-normal
	NF24	Elysian Park ($M_w = 7.1$)	Fault-parallel
3	NF25	Elysian Park ($M_w = 7.1$)	Fault-normal
	NF26	Elysian Park ($M_w = 7.1$)	Fault-parallel
4	NF27	Elysian Park ($M_w = 7.1$)	Fault-normal
	NF28	Elysian Park ($M_w = 7.1$)	Fault-parallel
5	NF29	Elysian Park ($M_w = 7.1$)	Fault-normal
	NF30	Elysian Park ($M_w = 7.1$)	Fault-parallel
6	NF31	Palos Verdes ($M_w = 7.1$)	Fault-normal
	NF32	Palos Verdes ($M_w = 7.1$)	Fault-parallel
7	NF33	Palos Verdes ($M_w = 7.1$)	Fault-normal
	NF34	Palos Verdes ($M_w = 7.1$)	Fault-parallel
8	NF35	Palos Verdes ($M_w = 7.1$)	Fault-normal
	NF36	Palos Verdes ($M_w = 7.1$)	Fault-parallel
9	NF37	Palos Verdes ($M_w = 7.1$)	Fault-normal
	NF38	Palos Verdes ($M_w = 7.1$)	Fault-parallel
10	NF39	Palos Verdes ($M_w = 7.1$)	Fault-normal
	NF40	Palos Verdes ($M_w = 7.1$)	Fault-parallel

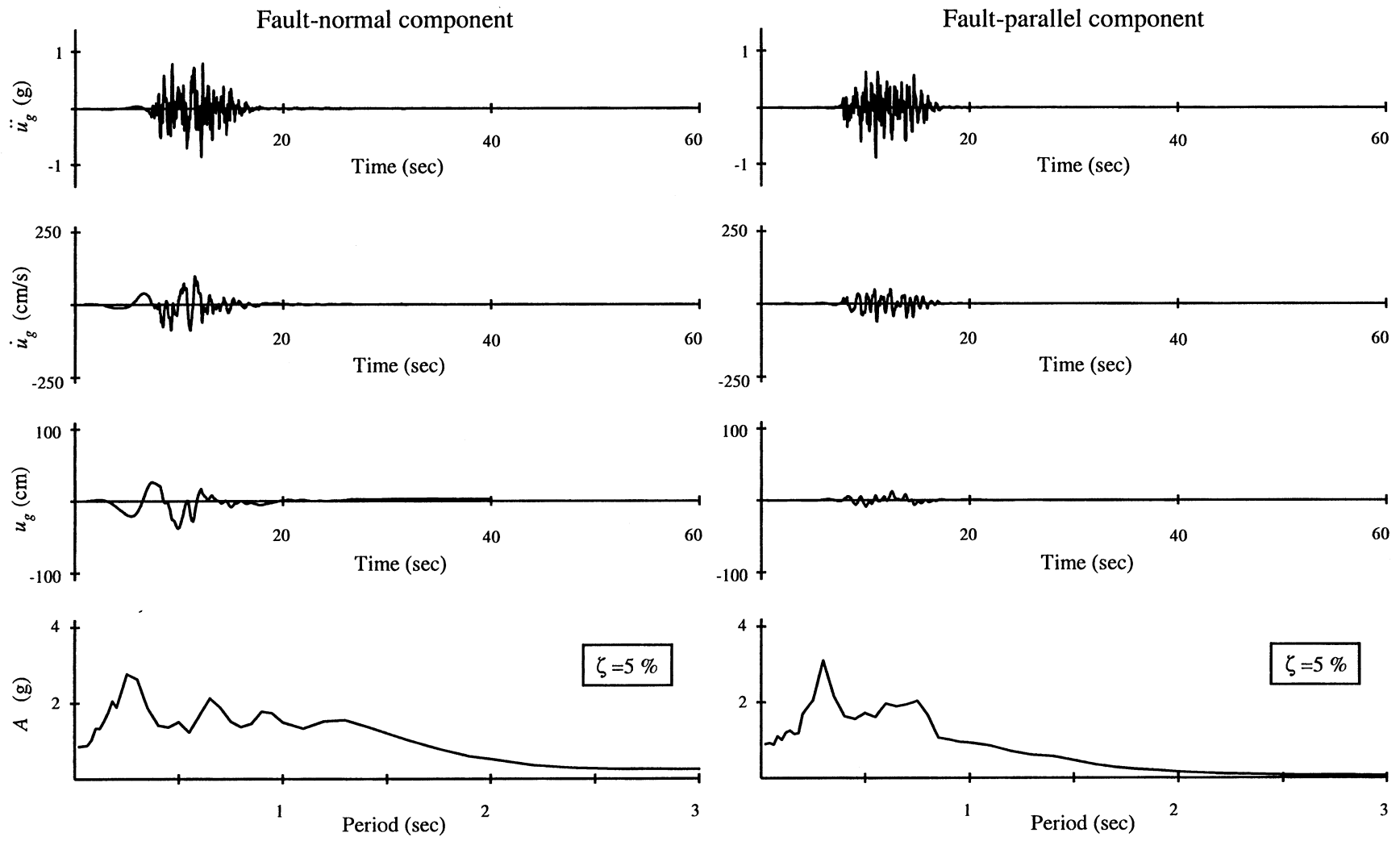

Figure C.1. Event # 1 in the ensemble of synthetic near-fault ground motions.

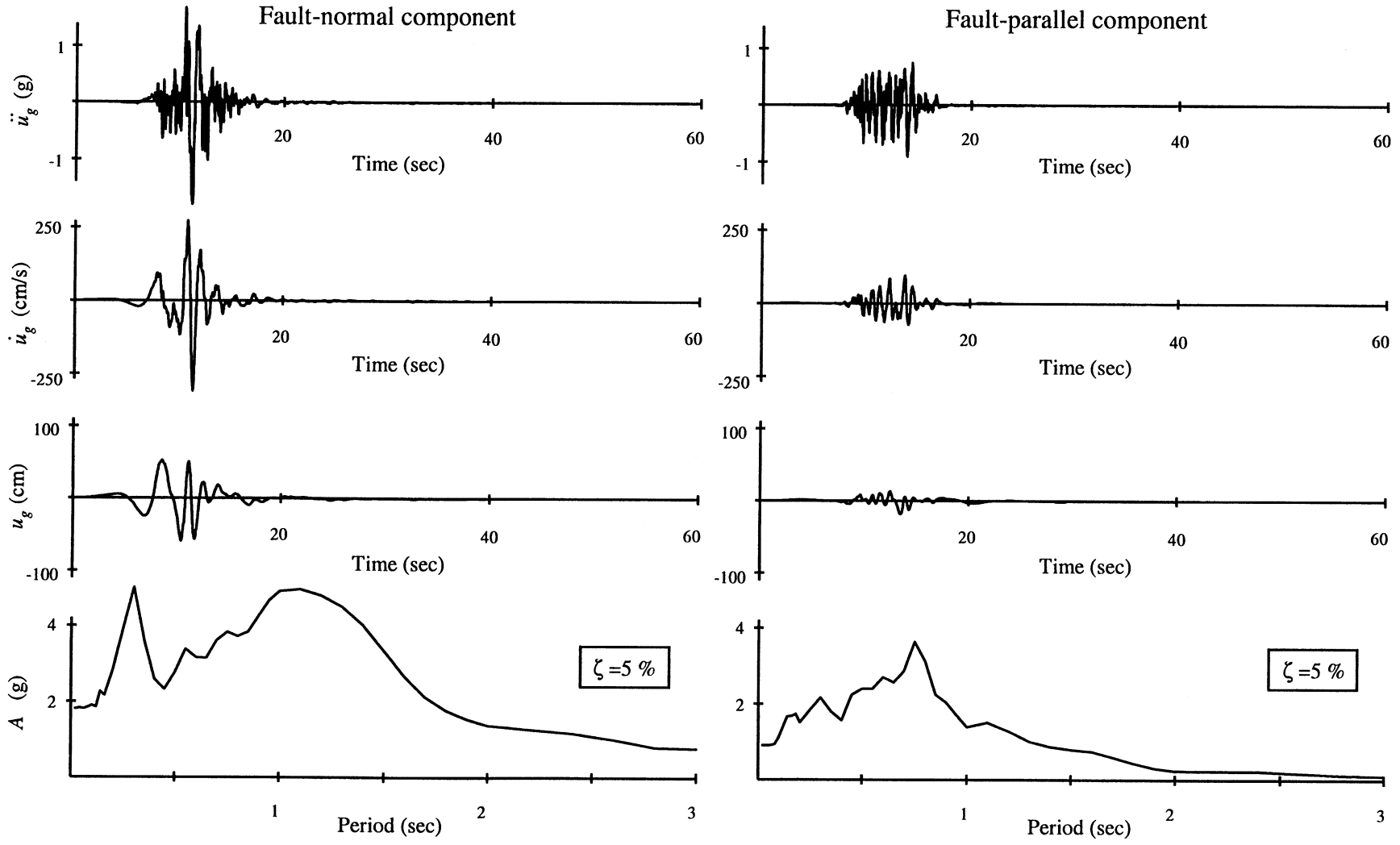

Figure C.2. Event # 2 in the ensemble of synthetic near-fault ground motions.

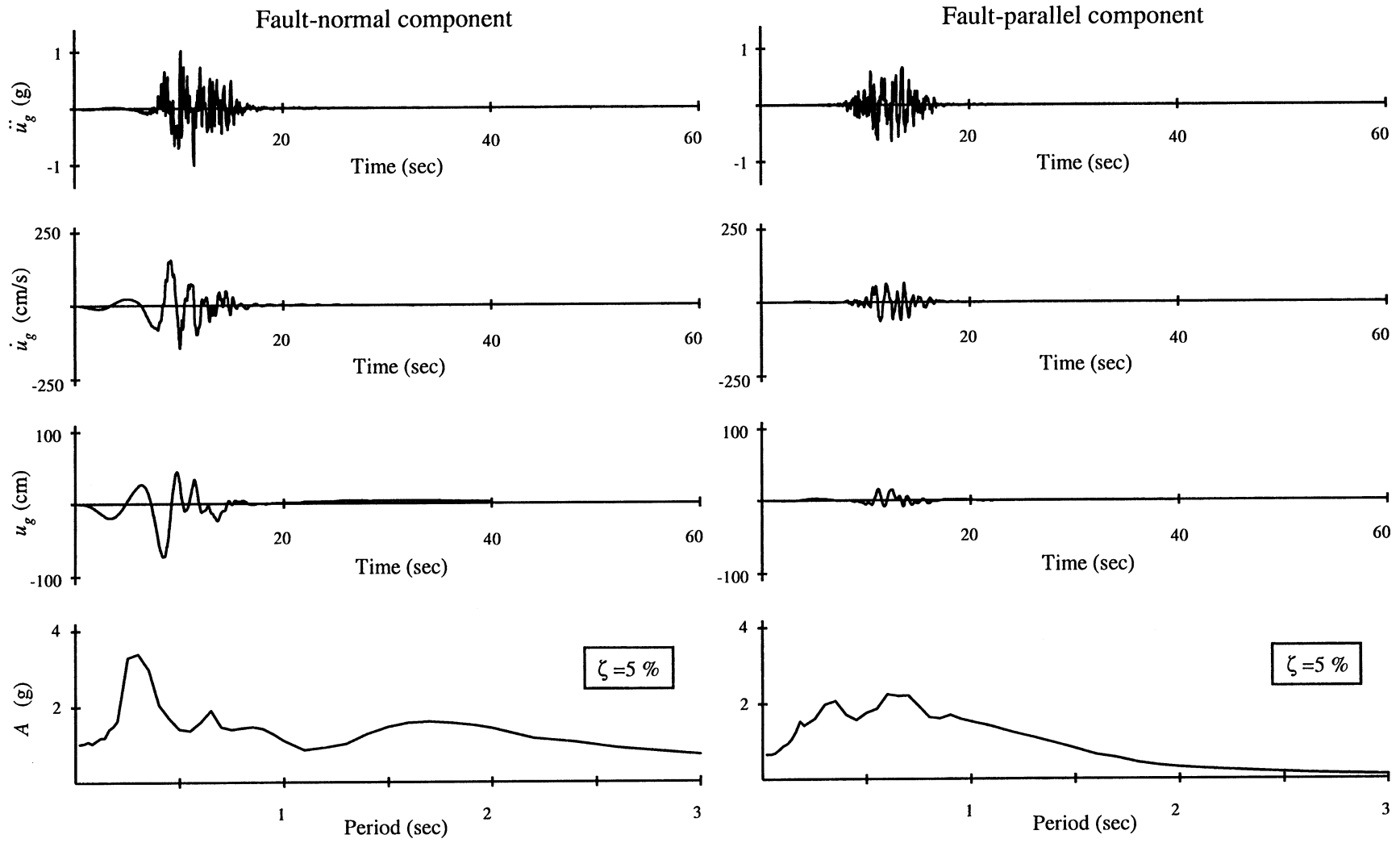

Figure C.3. Event # 3 in the ensemble of synthetic near-fault ground motions.

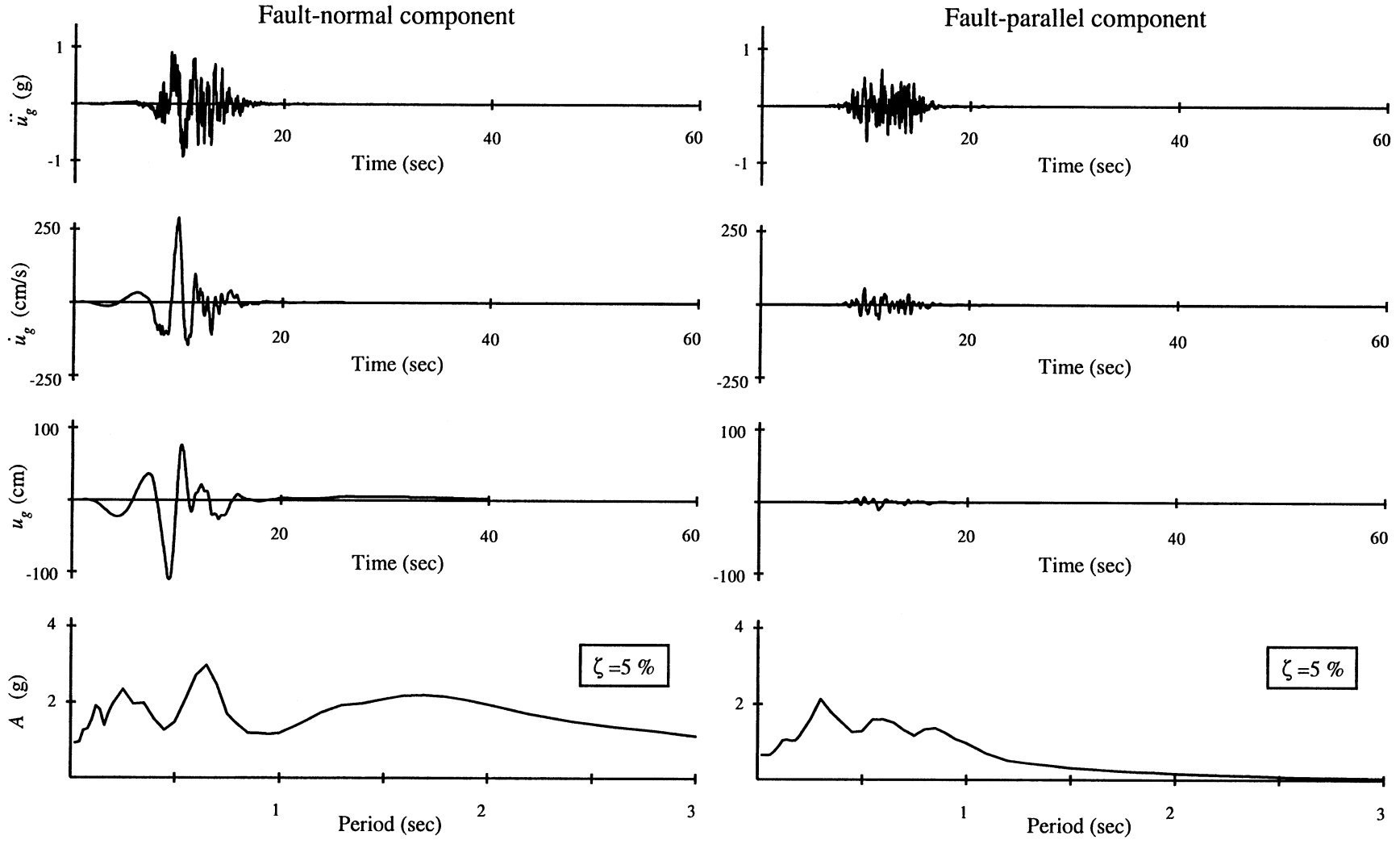

Figure C.4. Event # 4 in the ensemble of synthetic near-fault ground motions.

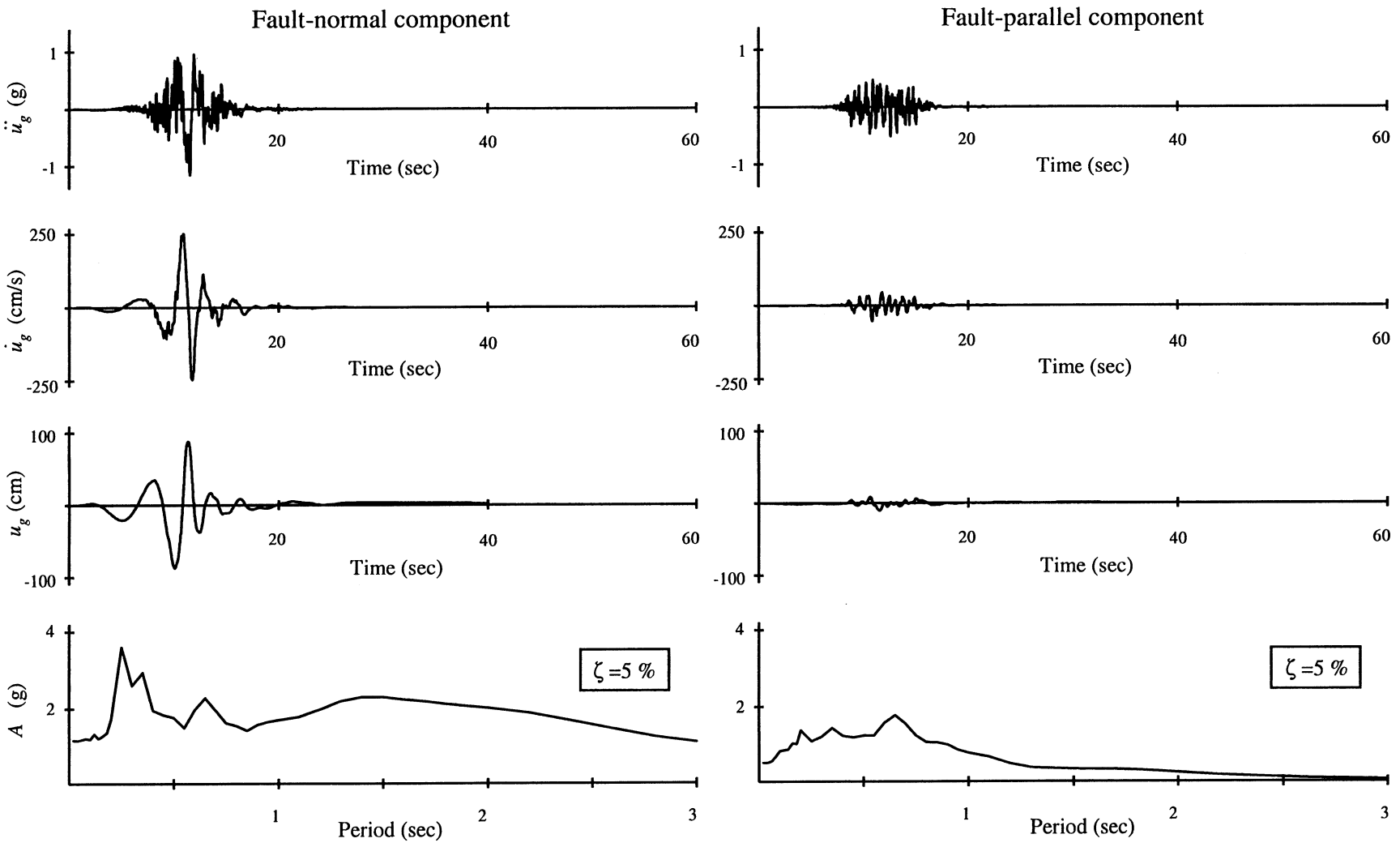

Figure C.5. Event # 5 in the ensemble of synthetic near-fault ground motions.

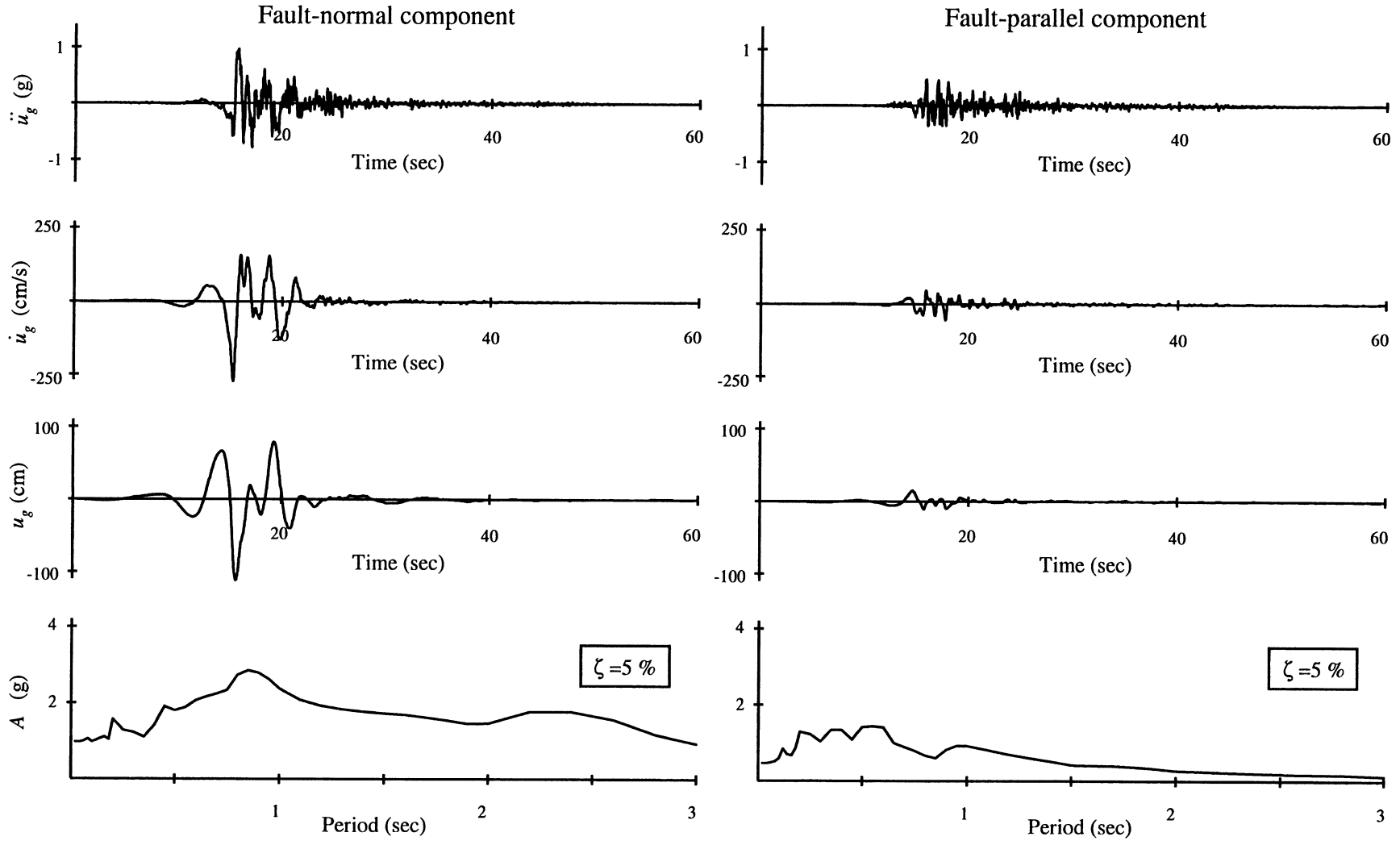

Figure C.6. Event # 6 in the ensemble of synthetic near-fault ground motions.

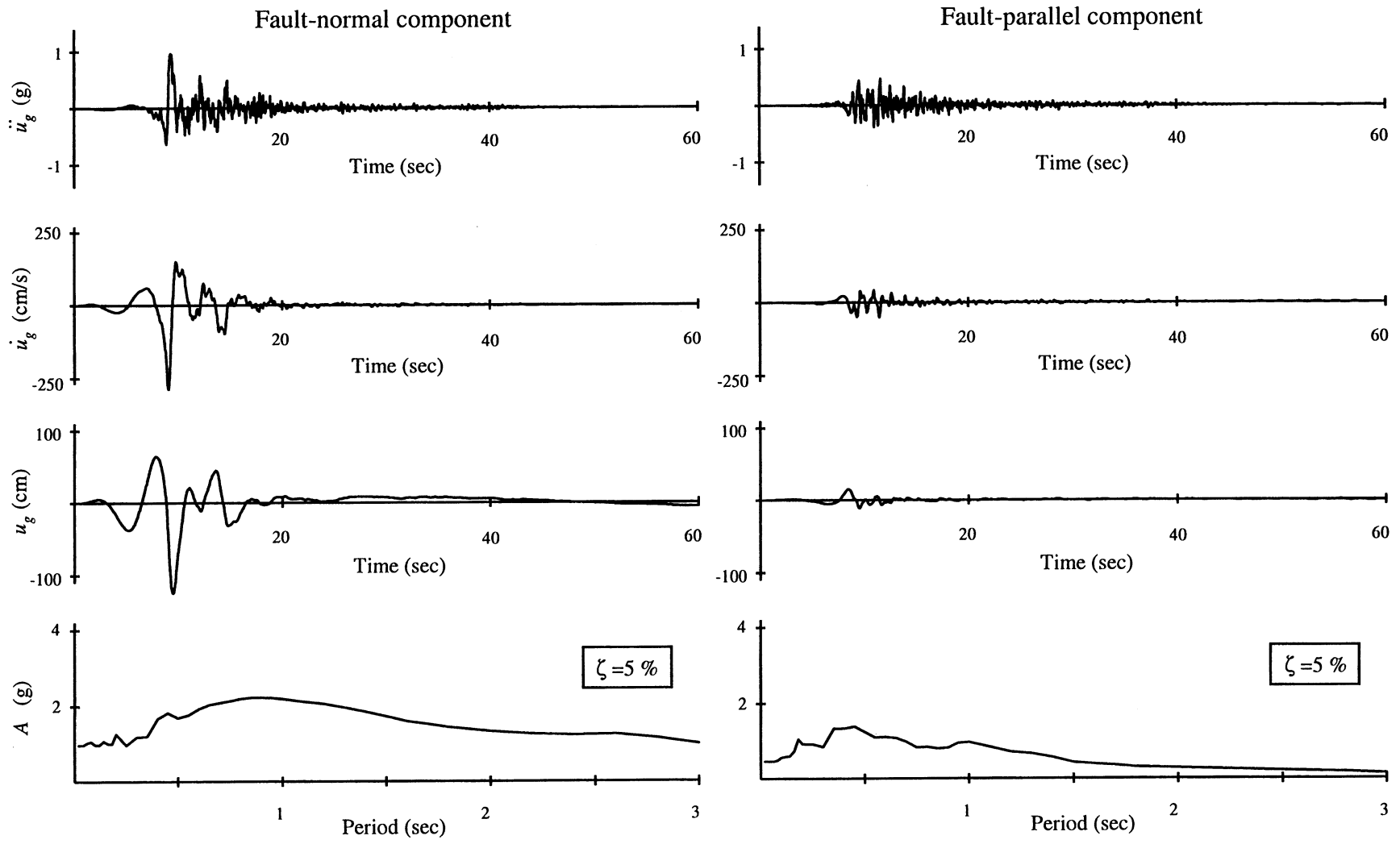

Figure C.7. Event # 7 in the ensemble of synthetic near-fault ground motions.

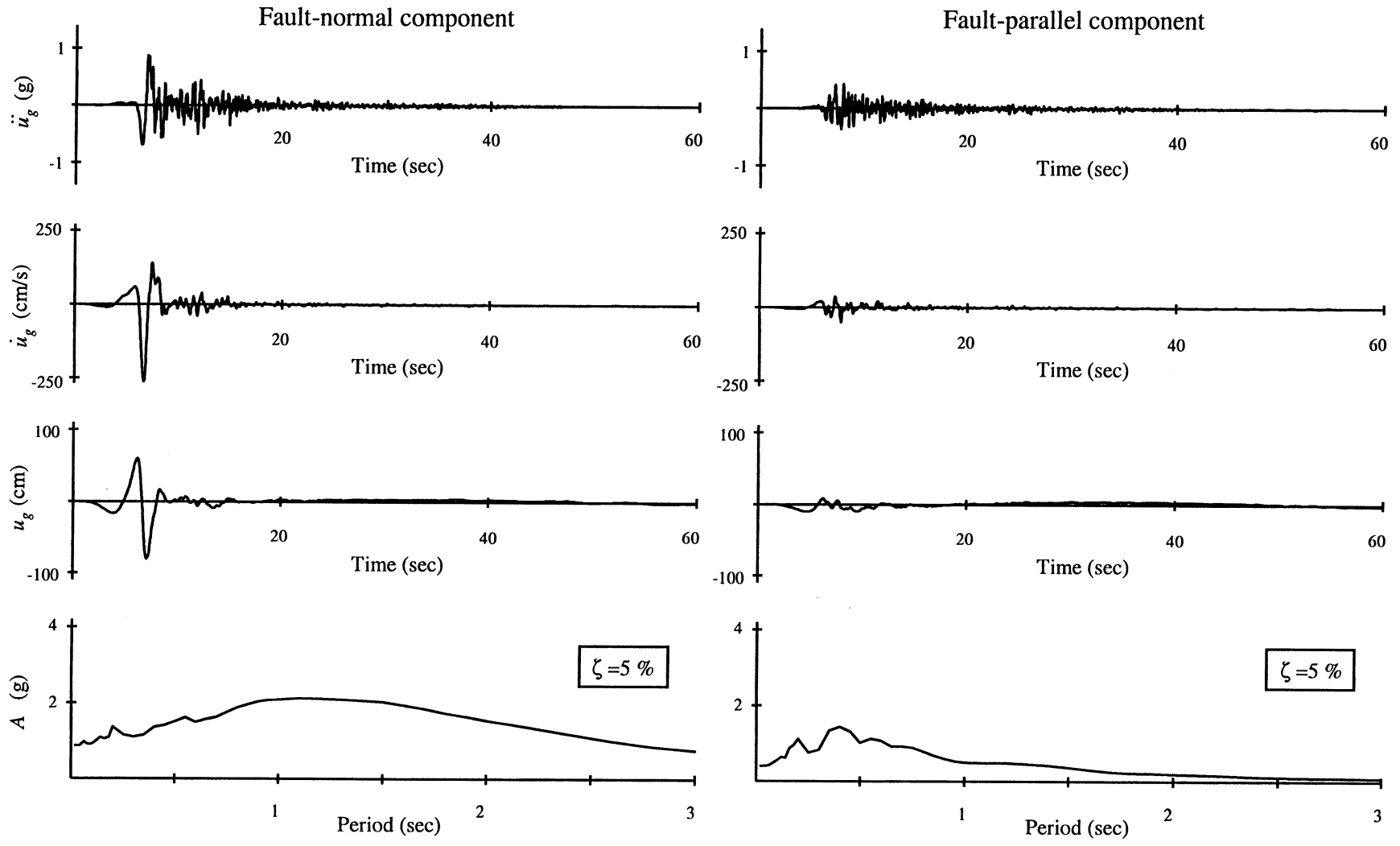

Figure C.8. Event # 8 in the ensemble of synthetic near-fault ground motions.

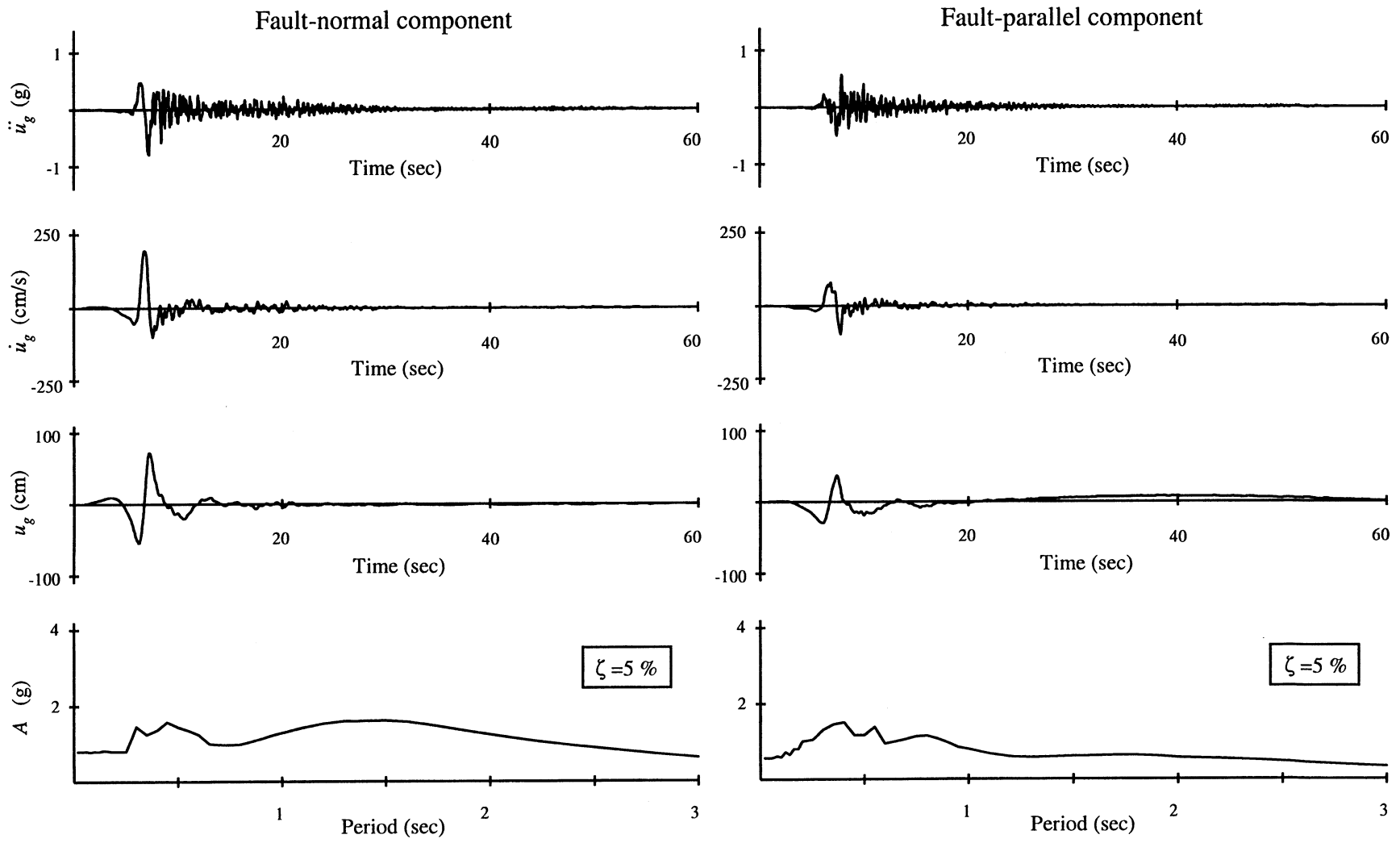

Figure C.9. Event # 9 in the ensemble of synthetic near-fault ground motions.

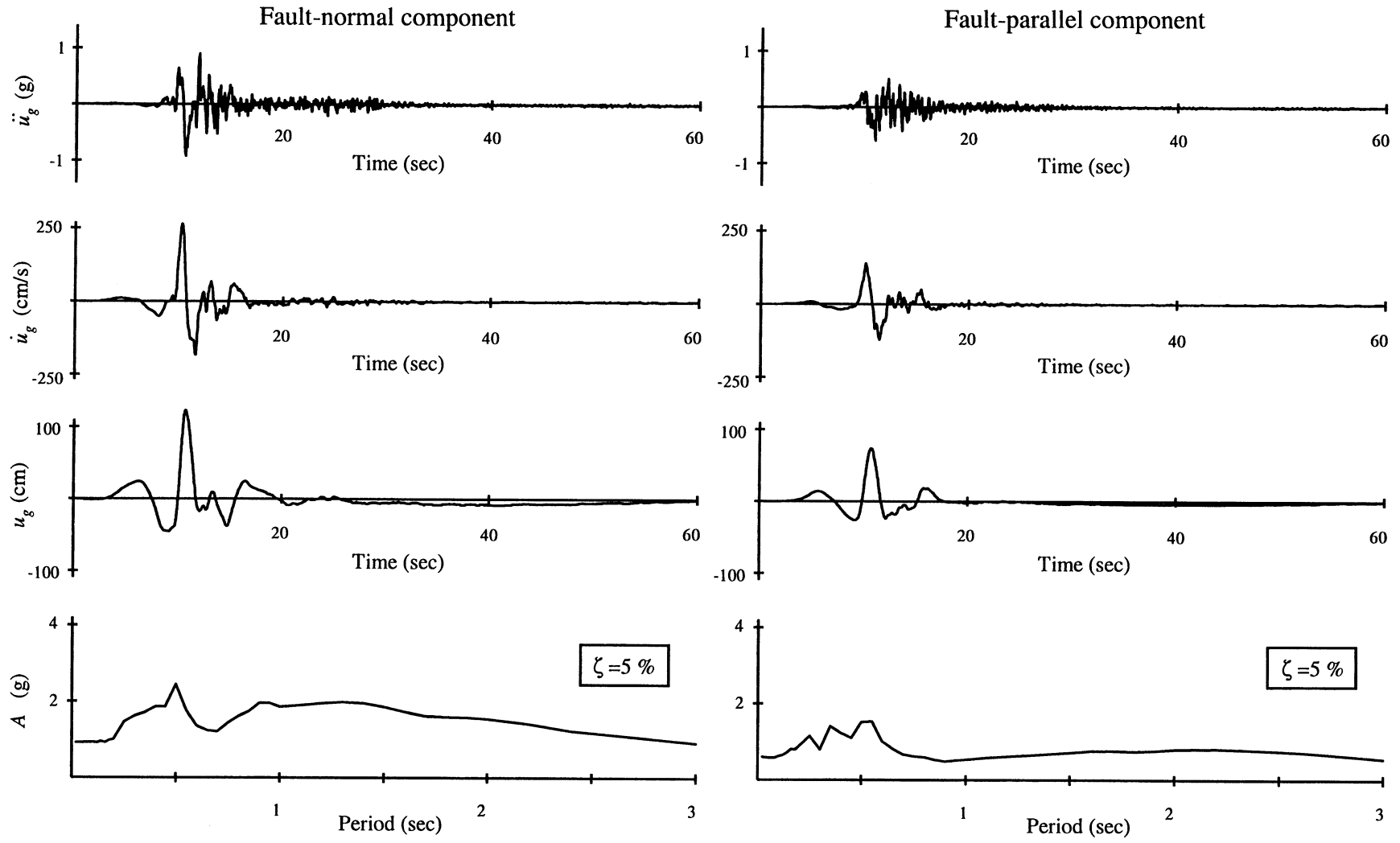

Figure C.10. Event # 10 in the ensemble of synthetic near-fault ground motions.